On the phenomenon and potential applications of pulsed laser-reshaped silver nanoparticles embedded in soda-lime glass

Mateusz Amadeusz Tyrk

Supervisors: Prof. Amin Abdolvand,

Prof. William Allan Gillespie

A thesis submitted to the School of Science & Engineering,
University of Dundee for the degree of Doctor of Philosophy
(PhD)

April 2018

Table of Contents

List of Figures

List of Tables

Acknowledgments

I would like to express my deepest appreciation to my supervisors, Professors Allan William Gillespie and Amin Abdolvand, for giving me the opportunity to complete my PhD in MAPS group at the University of Dundee.

I would like to thank all my colleagues from the University of Dundee for help and support, as well as all the people from the LA^{3}NET for having a great time!

I would like to thank the team in the Daresbury Laboratory for a great collaboration and many fruitful discussions about nonlinearities in nanoparticles.

I would like to thank my whole family for support: Tyrk, Jeśman, Lipka, Zapał and Morawska families.

Warmest thanks to my partner Dr Paulina O. Morawska for the day-to-day support, help and encouragement.

I am also very grateful to the PowerPhotonic team for support.

Another acknowledgment is owed to the *BassDrive* online radio. Without its crisp drum & bass I would have never finished writing this thesis.

Declaration

I, Mateusz Amadeusz Tyrk am the author of this thesis. I have consulted all the cited references. The work of which the thesis is a record has been done by me, and it has not been previously accepted for a higher degree.

Mateusz Amadeusz Tyrk

List of publications

The following publication of the author are related to this thesis:

1. M. A. Tyrk, W. A. Gillespie, G. Seifert, and A. Abdolvand, "Picosecond pulsed laser induced optical dichroism in glass with embedded metallic nanoparticles." *Opt. Express*, vol. 21, no. 19, pp. 21823–8, 2013.
2. M. A. Tyrk, S. A. Zolotovskaya, W. A. Gillespie, and A. Abdolvand, "Radially and azimuthally polarized laser induced shape transformation of embedded metallic nanoparticles in glass." *Opt. Express*, vol. 23, no. 18, pp. 716–718, 2015.
3. M. A. Tyrk & S. A. Zolotovskaya, A. Stalmashonak, W. A. Gillespie, and A. Abdolvand, „On second harmonic generation and multiphoton-absorption induced luminescence from laser-reshaped silver nanoparticles embedded in glass." *Nanotechnology*, vol. 27, 435703, 2016.

The following presentations of the author are related to this thesis:

4. M. A. Tyrk, W. A. Gillespie, and A. Abdolvand "Elongation of spherical silver nanoparticles embedded in a glass matrix using picosecond laser irradiation", CLEO Munich 2013
5. M. A. Tyrk, A. Abdolvand, W. A. Gillespie, S. A. Zolotovskaya "A novel 'Metamaterial' for Electro-Optic Electron Bunch Profile Monitors", FEL 2014 Basel, Switzerland
6. M. A. Tyrk, S. A. Zolotovskaya, W. A. Gillespie, and A. Abdolvand "Polarisation dependent reshaping of metallic nanoparticles embedded in a glass matrix using picosecond pulsed laser irradiation" NANOSMAT 2014, Ireland
7. M. A. Tyrk, W. A. Gillespie, and A. Abdolvand "An Advanced electro-optic bunch time profile monitor for CLIC (development of novel materials and techniques)", LA^{3}NET 1st school on laser applications, 2012, France
8. M. A. Tyrk, A. Abdolvand, and W. A. Gillespie "Nanotechnology for Applications at Accelerator Facilities", Symposium on Lasers and Accelerators for Science & Society, 2015, UK
9. M. A. Tyrk, A. Abdolvand, and W. A. Gillespie "Laser reshaping of metallic nanoparticles" LA^{3}NET Advanced School on Laser Applications at Accelerator, 2014, Spain

Other contributions of the author:

10. A. H. Quarterman, M. A. Tyrk, and K. G. Wilcox, “Z-scan measurements of the nonlinear refractive index of a pumped semiconductor disk laser gain medium.” APL, **106**, 011105, 2015

Abstract

This thesis presents studies on a novel ‘meta-material’ as a potential candidate to replace the traditional Electro-Optic crystals (GaP, ZnTe) used in ultrashort bunch monitors for electron/positron accelerators. This study is aimed at showing the linear and non-linear optical properties of such materials, and creating a toolbox for both optical characterisation and manipulation of their properties using of an ultra-short pulsed laser.

The material studied throughout this thesis is a composite of silver nanoparticles (a “nanocomposite”) embedded within soda-lime glass. The Surface Plasmon Resonance (SPR) is a feature of these particles that is responsible for its unique optical properties. It is shown in this work how SPR is utilised for shape modification of silver nanoparticles with the use of a ps- pulsed laser with various laser beam polarisations. The impact of linear polarisation irradiation is investigated. It is found that multipulse irradiation has the effect of elongating nanoparticles to form prolate spheroids, which results in a dichroic effect on the composite as a whole, caused by the anisotropic SPR band shift.

It is also shown that changing the laser polarisation from linear to radial and/or azimuthal changes the character of the reshaped nanoparticles. It was observed that a localised change of ellipsoid orientation is achieved, resulting in a non-directionally-dependent SPR band shift.

Second Harmonic Generation (SHG) has been observed from reshaped nanoparticles embedded in soda-lime glass. A comparison of the effect was made between ps-pulsed reshaped, fs-pulsed reshaped and mechanically stretched samples containing silver nanoparticles. Multiphoton Absorption Induced Luminescence (MAIL) was observed along with the SHG and characterised for the various laser polarisation components. The dependence of the aforementioned effects on the elongated nanoparticle aspect ratio was shown to have a great impact.

A novel method for reshaped nanoparticles characterisation is presented. It is based on the laser-induced SHG and MAIL signal and is proved to give a precise measurement of the nanoparticle shape and orientation.

Frequency Resolved Optical Gating (FROG) measurement of a fs-pulse is measured with great accuracy, in the case where the BBO nonlinear crystal is replaced by the

reshaped nanoparticle composite. This was demonstrated to be caused by the anisotropic SHG of the ellipsoidal nanoparticles.

Preliminary THz based measurements were performed as a part of a feasibility study of the application of these composites in the EO-based detection of ultrashort electron bunches. Future work is suggested in order to achieve more efficient EO detection.

1 Introduction

1.1 Overview and motivation

Electro-optic techniques have been used extensively worldwide to measure longitudinal bunch profiles of electron beams, especially in circumstances when a compact and non-destructive diagnostic is needed [1]–[7]. The current techniques are fundamentally limited by the optical bandwidth of the crystalline materials employed - these are typically ZnTe and GaP. Phonon resonances in the optical response of these materials can easily lead to artefacts in the measured bunch profile [8], [9]. In order to extend the optical frequency response of these materials it is essential to construct new materials or new techniques of measurement that could overcome this limitation. The goal of this thesis is based on finding novel materials that could potentially be used for this application.

The need for a novel material/crystal comes from the demand for ultra-short electron bunch lengths in machines worldwide. Advanced Light Sources like Free Electron Lasers will soon be using bunch lengths of ~10 fs (@FWHM) or shorter [10]. In addition, particle colliders like the Compact Linear Collider (CLIC) at CERN or International Linear Collider (ILC) involve e^- and e^+ collisions of short bunches (~300 fs rms) with high charge and quality [11]. Future electron and photon sources, especially the newly-developed Laser Plasma Wakefield Accelerators (LPWAs) currently under development in the UK, USA, Germany, among others, will generate bunches in the 1-5 fs (@FWHM) regime and even shorter, and therefore new methods need to be devised to characterise such ultra-short bunches with good precision [12]–[16]. In order to address these issues, ongoing improvements of already existing electron bunch diagnosis methods exist, especially in the field of transverse deflecting cavities [17], [18]. This method is however a destructive method of diagnostic and non-destructive methods are needed. The EO techniques that are being used so far rely on the interaction of the THz field induced in the crystal by the Coulomb field of the electron bunch that passes next to it [1], [3], [8], [9], [19]–[27]. The shorter the bunch becomes, the wider its profile in the frequency domain develops. This has to be addressed by the EO crystal, and with the crystals used so far, the THz bandwidth overcomes the bandwidth of the EO crystals and will overcome it even more in the future [8]. The intrinsic property of crystalline ZnTe and GaP is their optical response to

certain frequencies and the fact that the crystalline structure's phonons are being excited at ~4THz in case of thin (~100 μm) ZnTe and ~10 THz in case of thin GaP [28], [29]. The phonon response can effectively damp the resulting signal, destroying the reliability of the measurement itself [30]. The perfect material would therefore lack a crystalline structure but at the same time have a strong electro-optic coefficient. Because the EO techniques, which will be described in the next chapter, work on a principle of the Pockels effect in the crystal employed, a $\chi^{(2)}$ tensor is the characteristic property of the optical material [31], [32]. It is therefore the main motivation of this thesis to present a novel material which does not have a crystalline structure and still possess the main non-linear optical properties, which can be characterised in terms of a phenomenon that is also based on the intrinsic property of the material that possesses the $\chi^{(2)}$ tensor element - that is, Second Harmonic Generation. It has to be mentioned that other materials exist, which are potentially good candidates for EO detection (DAST [4], [32] or GaSe [33], [34]) but these will not be discussed in this thesis. The material presented in this thesis will be a silver–glass nanocomposite. The silver nanoparticles embedded in the soda-lime glass were shown to possess a SHG property when the nanoparticles were elongated[35] but detailed description of obtained effects is still necessary. A toolkit of methods and properties needs to be devised in order to optimise this type of material for the required application (here, EO-based detection).

1.2 The project

There exist a number of particle accelerators around the world that are being used either commercially or for scientific research. Applications that a particle accelerator can be used for are vast and range from medicine, through security, energy and more [36]–[41]. Limitations for particle acceleration using traditional techniques exist, however, along with limits for detection of accelerated particles. Optimisation of processes involving particle acceleration and detection was required in order to improve all aspects of these technologies. Laser based technologies turned out to be easily accessible as well as useful in many aspects of the optimisation process. A Marie Curie Network has been established for the purpose of exploring the possibilities that laser science can bring to the world of particle accelerators. The network was named LA^{3}NET [42], which stands for LAsers for Applications at Accelerator facilities. It consisted of 19 scientists coming from all over the world and based in various placements across the Europe. The consortium consisted of 40 international partners (universities, scientific institutions and

privately held enterprises) working in the field of either laser or accelerator technologies, or both [43].

This thesis is a result of a research being established within the University of Dundee along with a collaboration with STFC Daresbury Laboratory. The University of Dundee research group called MAPS [44] is a renowned group of experts in laser based processing of materials, and novel meta-materials production and applications. An established expertise in metal-glass nanocomposites (MGNs) and their optical properties manipulation by ultra-short laser processing was a key component of this research work. The research established with Daresbury Laboratory's laser group has been an ongoing collaboration aiming at solving the EO electron bunch characterisation problem, which was presented in the previous paragraph, by the introduction of MGNs in the EO detection scheme.

The work in this thesis describes research undertaken as a part of LA^{3}NET project. In this project the University of Dundee was responsible for the development and characterisation of an EO material in a form of an MGN. Collaborative work with Daresbury Laboratory was formed for the further characterisation of MGNs and initial tests in the EO measurement scheme.

1.3 The thesis

This thesis consists of eight main chapters. Theoretical background of metallic nanoparticles can be found in **Chapter 2**. Description of MGNs' optical properties will be explained along with related information about their interaction with intense laser beams. Relevant simulations and calculations will be presented.

Chapter 3 details all the experimental techniques used within this thesis. It describes equipment and technologies used for laser modification of MGNs and linear and nonlinear optical techniques used for characterisation. One of the applications of MGNs is also described there.

In **Chapter 4**, one can find experimental results of laser reshaping of MGNs with linearly polarised laser beam of ultra-short laser pulse length. Various parameters are described in this chapter, which are crucial to the process of laser reshaping. Resulting elongation of nanoparticles is described there in terms of their optical properties, namely Surface Plasmon Resonance (SPR) band modification. Ideas of optimisation of the SPR band modifications are detailed along with experimental results made using a

different MGN substrate type. This work was also finalised by a journal publication in Optics Express, *Tyrk MA, et al.* [45].

Chapter 5 considers the effect of linearly reshaped nanoparticles on their ability to frequency double the incoming laser light. Second Harmonic Generation (SHG) experiments are described there and various parameters describing this nonlinear process are shown. An optical peculiarity in form of a Multiphoton-Absorption-Induced Luminescence (MAIL) is also shown as an experimental result in this chapter. Different types of MGNs are presented: ps- and fs- pulsed reshaped nanoparticles as well as mechanically stretched nanoparticles. Their differences are studied and compared. This work was presented in a journal publication in Nanotechnology, *Zolotovskaya SA & Tyrk MA et al.* [46].

In **Chapter 6**, reshaping of MGNs with different laser polarisation states is described, namely radially and azimuthally polarised laser beams of ultra-short laser pulses. Reshaping process is described along with resulting shape of MGNs. A new technology is also presented that was developed precisely for characterisation of these types of MGN, utilizing SHG results from **Chapter 5**. This work was published in a journal publication in Optics Express, Tyrk MA et al. [47].

Chapter 7 presents the main comparison between types of samples. Comparison is being made on the basis of emitted SHG and MAIL signals that were captured and analysed with the experimental setup. Conclusions are also drawn that describe a potential candidate for the most efficient SHG conversion.

In **Chapter 8**, some preliminary results are shown from the experiments involving both SHG and Electro-Optical properties of MGNs. Future work is suggested in this chapter as a mean of showing a work plan towards finalising the search for a better EO crystal in ultra-short electron bunch monitors.

Work described in this thesis is presented in a way, which will guide the reader through various steps of the metamaterial optimisation for the EO detection application. The main motivation for the structure of this work is an aim of finding a nanoparticle shape/morphology that would increase its second order nonlinear properties. For that, a theoretical basis was needed to be established firstly, for both optical spectrum simulation as well as the ultra-short laser pulse interaction. Secondly, finding parameters for reshaping with the simplest laser beam polarization (linear) as the baseline for more sophisticated polarisation/reshaping parameters (radial, azimuthal).

Lastly, the second order nonlinear properties were needed to be characterised and compared between samples in order to find the best way for future optimization of the EO effects. Also, tests with well-established experimental techniques utilising the second order property was shown (FROG).

2 Theory and simulations

2.1 Introduction

This chapter will briefly introduce the theoretical concepts behind the light-matter interaction with regard to the metallic nanoparticles and ultrashort laser pulses. The first part will show the general behaviour of electrons under E-M field illumination. The concept of Surface Plasmon Resonance (SPR) will be explained and methods of calculations presented. Mie-theory along with its calculations will be discussed as well as the Discrete-Dipole Approximation (DDA) method. Based on these calculations, variations of certain parameters will be shown and their effect on the SPR. Lastly, Two Temperature Model (TTM) calculations will be presented for ps-pulse irradiations and temperatures that are created within each pulse of irradiation. Comparisons to experiments presented for fs-pulsed irradiation will be shown. A model for reshaping of silver nanoparticles embedded in a glass matrix will be presented and discussed.

2.2 Surface Plasmon theory

In order to understand the interaction of light with nanoparticles embedded in glass, a few preliminary ideas need to be explained. Firstly, this sub-chapter will explain the theory behind the interaction between the EM field and metals. This will introduce the behavior of metal's electrons and their impact on the optical behavior of the system. Secondly, a model of treatment of metallic nanoparticles will be presented where the nanoparticle sizes are << the wavelength of light leading to the Mie theory and followed by a modern approach of simulation.

2.2.1 Interaction of metals with an electromagnetic wave

All metals interact with an electromagnetic field by means of interaction of their electrons with the E-field of the wave. The simplest form of describing this interaction that is between an electron and an electric field $\boldsymbol{E}(t) = \boldsymbol{E}_0 * e^{-i\omega t}$, is by an equation of oscillating motion driven by an external force:

$$m\frac{d^2}{dt^2}\boldsymbol{x} + m\gamma\frac{d}{dt}\boldsymbol{x} = -e\boldsymbol{E} \qquad 2\text{-}1$$

Where m is the mass of the electron, e is the electron charge and γ is a damping coefficient. This external force is causing the electron to move in a motion described by $\boldsymbol{x}(t) = \boldsymbol{x}_0 * e^{-i\omega t}$. When phase shifts between the driving oscillating field and the resulting oscillation are taken into account, the solution yields [48], [49]:

$$\boldsymbol{x}(t) = \frac{e}{m(\omega^2 + i\gamma\omega)}\boldsymbol{E} \qquad 2\text{-}2$$

The resulting macroscopic polarisation induced on the electron can then be described by:

$$\mathbf{P} = -\frac{ne^2}{m(\omega^2 + i\gamma\omega)}\mathbf{E} \qquad 2\text{-}3$$

Where ω is the light angular frequency. In order to have an explicit description of the oscillating component of the electrons in the electric field, one has to remember that the displacement vector can be described by $\mathbf{D} = \epsilon_0\mathbf{E} + \mathbf{P}$, which yields

$$\mathbf{D} = \epsilon_0\left(1 - \frac{\omega_p^2}{i\gamma\omega}\right)\mathbf{E} \qquad 2\text{-}4$$

where ω_p is the *plasma frequency* of a free electron gas. From there the dielectric function can be written as:

$$\epsilon(\omega) = 1 - \frac{\omega_p^2}{\omega^2 + i\gamma\omega} \qquad 2\text{-}5$$

Were, $\epsilon(\omega) = \epsilon_1(\omega) + i\epsilon_2(\omega)$ and can be written as [50]:

$$\epsilon_1(\omega) = 1 - \frac{\omega_p^2\tau^2}{1 + \omega^2\tau^2} \qquad 2\text{-}6$$

$$\epsilon_2(\omega) = \frac{\omega_p^2 \tau}{\omega(1 + \omega^2 \tau^2)} \qquad 2\text{-}7$$

where $\tau = 1/\gamma$.

The derived dielectric function can be described in terms of its free-electron Drude-Sommerfeld susceptibility, that is [50]:

$$\epsilon(\omega) = 1 + \chi^{DS}(\omega) \qquad 2\text{-}8$$

This description of dielectric function however does not take into the account the interband transitions that are a result of excitation of deeper d band electrons. It is common to incorporate the interband transition susceptibility into the dielectric function in order to achieve a function that would fit to the experimental data (i.e. Johnson and Christy [51]].

$$\epsilon(\omega) = 1 + \chi^{DS}(\omega) + \chi^{IB}(\omega) \qquad 2\text{-}9$$

The derivation of $\chi^{IB}(\omega)$ is not a part of this thesis and can be found in [50]. This description of the dielectric function fits much more closely to the experimentally obtained data (for a certain wavelength range). It is recommended to aid any calculations for a wider range of wavelengths with experimental data of dielectric functions produced with methods like ellipsometry or others. The reason for this is that there will always be an intermediate region that will not be described correctly by either interband transition or the Drude-Sommerfeld free-electron gas model.

Below, can be seen the drawing of the real part of the dielectric function into the interband and free electron models. For lower energies the free-electron model describes the dielectric function better than the interband, whereas for energies greater than ~4 eV the latter describes it more accurately. The transition region can be clearly seen.

Knowledge of system's dielectric functions is crucial when calculating its optical properties (i.e. plasma resonance frequencies).

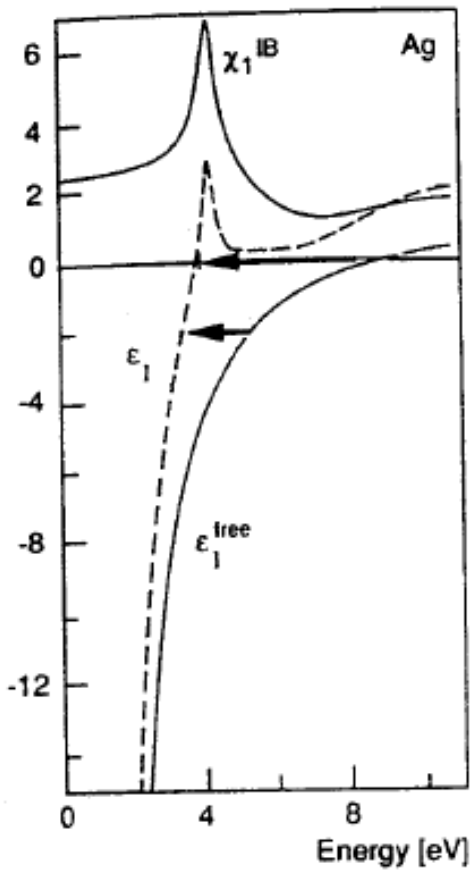

Figure 2-1 Experimentally measured dielectric function ϵ_1 for silver (broken line) and its decomposition into the free electron contribution ϵ_1^{free} and the interband transition contribution χ_1^{IB}. Graph taken from [50]

2.2.2 Interaction of localized metallic particles with an electromagnetic field in a quasi-static approximation

Whereas some optical properties for metallic surfaces can be described with equations shown in the previous part of this chapter, a different situation takes place for small nanoparticles. It has to be noted that small nanoparticles are these whose radius R is much smaller than the wavelength of the light that it illuminates ($R<<\lambda$). In order to analyze physical properties of such nanoparticles, one has to assume a *quasi-static approximation* of the system. Figure 2-2 shows how the theoretical treatment for a nanoparticle system without the *quasi-static approximation* (a) and with it (b). This is a useful approximation that is widely used for such systems [52]–[56]. It assumes a constant field across the nanoparticle volume, allowing for a classic "particle in an electrostatic field" problem.

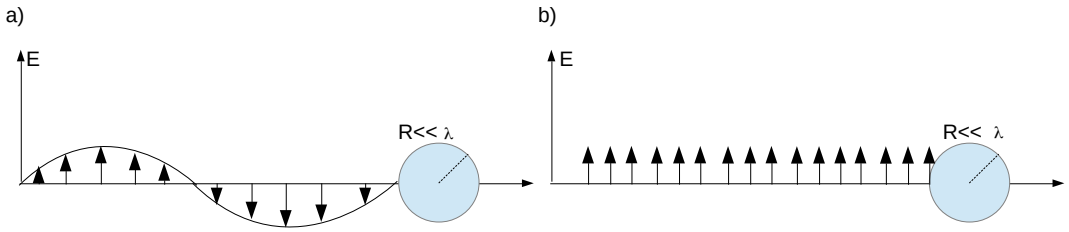

Figure 2-2 Schematic representation of electromagnetic wave interaction with a nanoparticle of radius << wavelength (a) and the quasi-static approximation used to describe the wave-nanoparticle interaction (b).

Let the field illuminating the nanoparticle in the presented approximation be described by $\mathbf{E} = E_0\hat{\boldsymbol{z}}$. The nanoparticle will be immersed in a dielectric medium of homogeneous and constant dielectric function ϵ_m, and having itself a dielectric function comprising of its real and imaginary components ϵ_1 and $i\epsilon_2$. Figure below describes this problem:

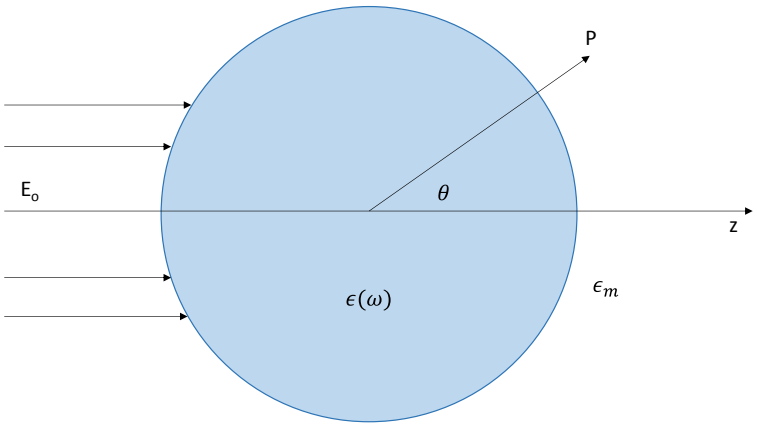

Figure 2-3 spherical nanoparticle placed into electrostatic field E ($\hat{z}$ is the direction of the electric field vector).

One can find solution to this in Jackson [57], where the field **E** is being calculated by solving the $\mathbf{E} = -\nabla\Phi$ equation. Where the potential Φ is eventually solved as:

$$\Phi(r,\theta) = \sum_{l=0}^{\infty}\left[A_l r^l + B_l r^{-(l+1)}\right]P_l(cos\theta) \qquad 2\text{-}10$$

Where $P_l(cos\theta)$ are Lagendre Polynomials, l their order, and θ the angle as depicted in Figure 2-3. After further treatment of the problem and applying the boundary conditions we get (Appendix A):

$$\Phi_{in} = -\frac{3\epsilon_m}{\epsilon + 2\epsilon_m} E_0\, r\, cos\theta \qquad 2\text{-}11$$

$$\Phi_{out} = -E_0\, r\, cos\theta + \frac{\epsilon - \epsilon_m}{\epsilon + 2\epsilon_m} E_0 R^3 \frac{cos\theta}{r^2} \qquad 2\text{-}12$$

When introducing the dipole moment **p**, the external potential equation can be rewritten as:

$$\Phi_{out} = -E_0\, r\, cos\theta + \frac{\mathbf{p} \cdot \mathbf{r}}{4\pi\epsilon_0\epsilon_m r^3} \qquad 2\text{-}13$$

Where,

$$\mathbf{p} = 4\pi\epsilon_0\epsilon_m R^3 \frac{\epsilon - \epsilon_m}{\epsilon + 2\epsilon_m} \mathbf{E}_0 \qquad 2\text{-}14$$

Also, one can describe the static polarizability of the sphere defined as $\boldsymbol{p} = \epsilon_m \alpha \boldsymbol{E}_o$, then:

$$\alpha = 4\pi\epsilon_0 R^3 \frac{\epsilon - \epsilon_m}{\epsilon + 2\epsilon_m} \qquad 2\text{-}15$$

It can be observed from the above equations that both the internal field in the nanoparticle as well as its polarizability can exhibit a resonance behavior when the equation denominator value approaches zero. The resonance condition therefore can be written as:

$$|\epsilon + 2\epsilon_m| \rightarrow min \qquad 2\text{-}16$$

Or with the explicit version of the complex dielectric function of the nanoparticle:

$$|\epsilon_1(\omega) + 2\epsilon_m|^2 + |\epsilon_2(\omega)|^2 \rightarrow min \qquad 2\text{-}17$$

The common relation can also be described for situations where the imaginary part of the dielectric function is small (<<1) or has a small frequency dependence. Then the condition would be in the form of:

$$\epsilon_1 = -2\epsilon_m \qquad 2\text{-}18$$

Knowing that the dielectric function has to be always greater than one (which is the value obtained for a vacuum), this gives a condition for the real part of the dielectric function of the nanoparticle to be negative. This particular resonance will be called the *Surface Plasmon Resonance* (SPR) from here on [58].

As this thesis is focused on silver nanoparticles embedded in soda-lime glass it is worth showing how this resonance condition would be obtained for these particular materials. From [59] we know that an approximated refractive index of soda-lime glass in the visible region is 1.52. From relation $\epsilon = n^2$ we can write that $\epsilon_m = 2.31$. Experimentally measured values of the refractive index (n) and the extinction coefficient (k) can be found in [51] and are plotted below:

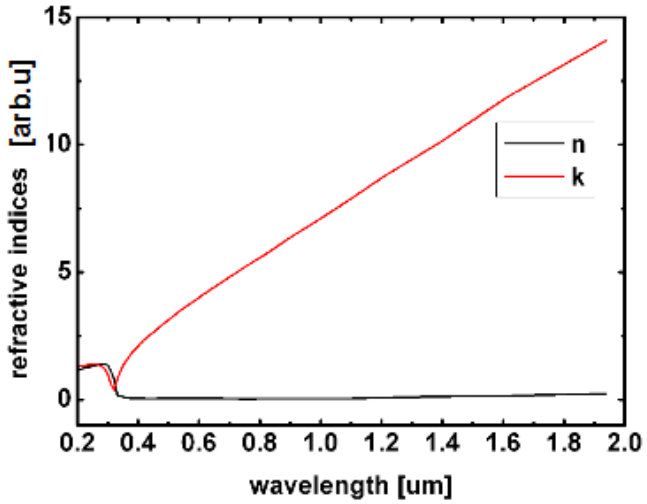

Figure 2-4 Plotted values of the refractive index (n) and the extinction coefficient (k), provided from Johnson and Christy [51]

From these measurements the real and imaginary dielectric constant values can be calculated from the relation:

$$n^{complex} = n + ik \qquad 2\text{-}19$$

$$(n^{complex})^2 = (n^2 - k^2) + i(2nk) = \epsilon_1 + i\epsilon_2 \qquad 2\text{-}20$$

Below, can be seen a figure representing the real and imaginary parts of the complex dielectric function of silver:

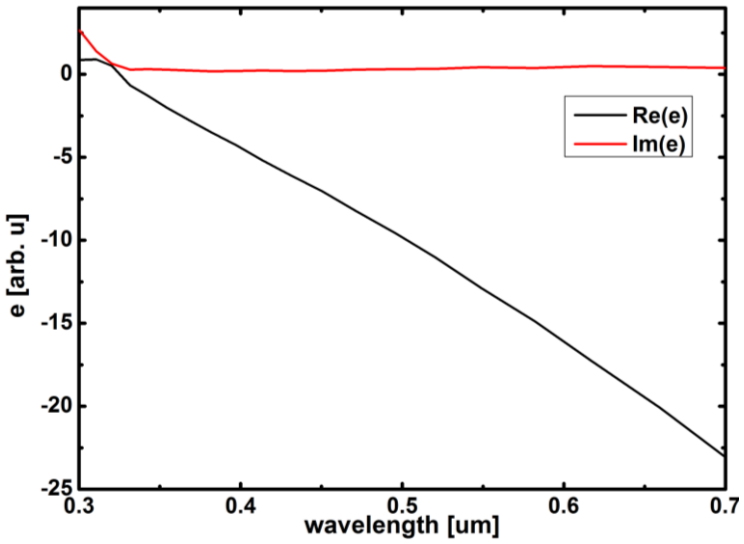

Figure 2-5 Silver real and imaginary dielectric constants taken from refractive index data published in [51]

Using equation 2-18 for the resonance condition along with plotted data shown in Figure 2-5, one can observe that the predicted resonance wavelength will be placed in vicinity of 400 nm (where a real part of the dielectric constant equals -4.62).

2.2.3 Interaction of nanoparticle with an electromagnetic field in the Mie Theory

For larger nanoparticles (but still smaller than the wavelength of light), however, the *quasi-static approximation* will not be valid and may point to misleading results of calculations. For this reason, more rigorous approach is required, which was fully described by Gustav Mie in 1908 in so called Mie Theory, which applies Maxwell equations to solve the scattering problem on a sphere. The exact derivation of the solution will not be a part of this thesis as it can be found in literature [60], [61]. It is however important to note that the Mie's calculations lead to cross section parameters for extinction, absorption and scattering from a nanoparticle.

$$Q_{ext} = Q_{abs} + Q_{sca} \qquad 2\text{-}21$$

where following notation from [48] one can get:

$$Q_{ext} = \frac{2\pi}{|\mathrm{k}|^2}\sum_{L=1}^{\infty}(2L+1)Re\{a_L + b_L\} \quad 2\text{-}22$$

$$Q_{sca} = \frac{2\pi}{|\mathrm{k}|^2}\sum_{L=1}^{\infty}(2L+1)(|a_L|^2 + |b_L|^2) \quad 2\text{-}23$$

$$Q_{abs} = Q_{ext} - Q_{sca} \quad 2\text{-}24$$

where

$$a_L = \frac{m\psi_L(mx)\psi_L'(x) - \psi_L'(mx)\psi_L(x)}{m\psi_L(mx)\eta_L'(x) - \psi_L'(mx)\eta_L(x)} \quad 2\text{-}25$$

$$b_L = \frac{\psi_L(mx)\psi_L'(x) - m\psi_L'(mx)\psi_L(x)}{\psi_L(mx)\eta_L'(x) - m\psi_L'(mx)\eta_L(x)} \quad 2\text{-}26$$

Where $m=n/n_m$ (n-complex refractive index, n_m- real refractive index of the surrounding medium), k is the wave number. ψ_L *and* η_L are Riccati-Bessel cylindrical functions and primes describe differentiation.

Also, Mie scattering theory has no size limitation and converges to the limit of geometric optics for large particles. For nanoparticles with diameters <10nm analysis of nanoparticle parameters may also be different than presented theory, because their size would be in the order of a free mean path of an electron, and other effects may dominate.

Using MATLAB code provided in [61] (full code in Appendix B), which calculates the extinction, scattering and absorption cross sections based on the aforementioned equations, one can calculate the SPR as in Figure 2-6. Refractive index data for silver was used from [51] and the surrounding medium refractive index was chosen to be 1.52. Nanoparticle radius was chosen to vary between 10 nm and 40 nm in 4 steps. It can be seen in the figure that according to Mie calculations, particle resonance occurs at around 400 nm wavelength (as predicted).

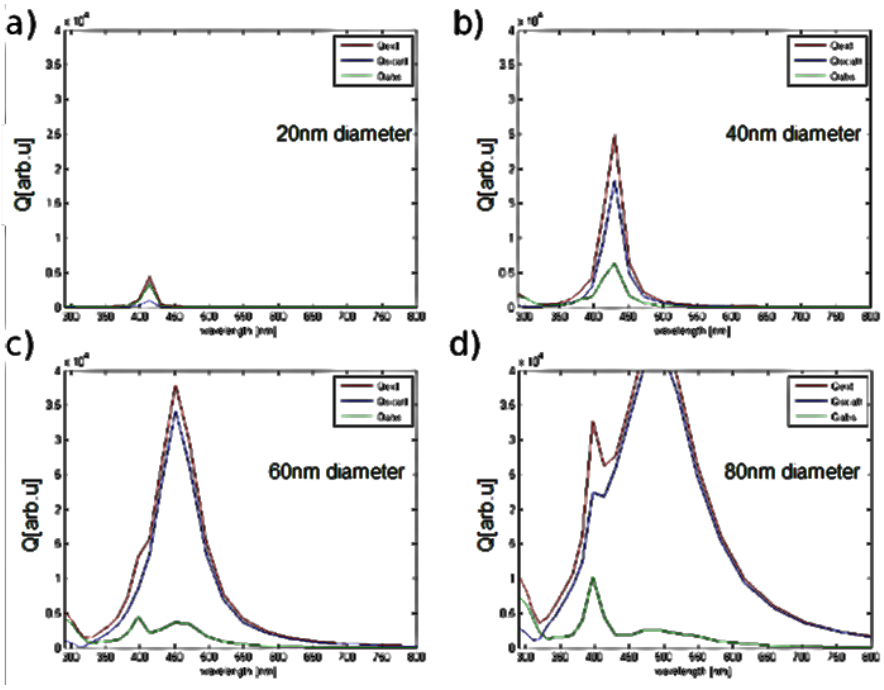

Figure 2-6 Calculated SPR resonances of a spherical nanoparticle of varying size diameter: a)20 nm, b)40 nm, c)60 nm, d) 80 nm. Extinction (Q_{ext}), absorption (Q_{abs}) and scattering (Q_{scatt}) cross sections are shown.

Four main characteristics can be observed from this simulation:

1) The SPR intensity increases along with the nanoparticle diameter
2) Absorption becomes more dominant for smaller particles and scattering for larger particles
3) Smaller nanoparticles resonate in a dipolar manner leading to a single SPR peak, whereas larger nanoparticles SPR is wider and possesses secondary peaks, which is caused by particle resonating in a quadrupolar manner [62]–[64]
4) Increase in nanoparticle size leads to a red shift in the SPR

2.2.4 Calculation nanoparticle cross sections with the Discrete Dipole Approximation

It is relatively straightforward to simulate the interaction of a spherical nanoparticle in an electromagnetic field by the means of the Mie Theory (as shown in the previous sub-chapter). It is however much more complicated (if at all possible) to derive Mie type analytical equations for more complicated nanoparticle shapes and structures. The scope for this thesis is to reshape the silver spherical nanoparticles in order to research their optical and electro-optical properties, therefore it is important to decide on the numerical tool for simple as well as for more complex geometries if they arise. Numerical technique called the Discrete Dipole Approximation (DDA) was used

throughout this thesis. This method was first shown by DeVoe [65], [66] in 1964 in the treatment of particular aggregates and their response to optical wavelengths, and later in 1973 by Purcell and Pennypacker [67]. The particular numerical package used in this thesis was developed by Draine and Flatau – DDSCAT [68]–[70].

In essence, the DDA method is working on the principle of approximation of a continuum object with a matrix of dipoles, with their associated dipolar moments and polarisations when illuminated with a wave. In that way DDA can replace a source of scattering (i.e. a nanoparticle) with a set of interacting dipoles. It is therefore called a volume-based numerical solver (similarly as the finite difference time domain method (FDTD)[71]), in contrast to surface-based numerical solvers, like T-matrix method [72] or generalized multipole technique (GMT) [73], [74]. DDA is also one of the most powerful methods for calculation and easy to use, therefore chosen as a primary solver.

In DDA, as mentioned earlier, each object is approximated with a set of N number of dipoles [75]. Their polarisation can be described by the equation:

$$\mathbf{P}_i = \alpha_i \mathbf{E_{loc}}(\mathbf{r}) \tag{2-27}$$

Where the α_i is the i-th dipole polarizability element and $\mathbf{E}_{loc}$ is the sum contribution of the incident field and the N – 1 dipole contribution at position $\mathbf{r}$. The field contribution can be described by the equation [76]:

$$\begin{aligned}\mathbf{E_{loc}}(\mathbf{r}) = \mathbf{E_0}\exp(i\mathbf{k}\cdot\mathbf{r} - i\omega t) \\ - \sum_{j\neq i} \frac{\exp(ik\mathbf{r_{ij}})}{\mathbf{r_{ij}}^3}\left\{k^2\mathbf{r_{ij}} \times \left(\mathbf{r_{ij}} \times \mathbf{P}_j\right) + \frac{\left(1 - ik\mathbf{r_{ij}}\right)}{\mathbf{r_{ij}^2}}\right. \\ \left.\times\left[\mathbf{r_{ij}^2}\mathbf{P}_j - 3\mathbf{r}_{ij}\left(\mathbf{r_{ij}}\mathbf{P}_j\right)\right]\right\}\end{aligned} \tag{2-28}$$

This equation can be written in a simpler form as:

$$\mathbf{P_i} = \alpha_i\left(\mathbf{E_{inc,i}} - \sum_{j\neq i}\mathbf{A_{ij}}\mathbf{P_j}\right) \tag{2-29}$$

Where the $\mathbf{E}_{inc,i}$ is the electric field at position i, caused by an incoming plane wave. The $-\mathbf{A}_{ij}\mathbf{P}_j$ is the contribution of an electric field caused by the dipole at position j. Also, $\mathbf{r}_{ij}=\mathbf{r}_j-\mathbf{r}_j$. As it can be seen, this equation relates separately to electric fields being at position i, and in positions j. When however an assumption is made in order to formulate an equation that will relate to all the positions, that is to j-th position as well as i-th (i=j), then a component $\mathbf{A}_{ii}=\boldsymbol{\alpha}_i^{-1}$ needs to be introduced. This in effect reduces the complex problem into linear set of equations in the form of:

$$\sum_{j=1}^{N} \boldsymbol{A_{ij}P_j} = \boldsymbol{E_{inc,i}} \qquad 2\text{-}30$$

Solving these for $\mathbf{P}_j$ gives equations for the cross sections of extinction and absorption:

$$Q_{ext} = \frac{4\pi k}{|\boldsymbol{E_0}|^2}\sum_{j=1}^{N} Im\left(\boldsymbol{E^*_{inc,i}}\cdot\boldsymbol{P_j}\right) \qquad 2\text{-}31$$

$$Q_{abs} = \frac{4\pi k}{|\boldsymbol{E_0}|^2}\sum_{j=1}^{N}\left\{Im\left[\boldsymbol{P_j}\alpha_j^{-1}\cdot\boldsymbol{P_j^*}\right]-\frac{2}{3}k^3\left|\boldsymbol{P_j}\right|^2\right\} \qquad 2\text{-}32$$

The scattering cross section can be calculated from the simple relation: $Q_{scatt}=Q_{ext}-Q_{abs}$.

Also, one has to remember that for an accurate calculation a large number of dipoles needs to be selected within the DDSCAT simulation package.

Having a reliable tool for calculations of any arbitrary shapes and clusters of nanoparticles it is straightforward to create appropriate input files and simulate SPRs for various parameters. Kreibig and Vollmer [50] did extensive study on how the SPR changes with regards to certain parameters. In order to visualize how the SPR changes for the particular Ag nanoparticles that are embedded in soda-lime glass, DDSCAT was used.

Firstly, the refractive index was changed from 1.0 to 1.6 (1.52 is the soda- lime glass refractive index) and extinction cross-sections were plotted in Figure 2-7.

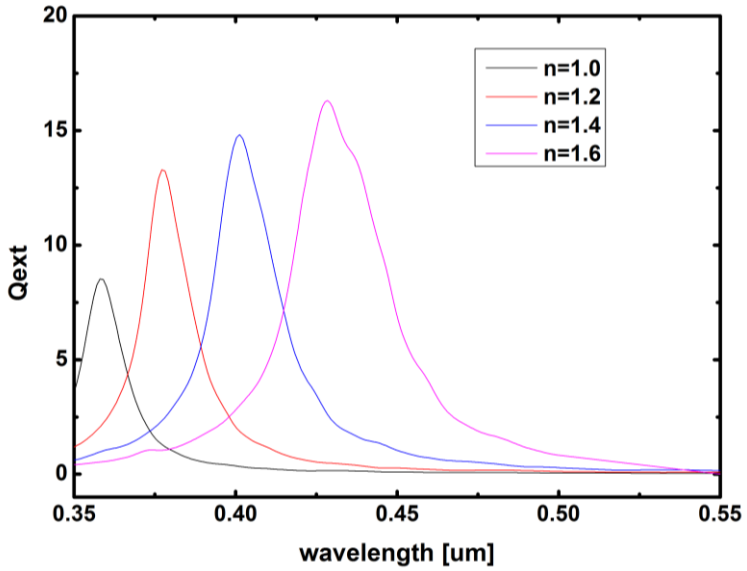

Figure 2-7 DDSCAT calculations showing the SPR position change as a function of the embedding medium refractive index (variation between 1.0 and 1.6). Silver nanoparticle diameter was set to constant value of 30 nm.

It can be seen here, how significant the appropriate choice of the embedding medium for SPR manipulations is. In case of soda-lime glass the SPR was placed around 430 nm which matches experimentally obtained spectrum seen in the next Chapters.

Secondly, the aspect ratio of the silver nanoparticle was changed from spherical (1:1) up to 1:2.5, while maintaining the refractive index of 1.54 (for comparative reasons with the soda-lime glass samples used in the experimental chapter). Figure 2-8 shows results of this simulation.

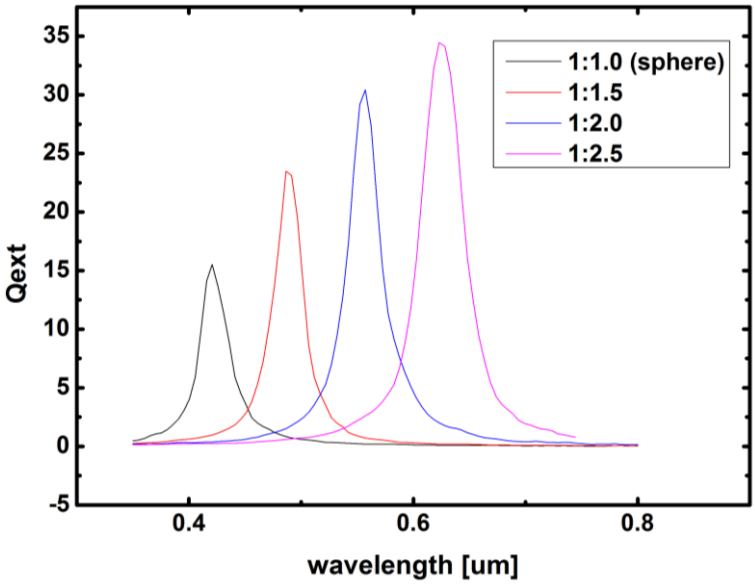

Figure 2-8 DDSCAT calculations showing the SPR position change as a function of the elongation ratio of the nanoparticle. The short axis size of the nanoparticle was kept constant at 30 nm, long axis was varied in ratios of 1:1 up to 1:2.5, and the refractive index of the medium was kept as 1.54 for comparison with soda-lime glass.

The position of the SPR changed significantly more than for the refractive index change. Knowing that the nanoparticles used in next chapters will have their size distribution of around 30 nm in diameter, the same size was used in these simulations, while the long axis was varied in size.

The dependence of the SPR on the nanoparticle size was already shown in Figure 2-6 where the analytical Mie equations were used for a spherical nanoparticle.

It can also be shown that the SPR bandwidth changes depending on the size of the nanoparticle, which was plotted in Krebig Vollmer (Figure 2-9) [50]. These calculations were made for three types of embedding medium: air (ε_m=1), glass (ε_m=2.25), and Titanium Oxide (ε_m=6.25). It can be seen there that the diameter of nanoparticles used in this thesis lies just in the valley of the middle graph, giving a good indication for further experimental analysis of how the nanoparticle size changes while knowing the SPR bandwidth.

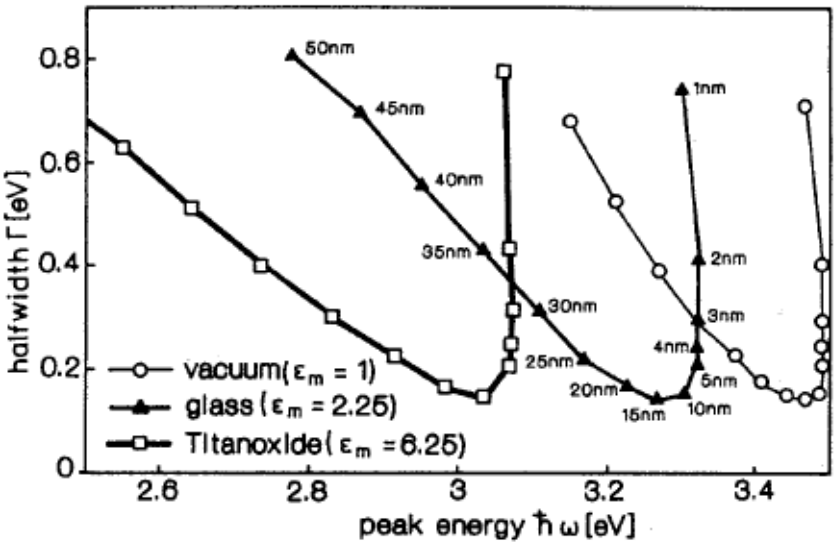

Figure 2-9 SPR bandwidth change as a function of nanoparticle size. Relations presented for three embedding media: a) vacuum, b) glass, c) titanium oxide. Graph taken from [50]

It is worth mentioning that the DDSCAT calculations shown in both Figure 2-7 and Figure 2-8 present dipolar SPR bands even for elongation to high ratios (higher order nanoparticle excitation show up as additional SPR peaks)[62].

It's important to point out that dielectric composites containing metallic nanoparticles can also be treated as whole materials. It is usually useful to treat such MGNs with approximating theories like the Maxwell-Garnett theory which describes SPRs quite well [77], [78], taking into consideration the proportion of nanoparticles to the surrounding medium. Because this thesis will be focused on physical modification of nanoparticles into different shapes and orientations, DDSCAT will be the main simulation technique used as it treats the nanoparticle separately. It is thought that it makes more sense to realize the effect of a single nanoparticle first before considering it as a collective, where various multipolar interactions needs to be taken into account. DDSCAT will be primarily used in explanation of non-linear optical properties of reshaped nanoparticles.

2.3 Laser – nanoparticle interaction

This part of the thesis will show how to treat ultrashort laser – nanoparticle interaction in temperature terms. Various regimes exist when treating laser interaction with nanoparticles. The very obvious division is often described for different laser pulse

lengths [79]–[84]. It is widely known, that when interacting with nanoparticles with pulse lengths longer than few tens of picoseconds up to continuous waves, it leads to slow heat increase within the whole particle system [85]–[89]. Nanosecond pulse irradiations for example can lead to Oswald ripening between silver clusters and creation of silver layer on the surface of glass or to the increase of a nanocluster size [83]. For ultrashort pulses however, the interaction tends to be non-thermal, which means that because of such short laser interaction between the nanoparticle and the laser pulse, only electrons accumulate the induced temperature which later undergoes relaxation to the lattice and the surrounding [90], [91]. It was shown in various publications how metallic nanoparticles in glass behave when treated with a femtosecond laser pulses [92]–[95]. Here, this theory will be described and related to ps- pulsed irradiations.

One can also divide laser nanoparticle interaction into weak and strong regime. In such case, the weak regime relates to the peak power that is added to the nanoparticle system which does not cause any shape modification nor any other long term deviation from initial nano cluster parameters. Various research groups have studied such regimes when they interacted with the nanoparticle with a weak peak power laser pulse in order to measure its optical parameters [96]–[100]. Strong interaction however, refers to the regime where the laser peak power is strong enough to cause nanoparticle shape modification, dissolution or fragmentation. In this regime reversibility of achieved parameters is not possible. Usually the nanoparticle temperature changes in this regime as well as their temperature relation to their environment. Emission of electrons usually takes place [101].

One of the works by Bigot [102] describes this interaction of nanoparticle with a fs-pulse- this can be easily related to <10 ps pulse interaction too. He described there the interaction between electrons' and phonons' temperature. The figure below is taken from this very publication as it describes schematically the process very well.

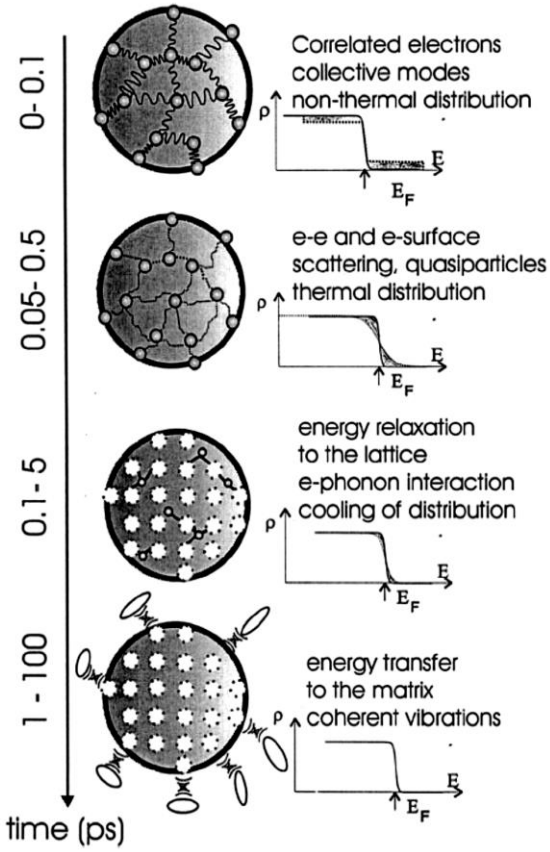

Figure 2-10 Schematic illustration of thermalisation and heat exchange processes arising during ultra-short laser pulse interaction with a nanoparticle. Drawing taken from [102].

Firstly, upon the interaction with an ultrashort pulse, the energy of the laser pulse is absorbed by the electron by the inter- and intraband transitions (0- 0.1 ps). This creates an electron state where the phase between the electronic state and the electromagnetic wave is conserved. This process is not yet thermal.

After the initial interaction with the electromagnetic wave of an ultrashort pulse, the collective oscillations in phase are being lost and the electron thermalisation process begins (0.05 – 0.5 ps). The distribution that electrons are representing at this stage resembles the Fermi-Dirac distribution with its function shape that highly depends on the temperature delivered by the laser pulse. Temperatures achieved by electrons are much higher than the temperature of the nanoparticle lattice as well as the temperature of the nanoparticle before the laser excitation. In [103]–[106] it was shown that it takes a few hundreds of femtoseconds. Time scale of this process is highly dependent on the nanoparticle size. In general, the scattering times decrease along with the nanoparticle diameter [97], [107]–[109].

The next effect, which takes place in a relatively similar timescale to the previous one, is energy transfer to the nanoparticle lattice (0.1 – 0.5 ps) [110]–[113]. The fact that the timescale of this effect is similar to the previous means that this process (electron-phonon, or e-ph) competes with the electron-electron (e-e) thermalisation in the beginning, and later takes over completely. It also eventually leads to heating of the nanoparticle lattice to higher temperatures than it was before the interaction with the laser pulse. It can be seen as simultaneous cooling of hot-electrons along with heating of the lattice, resulting in an equilibrium temperature eventually.

The last step of the pulse interaction is the energy transfer to the surrounding medium (1 – 100 ps). This process corresponds to the heat diffusion from the nanoparticle to the surrounding medium, which can vary depending on the heat properties of the medium [114], [115]. Because there is such dependency, this process will influence the nanoparticle shape modification. It will be shown later in this chapter that the thermal equilibrium between electrons and the lattice will take place in the timescale of 30 – 40 ps.

2.3.1 Two Temperature Model

The Two Temperature Model (TTM or 2TM) is usually implemented in order to model the thermal behaviour of a nanoparticle illuminated with an ultrashort pulse [116], [117]. The name comes from the fact that electron heating is being treated separately, after which its heat transfer to the matrix is being included, leading to precise calculations of the equilibrium temperature of the nanoparticle as a function of time. As it was mentioned earlier, the electron dynamics is defined by two mechanisms: e-e scattering and the e-ph energy relaxation. By the use of two coupled differential equations, the TTM model can be described as [118], [119]:

$$C_e(T_e)\frac{\partial T_e}{\partial t} = -G(T_e)(T_e - T_l) + S(t) \qquad 2\text{-}33$$

$$C_l\frac{\partial T_l}{\partial t} = G(T_e)(T_e - T_l) \qquad 2\text{-}34$$

Here, the electron temperature is described by T_e and the lattice temperature by T_l. The $C_e(T_e)$ is the electronic heat capacity whereas C_l the lattice heat capacity. $G(T_e)$ is the electron-phonon coupling factor, and S(t) is the laser source term described by:

$$S(t) = \frac{I\sigma_{abs}}{V_{np}} \exp\left[-4\ln 2 * \left(\frac{t}{\tau_{FWHM}}\right)^2\right] \qquad 2\text{-}35$$

Here, I is the laser intensity, σ_{abs} the absorption cross section, V_{np} nanoparticle volume and τ_{FWHM} is the laser pulse length defined at its full width at half maximum. It is also important to mention that for parameters like C_e and G the dependence on the temperature of electrons must not be ignored. It is common to use this terms as constant values for regimes where the temperature does not increase significantly. In this thesis the ultrashort excitation of nanoparticle will be studied. This means that very high temperatures of electrons will be achieved and induced fields within the nanoparticle will also involve the deeper d-band electrons in the thermal process [120]. In order to reliably predict nanoparticle temperature, it is important to include the temperature dependency on the aforementioned parameters. In the same time C_l dependence on the lattice temperature can be taken as a constant as it will not include any major temperature changes ($C_l = 3.5*10^6$ $Jm^{-3}K^{-1}$ at room temperature). Tabularized data was used for this purpose, obtained from [121]. These values were calculated using the VASP simulation package (*Vienna Ab-initio Simulation Package*) and were applicable to temperatures up to 50'000K. Values of C_e and G show significant discrepancies from linear behaviors for temperature higher than ~5000K, and as it is shown in various publications refereeing to ultrashort pulse irradiation of nanoparticles, temperatures that electrons achieve in these processes highly exceed that threshold [122], [123]. In this thesis, <10ps pulse irradiations will be studied therefore it is fair to assume that the temperature achieved will also be higher than 5000K. Both C_e as well as G are functions of density of states (DOS) and the chemical potential μ which varies with high temperatures too. The data used for calculations can be seen in Figure 2-11.

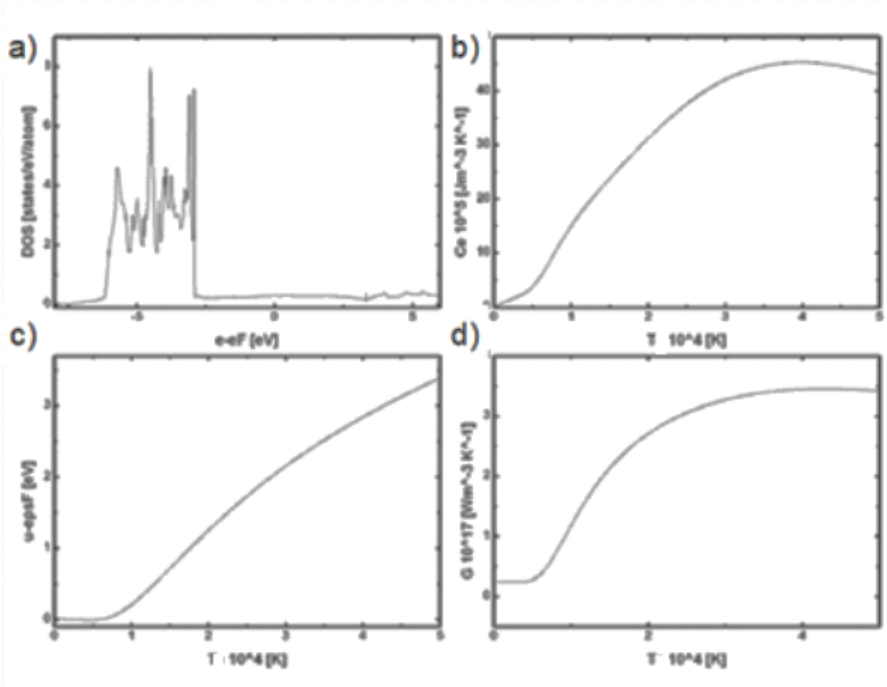

Figure 2-11 Plotted values calculated with VASP of a) silver DOS, b) C_e, c) chemical potential, d) G. Values presented as a function of temperature T. Data obtained from [121]

Before calculating the electron and the lattice temperatures it is important to determine the σ_{abs} parameter. In order to do this, the absorption cross section was calculated for a 15 nm radius silver nanoparticle in 1.52 refractive index environment. A spherical nanoparticle was chosen as it is the shape that a laser pulse would first encounter. Below the cross sections:

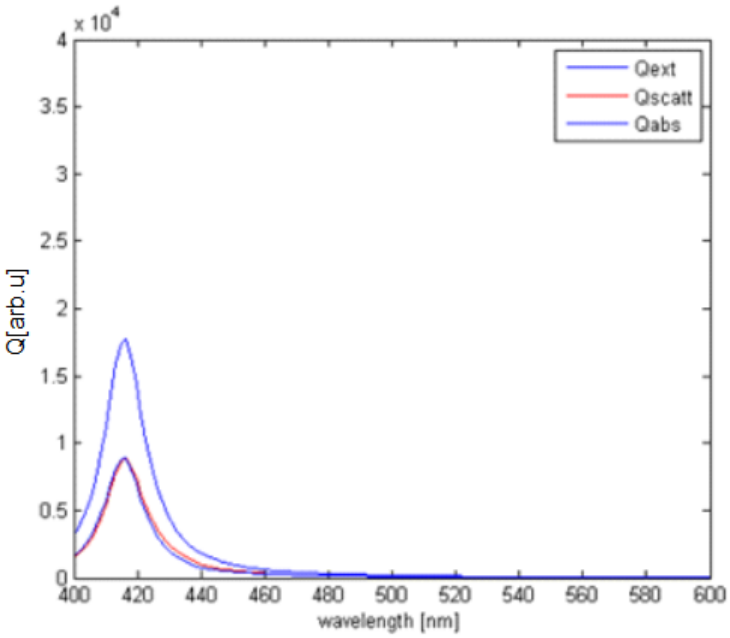

Figure 2-12 Calculated SPR of spherical nanoparticle of 30 nm in diameter

It can be seen in the figure that the absorption cross section for these parameters is in the range of ~50 nm^2 for the wavelength of 532 nm (which is the laser wavelength that will be used for later irradiations).

The input parameters taken for the TTM calculations were as in Table 1:

Parameter	**Value**	**Unit**
Fluence	88.42	mJ/cm^2
I	1.77×10^{14}	W/m^2
Nanoparticle radius	15.00	nm
C_l	3.50×10^6	J/m^3K
σ_{abs}	50.00	nm^2
τ_{FWHM}	5.00	ps

C_e	From VASP	N/A
G	From VASP	N/A

Table 1 Parameters used for TTM modeling

The calculated temperature relation can be seen in Figure 2-13 a). It can be seen there that temperature achieved for electrons of a silver nanoparticle reaches around 7000K. This temperature is a direct result of interaction with a ps- pulse. Fluence was chosen to match the fluence used in Chapter 4 for ps- pulsed nanoparticle shape modification. In the figure below it is clearly shown that the equilibrium temperature of around 1500K is reached after around 30 ps. Knowing, that the laser repetition rate used later for modification will be 200 kHz, the pulse temporal separation will be around 5 µs. Therefore, multipulse irradiation will increase the electron temperature to a roughly similar level with every pulse.

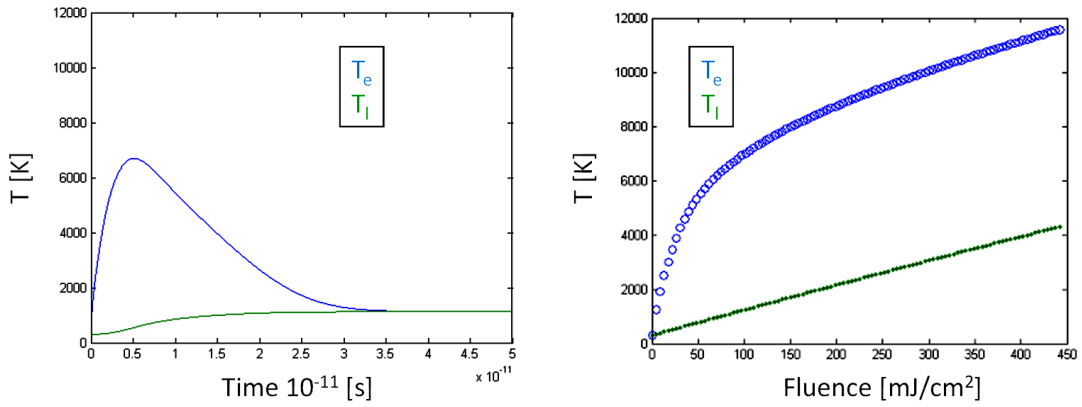

Figure 2-13 TTM calculated values for a) electron and the silver lattice temperature under 1 ps- pulse illumination, b) electron and lattice temperatures as a function of ps- pulse fluence.

The model used here does not however include any energy exchange between the lattice and the surrounding, therefore it can be concluded that after around 5 µs the equilibrium temperature will be significantly lower. It will be however shown in the Chapter 4 that the total equilibrium temperature will not dissipate to the surrounding completely, or/and the surrounding will not dissipate its local temperature completely, as the multipulse irradiation will lead to dissolution of nanoparticle in this regime. Figure 2-13

(b) shows relation between the electron and lattice temperatures and the pulse fluence used for irradiations. It can be seen that the increase in the electron temperature is at much higher gradient up until ~6000K. It was mentioned earlier that the dependence of parameters like C_e and G becomes nonlinear after 5000K. This can be seen here too with a slight discrepancy (~1000K), due to the slow heating nature of a picosecond pulse (in comparison to fs- pulsed irradiation).

Due to the fact that vast work on this subject has been done in regards to fs- pulsed irradiation [98], [124]–[129], a comparison has been made to parameters used in [130], where the nanoparticle has been irradiated with a 15o fs pulse at 400 nm wavelength at fluence of ~20 mJ/cm^2. Figure 2-14 shows the direct comparison between the fs- and ps- regime. Smaller equilibrium temperatures are achieved for ps- irradiation than in fs- irradiations, but still slightly above the bulk silver melting point of ~1500K. Longer input pulses would increase the lattice temperatures significantly eventually leading to simple thermal interaction with a laser.

A direct result of this comparison is that the surrounding glass around the nanoparticle will be heated up to smaller temperatures. Higher repetition rates (200 kHz instead of 1 kHz) of a ps- laser will however make up for this heat loss leading to efficient reshaping. According to the TTM presented for fs- irradiations each pulse during irradiation accumulates the effect of elongation by heating up the nanoparticle and then spreading its heat to the glass matrix by heat diffusion.

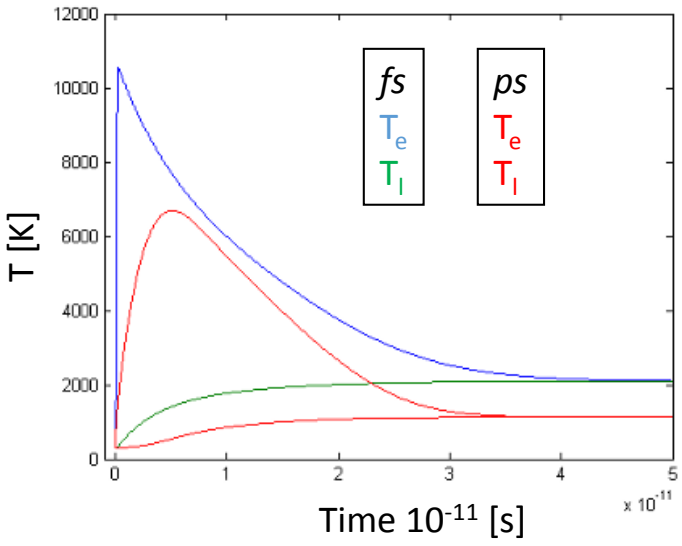

Figure 2-14 ps- (<10 ps) and fs- (150 fs) TTM calculation comparison of electron and the lattice temperatures.

The overall effect of reshaping increases for each pulse because the system relaxes to a slightly higher temperature than it had before. Approaching high temperatures results in dissolution of the nanoparticles in the glass matrix due to the increase mobility of the emitted silver ions and their diffusion into the glass matrix during the irradiation [45]. Therefore too high repetition rates or firing large number of pulses per spot can lead to undesirable effects.

2.3.2 Nanoparticle reshaping mechanism

There has been a great amount of literature regarding the mechanism of reshaping the nanoparticle with an ultrashort pulse [95], [130], [131]. Here, a short review of this process will be shown and then related to the ps-pulsed reshaping.

The main contributor to nanoparticle modification during the reshaping process is the ejection of electrons and the nanoparticle ions into the glass matrix in the vicinity of the nanoparticle. Upon illumination with an ultrashort pulse that possesses a high peak power, a single- or multi-photon ionization can be present as well as the tunneling ionization, where the energetic bands of silver can be bend due to the high electric field leading to tunneling of electrons through it.

Secondly, there can be distinguished two other types of ionization that is present in nanoparticle irradiation. These are isotropic photoemission of electrons by the nanosphere and anisotropic E-field enhanced photoemission which gives rise to the prolonged shape of nanoparticle. These two types of photoemission can be described on an energy level scheme taken from [132]:

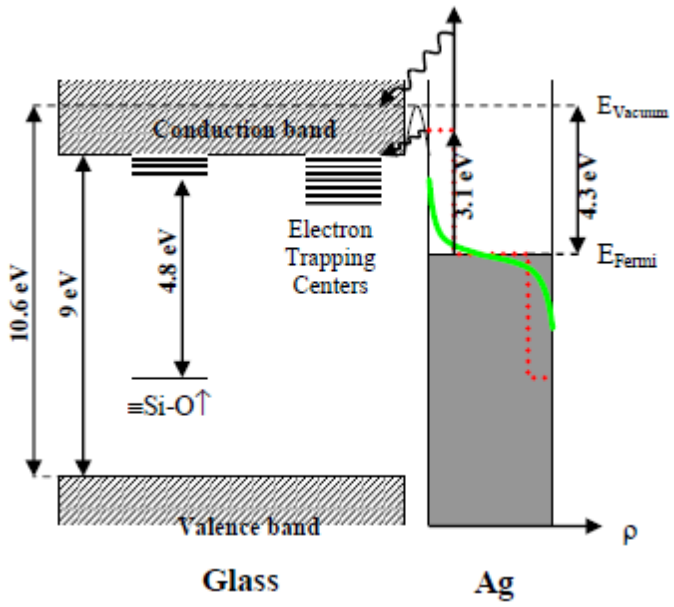

Figure 2-15 Schematic representation of silver/glass in terms of energy levels. Red dotted line represent the laser induced electron states, green line the f-d electron distribution. Drawing taken from [132].

Here, the nanoparticle embedded in glass is assumed to follow a silver/glass junction representation. In this description of a photoemission process the electrons from the silver Fermi energy level can be emitted to the conduction band of the glass once the appropriate energy will be obtained (>2.7 eV). In the figure, this condition is met when the non-thermal electron distribution is taking place (red dotted line). While for fs-irradiation at 400 nm that was the case (3.1 eV), off-resonance irradiation at ps-pulses does not exceed this energy requirement (532 nm ~2.3 eV). It was however shown in [133] that illumination of a metallic nanoparticle close to the resonance SPR band can produce near-field enhancement that will enhance the multi-photon ionization probability. This is also shown in the figure in the form of a two photon ionization. This means that even though hot-electrons cannot easily be ionized into the conduction band of glass by isotropic process, the anisotropic enhancement around the nanoparticle poles can definitely be the biggest factor allowing to eject electrons to the glass matrix. It was also shown by Podlipensky[132] in Figure 2-15, that once the electrons are ejected to the glass, colour centers form which increase the conductivity of the glass itself (lowered conduction band level). This effect can certainly promote the anisotropic electron ejection during the ps-pulse irradiation, after certain condition band level in the glass will be achieved.

E-field enhancement occurs due to SPR at the poles of the nanoparticle in the direction of the incident laser polarisation [134]–[137]. This field can increase the distance that the electron or ions of silver could travel (which is also a process dependent on the temperature in the vicinity). It is therefore thought to be the most significant parameter during the shape modification of nanoparticle, as the most electrons will become trapped in the colour centers exactly where the highest E-field enhancement is – at the nanoparticle poles.

In summary, the reshaping of a nanoparticle upon an ultrashort laser pulse proceeds as follows (Figure 2-16):

a) Excitation of nanoparticle, as it was already mentioned, increases the probability of injection of electrons into the glass matrix. Two types of electron injection are present. The isotropic injection caused by the general temperature increase in the nanoparticle and the anisotropic injection caused by the laser pulse and in the direction of its polarisation. The latter is the most pronounced as described earlier. Additionally, colour centers form in glass where the electrons are being trapped.

b) The resulting and in the same time positively charged nanoparticle core begins to destabilize, leading to so called Coulomb explosion [131]. This effect leads to ejection of positively charged silver ions into the glass matrix isotopically.

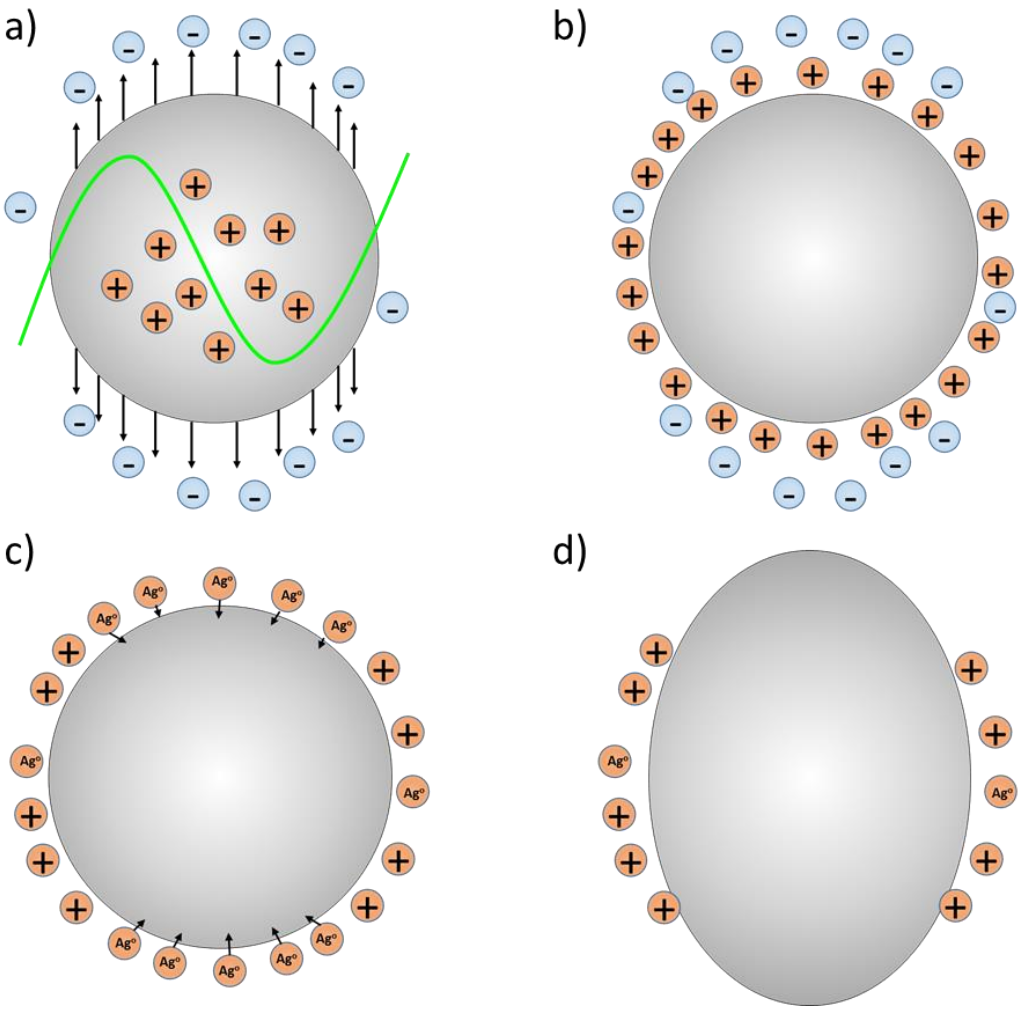

Figure 2-16 The main processes arising during ultrashort laser pulse irradiation of nanoparticle, resulting in nanoparticle elongation: a) ejection of electrons to the glass matrix, b) Coulomb explosion, c) silver ions reduction and return to the nanoparticle, d) resulting shape of nanoparticle after multi-pulse interaction

It was measured by Podlipensky and Stalmashonak [131], that this process takes place by direct TEM images as well as the luminescence studies [138] which showed not only presence of simple Ag^{+} ions but also clustered Ag species (this study will be also performed in the later part of this thesis for luminescence explanation during the Second Harmonic Generation). It is important to mention at this stage that the distance at which the ions travel depends highly on the temperature in the closest vicinity of the nanoparticle. In case of ps- irradiation the temperatures that promote increased ion mobility would be higher than for fs- irradiations due to the fact that the nanoparticle would have substantially more time to transfer heat to the glass matrix. In the same time high repetition rate of a ps- irradiation would create efficient reshaping (TTM model). Also, too high temperatures will increase the area of higher temperature to the stage that

ions will simply flow too far away from the nanoparticle leading to dissolution (this will be shown in the next chapter for irradiation with multi pulses per spot as well as for high repetition rate irradiation).

c) The emitted ions begin to reduce thanks to all the trapped electrons at the poles of the nanoparticle creating silver atoms Ag^{o}. Because of their natural charge, they will then precipitate and form small clusters that will eventually join the nanoparticle.

d) Each additional pulse added to the nanoparticle will repeat the process, which will cause a buildup in nanoparticle size on its poles. In the same time each Coulomb explosion will reduce the amount of silver atoms in the orthogonal axis leading to elongate the nanoparticle.

2.4 Conclusions

In this Chapter, the theoretical background of interaction between a laser pulse and a metallic nanoparticle was presented. Behaviors of electrons upon the EM field were firstly shown, followed by the *quasi-static approximation*, Gustav's Mie model and the Discrete Dipole Approximation (DDA). Surface Plasmon Resonance was defined and its modification as a function of nanoparticle size and the refractive index of the embedded medium were presented. These aided calculation of local temperatures of the metal-glass system, which was performed using the Two-Temperature Model (TTM).

Detailed description of the interaction between an ultrashort pulse and the nanoparticle was presented: timescale of electron/phonon excitation and relaxation, behavior of electrons and core ions leading to effective elongation of nanoparticle, and an energetic model of elongation which showed the importance of colour centers forming in the glass.

3 Experimental methods

3.1 Introduction

Chapter 3 will present the main experimental techniques used in the thesis. These include:

1) Preparation of silver-glass nanocomposites,
2) Techniques used for characterisation of MGNs that utilized their linear optical properties,
3) Laser techniques for photo modification of nanoparticles,
4) Short pulsed laser characterisation techniques utilizing nonlinear optical properties of prepared composites,
5) Scanning Electron Microscopy (SEM) technique of nanoparticles' characterisation.

Samples containing silver nanoparticles and silver ions were provided by CODIXX AG. Technology used for their production and morphology of the resulting composites will be discussed in this chapter.

3.2 Metal-Glass Nanocomposites (MGNs) preparation

Samples that were used for all of the experiments in this thesis were prepared by the Ag-Na ion-exchange method. This method is well established for production of nanoparticles in glasses. It has been used for almost a century and it was even demonstrated in 1913 [139], [140] that monovalent cations contained in glass could be exchanged when a sodium-containing silicate glass was immersed in molten silver nitrate. The glass matrix used for this thesis purpose was soda-lime glass. Soda-lime silicate glasses are commonly used commercially. In general, the glass network base is a silicon-oxygen tetrahedron with modifier cations (Na^+ and Ca^{2+}) introduced to the non-bridging oxygen units (NBO) that form during the melting process of SiO_2 with Na_2O and CaO [141], [142]. A schematic diagram of a structure of a soda-lime glass is presented in Figure 3-1. In this thesis, soda-lime glass used for the experiments consisted of: (wt.-%) 72.5 SiO2, 14.4 Na2O, 6.1 CaO, 0.7 K2O, 4.0 MgO, 1.5 Al2O3, 0.1 Fe2O3, 0.1 MnO, and 0.4 SO3. As mentioned before, the Ag-Na ion-exchange method has been used for formation of silver nanoparticles.

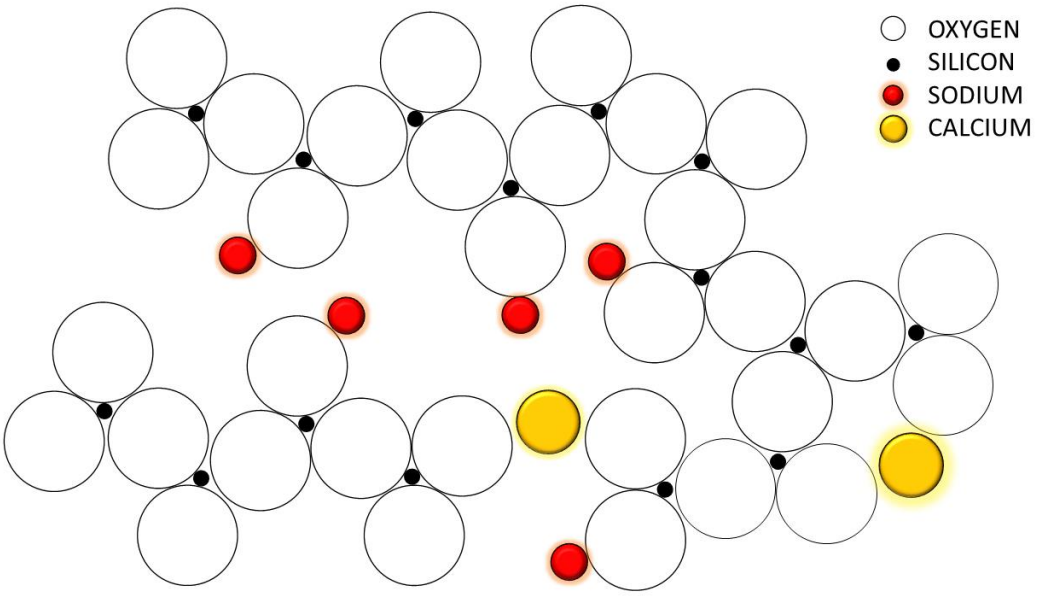

Figure 3-1 Two dimensional structure of a soda-lime-silicate glass. If a three dimensional picture was to be drawn, a fourth oxygen would be present above each silicon.

For production of silver nanoparticles, a flat soda-lime glass substrate is immersed in a molted salt of $AgNO_3$ and KNO_3 and the overall temperature of such a system is elevated to 400°C. In such environment sodium ions' (Na^+) mobility increases to a point that it can exchange with silver ions that are present in the molten salt, followed by silver ions being associated with the non-bridging oxygen. This results in formation of silver ion (Ag^+) clusters in the glass volume. Annealing process in H_2 reduction atmosphere is later needed in order to start reduction of silver ions (Ag^+) into atoms (Ag^0), according to the reaction[143]–[145]:

$$\equiv S - O^- Ag^+ + \frac{1}{2} H_2 \leftrightarrow \equiv Si - O - H^+ + Ag^0 \qquad 3\text{-}1$$

When an oversaturation of the glass matrix with silver atoms becomes critical nanoparticle formation takes place [143]. Parameters used in the process (time, temperature, weight concentration of AgNO3, etc.) are set so that the size and distribution of Ag nanoparticles is known and as desired.

For the purpose of this thesis, samples were supplied by Codixx AG whose manufacturing technology (ion exchange and annealing processes) allowed them to deliver samples containing spherical silver nanoparticles with a mean diameter of 30 – 40 nm, located ~30 nm below the glass surface in a thin layer of about 20 µm thick. Two-sided samples were fabricated of an overall sample thickness of ~1 mm. It has to be mentioned that the method presented above produced nanoparticles being spread in

the glass matrix volume in various concentrations (as a function of the glass depth) - poly-dispersed samples. In such type of samples, the volume filling factor changes gradually below the glass surface. It can be defined as a ratio of the volume of silver nanoclusters (V_{Ag}) to the unit volume of the whole sample (V_{total}):

$$f = \frac{V_{Ag}}{V_{total}} \qquad 3\text{-}2$$

The graphical representation of the filling factor as a function of the sample depth can be seen on the Figure 3-2. It was estimated by Podlipensky and Deparis et al. [146], [147] how the volume filling factor behaves for such systems. First method included etching layers of nanoparticles in steps, with a 12% concentrated HF acid and taking SEM images for estimation. Second method involved fitting a theoretical model for the optical extinction to the measured extinction for each etching step. It was concluded that the volume filling factor at ~0.29 is created near the glass surface and decreases to zero after some micrometers into the volume of the glass (~20 µm in this case).

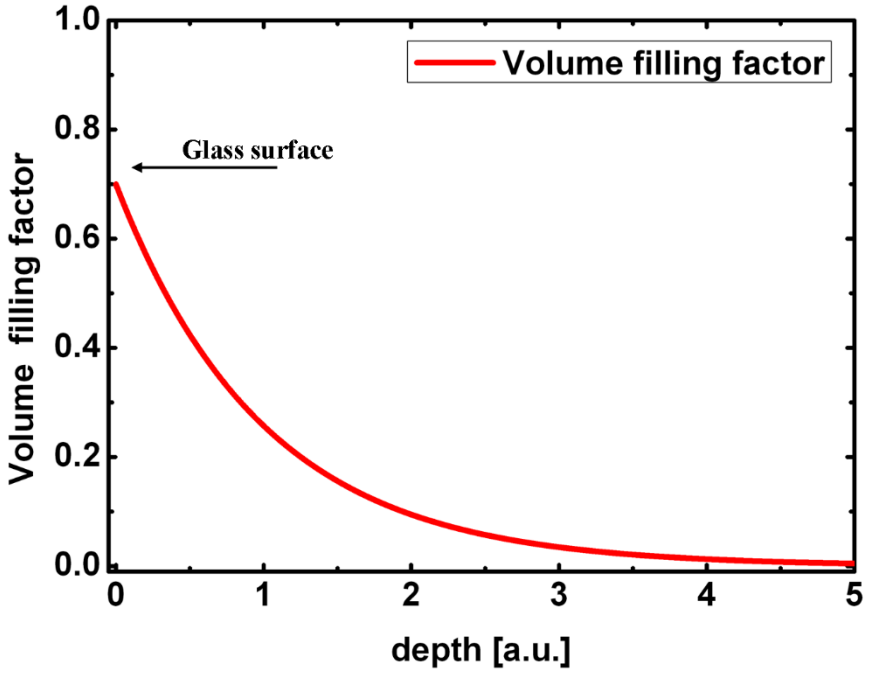

Figure 3-2 The volume filling factor as a function of depth of the samples volume

Furthermore, in order to visualize the depth profile of the silver particle-containing layer, one of the samples was cut and a thin slice was prepared. Figure 3-3 presents the cross-section of the nanoparticles area. For this, the sample was embedded in the epoxy resin (Specifix-20, Struers Limited) to prevent chipping of the glass and to make it physically manageable for grinding, polishing, etc. The resin cured at room temperature. The ~30

μm thick section was polished on both sides. One-sided samples were used in all the further experiments and were obtained by etching one side of each sample by a 12% concentrated HF acid. Preparation of the sample for etching involved cleaning its surface with a degreasing agent and washing with warm and then cold deionized water for 10 minutes. Next, the sample was dried with nitrogen gas and placed into a sonic bath of acetone for 15 minutes, after which in isopropyl alcohol for another 15 minutes. Sample was then dried again with nitrogen and put on to a hotplate that was warmed up to 105^{o}C for a few minutes. After that, a photoresist was spin coated on the sample with 2000 rpm and 20 seconds of spin. Resulting coated sample was then placed for a soft bake onto a hotplate on 90^{o}C for 10 minutes and later for a hard bake on 140^{o}C for 10 minutes. Sample was then left to cool down slowly in order to reduce any stress being induced on the surface of the resist. With the resist prepared on one side of the glass, sample was placed in a beaker filled with HF acid for ~5 minutes for etch. All of the above steps were performed under a wet deck.

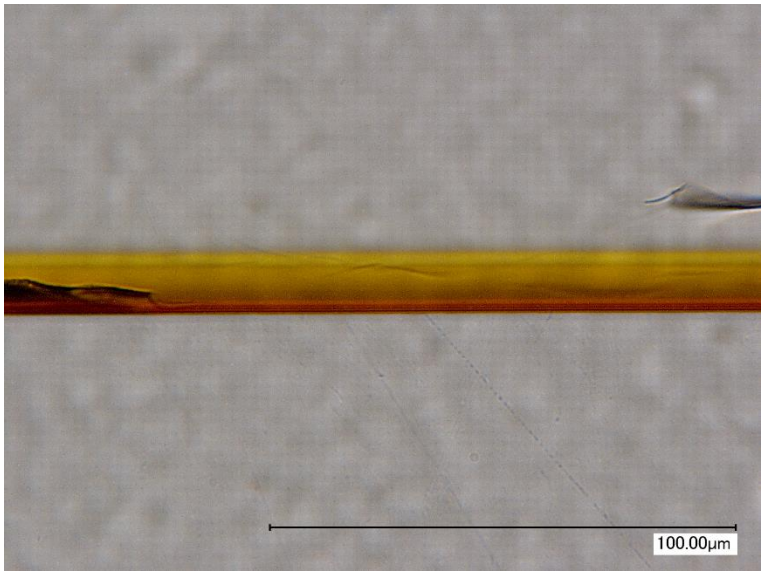

Figure 3-3 Cross section of the sample showing the layer of silver nanoparticles embedded in the glass

Two other types of samples were also used for certain experiments that will be presented in the forthcoming chapters: 1 mm thick and high filling factor sample and ~250 μm thick mechanically stretched sample with the same filling factor stated before.

3.3 Linear optical characterisation

In order to characterize samples in terms of their linear optical properties, a Surface Plasmon Resonance spectrum needed to be acquired. For this purpose a UV-VIS-NIR spectrophotometer was used (JASCO V-670 UV-VIS-NIR), with high resolution (down to 0.1nm) and readout linearity (correlation coefficient of 0.9 up to 10 abs). The instrument also consisted of a sample holder and a reference sample holder. The sample holder could be adjusted as presented in Figure 3-4. The incoming light I_0 was not polarised and an additional polariser had to be added at the entrance light path in order to linearly polarize the I_0.

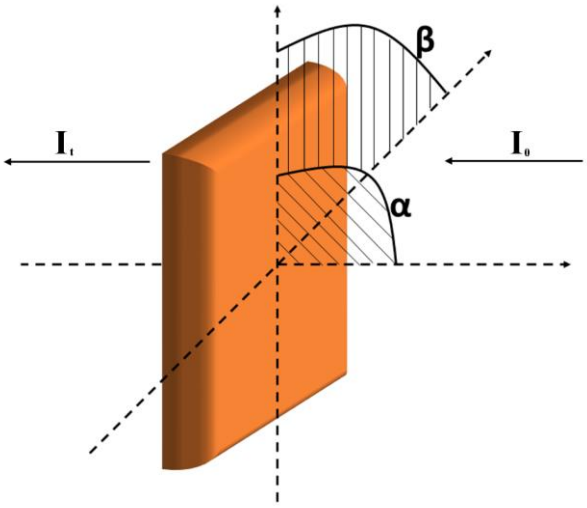

Figure 3-4 A graphical description of how the sample holder position could be altered in order to fully characterize samples containing nanoparticles. I_0 is the incident light intensity and I_t is the transmitted light intensity.

The reference holder was equipped with an ND filter (the second light path was used for holding the MGN sample). It allowed the detection of extinction peaks of some MGNs that would otherwise have been outside the measurement range (due to the extremely high extinction ratio of nanoparticles). Extinction spectra (defined as a sum of absorption and scattering on nanoparticle) were calculated from the absorbance that was measured in the spectrophotometer using equation 3-3:

$$Extinction = -ln(T) = -ln\left(\frac{I_0}{I_t}\right) \qquad 3\text{-}3$$

The extinction spectrum obtained can be seen in Figure 3-5. It is shown that the light-nanoparticle interaction causes such high extinction that it exceeds the spectrophotometer maximum limit. It should be noted that the use of an ND filter in the

reference light path did not always allow to show the SPR peak (especially in spherical nanoparticles and with high filling factors).

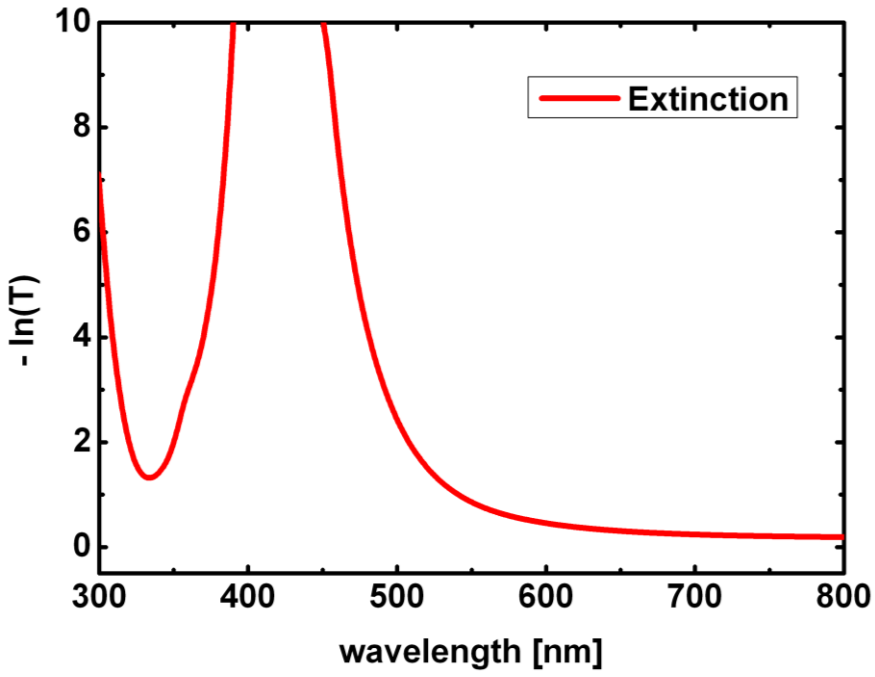

Figure 3-5 Example extinction spectrum taken from sample containing spherical nanoparticles of silver embedded in soda-lima glass

Additionally, for characterisation purposes a digital optical microscope was used to visualize the surface of the sample pre- and post- irradiation with a laser.

The microscope system can be seen in Figure 3-6. Microscope objectives used were the VH-Z100R and VH-Z500R. The former allowed magnification of 100x down to 1000x, and the latter from 500x down to 5000x. Samples could have been illuminated in either transmission or reflection mode. Two additional linear polarizers have been added in the transmission mode in a crossed polarizer configuration in order to determine polarisation dependency of the irradiated areas. A halogen lamp was used as the illumination source and optical waveguides were used to transfer light to the objective and the sample.

Figure 3-6 Keyence VHX-1000 imaging system [148].

3.4 Nanoparticles size distribution

It was described in section 3.2 that MGNs used in this thesis are poli-dispersed and have certain filling factor (here 0.29). It is therefore important to evaluate nanoparticles in terms of their size distribution within the nanoparticle layer. This will be useful in determination of tolerances on all other measurements presented in this thesis.

Direct measurement of the size distribution was not performed within this thesis. It was known however that CODIXX AG supplied the samples with a nanoparticle mean diameter of 30 – 40 nm. In order to determine the size distribution of nanoparticles in ion-exchange processes, a literature review will be presented. It was shown by Schicke et al. [149] how the nanoparticle size depends on the penetration depth of silver during the ion-exchange process. It was concluded there, that Ag particles exhibited a narrow size distribution of Gaussian shape (between 0.7 to 0.9 nm FWHM). Cai et al. [150] argued that however the size distribution of nanoparticles broadens the SPR bandwidth, its position is rather insensitive to the occurrence of a size distribution with log-normal, Gaussian or triangular and narrow function. He stated that for small Ag particles the Mie resonance shift is weakly depended on the size distribution of nanoparticles and on the dielectric constant of the surrounding medium. In work presented by Berger et al. [151] the silver nanoparticle size distribution was shown to be Gaussian in shape. It was also stated that the mean particle size is nearly independent on the penetration depth. A

conclusion was also made that the extinction spectrum was the superposition of different bands from various nanoparticle sizes. It can therefore be possible to partially predict the nanoparticle size distribution by simulating single nanoparticle SPRs for various nanoparticle sizes, where the sum of their SPRs will not be greater than the experimentally measured. Berg et al. [152] showed in his work, how concentration and size change of nanoparticles in ion-exchange process influences the Mie resonance. He stated that the size distribution of silver is well described by a Gaussian function with a standard deviation of $\sigma = 0.28 * \overline{2R}$ (where R is a radius of a spherical silver nanoparticle). It was also shown there how the bandwidth of the SPR changed with a nanoparticle radius and the SPR position, and how it compared to graphs presented in [50] (Figure 2-9 in section 2.2). From there, one could estimate that for a silver nanoparticle of $\overline{2R} \cong 35\text{nm}$ the SPR bandwidth can range between 40 and 90 nm (depending on the ion exchange process type). A more directly relevant and experimental results were given by Graener et al. [153] where silver nanoparticles embedded in soda-lime glass were experimentally measured for their size distribution. There, a quantitative SAXS analysis results were shown, giving a mean nanoparticle diameter of 29nm with a size distribution width of σ = 4nm ($\sim 0.14 * \overline{2R}$). In work presented by Wackerow et al. [154], an experimental method of MGNs production was changed from heat assisted ion-exchange to E-field assisted. There, silver ions were forced into the glass matrix and annealed in order to create silver nanoparticles embedded in soda-lime. These experimental results also showed that the size distribution is not greater than presented previously ie. NPs at 200 μm depth had distribution of ~ 6nm +/- 1 nm ($\sim 0.16 * \overline{2R}$).

From Figure 3-5, which shows the SPR of a spherical MGN used throughout this thesis, it can be observed that the SPR bandwidth is ~ 80nm, which agrees with aforementioned results from Berg. Also, applying the experimentally obtained formula, one can calculate that $\sigma = 0.14 * 35 = 4.9$ nm.

As stated earlier, the measured SPR could be interpreted as a superposition of Mie resonances of various NPs contained within the NP layer. DDA simulation was performed for NP diameters: 20 – 50nm, and compared with spherical NP measured experimentally (below).

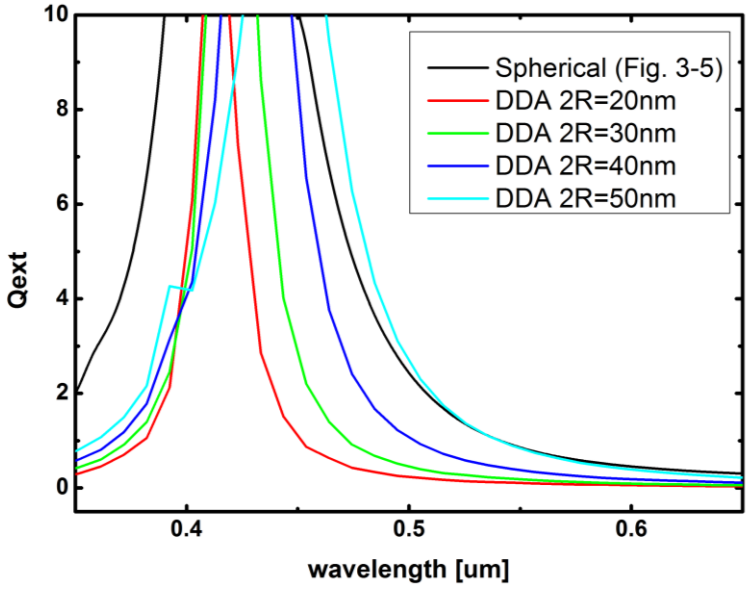

Figure 3-7 Experimentally measured SPR for spherical MGN (black) compared with simulated with DDA for various NP diameter {20, 30, 40, 50}.

The red-shift can be easily observed in the simulated SPR along with their broadening. While 40 - 50nm diameter simulation matches the longer wavelength range of the experimental SPR, diameter of 20nm simulation does not match the short wavelength part of the experimental SPR. This is due the fact that a diameter change in a single nanoparticle model does not increase the SPR bandwidth significantly, but rather shifts the SPR position. This model can however be useful to estimate which simulated NP diameters have their SPR in the centre of the experimental SPR band. Here, 30nm diameter simulation was the most central, which agreed with previously assumed value of the mean NP diameter of ~35nm. Also, it can be observed that a range of 25nm – 45nm NPs would be still well within that experimentally measured SPR bandwidth. Taking that into consideration, along with the formula of $\sigma = 0.28 * \overline{2R}$, which for a mean diameter of 35nm gives range of <25.2nm:44.8nm>, it can be assumed that the MGN presented in this thesis has that very range of NP diameters. This range becomes smaller when taking the formula from experimental reference work presented earlier ($\sigma = 0.14 * \overline{2R}$), which gives <30.1nm:39.9nm>. The SPR bandwidth of between 40-80nm (stated earlier in this subsection and taken from ref.[152]) for a 35nm diameter NP, provides a well determined assumption that the nanoparticles used in this thesis are 35nm +/- 4.9nm. It can be assumed that this range can be directly translated to reshaped nanoparticle size distribution, as each NP will have a different extinction peak value leading to a different ratio of reshaping. It is fair to state however that this size distribution is rather tight, and that during the reshaping process, even though there will

be broadening of the SPR band, peak positions of that bands will be analyzed with fitting a simulated DDA results to it in order to calculate the elongation ratio and relate it to the SHG and MAIL slope.

3.5 Laser system

Experiments presented in this thesis are based on using a ps-pulsed laser system for both laser processing of MGNs as well as optical characterisation. The laser system used for the aforementioned applications was a Talisker laser manufactured by Coherent. It was an industrial type of turn-key laser system that could produce short (~5-10 picosecond) laser pulses at three main wavelengths: 1064nm, 532nm (frequency doubled), and 355nm (frequency tripled). Talisker was a fibre based laser system where the fibre modelocked laser was used to produce ultra-short pulses that were then amplified in a regenerative amplifier to produce high energy pulses at high repetition rate. The laser output was a Gaussian beam of about 1 mm in diameter (at $1/e^2$). Parameters that could be varied were: laser repetition rate, pulse energy and harmonic wavelength. The laser system can be seen in Figure 3-8.

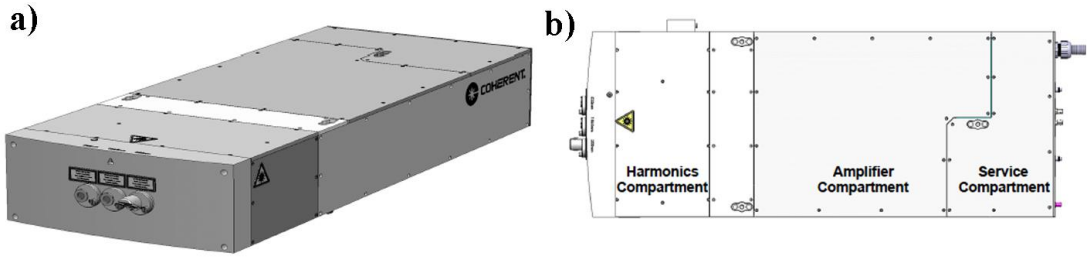

Figure 3-8 Talisker laser system a) rendered image b) system schematics [155]

The laser consisted of three compartments: the harmonic compartment (where the initial 1064 nm wavelength beam was converted to either 532 nm or 355nm), the amplifier compartment where the initially mode-locked laser pulses were amplified and the service compartment where all of the non-optical components were placed (i.e. Interconnection between laser and the power supply, laser chiller, harmonic controller). The Fiber Array Packages (FAPs) were located in the power supply (producing low power mode-locked laser pulses at 1064 nm wavelength) from where pulses were delivered by a fibre optic cable to the amplifier compartment. FAPs produced ~5 ps pulses at repetition rate of 40 MHz. Once light pulses were injected to the amplifier they underwent a multipass regenerative amplification. The amplification gain medium was

selected to provide amplification at 1064 nm. Ejection of amplified pulses was accomplished by a Pockels cell and polarisation-dependent optical elements. The system was designed so that the repetition rate of the amplified pulses was set to 200 kHz, but it could have been changed in the later stages by the use of an Acousto-Optical Modulator (effectively from one shot to 200 kHz). Just before the beam entered the harmonics compartment it passed through a half-wave plate in order to control its polarisation state. The harmonic compartment consisted of two Lithium Triborate crystals (LBO) for producing second- (532 nm) and third-harmonic (355 nm), therefore three output windows existed for using three laser beams. The maximum average power for them are ~16 W for 1064 nm, ~8W for 532 nm, and ~4W for 355 nm beam and M^2<1.3.

This laser system was used for laser reshaping of nanoparticles as well as for luminescence studies and Second-Harmonic-Generation (SHG).

3.5.1 Laser system used for MGN reshaping

Talisker laser system was used for reshaping of nanoparticles. Two types of laser polarisation states have been used for that purpose, and that required a specially designed laser processing setup. Such setup was built for the purpose of this thesis utilizing the aforementioned Talisker laser, galvo scanners, and CPU control. The experimental setup for elongation of nanoparticles can be seen in Figure 3-9.

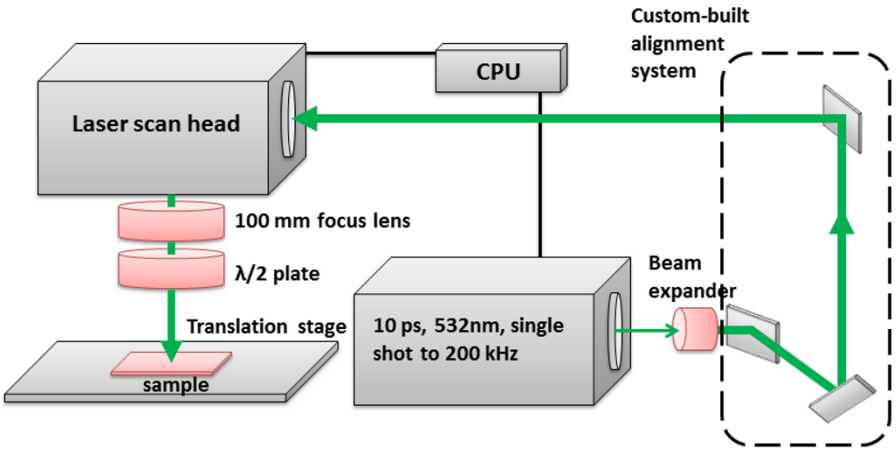

Figure 3-9 Laser reshaping setup for elongation of nanoparticles embedded in soda-lime glass

A 532 nm beam was used for reshaping. The beam was firstly expanded by a variable beam expander and then aligned with the laser scan head entrance pupil by the custom-built alignment system. The beam diameter was ~8 mm (at $1/e^2$) at the scan head entrance. A 100 mm focal length f-theta focusing lens was used to focus the beam to the

sample plane resulting in a waist diameter of ~12 μm. The f-Theta lens allowed for a focusing on a flat plane while maintaining the depth of focus. A λ/2 plate was also installed in the beam path in order to control the beam polarisation state. MGNs were put on a 3-axis translation stage below the scan head.

The scan head was manufactured by Nutfield Technology – model XLR8 (seen in Figure 3-10). The scanning system consisted of two galvanometer scanners: X-Galvo and Y-Galvo that were computer controlled. This allowed for precise movement of mirrors that were attached to the galvanometers and which directed the laser beam in the X and Y axes.

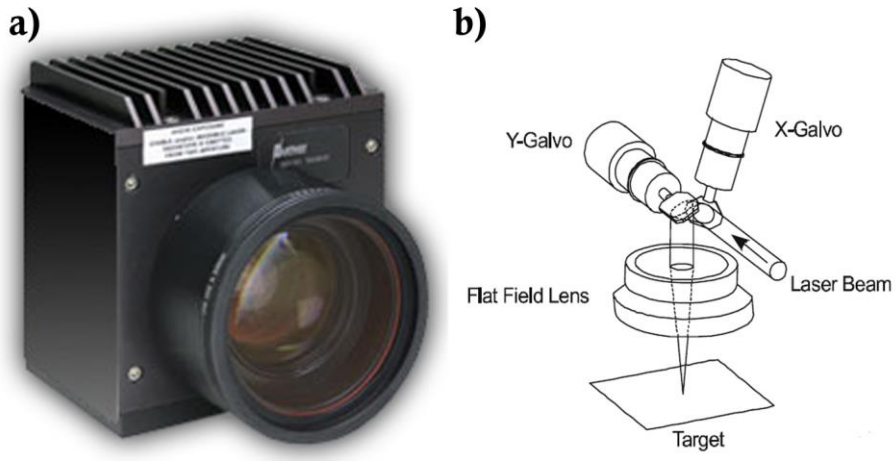

Figure 3-10 XLR8 Scan Head system a) image of the system b) technical drawing showing galvanometers, laser beam entering the scan head and a f-theta lens [156]

Laser system used for reshaping nanoparticles was also used for processing MGNs with radially and azimuthally polarised laser beams. For this purpose the setup was rebuilt, where the λ/2 plate was replaced by an S-wave plate. This was configured so that either state of polarisation could have been chosen. The adjusted setup can be seen in Figure 3-11. An S-wave plate is a commercially available optical element manufactured by Altechna. It changes the initially linearly polarised laser beam into radial or azimuthal (see inset of Figure 3-11). The S-wave plate could have also been used for the creation of optical vortices but this particular property was not used for further experiments.

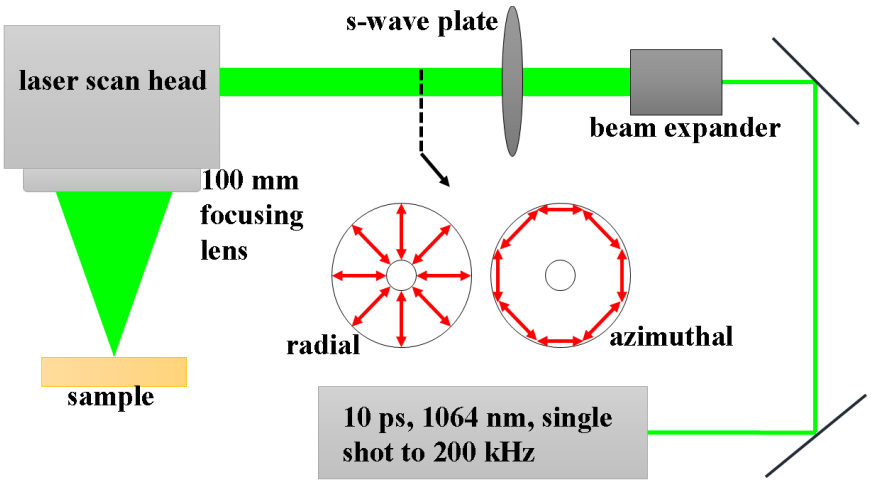

Figure 3-11 Experimental setup used for reshaping of nanoparticles with the use of either radial or azimuthal polarisation state of the laser beam.

3.5.2 Laser system used for SHG and luminescence studies

The Talisker laser was also used in measurements of the Second-Harmonic-Generation (SHG) produced by the elongated MGNs. A separate experimental setup was built for this purpose and can be seen in Figure 3-12. All of the optical components were chosen and incorporated into the newly build experimental station in a cage system.

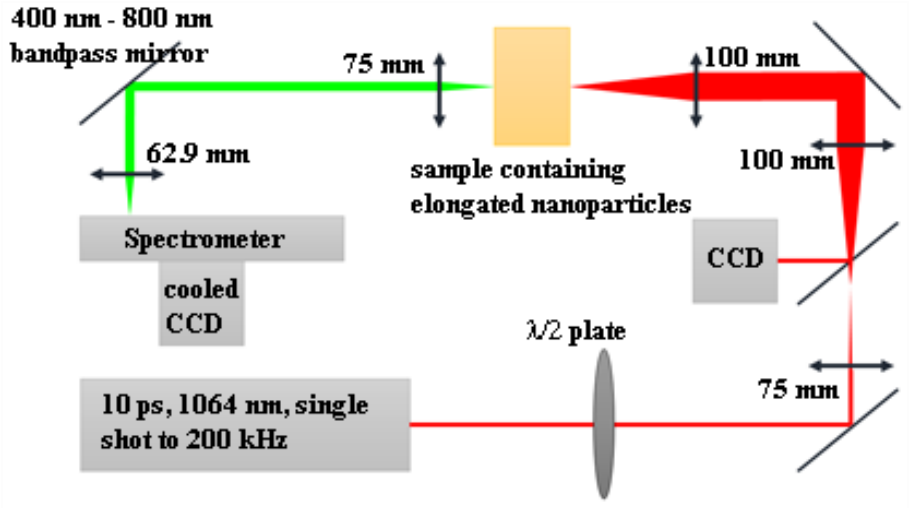

Figure 3-12 Experimental setup used for Second-Harmonic-Generation

A 1064 nm wavelength was used as the fundamental beam, which was produced by a Talisker laser system. A beam expander was used to expand the beam with two achromatic doublets of focal lengths of 75 and 100 mm. A 100 mm focal length lens was used to focus the beam to ~64 μm in diameter. The reflected 1064 nm beam passed

through a beam splitter and hit the CCD camera that was used for alignment purposes. The SHG beam was collimated by the 75 mm focal length lens and then focused again with a 62.9 mm focal length lens into the spectrometer slit, which had a cooled CCD camera attached (effectively a double monochromator with a CCD attached).

This experimental setup was designed so that it could have also been used for measurements of SHG in reflection from the MGNs, which can be seen in Figure 3-13 (a beam block was used in order to block the unwanted SHG signal from the transmission line). Here, the reflected 532 nm beam would be collimated back through the 100 mm lens and pass through a dichroic mirror. Then it would be focused with the same 62.9 mm focal length lens on the spectrometer. In both cases (that is transmission and reflection geometries), spectral filtering mirrors were used (400nm-800nm band-pass mirrors) for blocking the 1064 nm beam. The polarisation state of the fundamental beam was controlled with the λ/2 plate (also a λ/4 plate was used in some experiments in order to achieve a circularly polarised laser beam). The fundamental beam (1064nm) was also filtered with a laser line filter in order to reduce any unwanted light (like SHG and/or THG internally produced in the harmonics compartment of the Talisker).

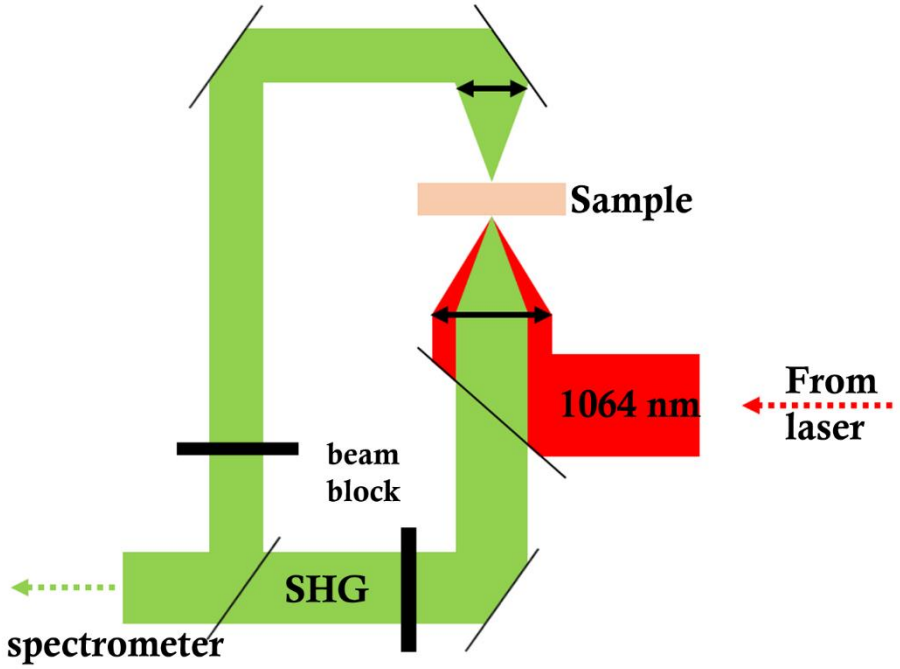

Figure 3-13 Schematic of two geometries that were used for measurements: transmission and reflection

The SHG light was also analyzed with the use of a linear polariser that was placed just before the 62.9 mm lens. Its polarisation direction was varied in order to detect polarisation components of the measured beam.

A modified version of the above setup was built for luminescence studies of MGNs where the fundamental beam was 532 nm. Laser line filter at the input was then changed to the 532 nm filter and a 532 nm notch filter was placed at the output in order to filter out the fundamental beam. The resulting signal was analyzed in band-pass filtering mirrors, range 400 and 800 nm.

A separate illumination source was placed above the sample for imaging purposes. The illuminated image of the MGN's area was visualized on the CCD camera (used previously for alignment) - an inverted microscope geometry.

In order to protect the Talisker laser from unwanted reflections from the measurement system, an optical isolator was present at the output of the laser.

3.5.3 Laser SHG setup used for characterisation of MGN morphology

During the irradiation process, it was important to measure the nanoparticle morphology in order to realize how the laser reshaping process influences the MGN. In order to further characterize the irradiated areas, the SHG setup presented in the previous sub-chapter was adopted and can be seen in Figure 3-14. Its design and built was part of this thesis, which proved to be extremely useful tool for future characterizations of MGNs. Here, a 1064 nm wavelength beam was used as fundamental. Incident polarisation was controlled with a λ/2 plate.

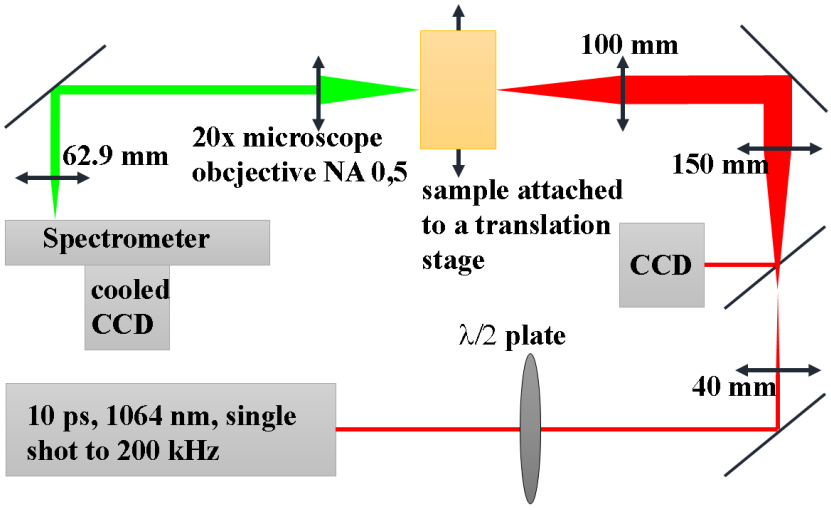

Figure 3-14 Experimental setup used for nonlinear characterisation of reshaped samples

The beam was expanded with a two lens telescope system (4x) and then focused to the sample with a spot size of ~20 μm in diameter. A CCD camera aided the sample alignment. A high-precision translation stage was used in order to scan the sample at small steps across the excitation laser beam. The signal form the sample was collected

with a 20x microscope objective (Nikon, NA = 0.5) and then focused with a 62.9 mm focal length lens on to a spectrometer. This experimental setup allowed for characterisation of finely irradiated areas in terms of the nanoparticle directionality and shape. The procedure used for measurements was prepared so that for each step of the translation stage, signal was acquired for various incident beam polarisations.

3.6 Frequency Resolved Optical Gating (FROG)

Second order nonlinearity of MGNs was used in the Frequency Resolved Optical Gating (FROG) measuring system where the β Barium Borate (BBO) was replaced with a reshaped MGN [157], [158]. Measurement of a 50 fs pulse length and phase was performed. The measurement setup can be seen in Figure 3-15.

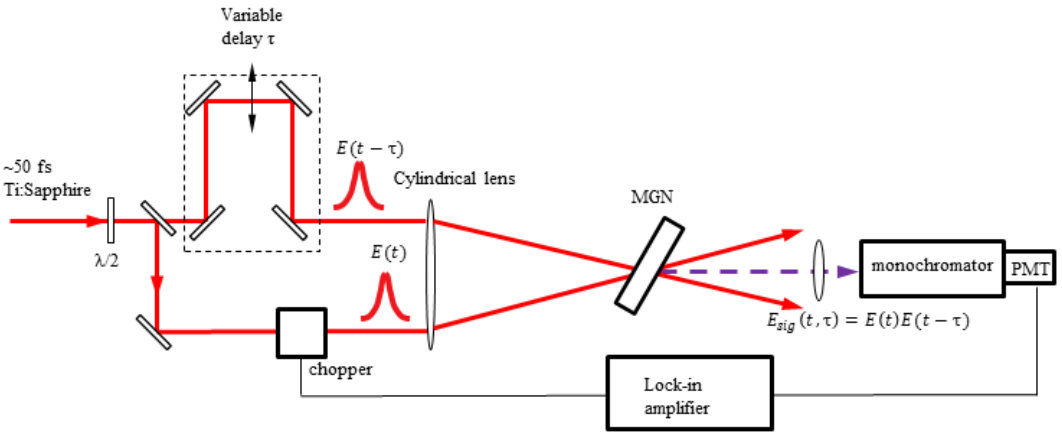

Figure 3-15 Frequency Resolved Optical Gating measurement system, where the BBO was effectively replaced by reshaped MGN. MGN was placed as certaing angle and orientation to maximise efficiency

The fs-laser beam was passed through a λ/2 plate for polarisation state control, then separated into two beam paths. One of the optical paths was designed to add a time delay to the pulse. The MGN was placed in the focal plane of a cylindrical lens (cylinder was used in order to decrease the overall fluence of the beam on the sample). The resulting signal was captured with a monochromator and a photomultiplier tube.

These measurements were performed at the STFC Daresbury Laboratory with the invaluable help of Dr Edward Snedden.

4 Laser assisted reshaping of metallic nanoparticles with linearly polarised picosecond pulses

4.1 Introduction

Chapter 4 will present experimental work that was performed on reshaping MGNs with picosecond laser pulses with linear polarisation direction.

It was discovered recently that femtosecond (fs) pulsed laser irradiation of Ag spherical nanoparticles embedded in soda-lime glass lead to formation of dichroic areas [131], [132], [147], [159], [160]. The origin of the effect was identified as the laser-induced permanent deformation of nanoparticles from spherical to spheroidal, along the polarization direction of the laser beam. It was identified that trapping electrons emitted from a nanoparticle during the reshaping process in the glass matrix was directional and depended strongly on the laser polarisation state (this effect is described in Chapter 2).

In this chapter the work on picosecond (~10 ps) reshaping will be presented. A linearly polarised laser beam was used, where the wavelength of the laser light (532 nm) was not directly aligned with the SPR of nanoparticles (~430 nm). This so-called 'off-resonant' reshaping is presented here. Various optical parameters are investigated in order to show more insight into the reshaping process - laser fluence, laser repetition rate, number of pulses fired per spot. Irradiation under an angle is also investigated for the purpose of identification of the exact shape of the nanostructures produced. Optimal parameters for reshaping with a picosecond laser beam are shown as a result.

4.2 Laser reshaping parameters

Laser irradiation of MGN samples has been performed while varying laser processing parameters. Laser fluence is one of the most important ones, and describes the amount of energy deposited at the surface of the sample per pulse. It can be defined as:

$$F = \frac{E_p}{\emptyset} \qquad 4\text{-}1$$

where E_p is the energy per laser pulse and ∅ is the beam spot area. Focusing ability of the beam was an important factor (laser pulse energy delivered could then be varied) which depended on the beam wavelength (directly proportional to the theoretically achievable diffraction limited spot). As described in **chapter 3,** a 100 mm focal length theta-lens was used in order to focus the beam to ~ 12 µm in beam diameter (measured at $1/e^2$). The spot diameter related to the beam waist as in Figure 4-1,

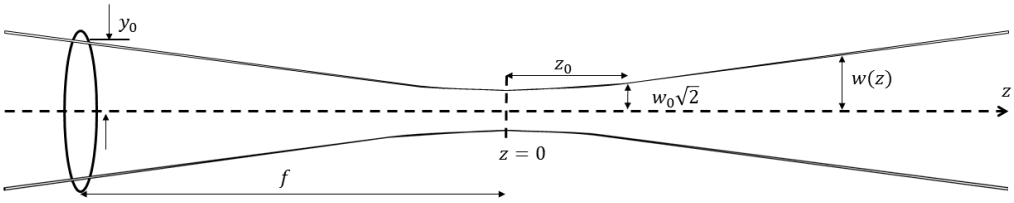

Figure 4-1 Beam propagation after focusing by a lens of focal length f. Collimated beam input is assumed.

where f was the lens focal length, y_0 was radius of the beam entering the focusing system, the beam waist was w_0 (minimum value of w(z), located at z=0), z_0 was the Rayleigh range that could be described with:

$$z_0 = \frac{\pi w_0^2}{M^2 \lambda} \qquad 4\text{-}2$$

Beam radius along the beam propagation direction (z-axis) could be described by:

$$w(z) = w_0 \sqrt{1 + \left(\frac{\lambda z}{\pi w_0^2}\right)^2} \qquad 4\text{-}3$$

Equation 4-3 calculates a theoretical value of a beam diameter at a given point in z direction. In order to obtain a realistic value, the M^2 of the laser system needs to be taken into account:

$$w(z) = w_{0real} \sqrt{1 + \left(\frac{\lambda z M^2}{\pi w_{0real}^2}\right)^2} \qquad 4\text{-}4$$

The beam waist for such focusing system can be calculated using:

$$w_0 = \frac{\lambda f M^2}{\pi y_0} \qquad 4\text{-}5$$

where M^2<1.3 for the Talisker laser system. Given all the parameters described in **chapter 3** the beam diameter for the reshaping system would be 11 µm (the measured value was however 12µm, as stated in Chapter 3). The depth of focus (DOF) is a parameter describing the distance over which the beam waist increases by $\sqrt{2}$ (twice the Rayleigh range). By implementing 4-2 we get:

$$DoF \cong 280\ \mu m \qquad 4\text{-}6$$

It has to be taken into account that the DOF might be even longer as the beam will be propagating through the glass near focus. Therefore it could be assumed that the distance for which the laser fluence was high enough to influence samples (either modify or destroy, depending on the pulse energy used) was ~280 µm and it was much bigger than the thickness of layer of nanoparticles present in the sample (~20 µm).

It is important for this type of laser processing to find the appropriate value of laser fluence during irradiation. Here, it was found experimentally.

Two main types of laser fluence thresholds exist: material (glass) ablation threshold and nanoparticle modification threshold. For the purpose of shape modification of silver nanoparticles the laser fluence was adjusted so that the modification threshold was reached, but was significantly lower than the glass ablation threshold (where the glass matrix would have been ablated by the laser beam). The modification threshold is illustrated in Figure 4-2.

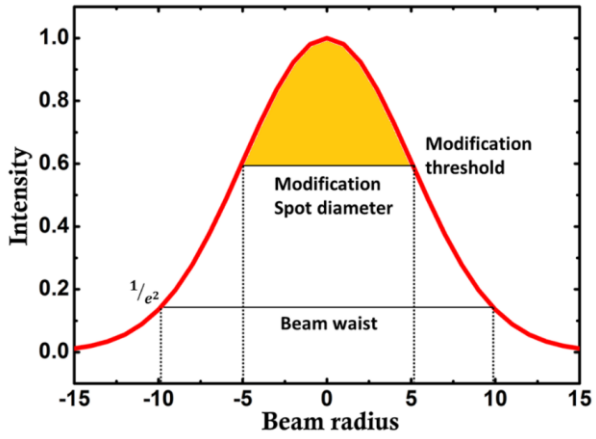

Figure 4-2 Intensity distribution of a laser spot. Modification intensity coloured in orange. Arbitrary units are used.

It can be concluded from the figure above that the effective beam diameter on sample changes when the ‘tip’ of the Gaussian intensity distribution is used for modification of nanoparticles. Figure 4-3 shows irradiation of MGN with a single pulse per spot. Each pulse energy was ~0.1 µJ. Diameter of the effective modified area was measured and was ~9µm.

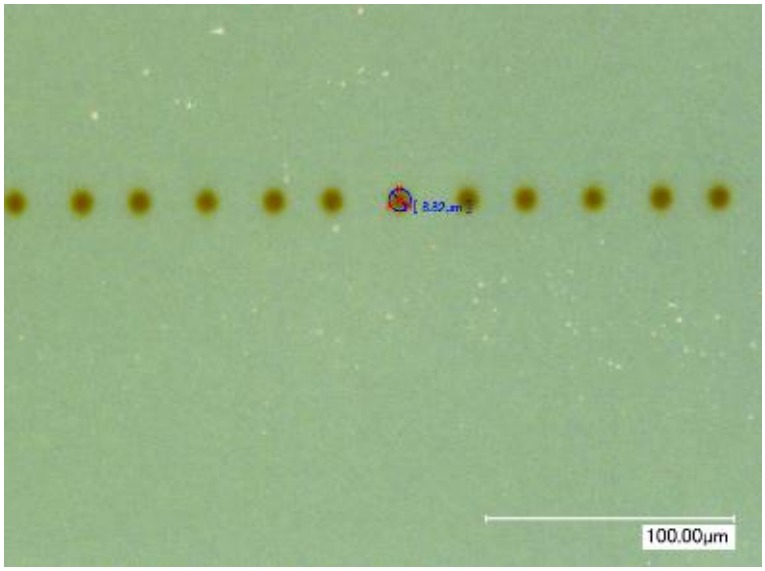

Figure 4-3 Microscope images of one pulse per spot irradiation of MGN.

4.3 Modification threshold

The laser modification threshold was found experimentally for the purpose of laser-induced shape change of nanoparticles. It was important to determine a threshold fluence for which the MGN changes its SPR position, so that appropriate value could be used for further experiments. Figure 4-4 (a) shows a microscope image of an area irradiated with different laser pulse energies: from 0.02 µJ to 0.08 µJ.

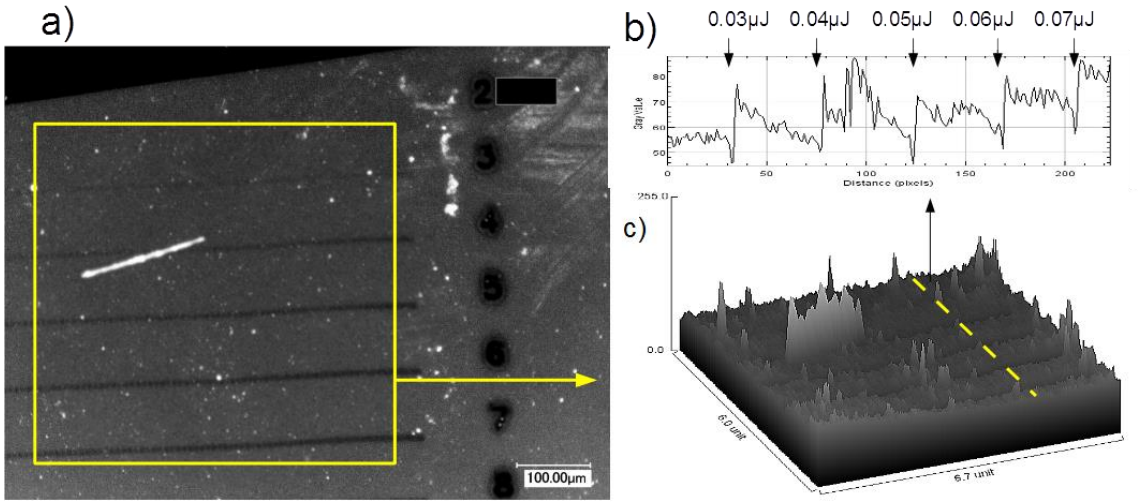

Figure 4-4 Single shot irradiation of MGN with varying laser pulse energies (0.02 µJ – 0.08 µJ). The yellow area in (a) is shown as a surface profile in (c). (b) is a cross sectional profile of (b) – yello dash line [161].

Laser repetition rate (ν) was set to 200 kHz and number of pulses per spot (N) to 1,

$$N = \frac{2w_0 * \nu}{V} \qquad 4\text{-}7$$

where V is the scan speed. Single spot irradiation was necessary in order to show the required laser energy flux required to perform the reshaping. Laser fluences corresponding to chosen parameters were $\sim 20\, {}^{mJ}/_{cm^2}$ to $\sim 70\, {}^{mJ}/_{cm^2}$. The yellow area (a) in Figure 4-4 indicates where the least visible modification occurred (0.03 µJ) by grey scale analysis of irradiated lines- hence the laser modification threshold was established to be$\sim 20\ {}^{mJ}/_{cm^2}$.

It was also important to establish the range of laser pulse energies that could be used for effective MGN shape modification. Higher fluence level threshold was also observed which caused the nanoparticle destruction. An experiment was performed in order to find the safe range of energies. A set of lines was irradiated with ~ 1 pulse per spot and with no overlapping between lines. Pulse energies were varied. Figure 4-5 presents the microscope image of irradiated areas illuminated from the back of the sample with unpolarised light.

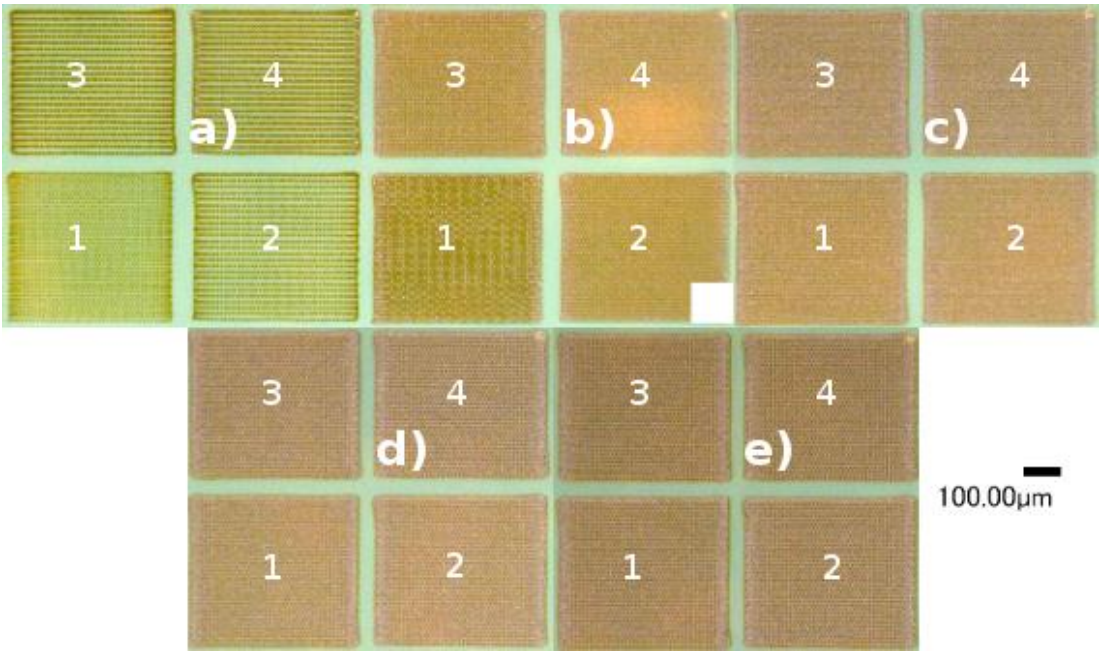

Figure 4-5 Microscope image of squares irradiated with various pulse energies. Squares are segregated in five groups- a), b), c), d) and e) for simplicity. Pulse energies used were (in µJ): a) 1-0.16, 2-0.26, 3-0.31, 4-0.39 b) 1-0.47, 2-0.55, 3-0.63, 4- 0.71, c) 1-0.79, 2-0.86. 3-0.94, 4-1.02, d) 1-1.10, 2-1.18, 3-1.26, 4-1.34, e) 1-1.41, 2-1.49, 3-1.57, 4-1.65.

It can be seen in the figure that a definite change in colour appears between groups a) and b), c), d), e). This was due to the destruction of the sample when the interaction with the laser beam occurred. Red levels (0 to 255) of presented images were analysed in order to determine the nanoparticle destruction threshold. Red levels increased from ~177 (0.16 µJ), to ~198 (0.71µJ) after which they decreased to ~155 (1.65µJ). A local minimum of 170 was present at (a)-4 (0.39µJ) after a small decrease from 178 (a)-2 (0.26µJ), which could be interpreted as a start of nanoparticle destruction. Figure 4-6 shows the same squares irradiated as in the previous figure, but illuminated from the front of the sample. It can be seen that not only areas b), c), d), e) were showing degradation but also the spot size of the laser on the sample increased (an effect described earlier). Degradation can be defined here as an area where the laser spot created a darker brown surface on the nanoparticle, followed by brighter grey in the centre- this correlates with red levels analysis from the previous figure.

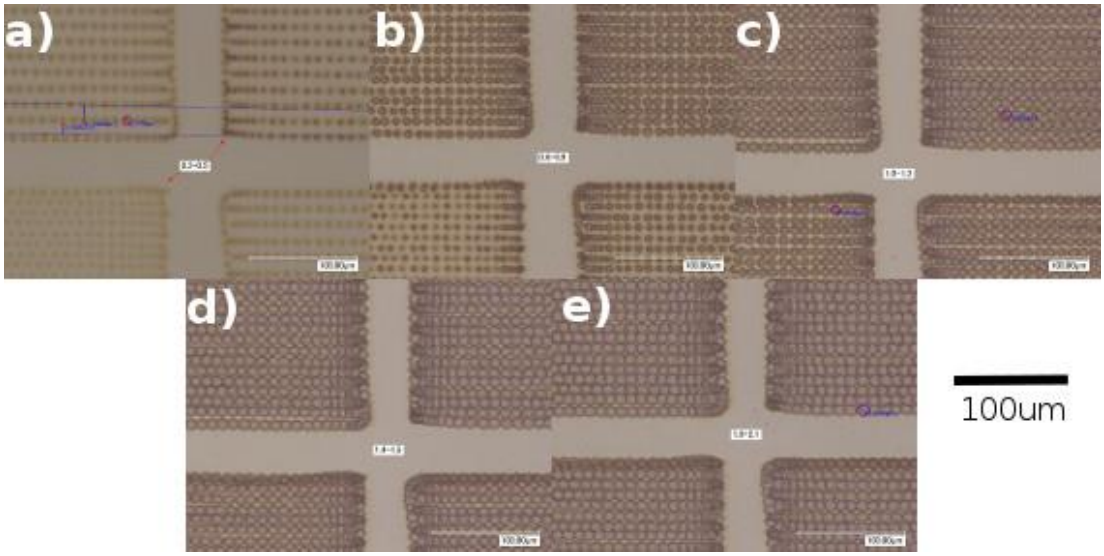

Figure 4-6 Zoomed in microscope images of areas shown on Figure 4-5. Front illumination.

It is shown in Figure 4-6 a) that the degradation of the sample by laser irradiation occurs in areas 3a and 4a. Magnified image showed that only 1a) and 2a) areas are degradation-free, which were irradiated with 0.16 µJ and 0.24 µJ. It was therefore assumed that for single spot irradiations laser energies between 0.02 µJ and 0.24 µJ could be used for non-destructive laser modification.

It is important to state that the modification of silver nanoparticles can occur in either a single pulse irradiation regime (as shown in Figure 4-4 - Figure 4-6) or in a multipulse regime. Femtosecond irradiations had shown that by increasing laser irradiation intensity in a single pulse per spot regime a splitting of SPR band was observable and the nanoparticles were eventually becoming oblate spheroids [123], [131], [138], [162]. The multipulse irradiation however, whilst allowing for lower laser powers, provided a method of shape change into prolate spheroids with much higher degree of SPR splitting [163]. For the purpose of this thesis a multipulse regime will be used in order to achieve effective reshaping into prolate spheroids with picosecond pulses. Having already established the range of pulse energies that can be used for single spot irradiation, another set of areas were irradiated with different number of pulses per spot (1, 10, 100 and 1000) and with two different pulse energies (0.24 µJ as this value shown to be the destruction threshold, and 0.05 µJ as this value was known to be destruction free and close to the modification threshold). Figure 4-7 shows the resulting irradiations. It can be observed that area a) experienced degradation for higher number of pulses per spot whereas area b) did not.

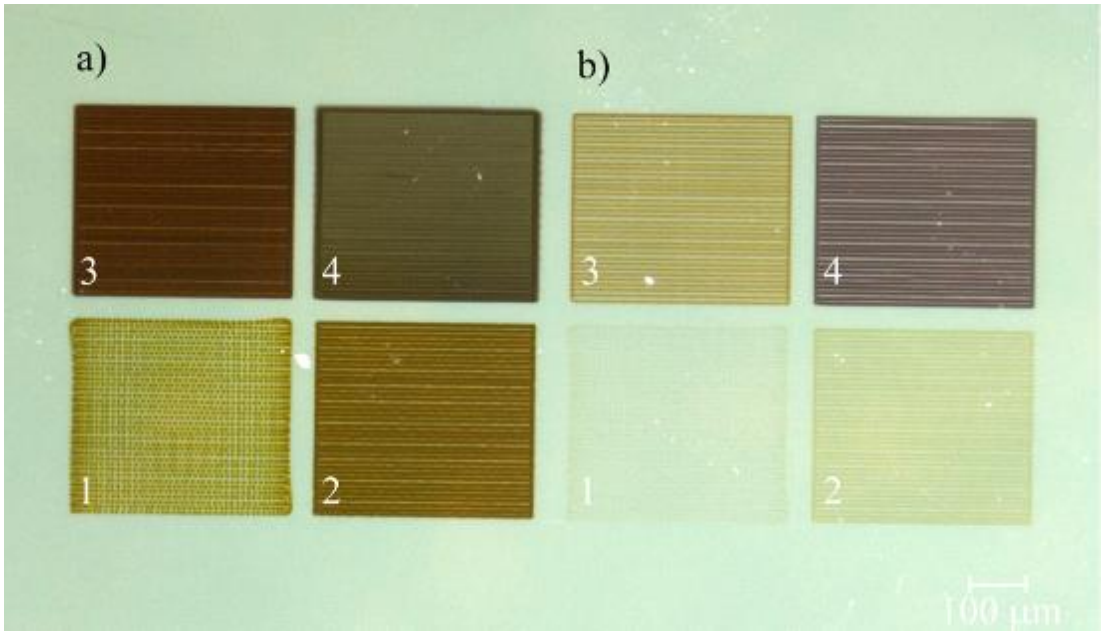

Figure 4-7 Microscope image showing two sets of irradiated areas a)- irradiated with 0.24 µJ and b)- irradiated with 0.05 µJ. Number of pulses per spot change from 1 to 4 as 1, 10, 100, 1000.

The colour change from yellow through dark brown is the effect of separation of the SPR (this effect will be described later in this chapter). Parametrization of this effect through image colour processing would be recommended in the future. Here however a simple descriptive observation will suffice followed by spectral analysis in the next parts of this chapter (simple red levels will not describe the effect properly).

For further investigation, magnified images were produced - Figure 4-8. It was shown that no degradation was present for lower pulse energies for this range of number of pulses per spot (degradation defined as previously). Higher pulse energies however showed areas in the middle of the irradiation line where degradation of sample occurred (3a). Increase of number of pulses per spot lowered the degradation threshold and an optimum laser modification fluence parameter.

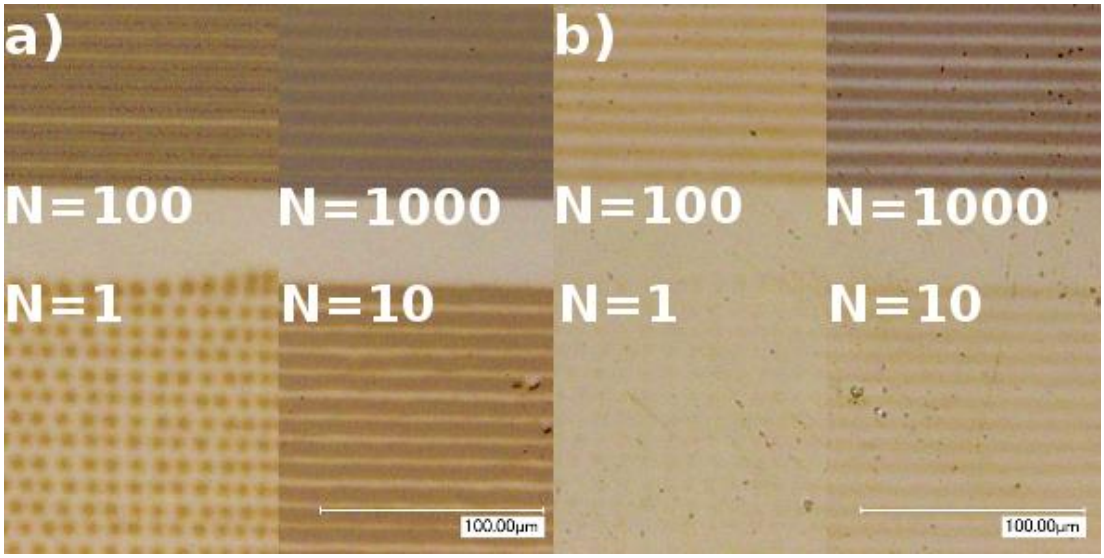

Figure 4-8 Magnified microscope images of areas irradiated in Figure 4-7. Front illumination.

An additional experiment was performed to show optimal laser reshaping parameters. Single lines were irradiated with 1000 pulses per spot and variable pulse energy.

Figure 4-9 shows irradiation of MGN with pulse energies much higher than the established single pulse modification threshold (which were between 90 nJ and 140 nJ: 80 $^{mJ}/_{cm^2}$ and 124 $^{mJ}/_{cm^2}$ respectively).

At around 106 $^{mJ}/_{cm^2}$ the line centre began to show a silver colour area which from now on will be referred to as 'silvering' and be described in more detail later in this chapter. For reshaping purposes it is an unwanted effect therefore the laser pulse energy was established for further irradiations at 0.1 µJ (88 $^{mJ}/_{cm^2}$) giving no silvering and effective nanoparticles shape modification at the same time.

Figure 4-9 shows also the thickness of each line that is irradiated on the sample. Multipulse irradiation moves the modification threshold of the MGN close to the focussed Gaussian waist, therefore the measured line thickenss was considered as the beam spot size at the sample. The beam spot on the sample was measured to be ~12 µm in diameter.

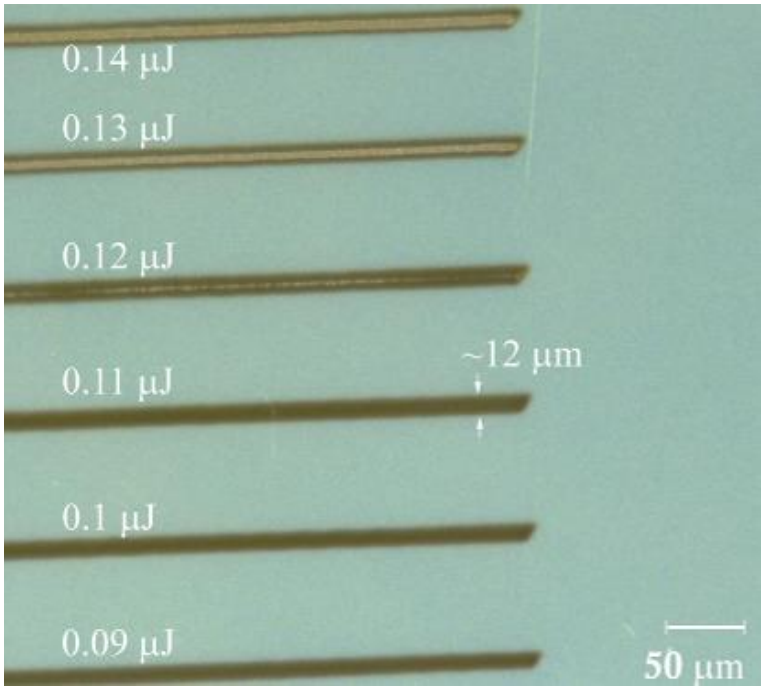

Figure 4-9 Lines irradiated from left to write with 1000 pulses per spot and with increasing laser pulse energy

4.4 Reshaping technique

Additional reshaping parameters needed to be taken into account when a homogeneous area on a glass substrate had to be irradiated. For further characterisation of irradiated areas, squares of 3 x 3 mm were produced. The laser scanning method had to be established. Figure 4-10 presents different ways that an area could have been irradiated along with benefits and drawbacks of each method (resulting from the galvo scanner itself). Each area was irradiated with a laser writing speed equivalent to the one needed for 1 pulse per spot irradiation. It was observed that for such parameters certain defects existed i.e. rounding edges in method 3 or uneven edges in method 1 and 4. Method 2 was therefore used for the rest of the irradiations as proven to give the best result. In that method (as seen in Figure 4-10) each laser line was irradiated in the same direction and with the same starting and ending positions. The distance between lines was chosen so that no overlapping existed. This distance (the hatch distance) was chosen appropriately to the diameter of the laser spot on the glass.

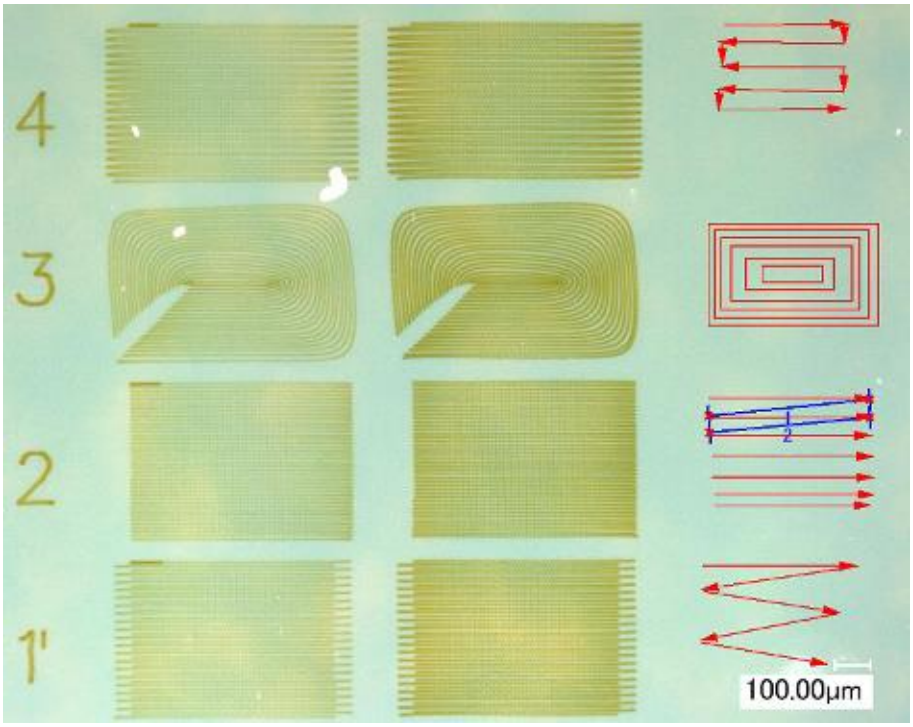

Figure 4-10 Direct laser writing methods for achieving homogeneous areas of reshaped nanoparticles (1 – 4)

The chosen method of writing was also important in terms of the intrinsic directionality of the laser beam. It had to be established that the "quill" effect was not present for irradiations of MGNs as it occurred in femtosecond irradiation of glass not containing metallic nanoparticles [164] (establishing the directionality of irradiations was of paramount importance for irradiations with laser polarisation directions other than linear- chapter 6).

First, a single line was irradiated with linear polarisation. Left-to-right direction was chosen and a vertical polarisation direction of the laser beam. It was then characterised with a simplified setup shown in Figure 4-11. The observation was performed by illuminating the sample with a daylight and placing a linear polariser between the sample and the observer. Depending on the polarisation direction of the polariser, two distinct colour changes were observed- blue (a) and red (b). They corresponded to the polariser direction parallel (a) and perpendicular (b) to the laser polarisation direction during irradiation. This effect could be described as dichroic and is an intrinsic characteristic of short pulsed irradiation of these types of MGNs [131]. The observation in Figure 4-11 can be divided into three stages: I- Unpolarised light is input on the MGN, II- the MGN extincts the light spectrum selectively depending on the nanoparticle orientation, III- the selectively extinct spectrum can be observed by passing only the desired polarisation to the observer.

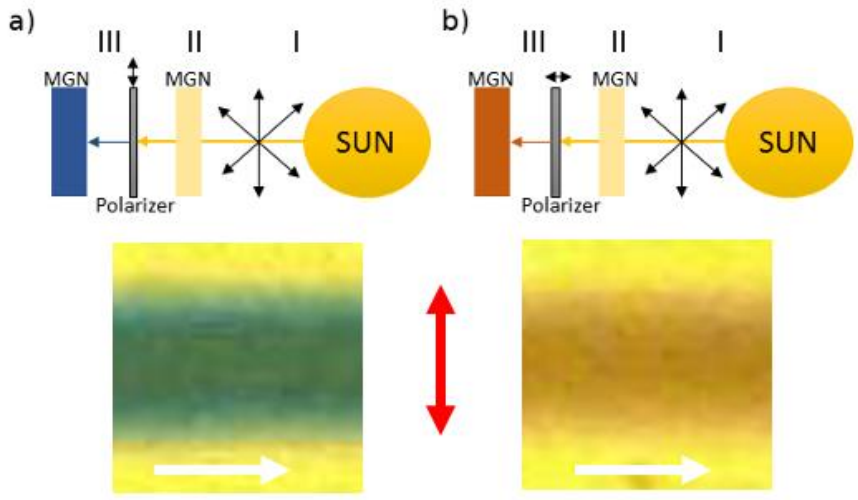

Figure 4-11 Simplified observation setup for a reshaped MGN with a vertical (a) and horizontal (b) polariser direction. Resulting MGN images below: (a) blue, (b) red. Red arrow indicates the laser irradiation polarisation direction, white arrow the left-to-right line irradiation.

Secondly, single lines were irradiated with four different laser polarisation directions: horizontal, vertical, +45°, -45°; and with two different writing directions: left-to-right and right-to-left. A schematic representation of this technique can be seen in Figure 4-12. This resulted in eight single lines that were characterised using the optical microscope. A crossed-polariser setup was incorporated to the optical microscope in order to see all of the polarisation components of the irradiated areas. Also, the 'quill' effect would have been observed if present, in the orthogonally set crossed polarisations due to birefringence effect in irradiated lines.

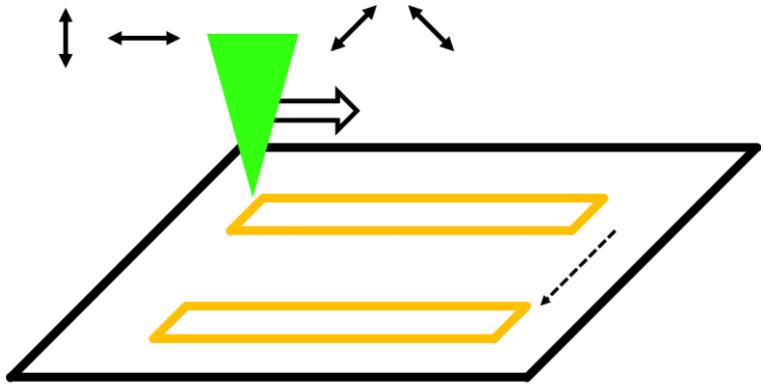

Figure 4-12 Technique used for single line irradiation. Black solid arrows indicate the polarisation state of the laser beam. Upper line was first irradiated from left-to-right then the laser beam moved below and irradiated the line from right-to-left.

Figure 4-13-L and –R show optical microscope images taken for lines irradiated with the aforementioned technique. These images are illuminated with linearly polarized light from the back of the sample- Figure 4-13-L with horizontally polarised light and Figure 4-13-R with vertically polarised light. White arrows represent the direction of irradiation (left-to-right or right-to-left). Green arrows indicate the polarisation state of the laser beam during irradiation. Figures are divided into four rows (a to d), (e to h), (i to l), and (m to p); and four columns (a to m), (b to n), (c to o), and (d to p). Each row shows images of lines with a polariser placed between the sample and the observer- $+45^{o}$ polarisation direction for (a to d), -45^{o} for (e to h), no polariser (i to l), and 0^{o} for (m to p) (90^{o} for (m to p) for Figure 4-13 R respectively). These are marked as red arrows.

It is also important to notice (especially in the third row which has no polariser between the sample and the viewer) how colours of irradiated areas change (modified area colour will be shown later as a one of the main indicators on the shape change and ellipsoids orientation). In this illumination, Figure 4-13-L (i) shows a red line colour that changed after irradiations from ‘spherical’ yellow.

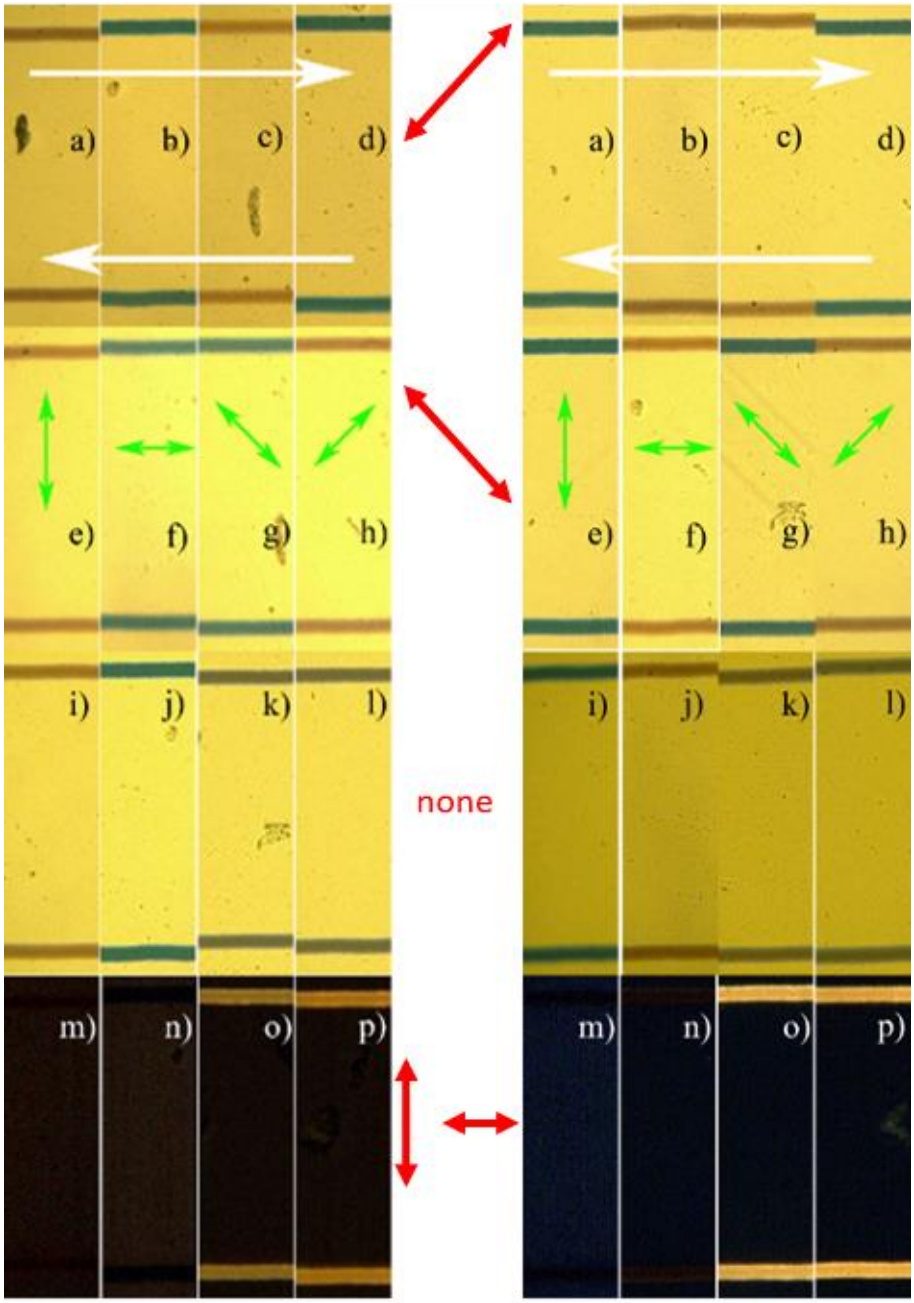

Figure 4-13 Left (L): Lines irradiated with variable linear polarisation and from left-to-right and right-to-left. Polarised illumination from the bottom- horizontal.

Right (R): Lines irradiated with variable linear polarisation and from left-to-right and right-to-left. Polarised illumination from the bottom- vertical

Figure 4-13-L (j) shows a blue line and Figure 4-13-L (k) and (l) show a mixture of these two colours. An explanation of this effect can be seen in Figure 4-14 -16.

Figure 4-14 describes the mentioned red colour effect, showing an s-polarised spectrum measured for irradiated MGN (where the polarisation of illumination light is perpendicular to the long axis of the nanoparticle).

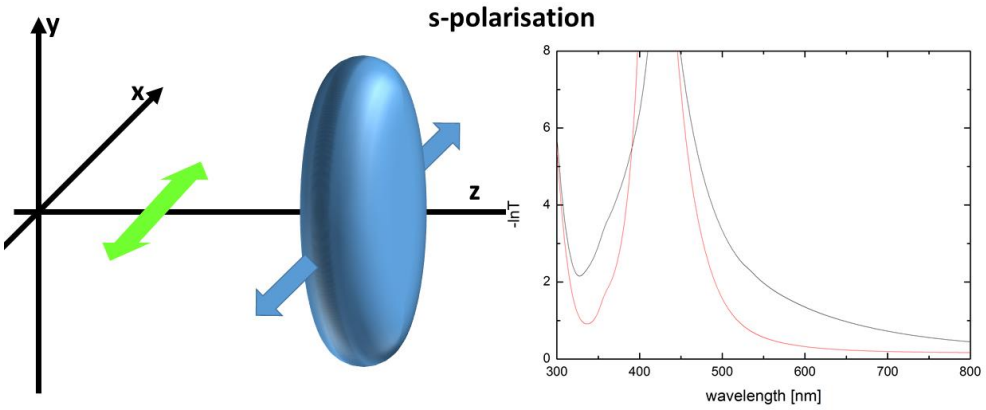

Figure 4-14 P-polarised extinction spectrum of Ag nanoparticle embedded in soda-lime glass. Incoming light polarisation travels in the z direction and is polarised along y direction. Spectrum in red – spherical nanoparticle, in black: s-polarised ellipsoid

Figure 4-15 shows the blue colour effect – p-polarised extinction spectrum of irradiated MGN (where the polarisation of illumination light is parallel to the long axis of the nanoparticle).

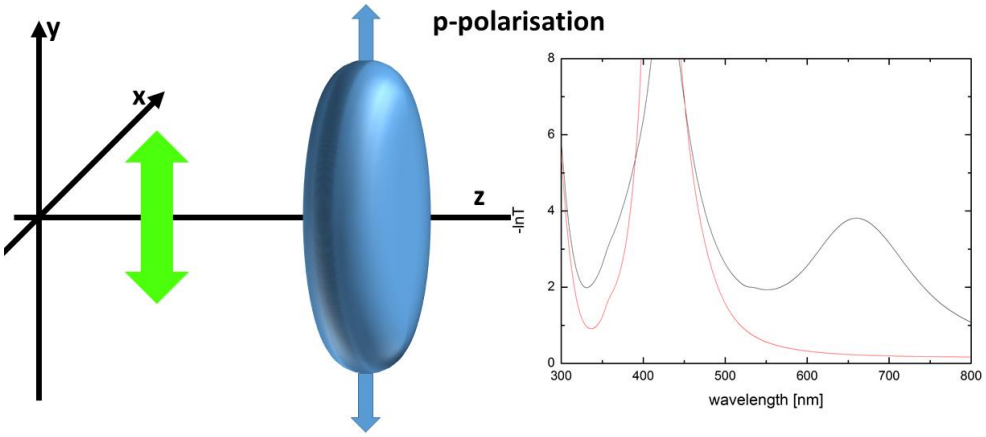

Figure 4-15 S-polarised extinction spectrum of Ag nanoparticle embedded in soda-lime glass. Incoming light polarisation travels in the z direction and is polarised along x direction. Spectrum in red – spherical nanoparticle, in black: p-polarised ellipsoid

As mentioned before, the mixture of colours is achieved for nanoparticles long axis being set +/- 45^{o} to the illumination polarisation direction. This effect is shown in Figure 4-16. According to the findings, both p- and s- polarisation modes of plasmons are being excited by light in presented configuration (as being the resultants of the polarisation direction vector).

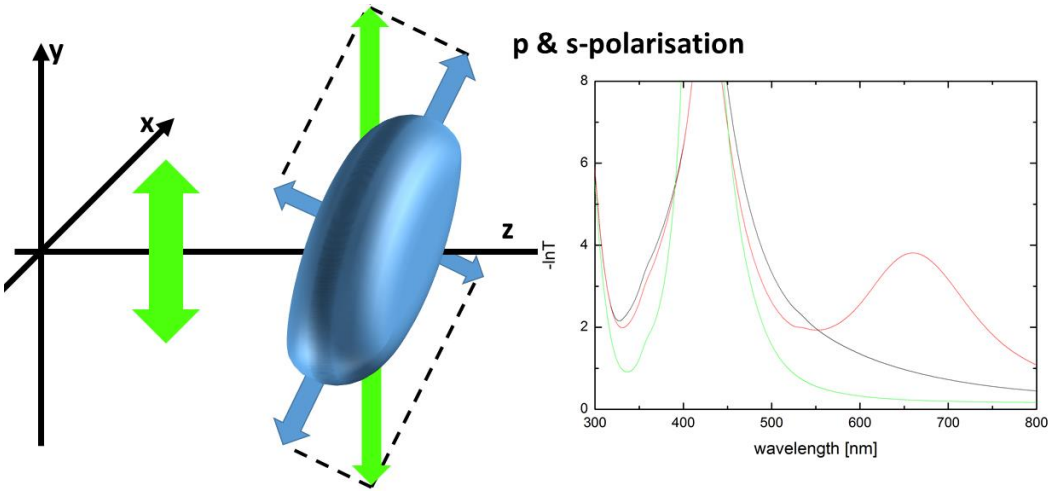

Figure 4-16 P and S-polarised extinction spectrum of Ag nanoparticle embedded in soda-lime glass. Incoming light polarisation travels in the z direction and is polarised along y direction. Spectrum in green – spherical nanoparticle, in black: s-polarised ellipsoid, in red: p-polarised ellipsoid

This effect can be proved by adding additional polariser to the microscope system- between the sample and the viewer. In this case, if the illuminating polarisation would be horizontal and the nanoparticle would be positioned with its long axis +45^o to the right, then according to what was previously stated, a mixture of s- and p- polarisation would be visible- excitation of plasmon modes along the +45^o and -45^o. When the additional polariser was added between the sample and the viewer, each of these polarisations could be cut-off. This is exactly shown in Figure 4-13-L (d). The colour of that line has changed from mixed as in Figure 4-13-L (l) to blue. That shows that the s-polarisation has been cut-off leaving only p-polarisation visible. Similarly, Figure 4-13-L (c) is red because of the nanoparticles positioned orthogonally (therefore showing only s-polarisation). Figure 4-13-L (g) and (h) show opposite spectra as the polariser is set orthogonally to the previous position. Different effect is of course present for the situation of nanoparticles illuminated with light polarised along their long or short axis. Figure 4-13-L (i) and (j) show s- and p- polarisations (respectively). By adding additional polariser with its direction of polarisation of +/- 45^o, the occurring effect is the intensity change in the spectrum (attenuation). In this sense, it is clear that for this situation either p- or s-polarisation can be present and in the previous situation both of them. Figure 4-13-R shows the same lines but illuminated with vertical (instead of horizontal) polarisation therefore all of the mentioned effects are in opposition but showing exactly the same principles.

The last row from both Figure 4-13-L and Figure 4-13-R show the crossed-polarisation setup. For that configuration (m) and (n) show nearly completely attenuated spectra of

irradiated lines (either s- or p-polarisations). On the other hand, (o) and (p) shows very bright lines. That is caused by the fact that even though the light polarisation and the polariser directions are set orthogonally, the p- and s- polarisations of the nanoparticle are rotated in this case by +/- 45^{o} therefore the light is being passed to the observer.

In order to visualise the macro effect of the irradiation directionality, entire squares of 3x3 mm were produced with the hatching method shown Figure 4-10. Only the direction of irradiation and laser polarisations were varied (similarly to the experiment involving irradiation of single lines). Figure 4-17 shows the exact technique used for irradiations.

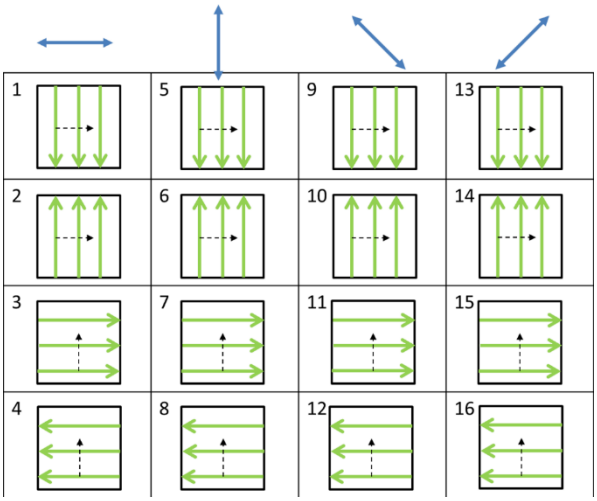

Figure 4-17 3x3 mm areas irradiated on the MGN. Directionality of laser writing was changed (green arrow): up-to-down in the first row (1, 5, 9, 13), down-to-up in the second (2, 6, 10, 14), left-to-right (3, 7, 11, 15) and right-to-left (4, 8, 12, 16). Hatching direction (black arrow) was either left-to-right (row 1 and 2) or down-to-up (row 3 and 4). Laser beam polarisation directions are indicated with blue arrows.

Pulse energy was chosen to be 0.1 µJ and 1000 pulses per spot were fired at 200 kHz repetition rate (highest repetition rate was set in order to achieve 1000 pulses per spot with the appropriate scan speed that was the main limitation). The change of spectrum of each square was to be measured as a function of different irradiation technique. Microscope images were made in crossed polarisation setup (as it was made for single lines). Figure 4-18 shows results for two out of 16 squares, 1st and 9th where the angle of crossed polarisers direction changed from horizontal/vertical to -45^{o}/+45^{o}.

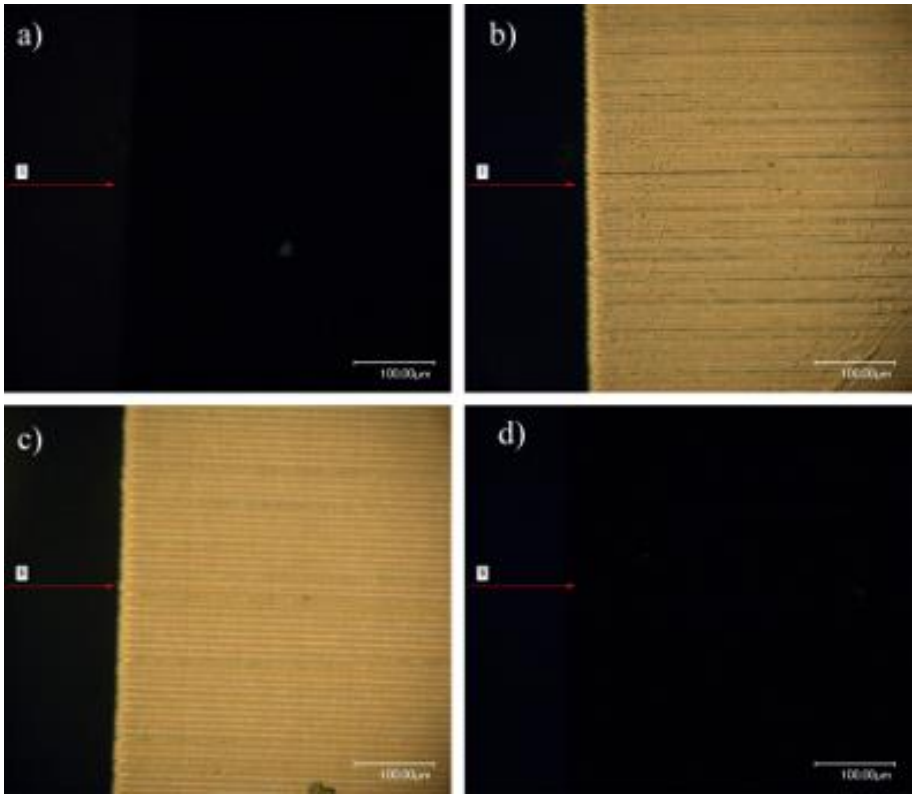

Figure 4-18 Microscope images of square 1 and 9 under a crossed polarizers setup. Images a) and b) show the 1st square (irradiated with horizontal polarisation) and c) and d) the 9th square (irradiated with -45^{o} polarisation). a), c) show polarizers in a horizontal/vertical configuration and b), d) in -45^{o}/+45^{o}.

Optical effects that can be seen in the figure are similar to what was shown previously for single lines- crossed polarisers aligned with the short or long axis of nanoparticles show no image, but polarisers rotated +/- 45^{o} show bright image, due to the fact that the light passing through the first polariser excites two SPR modes of the nanoparticle while the second polariser only attenuates them slightly showing bright areas.

Other squares behaved in the same manner as the previously presented lines. It confirmed that the irradiation of macro structures to be the same as the one established for single line irradiations.

Spectra were also produced with the use of a spectrophotometer. A linear polariser was attached in order to control the input polarisation direction of light on the sample, so that p- or s-polarisation could have been chosen. Figure 4-19 shows s- polarised spectra of squares irradiated as in Figure 4-17.

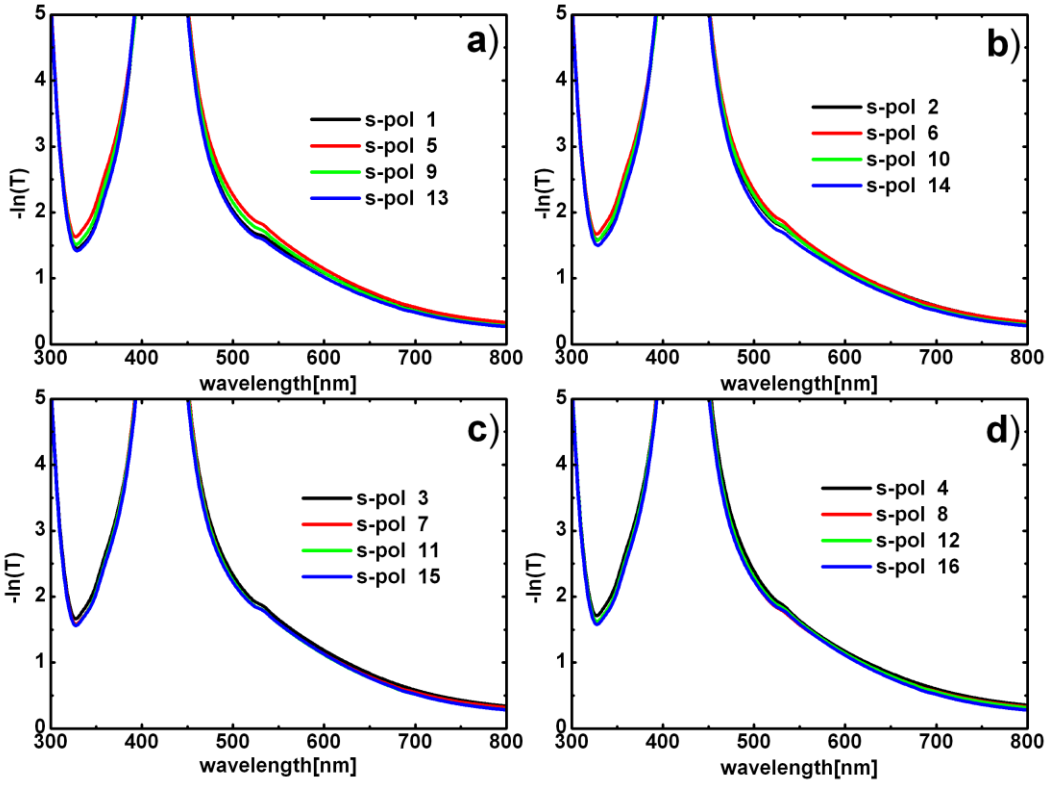

Figure 4-19 S-polarisation for a) up-to-down laser writing, b) down-to-up, c) left-to-right, and d) right-to-left. Spectra 1,2,3,4 show horizontal laser polarisation, 5,6,7,8 vertical, 9,10,11,12 -45^{o} and 13,14,15,16 +45^{o}.

No noticeable change between each sample is evident. A strong SPR near 430 nm can be seen, which is the remnant of the SPR produced from spherical nanoparticles that were left unmodified by the laser beam. The reason for it could be the laser beam being attenuated in the volume of the glass and also by the first sub-layer of nanoparticles, leaving some of nanoclusters unmodified due to the lack of laser power. The nonresonant laser wavelength was used (532 nm) which may have caused reshaping of not all of the nanoparticles in the glass volume.

Figure 4-20 shows p-polarised spectra of the irradiated nanoparticles with the writing method explained in Figure 4-17. A clear ‘red-shifted’ peak is visible at about 630 nm, which was created by the long axis mode of reshaped nanoparticles being excited by the incoming light.

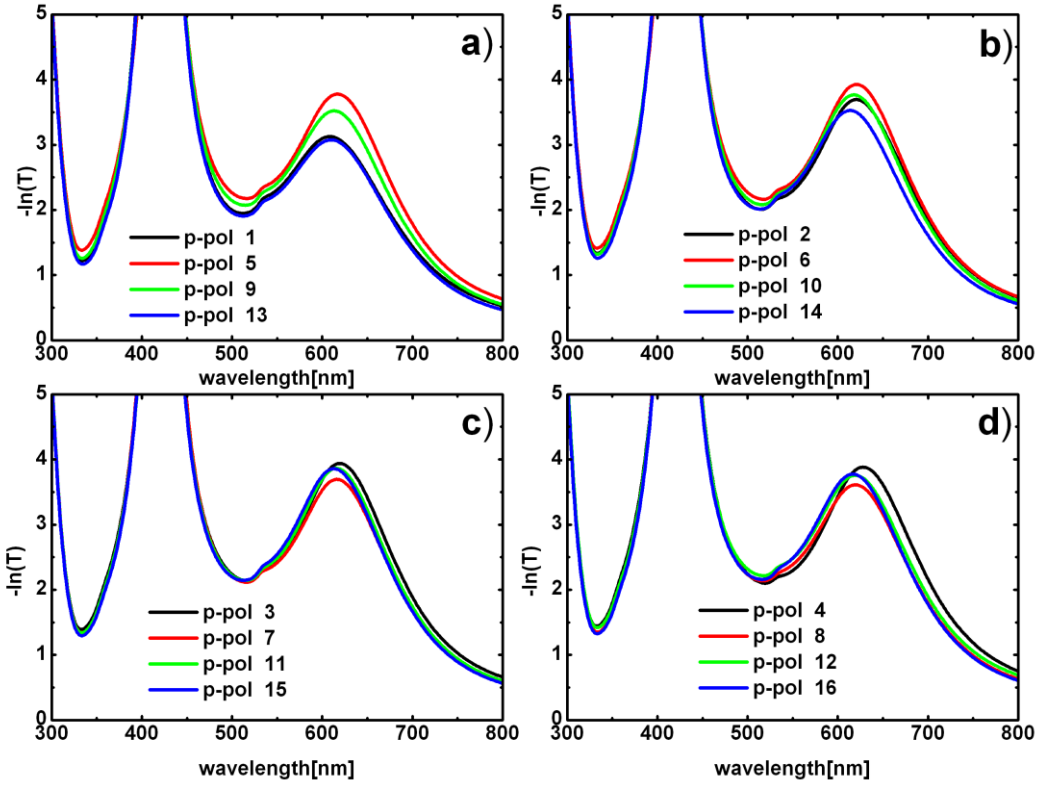

Figure 4-20 P-polarisation for a) up-to-down laser writing, b) down-to-up, c) left-to-right, and d) right-to-left. Spectra 1,2,3,4 show horizontal laser polarisation, 5,6,7,8 vertical, 9,10,11,12 -45^{o} and 13,14,15,16 +45^{o}.

A term 'separation gap distance' needs to be defined as the distance between the red peak of the p-polarised SPR and the blue peak of the s-polarised SPR band. The separation gap distance is of paramount importance when estimating the nanoparticle aspect ratio. It was shown before that instead of a clear blue-shifted SPR, a remnant of spherical band was present and was dominant over the blue-shifted band. Separation gap distance, therefore was the distance between the red shifted peak and the remnant of the SPR (unless a blue peak is present for certain parameters of laser irradiation). The separation gap distance for these irradiations is ~ 200 nm. It can be also seen on Figure 4-20 a) and b) that the squares 5 and 6 show the most intense red shifted peak, while squares 1 and 2 show much lower intensities. It could be due to the nanoparticle size distribution uncertainty (given in the previous chapter), and local defects in the supplied sample. The directionality was shown in the previous experiments to play a non-existing role in the reshaping process.

Additionally, four squares were irradiated to further determine the directionality of the process. Squares 2, 3 and 6, 7 from Figure 4-17 were compared with squares irradiated with same writing direction but with a different irradiation direction (up-to-down/down-to-up). Spectra were taken and are shown in Figure 4-21. No spectral

change with regards to this directionality was observed and therefore directionality has no influence on the reshaping process.

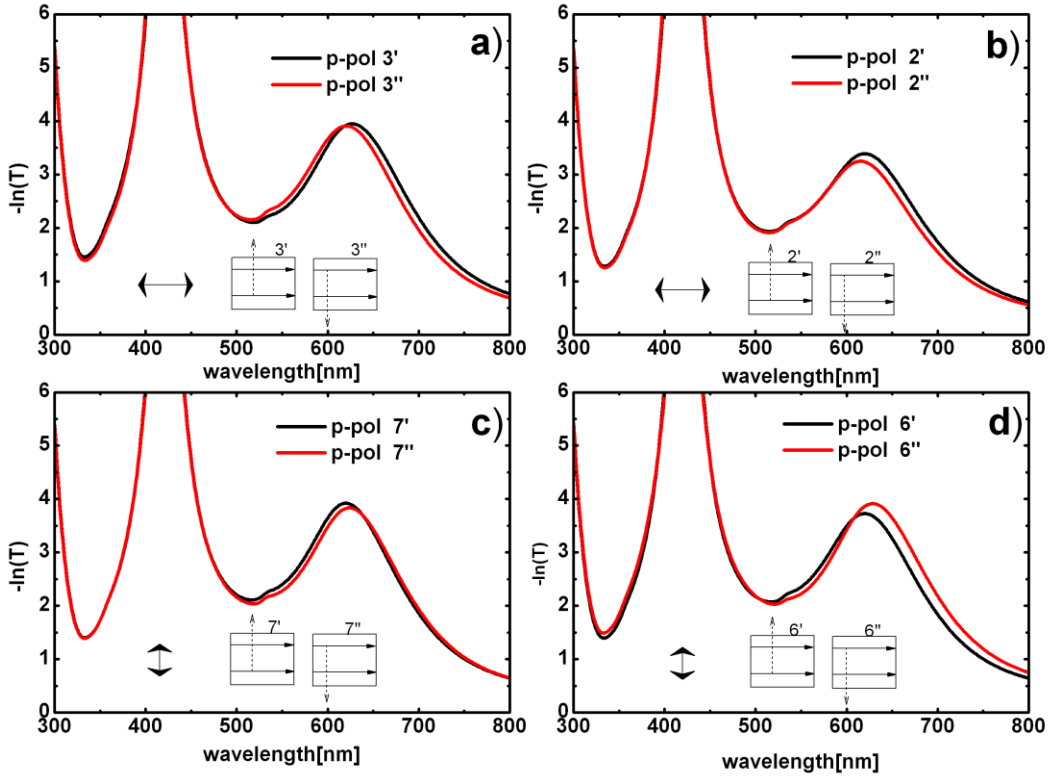

Figure 4-21 P-polarised spectra of squares irradiated with different hatching directions (insets of figures show the hatching method and direction). Black arrows indicate the polarisation direction of the laser beam during irradiation with respect to the geometry presented in the inset.

Effect of annealing after each irradiation was found to be presented. The sample has been put into the oven for and annealed at 200^{o} C for 1 hour, to remove colour centres and other defects in glass that could influence the quality of the optical measurement. The after irradiation heat treatment and its implications on the optical properties of MGNs was well documented elsewhere [138]. The temperatures used for the post-irradiation treatment used here are much smaller than the temperature required to dissolve nanoparticles. The only aim was to remove colour centres from the vicinity of nanoparticle.

Small changes were seen in optical spectra after the treatment as seen in Figure 4-22. It was observed in a)- s-polarisation, that no changes occurred which could be due to the fact that the remnant SPR was dominant. Figure 4-22 b) on the other hand shows p-polarised spectrum for which the red shifted band could be seen to drop in extinction intensity after the oven treatment, due to the destruction of aforementioned defects.

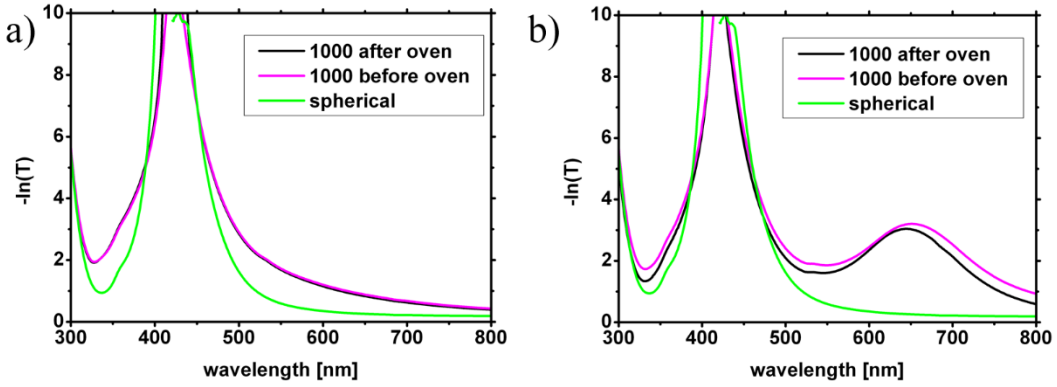

Figure 4-22 Optical spectra of irradiated MGNs before and after the post-irradiation annealing in 200° C. a) is the s-polarised spectrum and b) the p-polarised spectrum. Green line shows the unmodified spherical nanoparticles MGN spectrum

Colour centres formation is a mechanism that is involved in the process of reshaping of nanoparticles, due to the stimulated multiphoton ionisation in the host glass matrix. These centres are also one of the main reasons a nanoparticle can be reshaped with an off-resonant wavelength, as they create a shorter band gap between Fermi level of the free electron in metal inclusion and the conduction band of the glass matrix (Chapter 2). Trapped electron and hole colour centres are responsible for the induced absorption in the sample. No change in spectrum occurred after annealing (with the same parameters) of spherical nanoparticles sample as seen in Figure 4-23, which is in agreement with the theory presented.

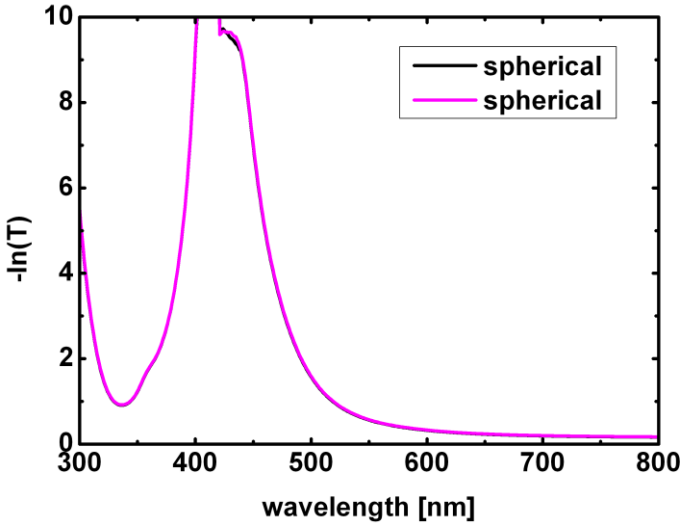

Figure 4-23 Spherical nanoparticles spectrum. Black line represents spectrum before annealing and the pink line after annealing.

Concluding, even though experiments have been shown to produce colour centres in silicate glasses for femtosecond pulse irradiation [165], no significant optical effect was shown for picosecond irradiation (which does not prove that colour centres are not

created, as they are). The reason for that was the intensity of the irradiation difference- GW/cm^2, in contrast to TW/cm^2, that was much smaller and added little to the ionisation and trapping of charges in glass.

Also, the irradiation technique was an important factor when planning the experiment. The hatching method had no additional effect on reshaping- for the non-overlapping lines. The experiment itself was a very important technique for reshaping characterisation with the laser beam polarisation different than linear. For radially and azimuthally polarised beams, experiments will be shown in the chapter 6.

It was established that in order to be in the optimal range of reshaping of the nanoparticle, laser fluence could not be higher than 212 mJ/cm^2 (0.24 μJ pulse energy) for single pulse irradiation due to the degradation of the MGN and not higher than 88 mJ/cm^2 (0.10 μJ pulse energy) for multi pulse irradiation due to the *silvering* effect. The lowest pulse energy that produced visible changes to the sample (the modification threshold) was established to be 20 mJ/cm^2 (0.02 μJ pulse energy).

For experiments shown in this chapter, a 1000 pulses per spot parameter has been used. Also, pulses at 200 kHz of laser repetition rate have been fired as the maximum limitation of what the galvo scanner could deliver at the time of experiment and the highest number of pulses per spot was desired. It was however important to establish reshaping parameters for irradiations below these values of parameters (number of pulses per spot and the laser repetition rate) in order to understand the elongation process and its limits for the picosecond laser irradiations.

4.5 Laser reshaping parameters

The ability of nanoparticles change their shape upon picosecond pulsed laser irradiation was proved in a number of experiments. Parameters such as the number of pulses per spot (change the irradiation density), laser repetition rate and laser fluence were investigated. As a result, a dichroic effect was observable and is shown in Figure 4-24 as a result of illumination with linear polarisation.

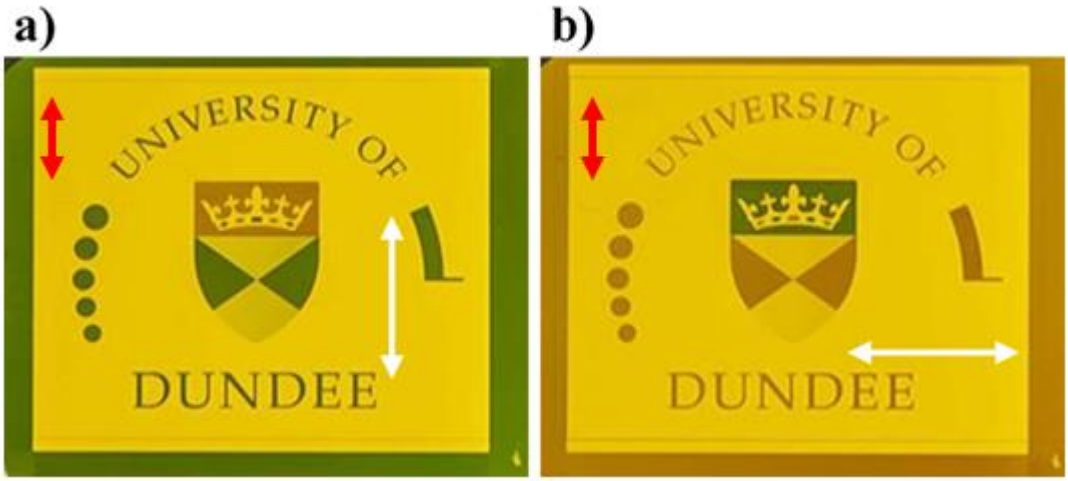

Figure 4-24 Logotype (16 mm x 20 mm) produced by ps pulsed laser assisted reshaping of a piece of MGN at 532 nm. The sample is shown for a) vertically and b) horizontally polarised illumination (indicated by the white arrows). Red arrow indicates the laser irradiation polarisation direction

The 'University of Dundee' logotype was irradiated with 1000 pulses per spot, 200 kHz laser repetition rate and laser wavelength of 532 nm. The irradiated areas had two distinct colours: red/brown and blue/green. The effect of colour change was presented before and showed the same changes in micro level (single line) as in here (macro – 16 x 20 mm). Splitting of the SPR was observed which was caused by selective extinction of polarised light penetrating the sample. The elongation direction of nanoparticles took place along the direction of the polarisation of the laser beam (red arrow). Also, these irradiated areas and the observed dichroism were homogeneous (island-free).

Figure 4-25 a) presents spectra of p- and s- polarisations of irradiated areas of nanoparticles reshaped with the same parameters as the logotype in Figure 4-24. Spherical nanoparticle MGN was irradiated in 3x3 mm squares. 1000 pulses per spot were fired and 200 kHz repetition rate was used at 532 nm. Clear separation of the SPR band can be seen. Figure 4-25 b) presents the effect of irradiation of the MGN with varying laser pulse energies (and fluences). Laser pulse energy was varied between 0.025 µJ and 0.10 µJ (22 mJ/cm^2 – 88 mJ/cm^2). The employed laser intensities were: 2.21 GW/cm^2, 2.65 GW/cm^2, 3.54 GW/cm^2, 6.19 GW/cm^2 and 8.84 GW/cm^2.

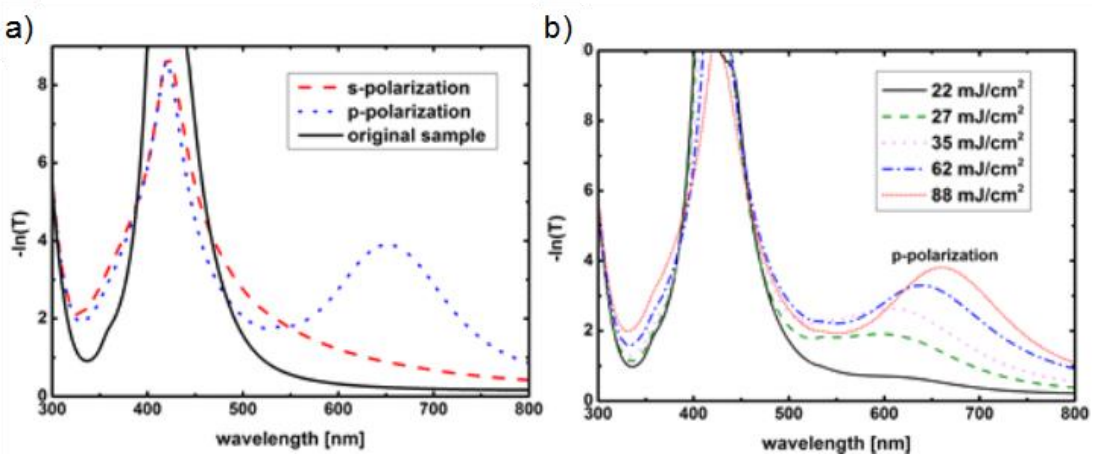

Figure 4-25 Extinction spectra as a function of wavelength. a) 1000 pulses per spot, 200 kHz repetition rate and ~80 mJ/cm^2 was used. P- and s- polarisations are shown b) 1000 pulses per spot, 200 kHz and varied laser fluence was used. P- polarisation is shown. Black solid line shows spectra of spherical MGN.

As can be seen in Figure 4-25, the SPR band (especially pronounced for the p- polarised light) experienced a shift towards the longer wavelengths and also exhibited higher extinctions as the fluence was increased. Peaks of the red shifted bands were formed at (lowest fluence to the highest): 590 nm, 596 nm, 607 nm, 639 nm, and 660 nm. Furthermore, it can be concluded that as the laser fluence increased more nanoparticles were uniformly reshaped. This exhibited itself as an increase in the peak of the extinction band.

Further experiments were performed in order to determine the evolution of the red shifted SPR band for laser repetition rates and number of pulses per spot change. It was shown earlier in this chapter that the maximum number of pulses per spot parameter was achieved with 200 kHz laser repetition rate and the highest laser scan head speed. This correlated to 1000 pulses per spot. Squares of 3x3 mm were irradiated with 0.10 µJ laser pulse energy and either 200 kHz repetition rate with varying number of pulses per spot- 100, 200, 300, 400, 500, 600, 700, 800, 900 and 1000 (as in Figure 4-28 a), or with 1000 pulses per spot and varying laser repetition rate- 20 kHz, 30 kHz, 60 kHz, 100 kHz, 150 kHz, 200 kHz. Figure 4-26 presents spectra measured for samples irradiated with varying number of pulses per spot.

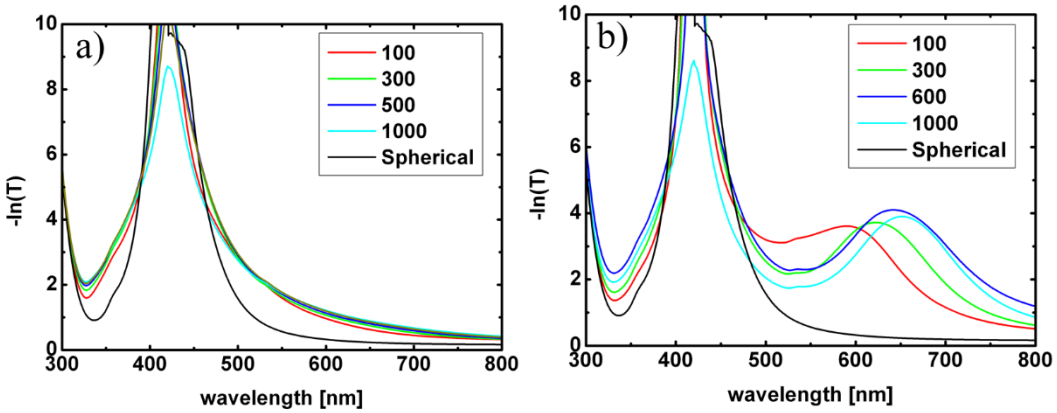

Figure 4-26 Extinction spectra as a function of wavelength for MGN irradiated with varying number of pulses per spot (0.10 μJ/cm^2 and 200 kHz repetition rate), a) is the s-polarised spectrum, b) is the p-polarised spectrum.

Only 100, 300, 600, 1000 (and spherical) pulses per spot are presented for clarity. It can be seen in Figure 4-26 a) that the s-polarised spectra did not differ significantly when number of pulses varied, but it has to be noted that the ~430 nm SPR peak showed both the blue shifted band and the spherical remnant decreased in extinction intensity for 1000 pulses per spot. Because of the limitations of the spectrophotometer, only values of extinction of up to ~10 could be measured but it was assumed that that SPR peak decreased gradually with the increasing number of pulses per spot. It means that the more pulses were shot on the sample the more spherical nanoparticles were reshaped. Figure 4-26 b) shows p-polarised spectra. It can be seen that the increase of number of pulses per spot had the effect of shifting the band to the longer wavelength. It can be observed that the red shifted extinction peak intensity increased to value of ~4, which could mean that the increase of number of pulses per spot not only increased the red shift (which correlated to the length of long axis of ellipsoidal nanoparticles), but also the overall amount of nanoparticles that were reshaped with the laser.

Figure 4-27 shows spectra measured for squares irradiated with varying laser repetition rate (while keeping 1000 pulses per spot constant). Figure shows only 60 kHz, 100 kHz, 150 kHz and 200 kHz (and spherical) for clarity. Similar effects to the previous experiment could be observed for varying laser repetition rate: decrease of the ~430 nm extinction intensity peak, shift of the p-polarised band towards the longer wavelengths and the increase of the extinction intensity of this band with the increase of the laser repetition rate.

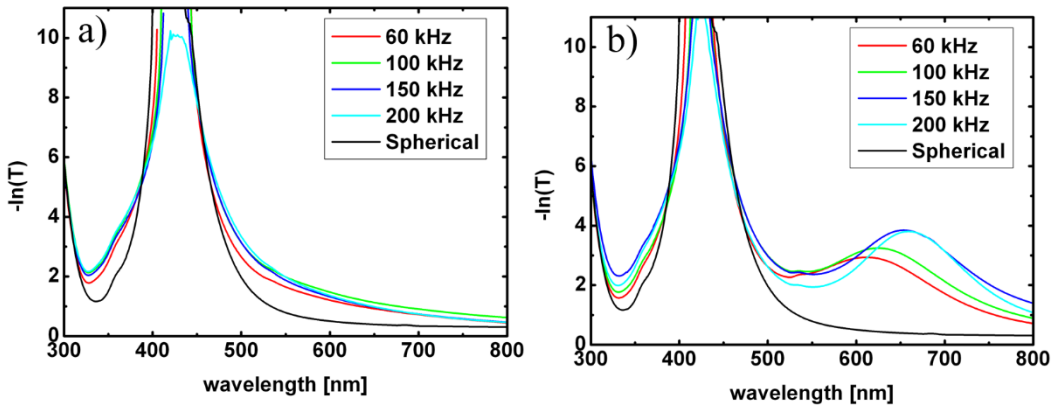

Figure 4-27 Extinction spectra as a function of wavelength for MGN irradiated with varying laser repetition rate (0.10 µJ/cm^2 and 1000 pulses per spot), a) is the s-polarised spectrum, b) is the p-polarised spectrum.

The separation distance as a rate of the nanoparticle elongation was calculated and presented in Figure 4-28. These observations are in agreement with the temperature model presented for pulsed laser modification in chapter 2 and in [130]. According to the model, each pulse during irradiation, accumulates the effect of elongation by heating up the nanoparticle (Two Temperature Model – Chapter 2) and then spreading its heat to the glass matrix by heat diffusion.

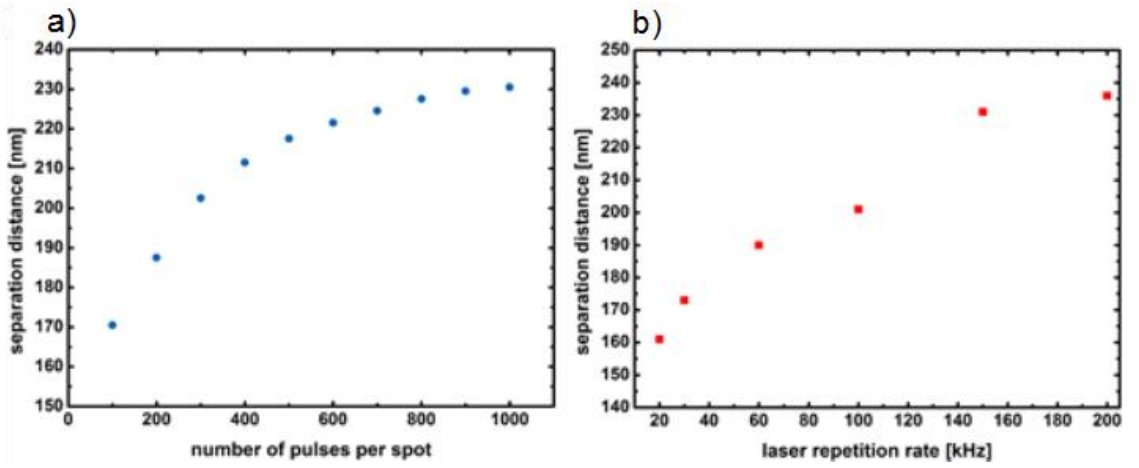

Figure 4-28 a) Surface Plasmon Resonance band separation distance as a function of number of pulses per spot. Irradiation was performed for 88 mJ/cm^2 (0.10 µJ for each laser pulse) and a 200 kHz laser repetition rate b) Surface Plasmon Resonance band separation distance as a function of laser repetition rate. Irradiation was performed with 88 mJ/cm^2 (0.10 µJ for each laser pulse) and 1000 pulses per spot.

The overall effect of reshaping increased for each pulse because the system relaxed to a slightly higher temperature than it had before. Approaching high temperature resulted in dissolution of the nanoparticles in the glass matrix due to the increase mobility of the emitted silver ions and their diffusion into the glass matrix during the irradiation.

Therefore high repetition rates or firing large number of pulses per spot could lead to undesirable effects.

Here, the maximum achieved SPR gap is about 240 nm. At this value the temperature in the close vicinity of the nanoparticles is approaching its maximum value for silver ions coupling with the electrons on the poles of the nanoparticles. Higher temperature would lead to diffusion of silver ions further away from the original silver lattice and electrons, leading to the dissolution of the nanoparticles into the glass matrix.

Figure 4-29 shows images of MGN sample irradiated with varying number of pulses per spot. Resulting dichroic effect can be clearly observed for varying irradiation parameters.

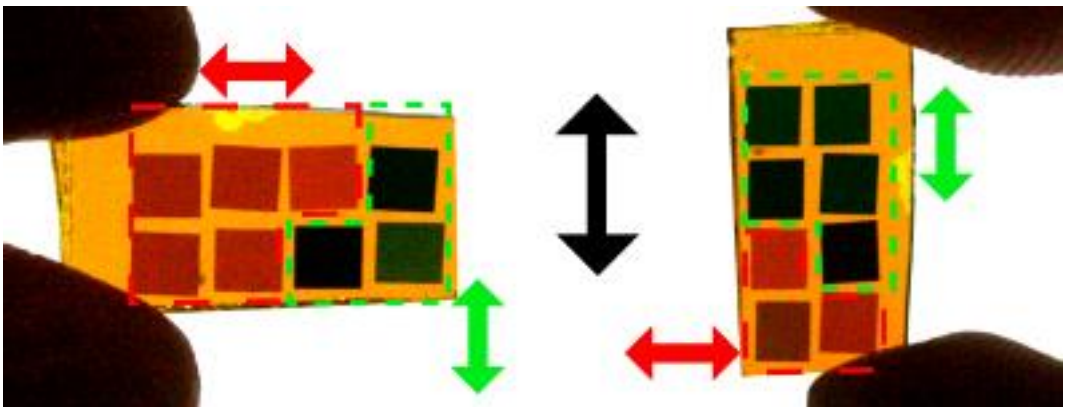

Figure 4-29 Images of 5x5 mm squares irradiated at 0.11 µJ pulse energy at 200 kHz. Number of pulses per spot in the irradiation areas on the left hand side are (from left to right): 500, 300, 100, 200 (top row) and 400, 200, 100, 100 (bottom row). The right hand side image shows the same as the one on the left but flipped 90^{o} clockwise. Black arrow represents the polarisation direction of light that is penetrating samples from the back (perpendicular to the paper). Red arrows represent the polarisation direction of the laser beam for irradiation of the areas grouped within the red dash-lines. The green arrow represents the polarisation direction of the laser beam for irradiation of the areas grouped writing the green dash-lines.

For 150 fs- laser irradiation at 400 nm the dissolution was reported to occur for the laser operating at just below 100 kHz repetition rate and the modification threshold was reported to be ~0.2 TW/cm^2 (~ 30 mJ/cm^2) [131]. These values are close to values obtained in this thesis. Picosecond laser modification threshold of ~20 mJ/cm^2 was observed. It is worth stressing the fact that the irradiation wavelength was spectrally far from the SPR peak absorption. For the picosecond pulsed laser irradiation at 532 nm most of the experiments have been performed using a laser intensity of ~9GW/cm^2 (~88 mJ/cm^2). The fact that pulses of ~10 ps duration can produce dichroism in MGNs similar to femtosecond pulses confirms the theory about the characteristic time scale of

the process of particle deformation [130], [131], [166] and that the emitted electrons during the process are penetrating and settling down in the matrix within 10-20 ps.

4.5.1 Silvering

It was shown earlier in this chapter that a *silvering* effect appeared on the irradiated areas for multipulse and high-energy irradiation. When irradiating a MGN with 200 kHz laser repetition rate, ~1000 pulses per spot and energies higher than ~0.12 µJ the *silvering* effect started to be more pronounced in the middle of each irradiated line. This paragraph will show this peculiar MGN behaviour.

Firstly, 3x3 mm squares were irradiated with 200 kHz repetition rate, 0.18 µJ pulse energy (~160 mJ/cm^2 of laser fluence, ~16 GW/cm^2 of laser intensity). Number of pulses per spot were varied between 100 and 1000 in order to observe changes to the SPR and compare it with the reshaping that was established earlier. Pulse energy was chosen far above *silvering* threshold in order to achieve full modification width of each line. Laser raster scan was utilized similarly as before.

Secondly, samples were photographed and can be seen in Figure 4-30 under the illumination from the back with a linearly polarised white light. The dichroic effect was visible between the p- and s- polarisations.

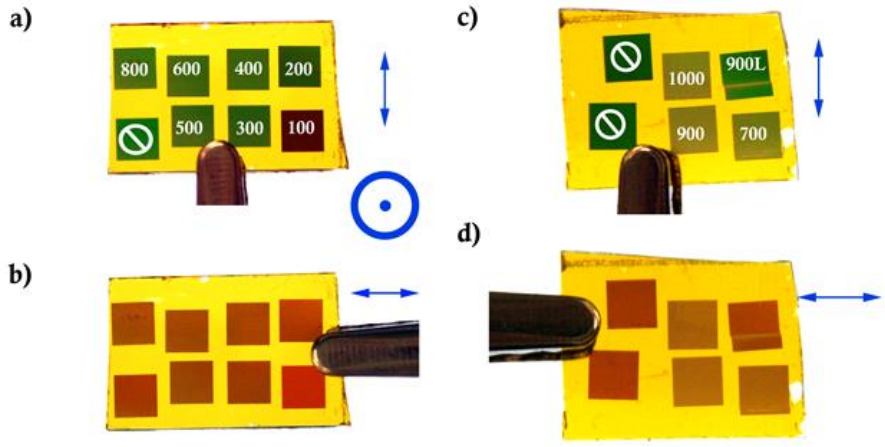

Figure 4-30 Squares irradiated with higher pulse energy and with different number of pulses per spot : 100, 200, 300, 400, 500, 600, 800 on the left hand side- a), b), 700, 900, 1000 on the right hand side- c), d). Blue arrows indicate the polarisation direction of light penetrating through the sample. Samples were irradiated with vertical laser polarisation. 900L represents a square for which the focus of the beam was swept vertically.

Figure 4-30 c) shows a '900L' square. This particular area was irradiated with laser beam slightly out of focus. Sample was then translated in the Z axis during the laser

raster scan resulting in a swipe along the beam propagation. The horizontal line in the middle of '900L' area shows the position of the sample within the laser focus. Laser fluence was effectively changed along the line cross section and the effect of that could be observed in Figure 4-31 .

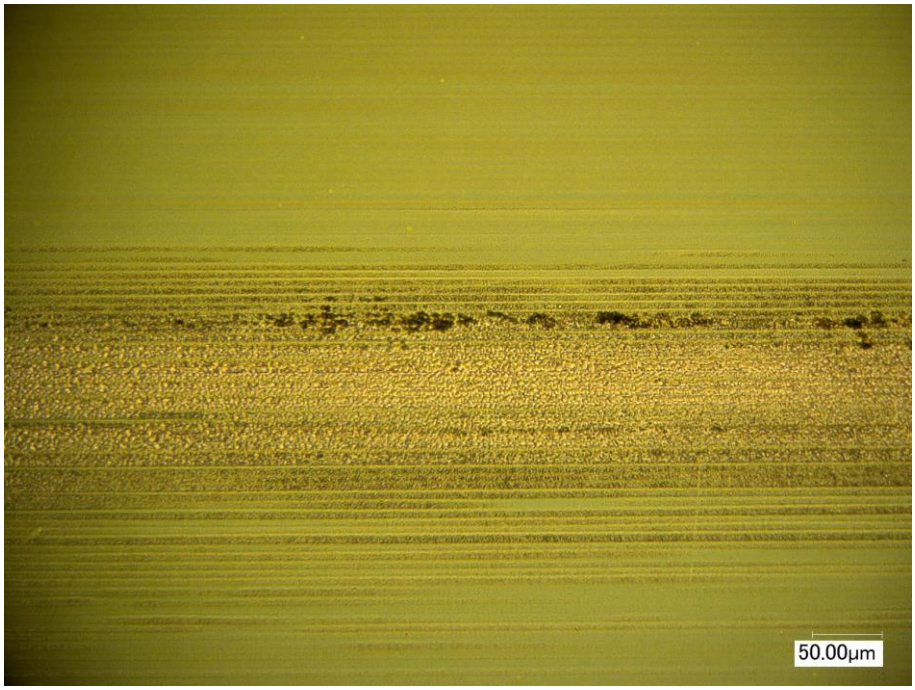

Figure 4-31 Microscope image of a sample irradiated with 900 pulses per spot and varying sample position within the laser focusing.

This experiment presented that not only the number of pulses per spot was responsible for the increase in the change of the sample morphology but also laser fluence, as most changes appeared in the middle of the irradiated area, when the fluence approached maximum.

Furthermore, Scanning Electron Microscopy images were taken. Figure 4-32 shows images for squares irradiated with 100, 300, 600 and 1000 pulses per spot. An important observation was made during the scan: contrast of images increased along with the number of pulses per spot fired which is clearly shown in the figure. Figure 4-32 a) does not show any particular features in comparison to the rest of samples. It has to be noted that the same SEM parameters were used for all of the samples, that is: 4000x magnification and 5 kV of electric field applied.

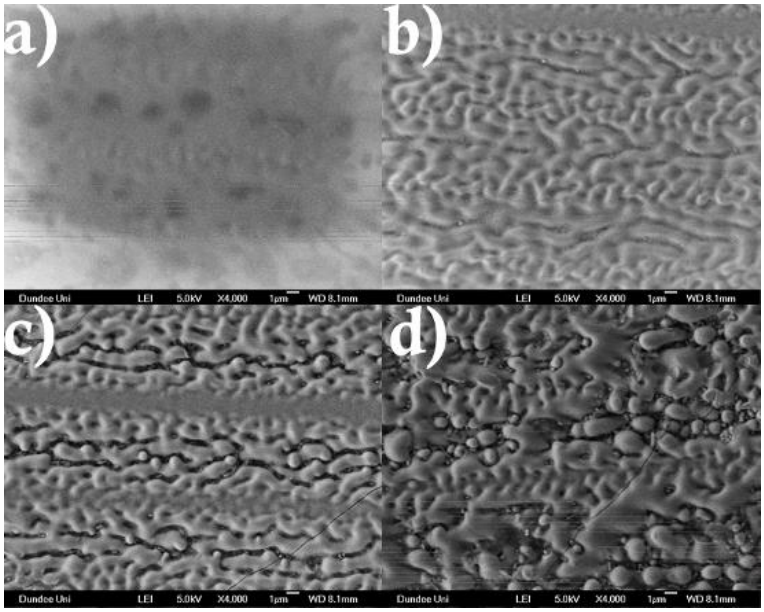

Figure 4-32 Scanning Electron Microscopy images of squares irradiated with varying number of pulses per spot: a)- 100, b)- 300, c)- 600, and d)- 1000. Magnification of 4000x was used.

The explanation of this lies in the increase of conductivity of the sample as SEM cannot show images of surfaces that are not conductive. Presented samples have not been coated with any conducting material therefore it is evident that the irradiation increased the sample conductivity at the surface. It would mean that every single laser pulse that was shot to the sample was 'moving' the nanoparticles towards the surface of the glass. The mechanism of this was explained in [167] for ns- irradiation where the multipulse irradiation caused the nanoparticles to form a solid layer on the glass surface. According to that work, laser irradiation caused melting of both glass and silver leading to coalescence and Ostwald ripening. Then, surface tensions of the melt would cause the liquid to be pulled away toward the cooler regions and eventually forming silver layer on glass surface. Higher amount of nanoparticles that are closer to the surface or already on the surface increased the resolution of SEM as the conductivity increased. Also, the morphology was visibly affected with the increase of pulses applied. It could be seen more clearly that when nanoparticles moved towards the surface, they collated and formed not only larger particles (in sizes exceeding 1 μm in diameter) but also silver layer close to percolation threshold.

Another SEM image was made with the '900L' area irradiated with varying fluence (by sample position change). Figure 4-33 shows cross sectional images of irradiated lines starting from the area on the sample with the lowest laser fluence used (a-b) and finishing with the area on the sample with the highest fluence (i-j) the middle of the irradiated line).

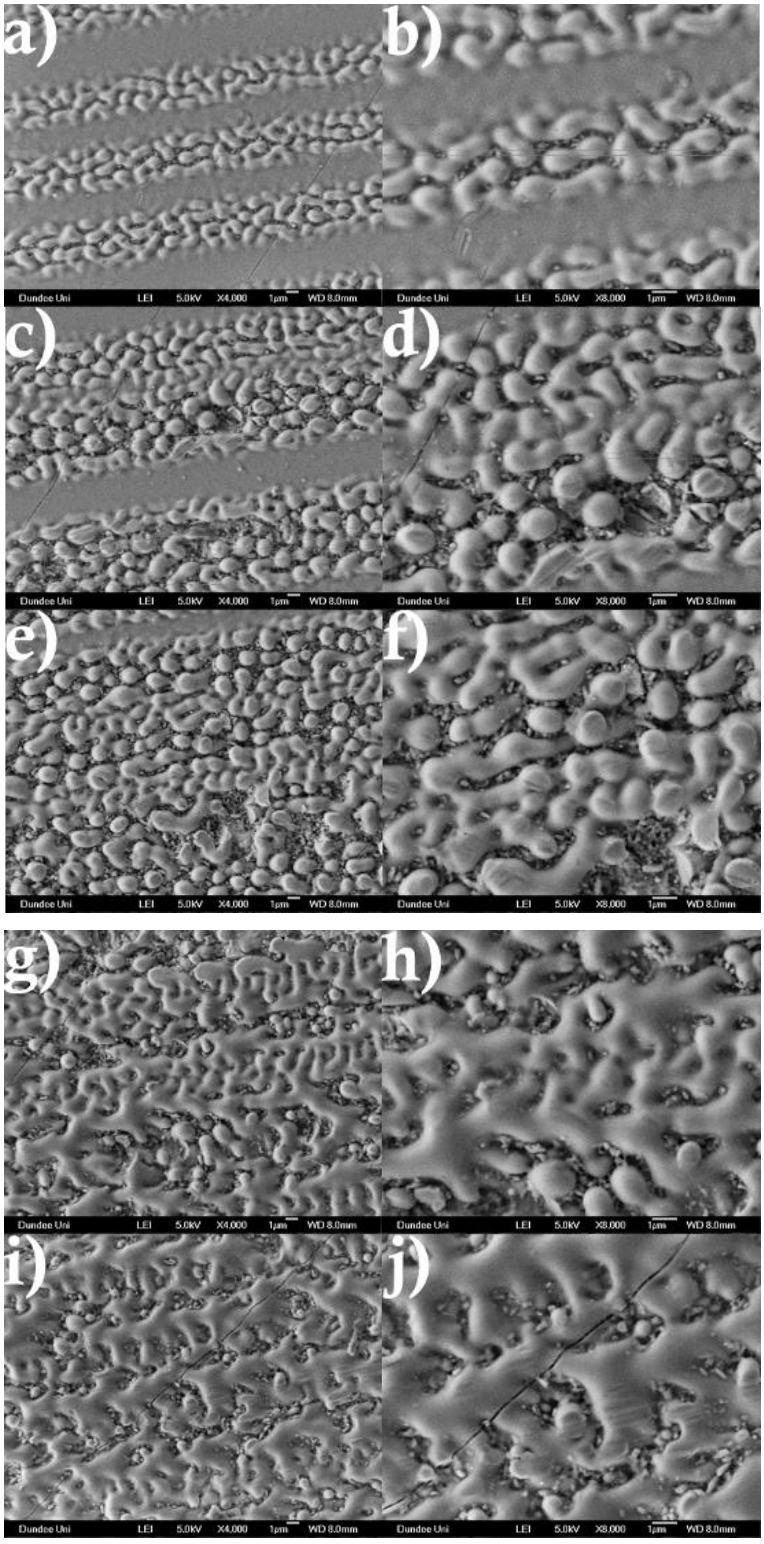

Figure 4-33 SEM images of the 900 pulses per spot line irradiated with varying laser fluence. a)-j) show a cross sectional images where a) is the irradiation with the lowest fluence and j) with the highest. Left column show 4000x magnification and the right column 8000x.

Figure 4-33 (a - d) shows micron size particle formation made of silver on the surface of the glass. Smaller nanoparticles were also visible in spaces between the micro particles. When however, laser fluence increased even further (Figure 4-33 (e - j), particles started

forming smaller lines and channels eventually leading to a thin layer of silver formation near the percolation threshold. It has to be noted that in the volume of the silver layer, nanoparticles that were still observable were divided into spherical and ellipsoidal. The elongated nanoparticles could be seen to reach lengths of even ~500 nm in some cases. More detailed work would be required to link the laser fluence increase to proximity to the percolation threshold, or to the effective melted area.

Calculation of an effective 'melted' area was performed. For that purpose, figures (b), (d), (f), (h) and (j) were processed in Matlab. Non-melted areas were firstly blanked and the remaining area was calculated and normalised to a number, which represented the whole of the image melted (whole image was blanked and an inverse calculation was performed). The increase of the melted from the smallest to the highest fluence used was: 37.6%, 55.5%, 69.2%, 81.2%, and 91.9%.

In order to estimate the reshaping ratio of produced samples, optical spectra were produced of irradiated areas. Figure 4-34 presents spectra of both p- and s-polarisations for 100, 300, 600 and 1000 pulses per spot. It can be observed that the increase in the laser pulse energy decreased the remnant SPR that was left after the spherical nanoparticles.

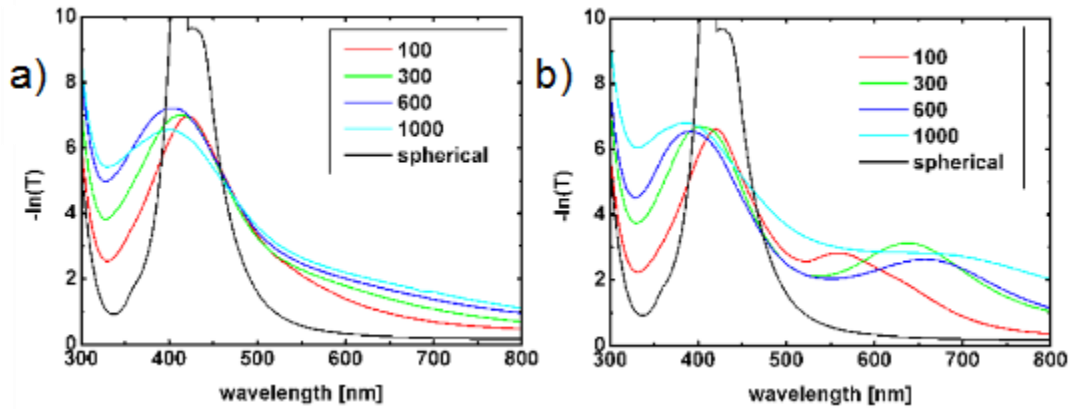

Figure 4-34 SPR of nanoparticles irradiated with 0.18 µJ of laser pulse energy. 100, 300, 600 and 1000 pulses per spot were fired. a) s-polarisation, b) p-polarisation.

That meant that (apart from the effective spot diameter increase on the sample) the higher the pulse energy the more nanoparticles were affected with the reshaping process (in comparison to lower pulse energy irradiations shown before). The increase of number of pulses per spot clearly shifted the p-polarised SPR towards the longer wavelengths and in the same time the s-polarised SPR towards the shorter wavelengths. Also, it can be seen that above 300 pulses per spot the p-polarised SPR decreased in intensity and the red shifted band broadened. For 1000 pulses per spot the p-polarised

peak degraded nearly completely- due to dissolution of nanoparticles. Also, the highest number of pulses per spot increased the overall extinction along broad wavelength range (apart of the small peak of 300 pulses per spot at ~630 nm). That could have been explained as an effect of formation of a molten layer of silver on the surface, therefore increasing the sample reflectivity.

Comparison between spectra of areas irradiated with low pulse energy (0.10 μJ) and high pulse energy (0.18 μJ) is shown in Figure 4-35, for 300 pulses per spot fired on the sample.

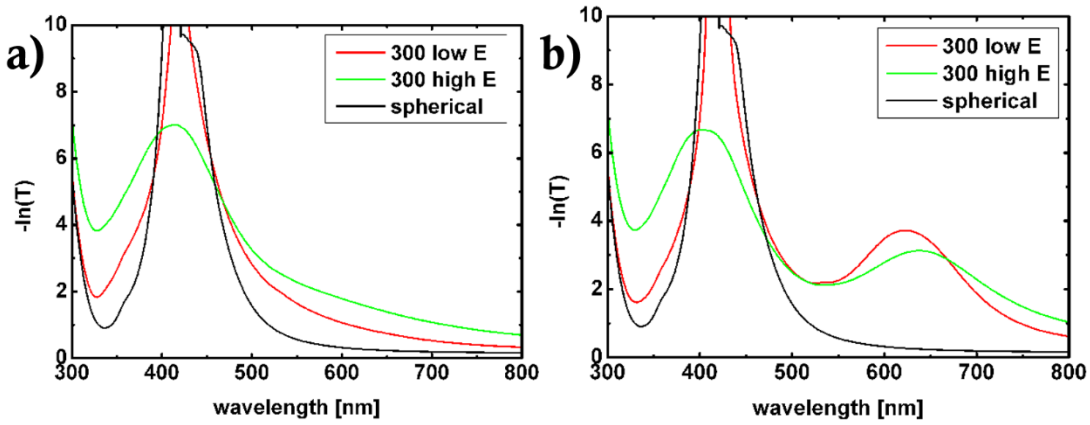

Figure 4-35 comparison of a) s-polarised and b) p-polarised spectra of nanoparticles irradiated with high pulse energy (0.18 μJ) and low pulse energy (0.10 μJ). 300 pulses per spot were fired.

600 pulses per spot irradiation can be seen in Figure 4-36, and 1000 pulses per spot irradiation can be seen in Figure 4-37. It can be observed that the change in the SPR around ~430 nm is evident- higher pulse energies decrease the SPR remnant that is left from the spherical particles.

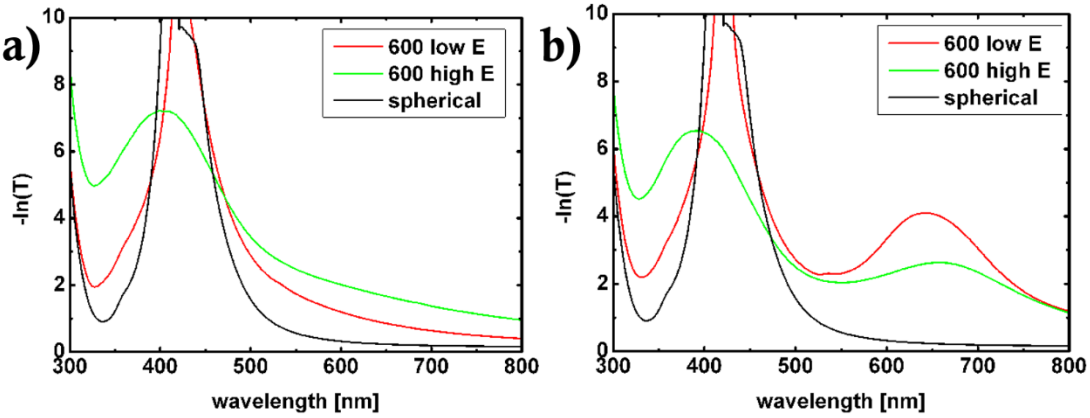

Figure 4-36 comparison of a) s-polarised and b) p-polarised spectra of nanoparticles irradiated with high pulse energy (0.18 μJ) and low pulse energy (0.10 μJ). 600 pulses per spot were fired.

Also, a blue shift can be seen for higher pulse energies irradiation. Higher extinction that was seen in the s-polarised spectra for wavelengths between 500 and 800 nm could be attributed to the *silvering* effect that was thought to increase of the reflectivity of the sample.

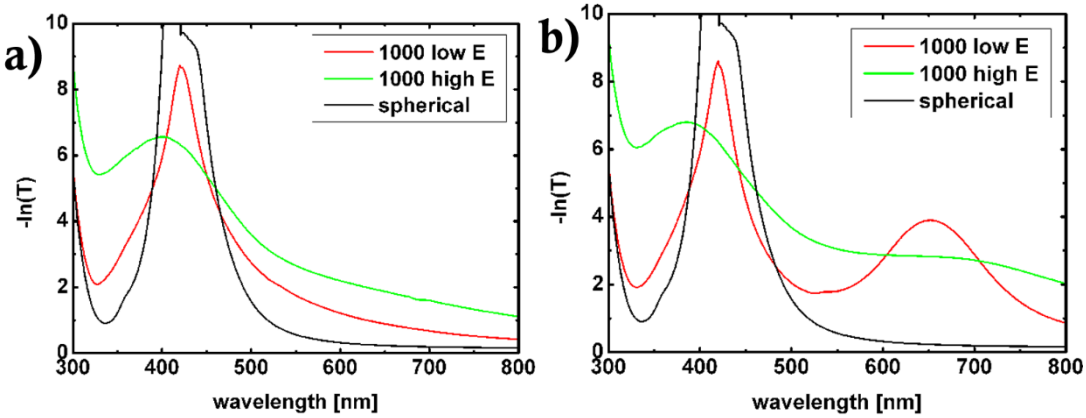

Figure 4-37 comparison of a) s-polarised and b) p-polarised spectra of nanoparticles irradiated with high pulse energy (0.18 µJ) and low pulse energy (0.10 µJ). 1000 pulses per spot were fired.

The blue-shifted SPR had also much higher bandwidth for the low pulse energy irradiation than the remnant SPR for the lower pulse energy irradiation. That could have been an indicator for presence of much smaller nanoparticles that are seen in both s- and p- polarisations- from the fact that the reshaping into ellipsoids had much higher rate for bigger nanoparticles. It was shown in [50] that small spherical nanoparticles have a wide SPR width and that the width decreases drastically when the size of nanoparticles increases from around 2 nm to 30 nm (in diameter). Also, the bandwidth increased with the number of pulses per spot applied, giving the impression that the dissolution process did not only take place for already reshaped nanoparticles but also for the spherical nanoparticles, leaving them smaller. P-polarised spectra showed the red shifted SPR peak that was attributed to the SPR coupling along the long axis of nanoparticles. Higher pulse energy irradiation led to higher elongation ratio but also to higher amount of dissolution of nanoparticles. Also, for 1000 pulses per spot the nanoparticles were completely dissolved in the volume of glass and formed a layer of silver on the surface, therefore no evident SPR around 600 nm could be observed.

Presented results are thought to be driven by the same processes as in the ns- pulsed irradiation (explained earlier). The nanoparticle equilibrium temperature for the fluence used here was calculated to be ~2000K (Figure 2-13 in Chapter 2), which is around 700K higher than what was stated in the by Fleming et al. Difference is however in the pulse lengths used, hence in the laser absorption mechanisms, leading to partial melting

of elongated nanoparticles (which are believed to be elongated during the first pulses fired). Elongated nanoparticles were visible under the SEM in between the molten layer. Taking the stated above as the main assumption, it is believed in this paragraph that a modified mechanisms was observed (comparing ns- irradiation to ps-). More experimental work is required however in order to characterise this process further and determine the exact effect of shorter laser pulse length.

4.5.2 Irradiation under an angle

One of the additional experiments that were performed on spherical MGNs was establishing the technique for nano ellipsoid orientation modification within the volume of the sample. Irradiation of MGNs with ~40° angle of incidence was performed. The irradiation setup previously used for irradiations had to be modified for this purpose. A translation stage was added in the focal plane of the laser beam and was rotated by 40°. Figure 4-38 shows the rotated stage.

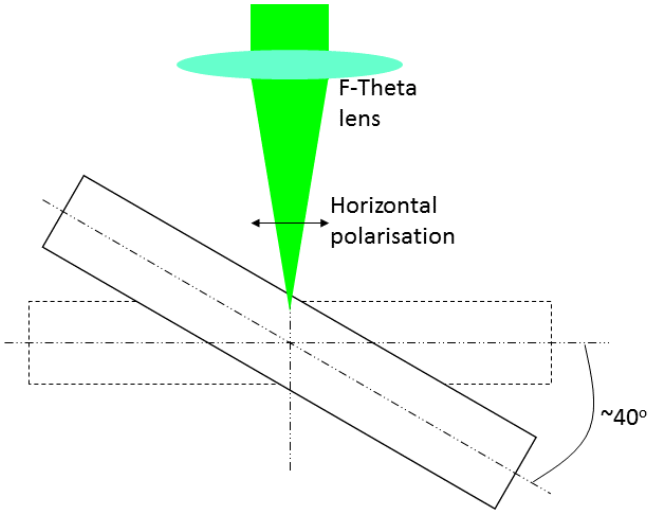

Figure 4-38 Schematic drawing of a translation stage that was added to the irradiation setup. Stage was rotated by 40°

Squares were irradiated with this technique with parameters described earlier in this chapter. Stage position in Z axis was being adjusted during the irradiation in order to keep the beam waist in the nanoparticle layer while translating. This resulted in reshaping of nanoparticles in the direction of the laser polarisation leading to re-orientation of nano ellipsoids within the volume of the glass by ~40°. Figure 4-39 presents the nano ellipsoids orientation.

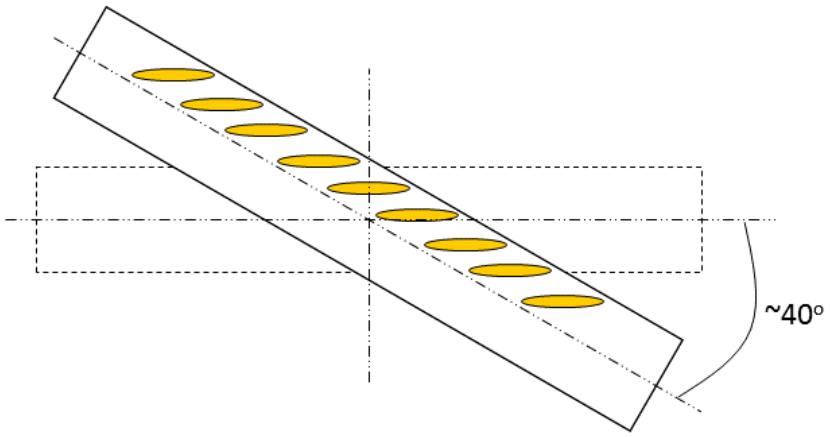

Figure 4-39 Schematic drawing of how the nano ellipsoids were oriented within the glass volume after irradiation under an angle

In order to be certain that the desired effect was achieved, irradiated samples were placed in the spectrophotometer with linear input polarisation and a rotational holder. Figure 4-40 presents the effect that was thought to be observed.

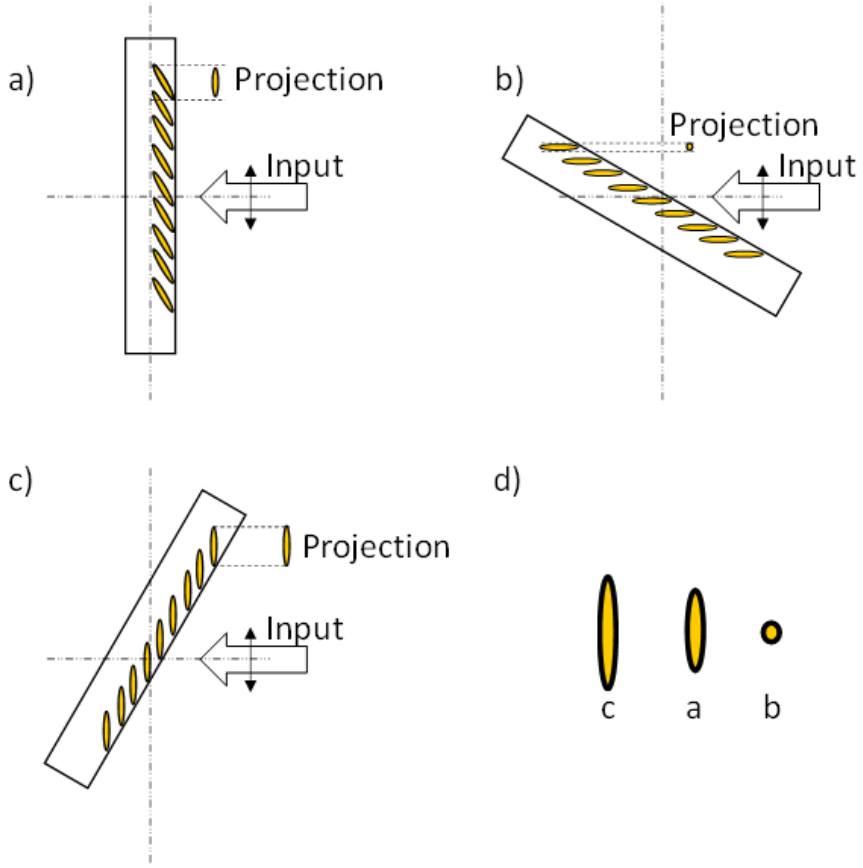

Figure 4-40 Schematic representation of the effect observable in the spectrophotometer extinction measurements (a-c), and projections of nanoparticles to the right hand side plane (d)

Rotation of MGN would result in either decrease or increase of the p-polarised SPR. The reason for that would be the effective nanoparticle size, represented as a projection of its shape to the entrance plane of the incoming light.

Figure 4-41 presents extinction spectra, measured for sample rotated anticlockwise (as in Figure 4-40 c).

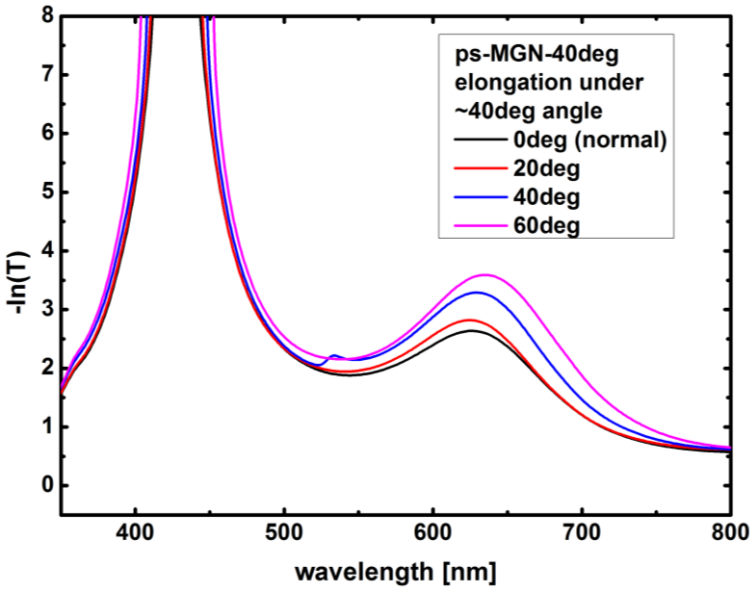

Figure 4-41 Extinction p-pol spectra of MGN irradiated under an angle and rotated anticlockwise in the spectrophotometer (bigger size of NP in the projection)

Desired effect was observed of the increase in the p-polarised SPR peak, due to the larger size of the projected nanoparticle to the plane of the incoming light polarisation. Also, measurements for rotation in the clockwise direction can be seen in Figure 4-42 (as in Figure 4-40 b). A decrease of the p-polarised SPR peak was observed for -60^{o} angle. It lead to the understanding that nanoparticles have successfully been elongated in the desired fashion when the irradiation was performed under an angle of ~40^{o}. This adds to the already known techniques of nanoparticles manipulation in shape and orientation, which can be used in applications utilizing the SPR tailoring. Also, this sample will be used in Second Harmonic Generation experiments in Chapter 5, adding to the knowledge of that nonlinear optical process.

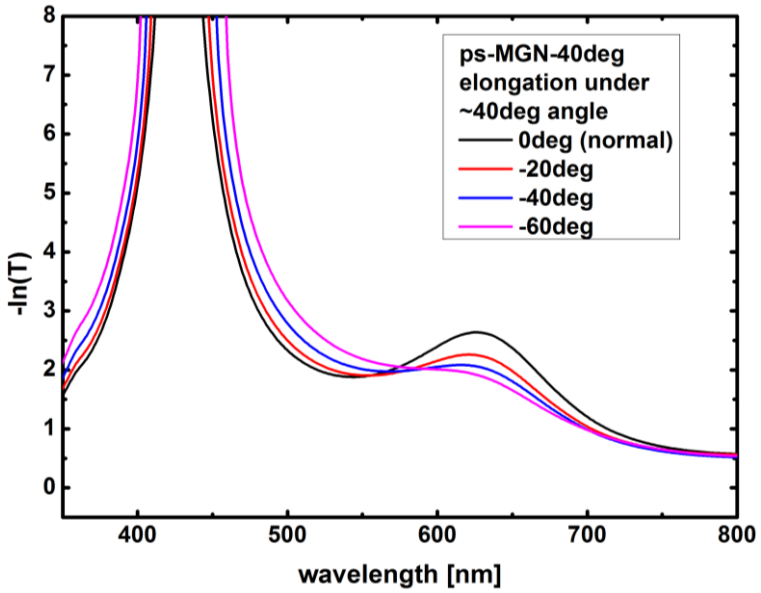

Figure 4-42 Extinction p-pol spectra of MGN irradiated under an angle and rotated in the spectrophotometer in the negative direction (smaller size of NP in the projection)

4.5.3 Optimisation of reshaping process

Reshaping parameters have been established for the picosecond reshaping process of MGNs in previous sub-chapters. Pulse energy of 0.10 µJ (~88 mJ/cm^2), 1000 pulses per spot and 200 kHz repetition rate gave the best elongation of nanoparticles and the highest number of reshaped nanoparticles. It was stated that not all nanoparticle in the volume of the nanoparticle layer was being reshaped in the process. This resulted in the spherical SPR peaking at ~430 nm. Therefore, it was important to develop a technique that would be more effective in reshaping the whole layer of nanoparticles. Questionable was also, which part of the layer achieves the most shape modifications. An experiment was performed to see the changes in the extinction spectrum after the reshaped area was etched with 12% HF acid. The area was reshaped with parameters established earlier. The spectrum was taken after which the sample was put into the HF acid for ~3 seconds (longer time was not required as the whole thin layer of nanoparticles could have been etched easily). Another spectrum was taken after the HF bath. Figure 4-43 presents the resulting spectra. It can be seen there that the remnant SPR decreased in width after etching and the red shifted peak did not change its spectral position significantly. Only slight shift towards shorter wavelength can be observed. It can be concluded that a small amount of spherical nanoparticles are placed at the very top surface of the nanoparticles layer and that they are not prone to reshaping with the existing technique. This conclusion is also in agreement with [168] where it was

experimentally shown that the upper layers of these type of MGNs hinders the reshaping of nanoparticles that are deeper in the volume.

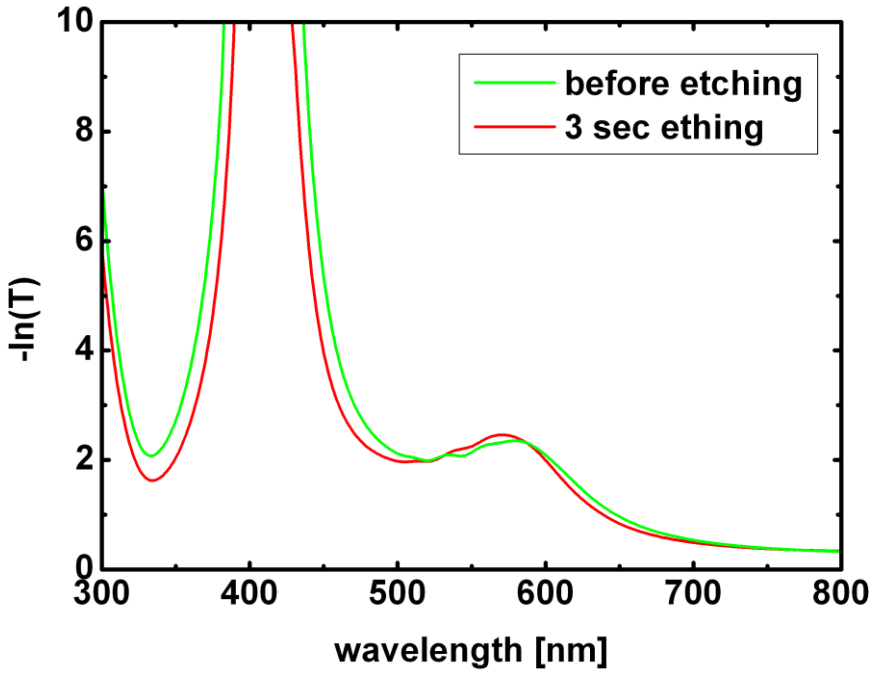

Figure 4-43 P-polarisation of reshaped nanoparticles area. 10 µJ, 1000 pulses per spot and 200 kHz was used.

It is believed that silver ellipsoids were formed deeper in the volume of the nanoparticle layer. It was also assumed that spherical nanoparticles also existed below the ellipsoids as the remnant SPR was still very strong after etching. An illustration of how the layer might have looked like is presented in Figure 4-44. In order to improve the nanoparticle reshaping rate a technique was developed that required two staged process of reshaping.

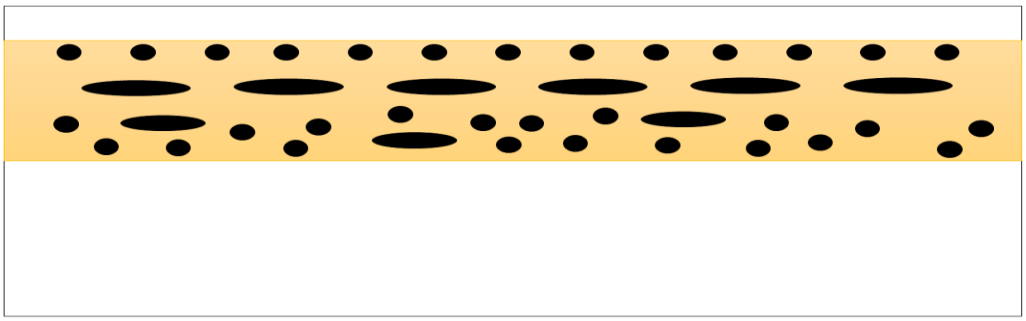

Figure 4-44 Image of the nanoparticles distribution after irradiation with a picosecond laser.

Figure 4-45 presents steps taken in this technique. First, an area was irradiated with the parameters that were established to be the most optimal (1000 pulses per spot- Figure 4-45 a). Secondly, another area was irradiated but with only 500 pulses per spot, for later comparisons (Figure 4-45 b).

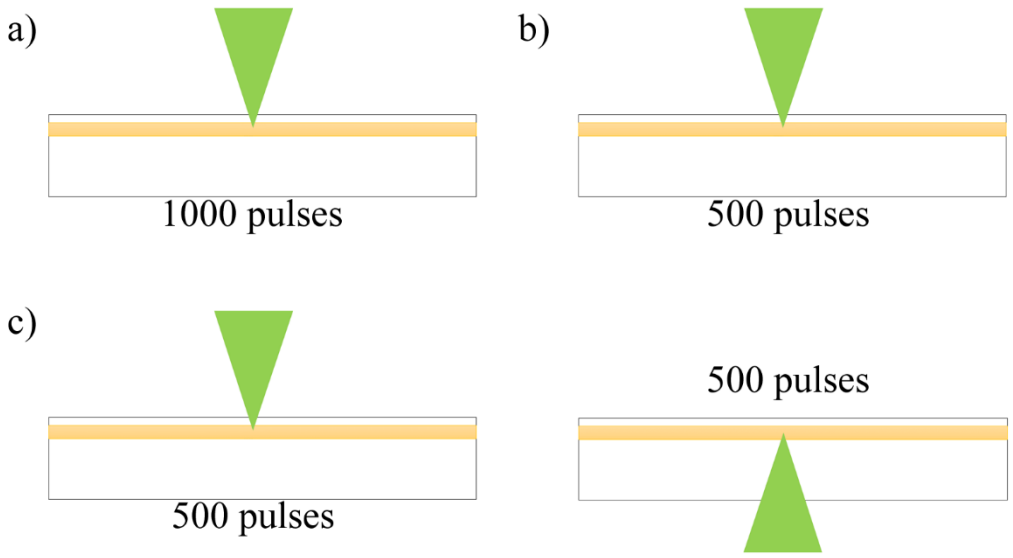

Figure 4-45 Experiment that was designed to optimize the shape modification of silver nanoparticles a) reshaping with 1000 pulses per spot, b) with 500 pulses per spot c) two staged reshaping with 500 pulses per spot.

Next, an area of 500 pulses per spot was irradiated, after which the sample was turned upside down and another 500 pulses per spot were fired. Also, the writing direction and the polarisation direction was set so that both areas matched with each other, forming one area irradiated from the top and from the bottom of the sample. Areas irradiated with 1000 and 500 pulses from the top only were there to guide the understanding about the size of reshaping that would be shown for the two staged process.

Spectra were taken and are presented in Figure 4-46. It can be noticed that the s-polarised spectrum for the two staged irradiation showed an additional band formation at ~550 nm, which could have been caused by misalignment of the sample during the second irradiation (from the bottom). P-polarised spectrum showed the red shifted bands. The two-staged irradiation band exhibited a high extinction peak, formed with two smaller peaks, one at ~630 nm (in the vicinity of the 1000 pulses per spot irradiation) and second at ~550 nm. It was concluded that the first band showed the nanoparticles that were irradiated from the top but irradiated again from the bottom which elongated them to the same length as if they were irradiated with 1000 pulses per spot. The second band would then show nanoparticles that were not irradiated from the top in the first place. It had also stronger extinction peak, which could mean that more nanoparticles were elongated from the bottom than from the top.

Overall, much higher reshaping efficiency was shown to be caused by two staged irradiation process. The remnant SPR however still stayed at ~430 nm which would suggest that remnant spherical nanoparticles still stayed in the volume of the

nanoparticles layer and couldn't be reshaped as efficiently as in the femtosecond reshaping process due to the lower laser intensities that could be achieved (~GW/cm^2 instead of ~TW/cm^2).

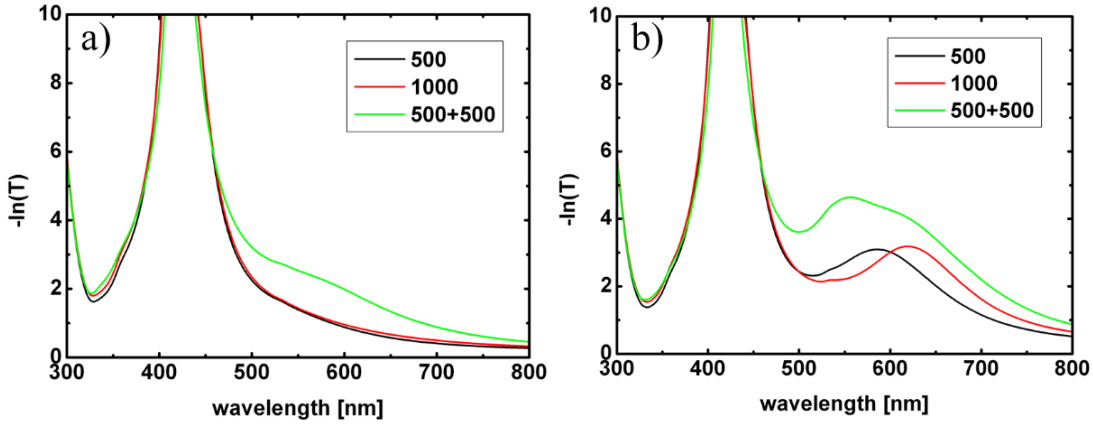

Figure 4-46 Spectra taken for the areas irradiated with 500, 1000 and 500 + 500 pulses per spot a) s-polarisation, b) p-polarisation.

4.5.4 High filling factor sample

Filling factor (*f*) as one of the important factors of the MGN samples themselves was taken into consideration. While the lower *f* samples proved to have a good rate of reshaping (as shown in the previous part of this chapter), the high *f* MGN sample was still unknown.

A high *f* sample was acquired from Codixx AG. The same technology of manufacturing as presented earlier was used to produce it. As already stated, the filling factor is the rate of the silver volume within the nanoparticle layer volume, therefore it can be easily assumed that the new sample was more silver rich (more nanoparticles and more densely packed). Figure 4-47 shows images of the high *f* sample and the low *f* sample. It could be clearly seen that the colour of samples was much different. The darker colour of high *f* sample was there due to the fact that the nanoparticles in the volume of MGN extinct the visible light more intensely than the nanoparticles in the low *f* sample.

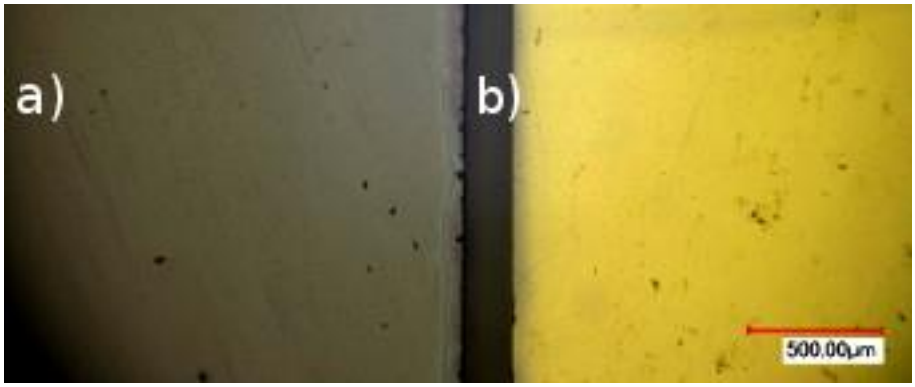

Figure 4-47 Photography of a) high fill MGN b) low fill MGN. Showing difference in their colour

Spectra of both of these samples can be seen in the Figure 4-48. The high *f* sample had much wider SPR than the low *f* sample. The width of the SPR measured for the extinction of 8 [arb.u.], for the high *f* was 134 nm whereas for the low *f* was 39 nm. The difference in the extinction values themselves were clearly visible- the high *f* sample extinct much more light in the blue/UV as well as in the visible region.

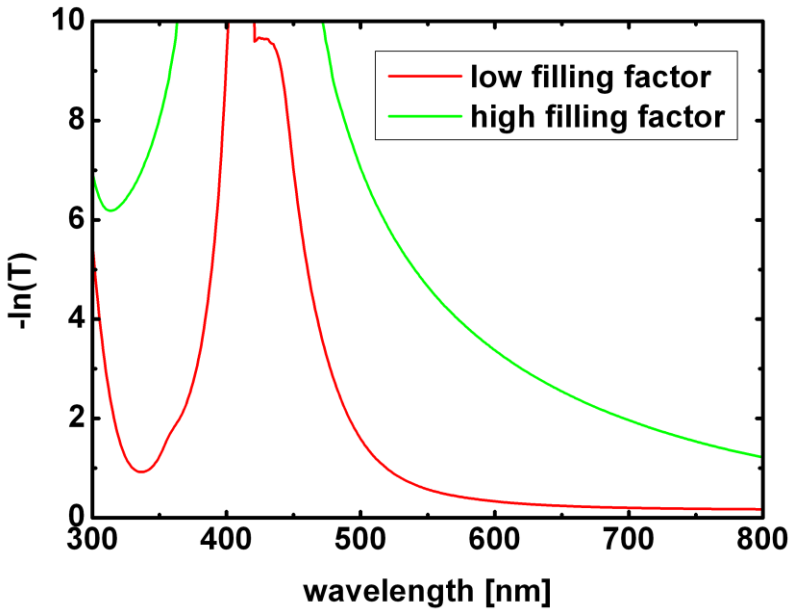

Figure 4-48 Extinction spectra of spherical silver nanoparticles for (red) low filling factor MGN and (green) high filling factor MGN.

The extinction in the visible region was the reason for the dark colour of the sample. The width of the SPR could be explained by the fact that in the Mie theory, the SPR of smaller nanoparticles was much broader than the one for nanoparticles with radius of ~15 nm. Smaller nanoparticles embedded in the glass volume were concluded to be present. High *f* factor MGN was assumed to be caused by smaller distances between nanoparticles (densely packed) but not small enough to produce additional SPR peaks (from the quadrupolar nanoparticle-nanoparticle interactions). Estimating size of

nanoparticles in high *f* samples from Figure 2-9 in Chapter 2 (calculated plots of Mie resonance bandwidth as a function of nanoparticle size) one can say that the NPs diameter here is <10 nm.

Also, in order to see the efficiency of reshaping in this type of samples, the reshaping setup was used in the same manner as described in the previous part of this chapter. Three 5x5 mm squares were irradiated with 200 kHz laser repetition rate, 1000 pulses per spot and pulse energies of 8 µJ, 10 µJ and 13 µJ. Spectra were measured and can be seen in Figure 4-49.

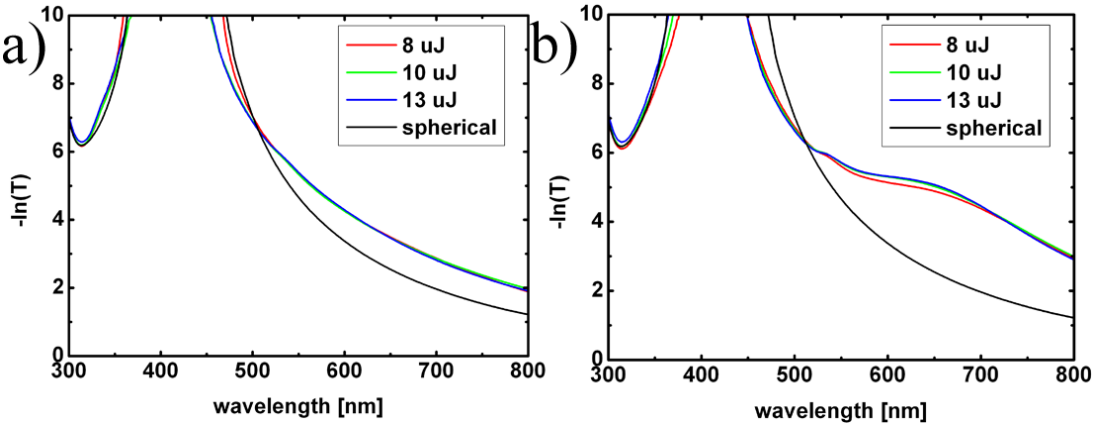

Figure 4-49 Spectra of the reshaped areas of the high filling factor sample a) s-polarised spectra and b) p-polarised spectra. Spectrum for the non-reshaped nanoparticles is shown in the black line.

It can be seen that for the s-polarisation, similar effect can be noticed as in the low *f* MGN, which is a decrease in the SPR width and increase of the extinction strength along the visible range of the light spectrum. The p-polarisation showed on the other hand very small change to the SPR. There was a red shifted band forming at around ~650 nm, but was very small in comparison to the low *f* sample with the irradiation in the same range of fluences. The comparison can be seen in Figure 4-50.

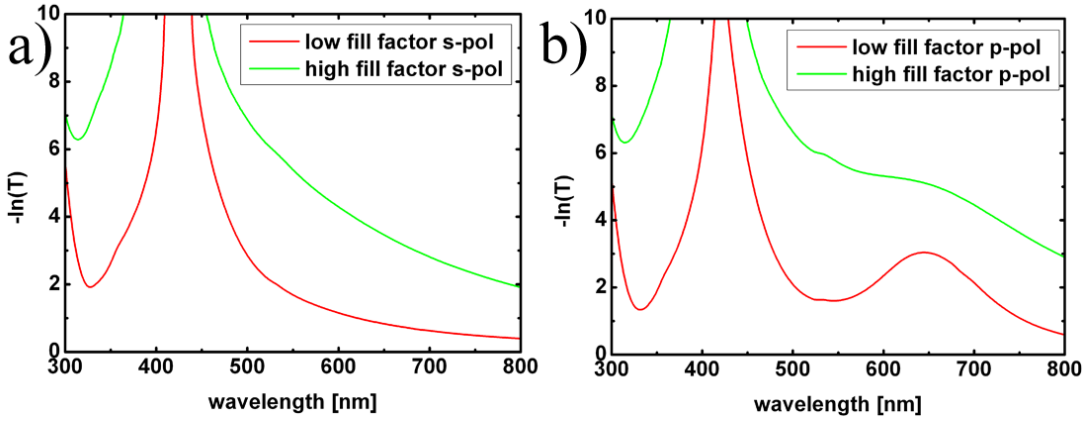

Figure 4-50 Spectra comparing two type of samples a) s-pol b) p-pol.

Figure 4-50 b) shows the p-polarised spectra of both samples. The red shifted SPR for the high *f* was less pronounced than the SPR for the low *f*. However, the overall extinction for around 650 nm was much stronger. This effect could be seen when looking at the samples themselves with a linearly polarised light illumination from the back - Figure 4-51. The reshaped areas were much darker because of the fact that the extinction ratio was much stronger for the p-polarisation. Also, the dichroism was much less visible on the sample because of the much lower contrast between p- and s-polarisation at ~650 nm (there is nearly no difference between squares in Figure 4-51 a) and b).

Figure 4-51 Photography of the reshaped areas of the high fill factor sample. Linear polarisation illumination is shown for two orthogonal directions in (a) and (b)

It can be concluded that the high *f* sample was much harder to achieve effective dichroism when irradiating with similar laser parameters to the optimal ones that were found earlier. Also, the reshaped areas were hardly distinguishable from the rest of the sample because of the overall high extinction ratio over the visible range.

Also, the red-shifted band in the high *f* sample formed at the same exact spectral position than as for the low f sample. The spectral gap therefore was the same. That showed that even though there was much lower contrast for picosecond irradiation of high *f* samples, the elongation ratio of the nanoparticles within the sample should have been comparable as in the low *f* sample. Concluding, only some of the nanoparticles in the densely packed layer of high *f* sample were reshaped, but also the same long axis length was achieved. It was shown in [168] that the increase of the filling factor changes the refractive index of the MGN. This directly affects the reflectivity of the sample, which could have been the reason for difficulties with efficient reshaping.

Even though high *f* sample may not have been the best candidates for reshaping with picosecond pulse irradiation, it will show good second order nonlinear effects in the chapter 5.

4.6 Conclusions

In this chapter, picosecond pulsed irradiation of metal-glass nanocomposites has been presented. Its effect of shape modification on the silver nanoparticles embedded in soda-lime glass was shown - elongation of nanoparticles along the direction of laser polarisation. Laser reshaping parameters were established: laser fluence, laser modification threshold, laser degradation and *silvering* thresholds under multipulse irradiation. Laser scanning method was shown along with optical techniques used to characterize produced samples. Effects of parameters change on single irradiated lines as well as on whole irradiated areas were shown. Shift of the SPR band under p-polarised illumination was established to travel along with the change of number of pulses per spot fired and laser repetition rate. Also, the *silvering* effect was described. It was shown that it led to creation of a molten layer of silver on the surface of glass. Also, change of number of pulses per spot showed variation in SPR position and nanoparticles dissolution. A method for nano ellipsoid orientation change within the glass volume was also shown and its effects on the SPR extinction spectra. The method of optimization of the reshaping process was presented which leads to increased p-polarised SPR peak intensity. Also, a high filling factor sample was presented and irradiation of it was performed.

Picosecond nanoparticle modification was proved to be an effective method of shape change of silver clusters. Utilizing picosecond lasers is a cost-effective process when comparing to femtosecond lasers. This technology could be directly applied into commercial manufacturing of i.e. high extinction ratio dichroic polarizers, leading to lower initial investment into this process. Various other potential applications of this type of material can be utilized in areas like data storage [160], optics and/or security.

5 Second-Harmonic-Generation and Multiphoton-Absorption-Induced-Luminescence from silver nanoparticles embedded in soda-lime glass

5.1 Introduction

In this chapter the nonlinear optical properties of nanoparticles will be described. As was shown in the previous chapter, laser-assisted shape modification of NPs leads to observation of local optical dichroism achieved via spatially selective modification of the SPR position dependent on the laser parameters. Another way of elongating Ag NPs is by simultaneous heating and tensile deformation of glass embedded with NPs, which results in a global shape modification and produces highly oriented nano ellipsoids in the direction of deformation. This method produces a good quality elongation and is therefore used for production of high contrast polarisers [169]. It was also shown in [35] that MGN produced with this method is able to show the phenomenon of Second Harmonic Generation (SHG) when excited with a fs- pulsed laser at 800 nm. Second-order optical properties of nanoparticles embedded in media have proved to be useful in applications like biological imaging where certain molecules are being tracked by observation of SHG from nanoparticles in their vicinity [170]–[173]. Similarly, Third Harmonic Generation (THG) from noble nanoparticles has been extensively studied as it showed to be a great candidate for imaging and labelling of both biological and non-biological species [174], [175]. THG has been also a preferable mean of using nanoparticles for these applications because centrosymmetrical clusters could be used as they are easy to manufacture. THG will, however, not be a part of investigation in this thesis. SHG as an optical phenomenon that requires non-symmetricity to be present is believed not to have a great impact on nanoparticles due to their spherical shape, and only have significant input to emitted optical signal when non-perfectly shaped nanoparticles are present [35], [176], [177] (breaking the symmetry with their shape).

Also, SH signals have been observed for small centrosymmetric NPs and are believed to originate from the symmetry breaking at the surface of the nanoparticle- such SHG response is then dominated by the electric dipole contribution and can be observed in a form of dipolar intensity response in the far field of the nanoparticle [178]–[180].

Linear optical properties of Ag nanoparticles embedded in soda-lime glass have been described in **chapter 4.** These are the ability of MGNs to extinct the incoming polarised light, making the composite optically dichroic. In this chapter the nonlinear optical properties will be studied (SHG) on elongated Ag nanoparticles that will be reshaped with three main methods: mechanical stretch, fs- and ps- pulsed laser reshaping.

The optical characterisation of the SHG as well as of the Multiphoton-Absorption-Induced Luminescence (MAIL) [181]–[186] - which will be present in the emitted signal - will be performed for elongated NPs embedded in soda-lime glass. Also, an explanation to the observation will be proposed, based on both the experiments and computer simulations.

5.2 Laser induced Second Harmonic Generation experiments

Metallic nanoparticles have gained a lot of attention in recent years due to their unique linear and nonlinear optical properties. Second Harmonic Generation (SHG) has been found in soda-lime glasses embedded with nanoparticles that were previously mechanically stretched under applied heat [35]. These MGNs have shown the highest intensity of SHG when illuminated with laser beam polarisation parallel to their long axis (Figure 5-1). In that work, the laser fluence used was ~1 mJ/cm^2, repetition rate 80MHz and pulse width was 80 fs. It was shown that increasing the incidence angle of the sample increases the SHG intensity, with highest SHG intensity being present at ~40^o incidence angle.

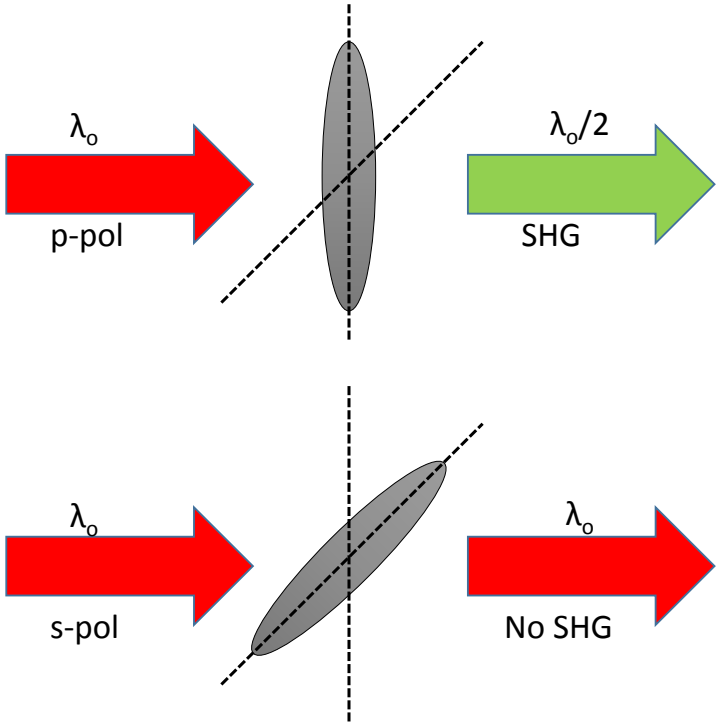

Figure 5-1 Schematic representation of the SHG formation as a function of nano ellipsoid absolute orientation within the MGN. SHG present for p-polarised fundamental beam and absent for s-polarisation.

There, the p-polarisation extinction peak of the measured MGN was ~ 600 nm while the SHG excitation wavelength was set to 800 nm. This work showed that the SHG was dependent on the nanoparticle arrangement and the field enhancement due to the SPR.

In order to investigate second order nonlinear optical properties of MGNs using ps-pulsed illumination, an experimental setup was prepared (detailed description in **Chapter 3**) and a three types of Ag NP-glass samples produced. For comparison purposes (with previously published work on SHG from Ag-glass MGNs) a mechanically stretched (MS) sample was prepared (supplied by Codixx Ag) with its p-polarised extinction band placed at ~900 nm. The measured extinction spectrum can be seen in Figure 5-2.

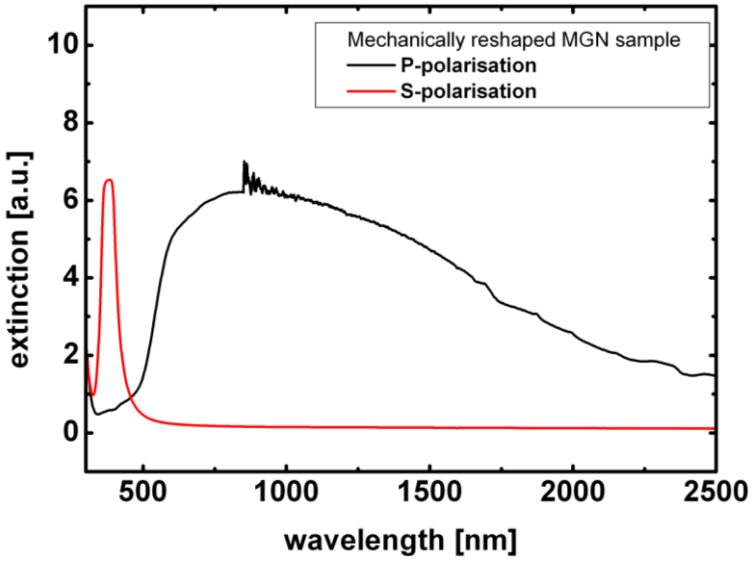

Figure 5-2 Extinction spectra of MS-MGN. P- and s- polarisations are shown.

The MS-MGN had a wide p-polarised band in comparison to ps- reshaped MGNs presented in **Chapter 4**, which resulted from the difference in process of obtaining such elongated nanoparticles. The mechanical reshaping of Ag NP was carried out by subjecting the MGN sample to tensile deformation with simultaneous heating below the transition temperature of the glass. Ag^+ / Na^+ ion exchange process was used to generate silver clusters in 1 mm thick soda lime glass. The total thickness of the MGN sample was ~200 µm with a layer of nanoparticles of ~10 µm. The highest intensity extinction of the band is placed at ~900 nm for p-polarisation whereas a high contrast s-polarisation is present at ~430 nm. This spectral characteristic of a MS MGN makes this composite a very high aspect ratio dichroic polariser which can be seen in Figure 5-3.

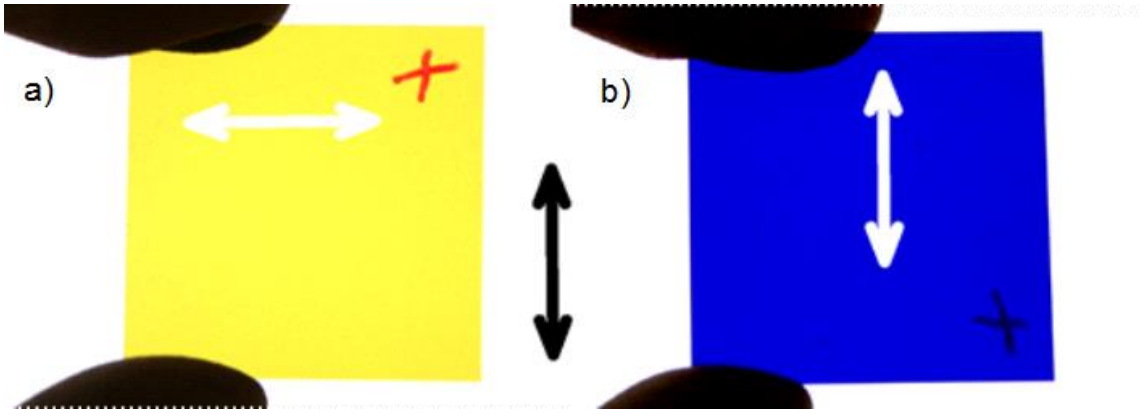

Figure 5-3 Photography of MS-MGN. Linearly polarised illumination from the back of the sample Is present (direction indicated by the black arrow). White arrows indicate long axis of elongated nanoparticles.

Single layered sample was obtained by immersing the MS-MGN in a 12% hydrofluoric acid (HF) - procedure described in previous chapters.

The second type of nanoparticles used for experimentation were MGNs irradiated with femtosecond laser pulses. 1 mm thick soda-lime glass was used with one-sided layer of nanoparticles (~20 μm thick). The light source used for reshaping was a 250 fs Yb:KGW MOPA (Pharos, Light Conversion Ltd) operating at 500 kHz. The laser beam was focused into a spot of 30 μm (measured at $1/e^2$). Different laser parameters used resulted in four samples with varying ratios of elongation. Subsequent irradiations of the sample area, by different laser wavelengths, were used to increase the aspect ratio between the axes of the elliptical NPs. 5 x 5mm irradiated areas were manufactured. First, all areas were irradiated with 515 nm while varying the number of pulses per spot (200, 300, 500, 500), then the fourth sample was irradiated again with laser wavelength of 750 nm and 500 pulses per spot in order to achieve higher elongation. This resulted in p-polarised extinction peaked at 547 nm (FEMA), 567 nm (FEMB), 585 nm (FEMC), and 792 nm (FEMD). Measured polarised spectra can be seen in Figure 5-4.

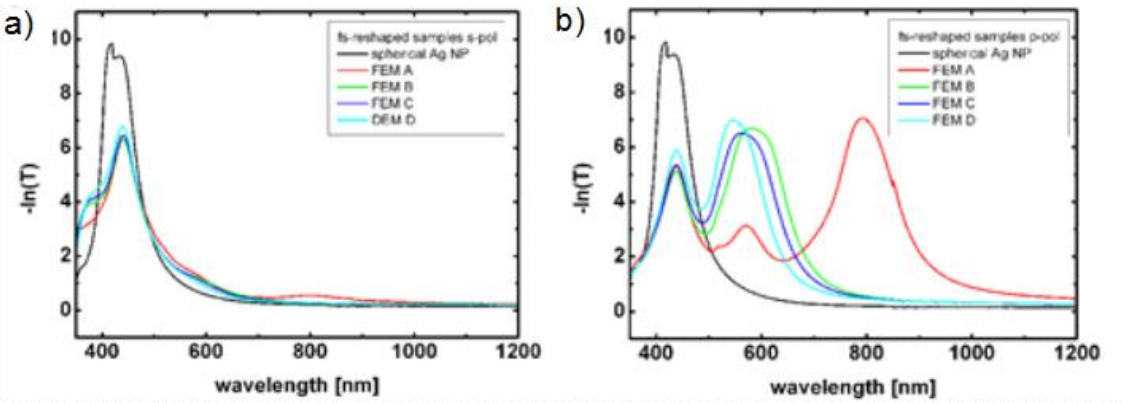

Figure 5-4 Extinction spectra of fs- reshaped MGNs. S- (a) and p- (b) polarised spectra are shown.

Laser intensities used were 0.362 TW/cm^2 (FEMA and FEMB), 0.317 TW/cm^2 (FEMC and FEMD-1st irradiation), and 0.288 TW/cm^2 (FEMD- 2nd irradiation). A 430 nm remnant of spherical nanoparticles was still present as well as the ~600 nm peak resulting from parts of nanoparticles that were not elongated for the second time with the 750 nm laser beam. Polarised images of fs- irradiated areas can be seen in Figure 5-5.

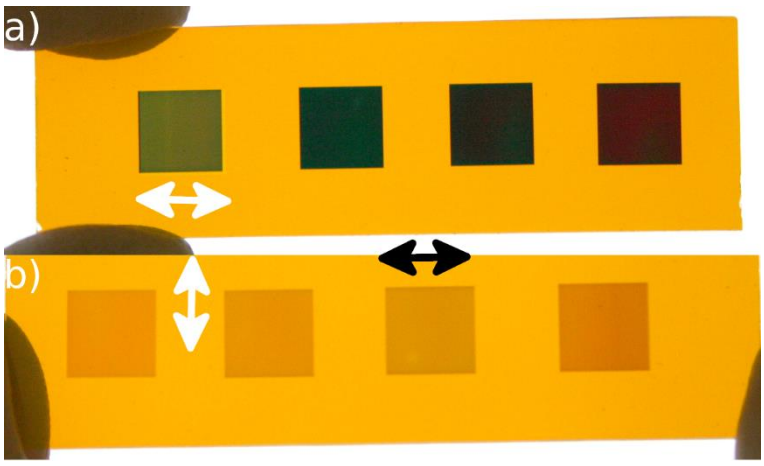

Figure 5-5 Photography of FEM MGNs illuminated with linearly polarsied light from the back of the sample (white arrow- polarisation direction). Black arrow indicates nanoparticles' long axis. Samples from right to left: FEMA, B, C, D.

It can be seen that the colour changes are similar to these presented for ps- assisted reshaping. Red/Brown colour of reshaped square indicates smaller elongation ratio due to most of the SPR band absorbing/scattering the short wavelength part of visible spectrum (FEMA). Also green/blue could be seen as the elongation ratio increased (FEMD).

The third type of reshaped nanoparticles were MGNs presented in **Chapter 4**- ps-pulsed reshaped nanoparticles with various number of pulses per spot used (100, 200,

300, 400, 500, …, 1000). Repetition rate was kept at 200 kHz. Optical spectra were measured and can be seen in Figure 5-6.

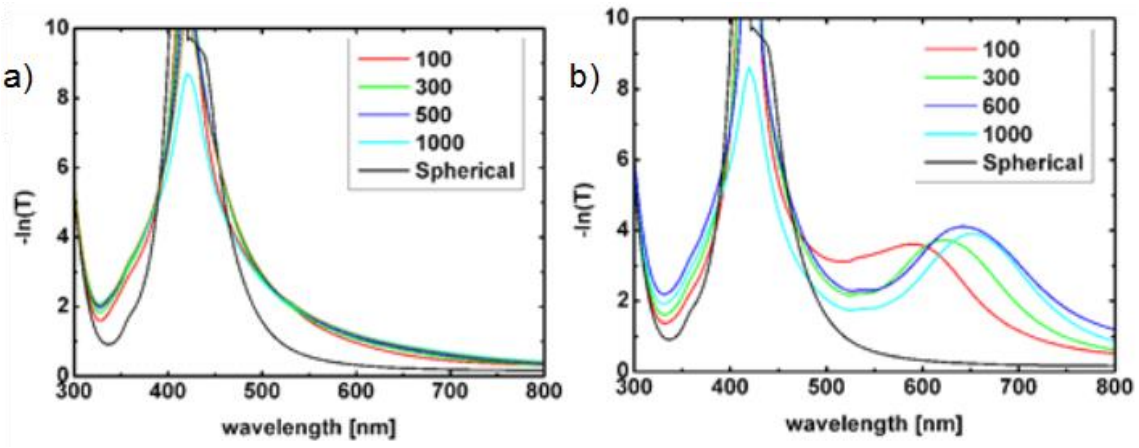

Figure 5-6 Extinction spectra of ps-MGNs, irradiated for various number of pulses per spot. 100, 300, 500, and 1000 are shown for clarity (figure taken from Chapter 4- fig. 4-26)

Increasingly changing separation gap could be observed and was documented in the previous chapter.

A linearly porlarised 10 ps- pulsed laser at 1064 nm wavelength and a repetition rate of 200 kHz (Talisker Ultra, Coherent) was used as an excitation source for the SHG experiment. Measurements were performed in transmission geometry as shown in Figure 3-13 of **Chapter 3**, with the fundamental beam focused at normal incidence on the MGN sample surface. A half-wave plate was used to control the polarisation direction of the fundamental laser beam. The beam was focused to ~26 μm diameter spot at $1/e^2$, and the resulting signal was filtered out by 400 – 800 nm bandpass mirrors.

The excitation wavelength at 1064nm was in the close spectral vicinity of the highest p-polarised peak of the MS MGN, which was assumed to give the best quality coupling with localized surface plasmons, with the appropriate beam polarisation.

5.3 SHG from soda-lime glass and Ag+ ion doped glass

SHG from glass is a known phenomenon [187]. Using the SHG experimental setup, pure soda-lime glass and Ag^+ doped soda-lime glass were excited with a ps- pulsed beam at 1064nm wavelength. It was of great importance to establish that the SHG signal that was measured on MGN samples was not present due to nonlinear effects taking place in the glass substrate itself. Figure 5-7 shows spectrally resolved data taken from irradiating samples with two different laser fluencies (0.5 mJ/cm^2 and 1 mJ/cm^2).

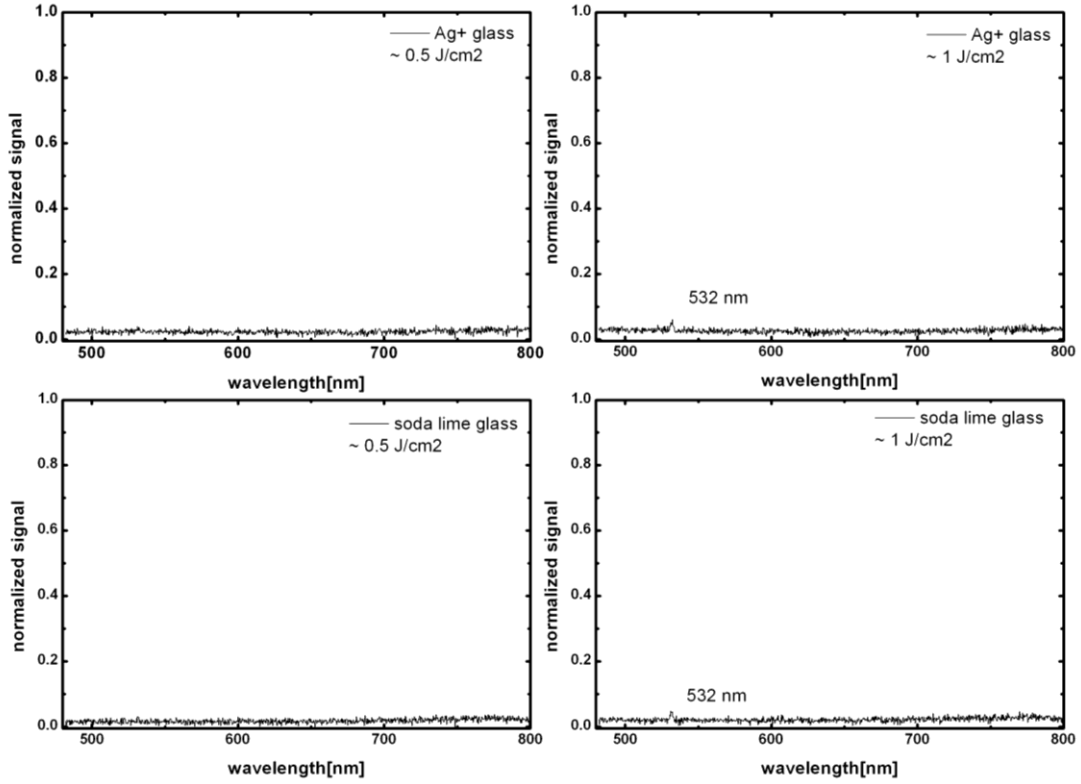

Figure 5-7 Spectral measurements taken for Ag+ glass and pure soda-lime glass. Two main laser fluences were used.

It was observed that a small intensity peak forms at 532 nm, where the SHG signal was expected, at 1 J/cm^2. Similar threshold was achieved for both samples indicating a purse soda-lime glass SHG formation without Ag^+ ions influence. More precise experiments would have had to be performed in order to describe this phenomenon in soda-lime glass as well as in Ag+ ion doped glass (which was not the purpose of this thesis). Both samples showed the same behaviour with varying input polarisations.

5.4 Mechanically stretched nanoparticles (MS-MGN)

Mechanically stretched sample (MS) had its SPR peak (~900 nm) in the vicinity of the fundamental beam, leading to the strongest plasmon coupling.

An experiment was performed in order to see the difference between transmission and reflection configuration of the experimental setup as well as between the properties of the MGN itself. Figure 5-8 shows the normalized intensity taken from MS sample placed in the focus of the fundamental beam. It can be seen that both configurations result in a broad band peaking at ~450 nm and a 532 nm peak. Two different excitation laser fluencies were used and results were normalized in order to show the difference in sensitivity of samples to the excitation beam. Transmission signal was recorded at ~1 mJ/cm^2 whereas the reflection signal at ~ 12 mJ/cm^2 in order to achieve a visible and spectrally resolved data. For future experiments only transmission geometry will be used as it has a higher output to input signal strength and will not result in too much energy dissipated in the sample leading to its modification. Next subchapter will show this effect in more detail.

Also, transmission geometry showed much higher 532 nm peak than the reflection which could suggest higher SHG efficiency. A few additional bands have been noticed at ~550 nm and >650 nm which could be a result of higher laser fluence used. The broad band that is visible in these spectrally resolved images will be described in the next subchapters along with the explanation of its formation.

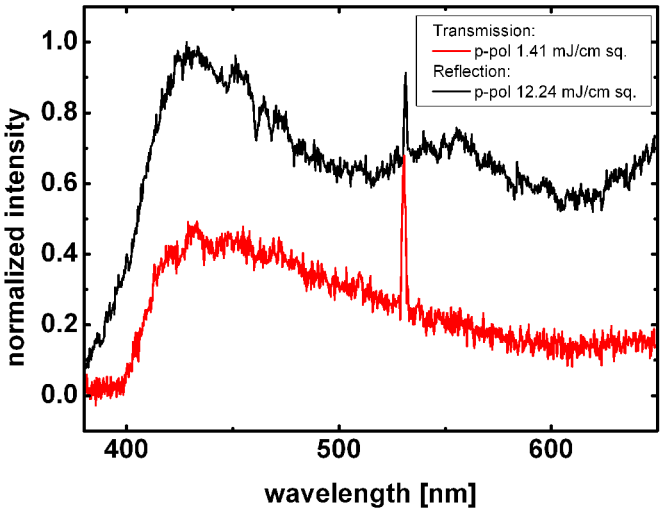

Figure 5-8 Normalized intensity measurement of SHG from MS-MGN for p-polarised laser beam in both transmission and reflection geometry.

Figure 5-8 measurements were performed for a p-polarised direction of the fundamental beam. The highest signal was achieved for incoming beam polarisation parallel to the long axis of the nanoparticles. It can be seen in Figure 5-9 in more detail that when the sample is rotated to p-polarisation the highest SHG peak is formed (along with the broad band signal in the background).

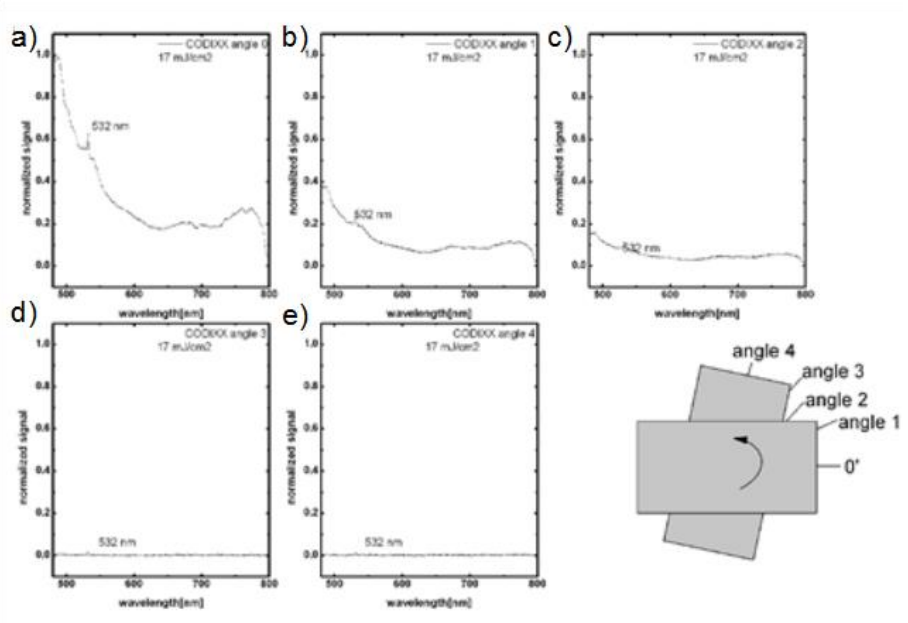

Figure 5-9 Transmission measurements of MS-MGN for various orientations of the sample. (a)- angle 0^{o}, (e)- angle 4.

Once the sample is rotated towards the s-polarisation, nearly no signal can be observed. That agrees with the theory that the highest coupling of the surface plasmon with a 1064 nm fundamental exists for the p-polarised beam as the p-polarised extinction spectrum shows the SPR band spectrally closest to the fundamental beam.

5.4.1 MS MGN signal change dependence on the spatial position change

In order to observe the behaviour of the SHG signal and its background signal, the sample was put in the focus of the fundamental beam and its position was changed relative to the focal plane of the focusing lens (Figure 5-10).

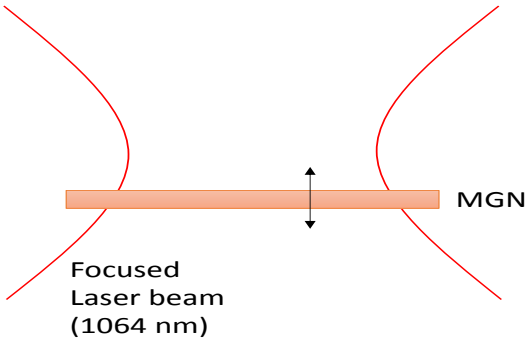

Figure 5-10 Through focus translation- graphical representation of measurement technique.

This resulted in changes in laser spot size on the sample, and hence the laser fluence. Measurements were performed for the p-polarisation of fundamental beam and laser fluence in the focus of 1.41 mJ/cm^2. This experiment served also as a calibration for sample position, for it to be exactly in the focal plane, therefore resulting in the highest SHG intensity. Figure 5-11 shows the through focus SHG signal change.

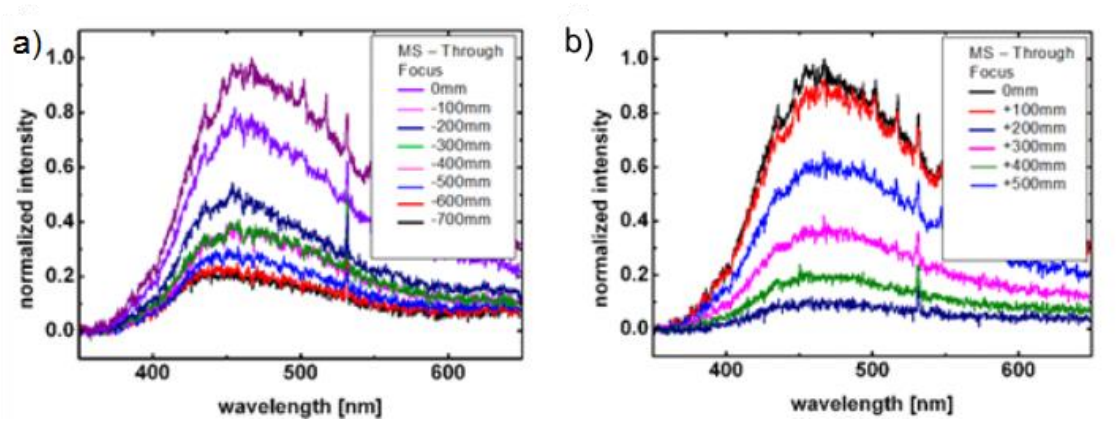

Figure 5-11 Signal measured for a through focus translation of MS-MGN; 0mm to -700mm (a) and 0mm to +500mm (b)

The background signal intensity followed the SHG and had the highest intensity in the focus of the fundamental beam and higher absolute intensity than SHG itself at ~450 nm.

SHG signal however was pronounced even for the out of focus positions (i.e. +500 µm). Signal spikes and noise along the whole bandwidth (seen especially in the focus position of the sample) could have been the effect of small incident fluence of the beam, hence smaller signals reaching the detector.

Secondly, another sample position variation was performed- in the flat sample plane. Results of translating the MS-MGN by 100 and 150 mm can be seen in Figure 5-12.

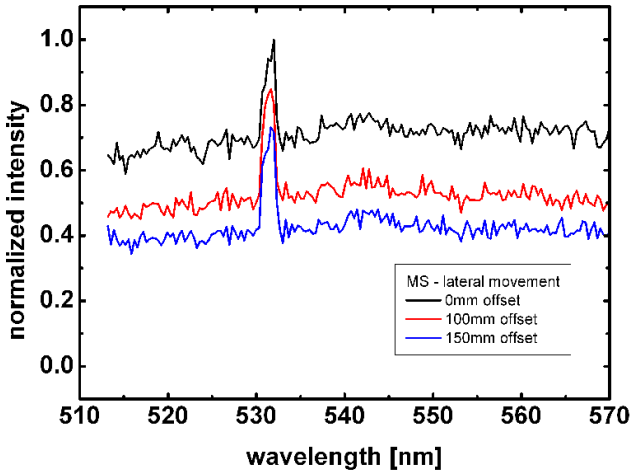

Figure 5-12 SHG signal obtained by translation of MGN along its surface plane

The signal shown there had decreased slightly as an effect of lateral translation of the sample. The explanation of this effect could lie in two mechanisms: 1) local changes in nanoparticle layer thickness formed in the MGN formation process (ion exchange). This effect could potentially be an underlying cause of the SHG signal change where in this particular example the first position (0 mm) resulted to be the thickest NPs layer part of the MGN (+150 mm translated signal for the thinner layer), 2) rotational misalignment of the sample leading to a small angle of incidence as well as a change of the fundamental laser spot on sample (lower fluence for the offset position).

A small angular misalignment (as in aforementioned ad. 2) was also introduced to the setup manually to a certain small degree ($<10^{o}$ fundamental laser incidence). This angular offset was distributed among 6 positions, where the signal was taken after the sample position was adjusted for the highest signal intensity (Figure 5-13).

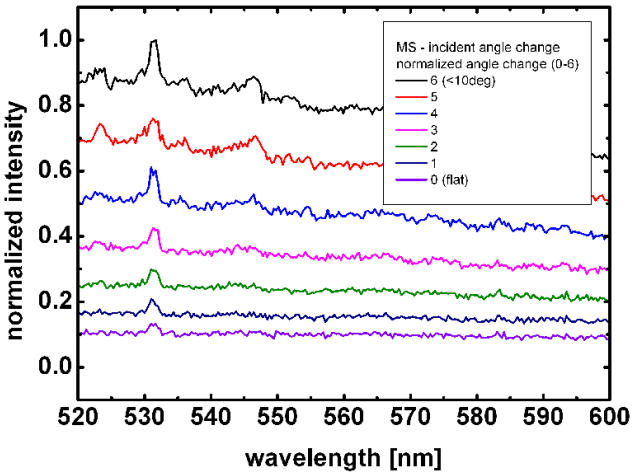

Figure 5-13 SHG signal obtained for MS-MGN for small angle of incidence variation ($<10^0$).

This experiment showed an increase in the signal while the sample had the highest rotational misalignment. This result was with agreement with what has been achieved with MS samples under fs- laser illumination [35]. There, the highest signals were shown to be realised for ~40^o laser incidence, where the optical path of the laser beam through the NPs layer was longer. A more thorough investigation of this property was performed at Darebsury Laboratory (thanks to Edward Snedden and Steve Jamison), where the laser setup used there was adjusted for precise angle of incidence measurement. A photomultiplier was used in transmission geometry where the 400 nm signal was captured. Collimated 800 nm beam was incident on the MS sample with ~1 mJ pulse energy and 50 fs pulse length. SHG intensity as a function of the incidence angle can be seen in Figure 5-14.

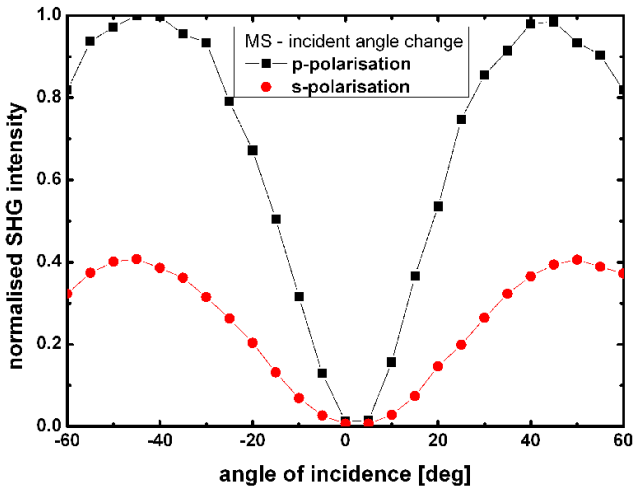

Figure 5-14 SHG intensity as a function of the incidence angle measured with a fs-pulsed laser and a MS-MGN

As mentioned previously, the highest intensity was achieved for ~40° angle. S-polarised signal was also measured and presented, which for a ps- pulsed setup was below the measurement ability- all further ps- measurements will therefore be performed at normal incidence.

5.4.2 MS MGN degradation under fundamental beam illumination

Additional measurements were performed in order to determine pulse energies for which the sample did not change its behaviour while being exposed to the fundamental beam. Experiments showing dependence of the signal intensity as a function of the laser pulse energy are important and delicate to perform therefore had to be accomplished in the energies regime where the experiment was stable or quasi-stable. Figure 5-15 shows how prolonged exposure to fundamental beam of certain fluence affected the resulting signal. In Figure 5-15 a) MS sample was illuminated with a laser beam corresponding to 2.83 mJ/cm^2 where the data was taken immediately and after ~1 minute of exposure. About 40% of the 450 nm peak intensity can be observed to be reduced and around 15% of the SHG peak intensity. The temporal behaviour of the 450 nm signal can be seen in Figure 5-15 b) where ~6 minutes of constant illumination at ~1.88 mJ/cm^2 is shown. It can be observed that a fast decline in the signal was present at the beginning, followed by stabilisation in a certain range. This effect was comparable for the whole spectral range of the resulting signal.

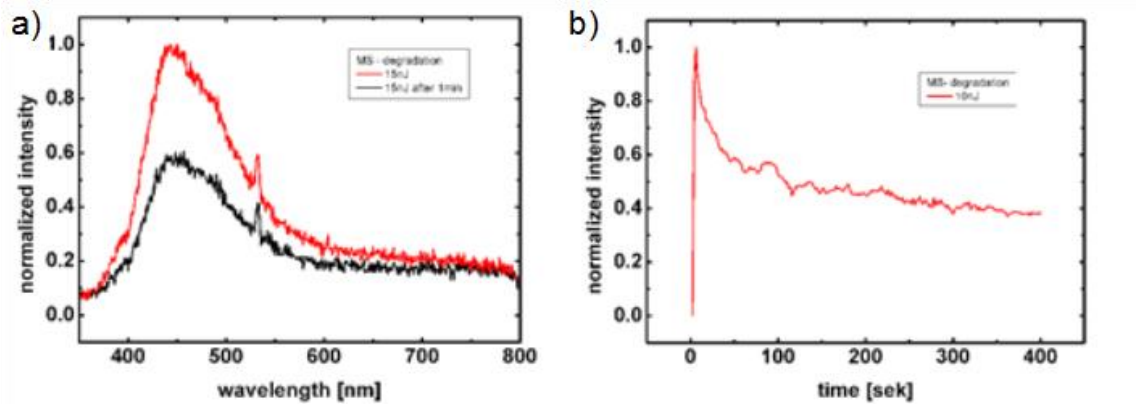

Figure 5-15 Degradation of MS signal after exposure to 2.83 mJ/cm^2 (a) and 1.88 mJ/cm^2

Smallest fluences used in this experiment, were in the range of 1.4 mJ/cm^2, but prolonged exposure also led to degradation. It was therefore concluded and measured that for small signal accumulations and short exposure times on the spectrometer (order of a few seconds) fundamental laser fluences lower than ~3.8 mJ/cm^2 could have been used- making the degradation not a significant issue and leaving a reasonable number of measurement points for experiments. Degradation then was not achieved, but the fluence range and measurement acquisition method made measurements reliable for further study. It has to be noted that different fluences value range can be expected for MGNs with a p-polarised SPR positioned further away from the fundamental beam wavelength, as the plasmon coupling was less pronounced.

5.4.3 Fundamental beam and output optical signal polarisation direction change effects

It was briefly discussed in the previous sub-chapter that the MS-MGN had a polarisation dependence on the SHG signal produced. It was shown that the highest SHG was achieved for the p-polarised fundamental beam and was diminished significantly when the polarisation direction was changed (Figure 5-9). Here, a more thorough experiment was performed in order to observe this effect. Fluences of ~3.77 mJ/cm^2 were used along with a reliable signal acquisition method. In the first experiment, the fundamental beam polarisation direction was rotated by 360^o and emitted signal from the MGN was recorded (Figure 5-16 c). SHG peaks were then integrated, and resulting signal plotted. Figure 5-16 a) shows how emitted signal changed with the input polarisation.

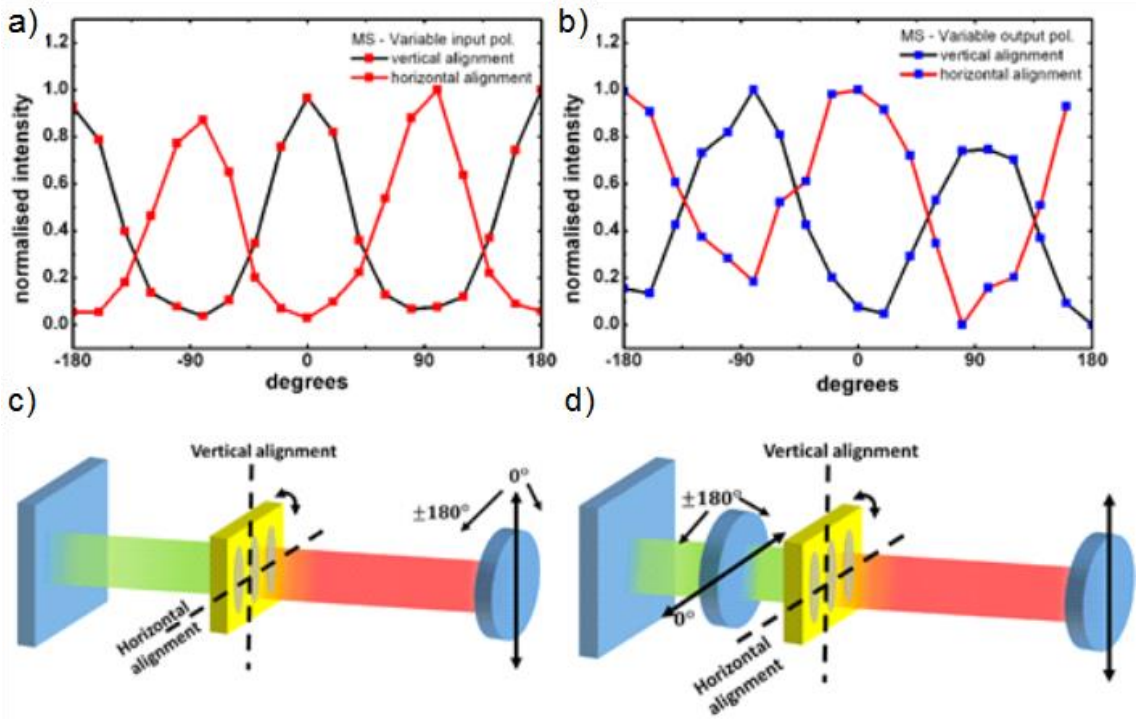

Figure 5-16 MS-MGN signal dependence on polarisation state of the fundamental beam (a) and p-polarised signal polarisation components measurements method (b).

The MS-MGN was then rotated by 90^o and the experiment was conducted again. It was observed from presented results that the SHG signal experienced high directionality and had the highest intensity when the fundamental polarisation direction was parallel to the long axis of nanoparticles (vertical alignment (VA) at 0^o, +/-180^o, and horizontal alignment (HA) at +/- 90^o). The lowest signal intensity appeared for illumination with fundamental polarisation perpendicular to the long axis of nanoparticles (VA at +/-90^o and HA at 0^o, +/-180^o). A second experiment (Figure 5-16 d) involved illumination of nanoparticles with p-polarisation of the fundamental beam and filtering the output signal with a variable polariser. The results achieved can be seen in Figure 5-16 b) where it is evident that the highest intensity SHG signal is experienced in the polarisation direction of the pump beam (VA at +/-90^o where this position represents the output polariser direction parallel to both the p-pol of the fundamental as well as to the long axis of nanoparticles). Sample was then rotated by 90^o and the experiment conducted again for p-polarised fundamental in order to exclude a possibility of any directionality induced by the experimental setup itself. Similar results were achieved - highest intensity for HA at 0^o, +/- 180^o which corresponded to polarisation component parallel to the long axis of nanoparticles as well as to the fundamental p-polarisation.

A second experiment was conducted and involved illumination of NPs with p- and s-polarised fundamental beam. Similarly to the previous experiment, one had to be certain that no directionality exists in the experimental setup itself and the only SHG signal was being obtained from nanoparticles. Extremely small signals were measured for input s-polarisation but measurable enough to show certain directionality as seen in Figure 5-17.

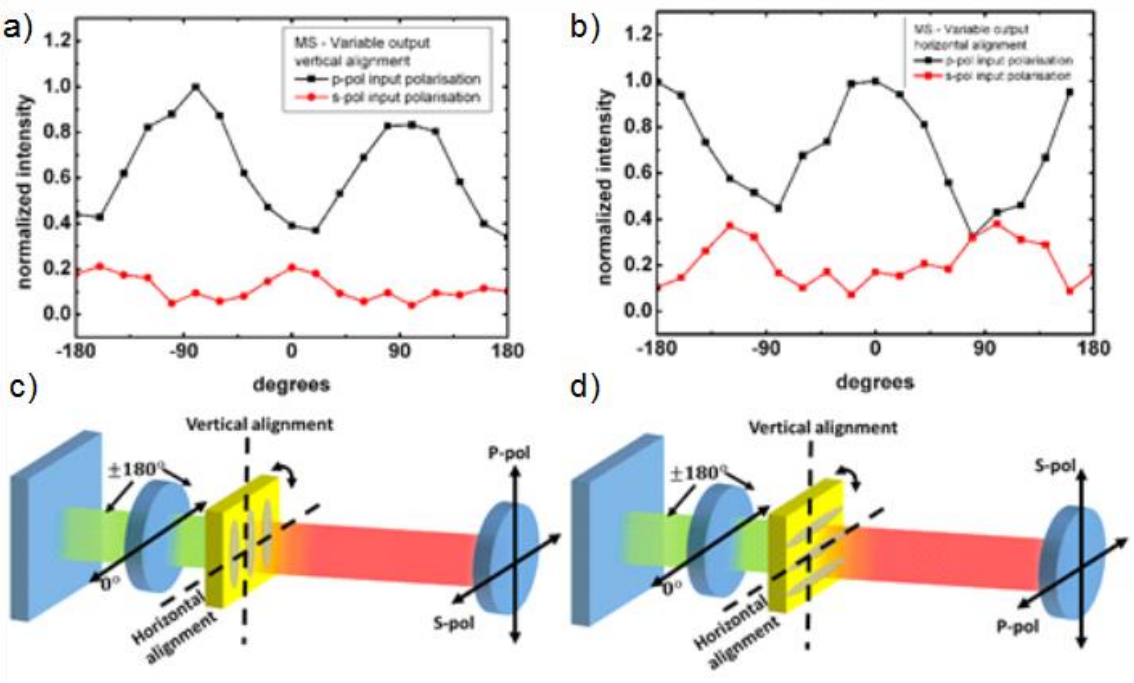

Figure 5-17 Variable output signal measuremetns of the MS-MGN. P- and s-polarisation fundamental beam was used for both VA (a) and HA (b).

Figure 5-17 a) shows VA for both p- and s-polarised fundamental beam. It can be seen that the highest signal follows the fundamental beam polarisation direction. Similarly for HA that is presented in Figure 5-17 b) the highest output signal intensities follow the input beam polarisation.

These three experiments showed very important MGN features. The SHG intensity was higher when plasmons coupled with the input beam the strongest. In the MS-MGN the p-polarised SPR peaked at ~900 nm and broadened across to 1064 nm with high extinction ratio. That caused the sample to not only be extremely delicate which led to degradation but also to experience high SHG signals. Rotating the sample, effectively, changed the SPR extinction band from ~900 nm to ~400 nm therefore lowering the coupling efficiency and the signal.

Second experiment showed the SHG signal polarisation components and how they changed with the incoming polarisation variation. It also showed that the SHG effect seen in the MGN was purely dipolar [179].

5.4.4 SHG signal intensity dependence on the laser pulse energy

An SHG experiment was performed that aimed at showing the dependence of the SHG signal on the pulse energy of the fundamental beam. According to the SHG theory, the optical intensity achieved from a nonlinear medium capable of SHG can be described with [188]:

$$I(2\omega) \sim \gamma * E^2(\omega) \qquad 5\text{-}1$$

where I(2ω) is the SHG optical intensity, $E^2(\omega)$ is the fundamental beam pulse energy and γ is a constant. It is therefore expected from MGNs SHG intensity to scale quadratically with the fundamental beam pulse energy. In order to see if this statement was correct, an experiment was performed in which MS-MGN was illuminated with varying pulse energies in range between 10 nJ to 20 nJ (which corresponds to fluences between 1.88 and 3.77 mJ/cm^2). Results were plotted on logarithmic scales and the resulting plot slopes were calculated by fitting a linear function. Figure 5-18 shows how the SHG intensity as a function of pulse energy. Linear fit showed slope of ~2.17 which was slightly higher than expected and could have been a result of the influence of the background signal seen below the SHG peak signal in the spectrally resolved images presented earlier. It is therefore possible that in Figure 5-18 it was shown both SHG and a higher order term, which influenced the signal intensity. It was shown that the broad background below the SHG has a peaked at ~450 nm which exceeded the SHG in intensity, therefore it could have been a result of a higher order process present in the MGN under 1064 nm illumination.

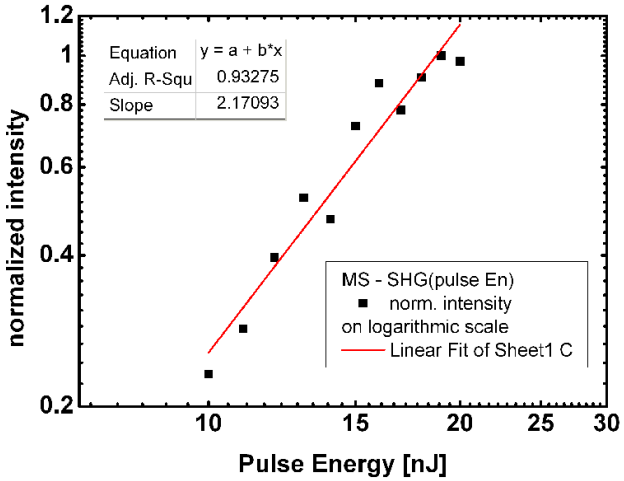

Figure 5-18 Log-log plot of SHG intensity as a function of fundamental laser pulse energy.

5.5 Laser reshaped nanoparticles (fs- and ps- pulsed irradiation)

After thorough investigation of MS-MGNs another set of samples was examined: ps-reshaped MGNs (with 100-1000 number of pulses per spot) and fs-reshaped MGNs (FEMA, FEMB, FEMC, FEMD). These samples were described in more detail earlier in this chapter. Three experiments were performed on these MGNs. First, with the aim of describing the degradation of nanoparticles under 1064 nm illumination (knowing that the p-polarised SPR extinction is spectrally placed within shorter wavelengths). Second, with a goal of showing polarisation components of such reshaped nanoparticles and third showing dependence of the SHG intensity on laser pulse energies.

5.5.1 Ps- and fs- reshaped MGNs degradation under fundamental beam illumination

It was shown in the previous sub-chapter how the MS-MGN degraded within a certain range of fluences. Hence, it was difficult to measure SHG signals precisely with long exposure times. In order to induce less or no degradation at all the fundamental beam focusing lens was changed giving a spot size on sample of ~64 μm (at $1/e^2$). This alternated setup was used for the rest of the thesis. Degradation was measured for MS-

MGN again for comparison purposes (Figure 5-19). A p-polarised fundamental beam was used.

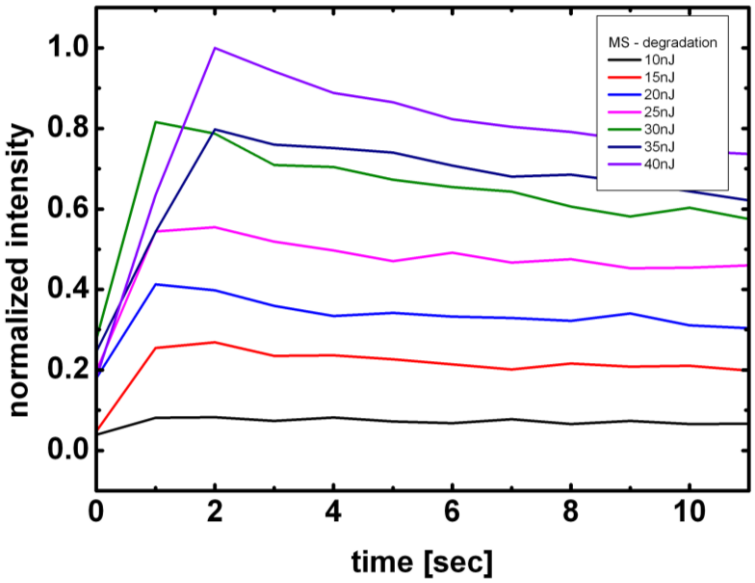

Figure 5-19 MS-MGN SHG signal degradation experiment for setup with focusing lens changed.

Fluences between 0.31 mJ/cm^2 and 1.24 mJ/cm^2 were used. It can be seen that degradation of signal started at ~1 mJ/cm^2 (30 nJ) and was less significant than the degradation shown for previous fluences (~3.5 mJ/cm^2).

Ps-reshaped MGN was also measured for degradation and can be seen in Figure 5-20. Sample irradiated with 1000 pulses per spot was placed under 1064 nm illumination. Fluences between 0.93 mJ/cm^2 and 1.71 mJ/cm^2 were used (30 – 55 nJ). It was observed that the degradation threshold was placed at around 1.71 mJ/cm^2 (55 nJ), which was around 0.8 mJ/cm^2 higher than that measured for MS MGN. Such big difference could be explained by the effect of plasmon coupling to p-polarised plasmon bands. Where the sample measured for 1000 pulses per spot irradiation had its p-polarised SPR extinction placed spectrally at ~ 650 nm (in comparison to MS MGN where it was ~ 900 nm). Smaller plasmon coupling was then expected and measured.

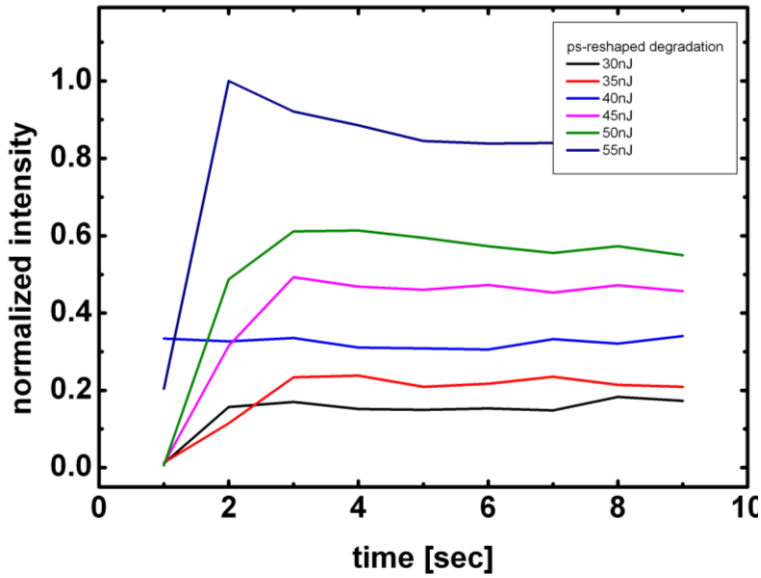

Figure 5-20 ps-MGN SHG signal degradation experiment

Also, degradation for fs- reshaped sample was measured. FEMD degradation can be seen in Figure 5-21. Fluences used here were between 0.62 mJ/cm^2 and 1.87 mJ/cm^2 (20 – 60 nJ). It can be seen that for laser fluence of 1.24 mJ/cm^2 degradation threshold was reached, which means that it lies between the MS MGN and ps MGN thresholds. The FEMD SPR p-polarised extinction band lies spectrally at ~ 800 nm which explains better plasmon coupling between NPs and the fundamental beam for this sample.

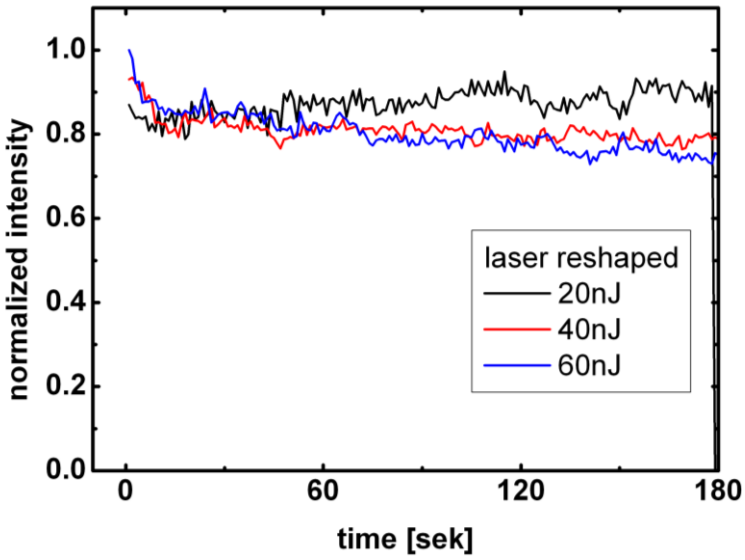

Figure 5-21 FEMD SHG signal degradation experiment

It has to be noted that even though the degradation thresholds were measured as a function of time, measurements with fluences slightly above those thresholds but with short exposure times can be also done with good reliability. Also, a possibility exists of making measurements for slightly higher laser fluences for longer than ~20 sec exposure times, as the signal stabilised by then in both ps-, fs- and MS MGN samples. In this thesis however it was chosen throughout all experiments to perform short exposure measurements of the order of <5 sec for consistent and systematic results.

It is important to say that MS MGN was much more sensitive to degradation therefore only lower pulse energies could be used for measurements - typically between 10 and 20 nJ. For laser reshaped samples, however, such low pulse energies would result in much smaller signals, and even not recognizable from background therefore much higher values needed to be used- typically between 30 and 80 nJ.

5.5.2 Fundamental beam and output optical signal polarisation direction change effects

It was shown in the previous sub-chapter how the SHG signal changed when variation of input beam polarisation direction existed. It was shown that the highest intensity signal was produced when the input polarisation direction was parallel to the long axis of the mechanically stretched nanoparticles. Also, a similar effect was shown when nanoparticles were illuminated with a p-polarised fundamental beam and the output polariser direction was varied.

Here, fs- and ps- reshaped nanoparticles were observed under the same circumstances for comparison purposes as the origin of elongation was quite different for both techniques. Figure 5-22 shows results of experiments performed for variable input polarisation (Figure 5-22 (a) and c) and variable output polarisation (Figure 5-22 (b) and d)- 1000 pulses per spot MGN.

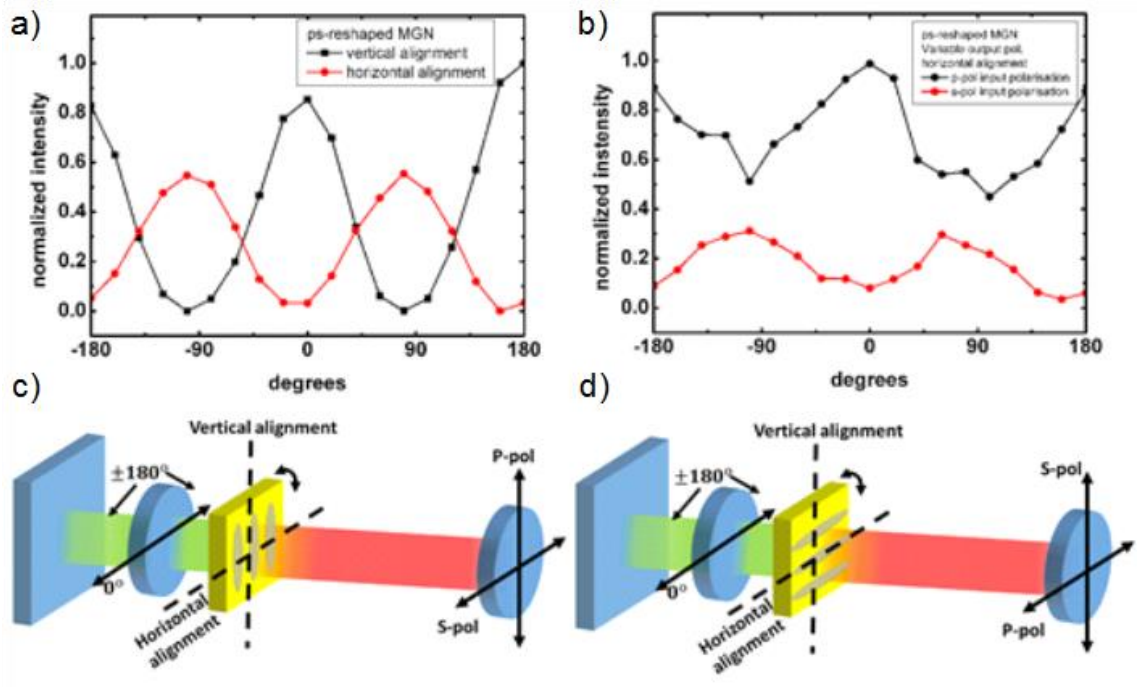

Figure 5-22 ps-MGN experimental results on SHG signal intensity as a function of the input polarisation variation (a) and output polarisation variation (b)

It can be observed there that nanoparticles reshaped with a ps- pulses show the very same behaviour as MS-MGNs. The highest SHG signal was obtained when illuminating with the polarisation direction parallel to the long axis of nanoparticles, and output signals parallel to the input beam polarisation direction.

Figure 5-23 shows the same experiment performed on fs-reshaped nanoparticles (FEMD). It can be seen there that similar effect as to MS MGNs and ps- reshaped MGNs was measured. The very same observation was obtained for other fs- and ps-reshaped samples.

A conclusion can be made that the method of producing MGNs does not induce a significant difference in emitted SHG signal or its polarisation components. Also, all of the measured samples showed the same behaviour of emitting highest SHG signal when the fundamental wavelength was coupled the most to the p-polarised plasmon, which was also the very explanation of this effect.

It is a well-known fact, that during short-pulse reshaping of nanoparticles small Ag^+ ions are captured in the colour centres in the vicinity of the nanoparticle (Chapter 2). It is however not evident that this particular fact has any effect on polarisation sensitivity for all types of reshaped MGNs.

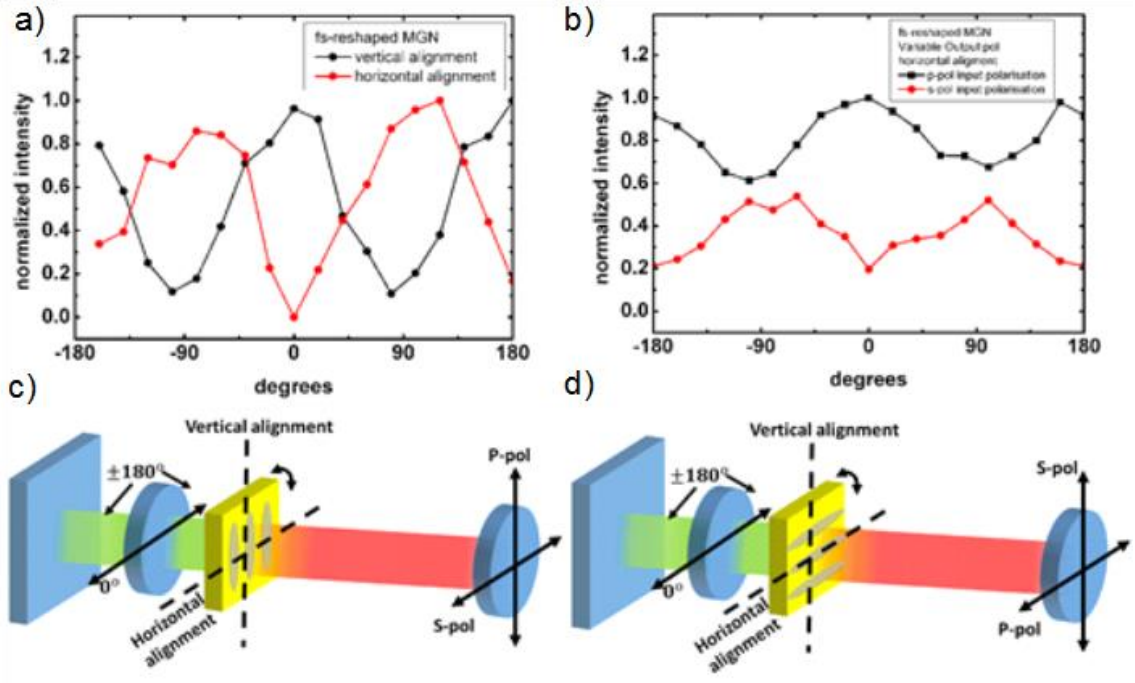

Figure 5-23 FEMD experimental results on SHG signal intensity as a function of (a) input polarisation variation and (b) output polarisation variation

5.5.3 SHG signal intensity dependence on laser pulse energy.

In order to determine how a change of the MGN reshaping process as well as the spectral position of the p-polarised SPR peak influenced the character of the emitted signal, the dependence on the input pulse energy on the emitted signal was determined. Figure 5-24 presents results for ps-reshaped MGN for pulses per spot used during reshaping of 100, 200, 300, 400, 500, 600, 700, 800, 900 and 1000. Pulse energies used here were between 30 and 80 nJ (corresponding to 0.93 mJ/cm^2 to 2.49 mJ/cm^2).

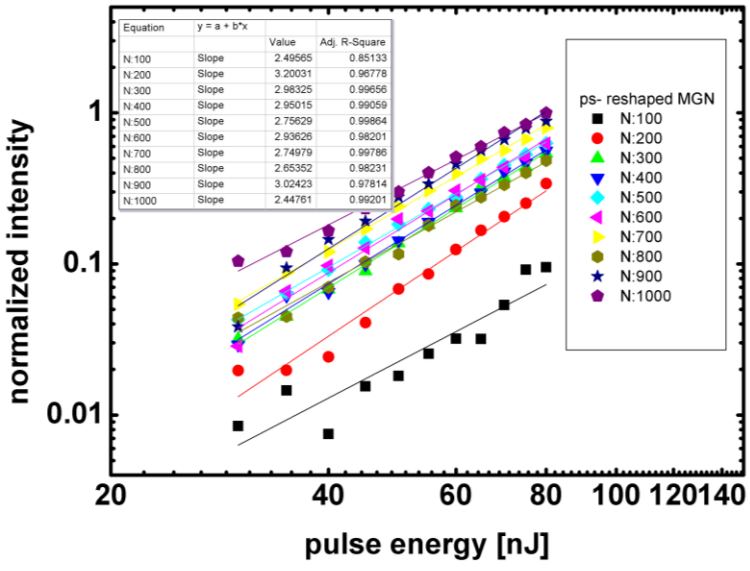

Figure 5-24 Log-log measurements of ps-MGNs SHG intensity as a function of fundamental pulse energy

It was explained in the previous sub-chapter that an increase of pulses per spot fired on the sample increased the spectral gap distance between the s- and p-polarised SPR bands. Effectively, the increase in pulses fired moved the p-polarised SPR further towards the longer wavelength range. It can be seen from the figure that not only higher number of pulses per spot samples resulted in higher intensity signal but also with a lower slope of the fitted linear function (Figure 5-25).

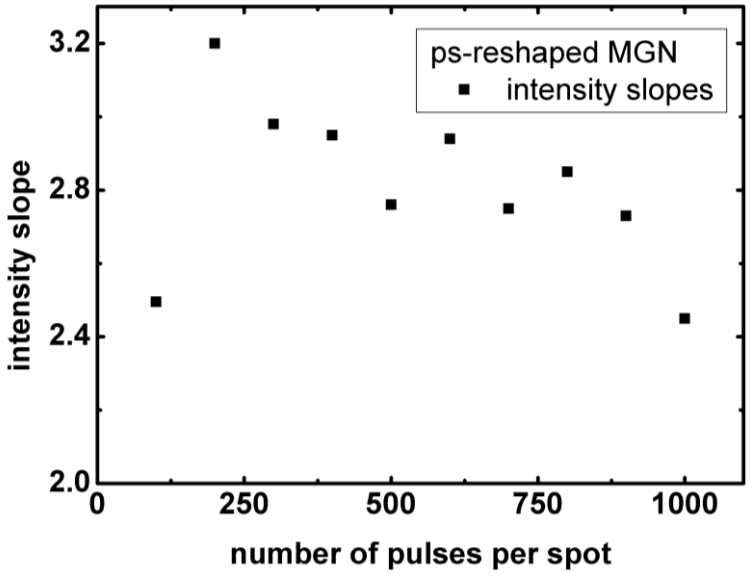

Figure 5-25 Fitted linear slope values as a function of number of pulses per spot fired on the ps- MGN

It was observed that apart from the sample irradiated with 100 pulses per spot, a trend could be seen of a decrease in slope from ~3.2 to ~2.4 as the number of pulses per spot was increased. Slopes in this range could mean that a higher order process was also observed. However, the increase of the plasmon coupling (by moving the p-polarised SPR band spectrally closer to the fundamental beam wavelength) produced a more pronounced second-order process. This effect will be investigated in a later part of this chapter as the increase of slope to ~3 may indicate a third-order process (Third Harmonic Generation or Three Photon Induced Luminescence) originating in the broad background signal seen along the SHG peak, and therefore luminescence investigation will be required.

Fs-reshaped MGNs were also measured with the same experimental environment as the ps-reshaped MGNs. Results plotted on logarithmic graphs can be seen in Figure 5-26.

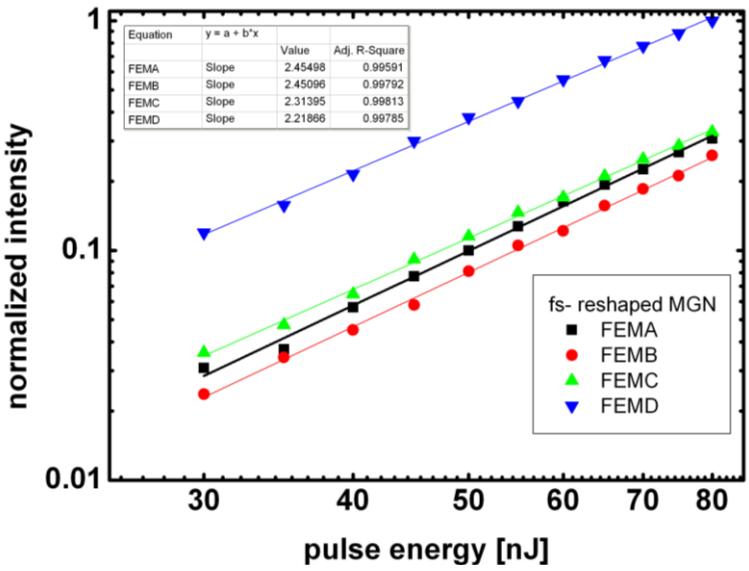

Figure 5-26 Log-log measurements of fs-MGNs SHG intensity as a function of fundamental pulse energy

Similarly to the previous experiment, a decrease in slope values could be observed between FEMA and FEMD. Also, a higher intensity signal was seen when the plasmon coupling was higher. Slopes plotted on a linear scale can be seen in Figure 5-27. Change in slopes varies between ~2.4 and ~2.2 with a decreasing trend towards FEMD sample.

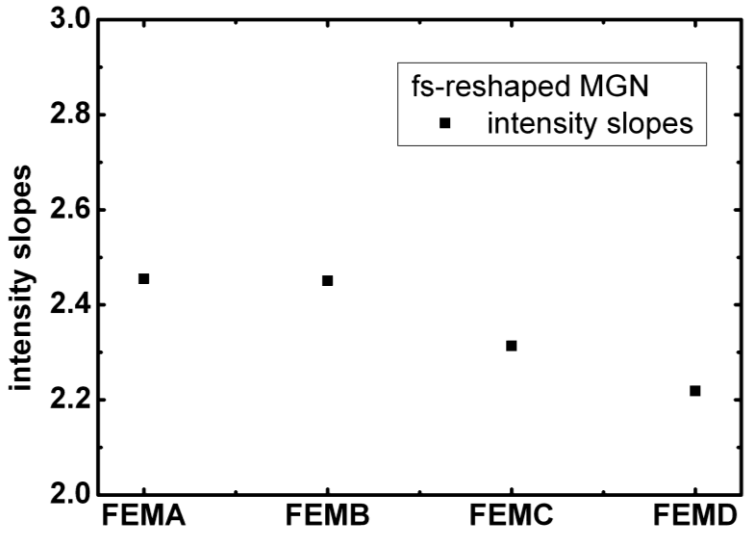

Figure 5-27 Fitted linear slope values as a function of number of pulses per spot fired on the fs- MGN

These results indicate that for fs-reshaped samples a second-order process is more pronounced in comparison to the ps-reshaped MGNs. It has to be noted that ps- MGNs' p-polarised SPR was spectrally placed between FEMC and FEMD. It is therefore evident that the close spectral position of the p-polarised SPR to the fundamental beam

wavelength (as a direct indicator of the plasmon coupling strength) does not have an absolute effect of diminishing the third-order process being present in the sample under illumination. A local effect however is present and its strength depends on the type of reshaped nanoparticles.

5.6 Luminescence study

It was discovered in the previous sub-chapter that on illumination of MGNs with a 1064 nm laser beam (ps-pulsed) SH is generated. It was also observed that for reshaped MGNs a broad background signal appears on top of the SHG. A measurement was performed to determine the SHG dependence on the input laser pulse energy which resulted in intensity slope values of between ~2 and ~3 indicating a third order process taking place- especially for ps-reshaped nanoparticles. In order to determine the origin and characteristics of the background signal a luminescence study was performed. The SHG setup was modified so that a 532 nm incoming laser beam could be used to illuminate samples. A 100 mm focusing lens was used to focus the 532 nm beam onto the sample, which resulted in a ~16 μm spot size on the sample. A 532 nm notch filter was used after the sample in order to filter out the input beam intensity.

Various samples were used:

1) Single and double layer Ag^+ ion glass
2) Single and double layer spherical NPs glass
3) Pure soda-lime glass
4) MS MGN

MS-MGN was used for luminescence measurements from the available reshaped nanoparticle samples. It was thought that it would represent pure elongation of nanoparticles (it was described earlier that laser reshaping produces various Ag species in the vicinity of the nanoparticle), with no additional effects involved. Also, fs-reshaped nanoparticles had been measured in terms of their luminescence in [138].

None of the samples were input polarisation direction sensitive apart from the MS-MGN, hence all samples were illuminated with a p-polarised polarisation direction. A polariser was placed at the output and the experiment was performed for two directions of polarisation (p- and s- polarisation). The luminescence achieved from these samples can be seen in Figure 5-28.

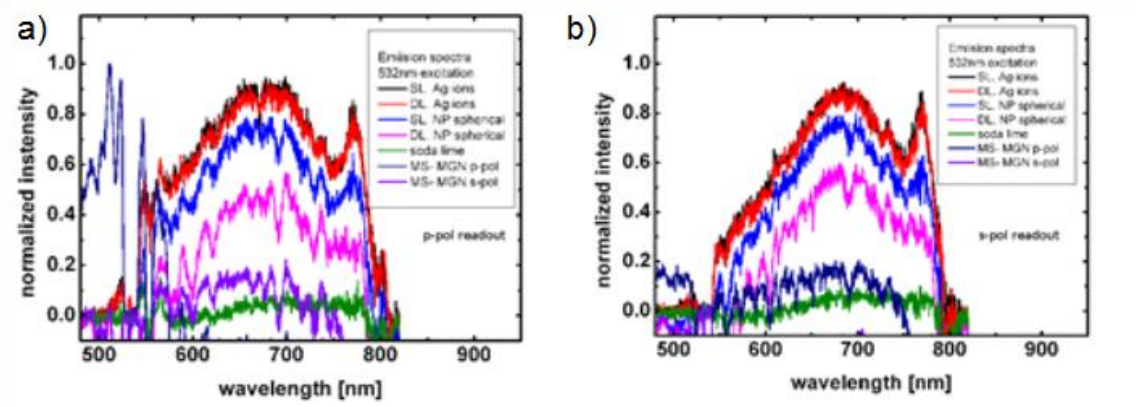

Figure 5-28 Luminescence spectral measurments. Readout polarisation direction was p- (a) and s- (b).

A pulse energy of 24 nJ was used for illumination. Luminescence spectra could be divided into three main peak intensities: ~500 nm, ~650 nm and ~780 nm. It was discovered however that the 780 nm peak was induced in one of the elements of the setup and could not have been corrected for (therefore not relevant for this study). In Figure 5-28 (b), s-polarisation readout, all of the samples show the ~ 650 nm peak, whereas in (a) - p-polarisation readout, the MS-MGN does not show this luminescence peak. It had however a pronounced peak located at ~500 nm (the only sample in this experiment). Highest luminescence intensity (described for peak at ~650 nm) was achieved for single and double layer Ag^+ ion glass, second highest intensity was achieved with single and double layer spherical NPs glass. The smallest intensity was observed with a pure soda-lime glass.

It can be seen in Figure 5-28 (a) that the ~500 nm peak for MS-MGN is the most pronounced even though the pump wavelength was 532 nm. It was therefore evident that a higher order process was a possible mechanism and may have originated from THG (355 nm when illuminating with 1064 nm- SHG here). Also, the short wavelength part of the slope of the 650 nm peak had its wings starting at ~500 nm which is also below the pump wavelength. This could have been a result of some nearby states being excited by 532 nm, which required a higher energy (this could be originated through non-radiative transitions).

Dependence of the luminescence signal on the laser pulse energy was also measured, and can be seen in Figure 5-29.

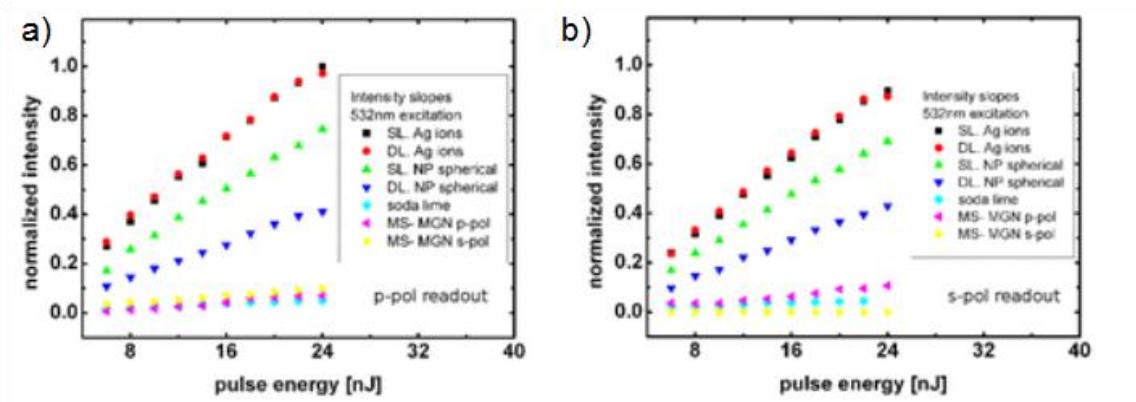

Figure 5-29 Integrated luminescence intensity as a function of pump pulse energy for two readout polarisations p- (a) and s- (b).

Laser pulse energies of 6 – 24 nJ were used which resulted in a linear behaviour of the induced integrated signal (this corresponds to fluences in the range of 3.00 – 11.94 mJ/cm^2). Here, slopes were not calculated but in this experiment they represent the rate of increase of the signal, which was discussed earlier and behaves in the same way as seen in Figure 5-28.

It can be concluded that single Ag ions influenced the luminescence from samples the most, and also that spherical nanoparticles played a significant role. Glass by itself did not show any noteworthy luminescence, similarly to MS-MGN in the ~650 nm band. MS-MGN however showed intense luminescence <532 nm, which was polarised along the long axis of the nanoparticles and may have been a result of non-radiative transition in the energetical vicinity of the NP's excited state.

More work is required in the future in order to determine the exact energetical structure of the sample along with all the radiative and non-radiative transitions present. Preferably a tuneable laser source would be required operating in <500 nm regions. Also, a different experimental setup would be recommended for future work in order to filter out only the pump source wavelengths (here bandpass mirrors were used that passed only light between 400 and 800 nm).

5.7 Multiphoton-Absorption-Induced Luminescence (MAIL) and SHG in elongated Ag nanoparticles in glass

It was shown earlier in this chapter that additionally to the SHG signal present in reshaped nanoparticles illuminated with 1064 nm laser beam, a broad band exists. Here, a proposed explanation of the band will be shown by both experimental work as well as simulated with DDA calculation method (introduced in the previous chapter). Previous experiments showed two main effects present in samples:

1) Increase in elongation ratio (shown as a relative position of the p-polarised SPR extinction spectrum) decreased the slope intensity, reaching value ~2 for MS MGNs where the elongation was the highest.
2) Laser reshaped nanoparticles showed higher than expected intensity slopes, with a higher values approached by ps- reshaping process.

It can be concluded that higher order processes arised in MGNs, especially in the laser reshaped MGNs. It could have been a result of colour centres and Ag^+ ion formation in the vicinity of the nanoparticle. Luminescence studies definitely showed the highest luminescence band formed at ~650 nm for samples of soda-lime glass filled with Ag ions. Mechanically stretched samples however showed a polarisation dependent luminescence band at <500 nm, which could be a result of a different (but also higher order) process. It was also established that the higher the elongation of NPs, the less of the higher order processes could be seen due to the fact that the intensity slope became smaller and closer to what was expected of a second order originated SHG. An effect described in the literature as a Multiphoton-Absorption-Induced Luminescence (MAIL) is proposed as a reason of broad luminescence bands formation [181], [189], [190]. This process originates from absorption and recombination of electrons in the sp-band with holes in the d-band [191].

Spectrally resolved images of each of the samples were taken for 1064 nm beam illumination. A p-polarised input beam was used, no polariser was present at the output. MS MGN emission spectra can be seen in Figure 5-30.

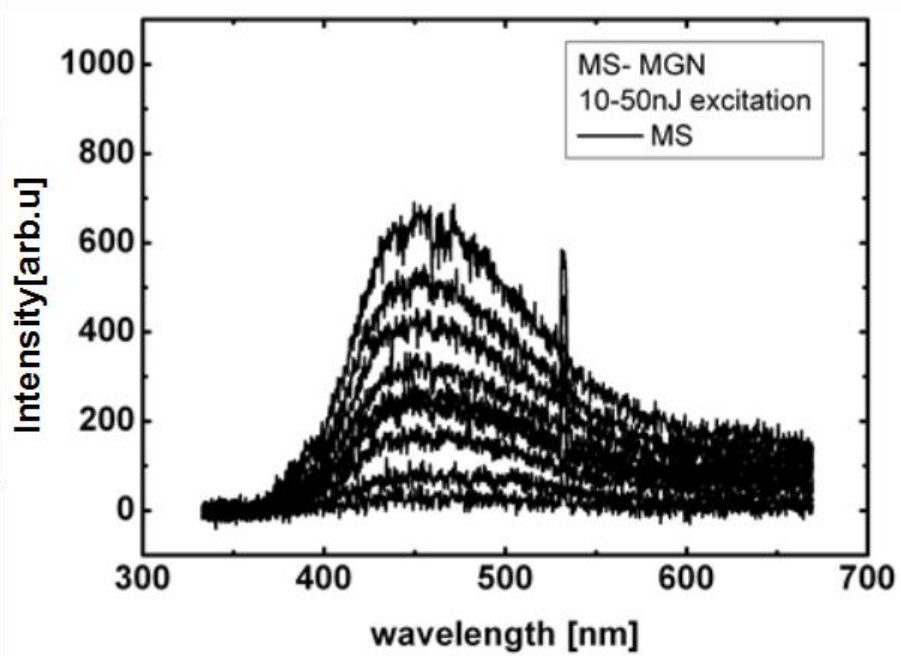

Figure 5-30 Spectrally resolved signal obtained from MS-MGN. Evolution of signal as a function of fundamental pulse energy is shown

Pulse energies between 10 nJ and 50 nJ were used (for reasons explained earlier in this chapter). It has to be noted that slightly higher pulse energies were also used for further comparison purposes with other MGNs less prone to degradation. A band that formed at ~450 nm was observed along with a pronounced SHG peak at 532 nm.

Fs-reshaped MGNs were measured in the same experimental setup (Figure 5-31).

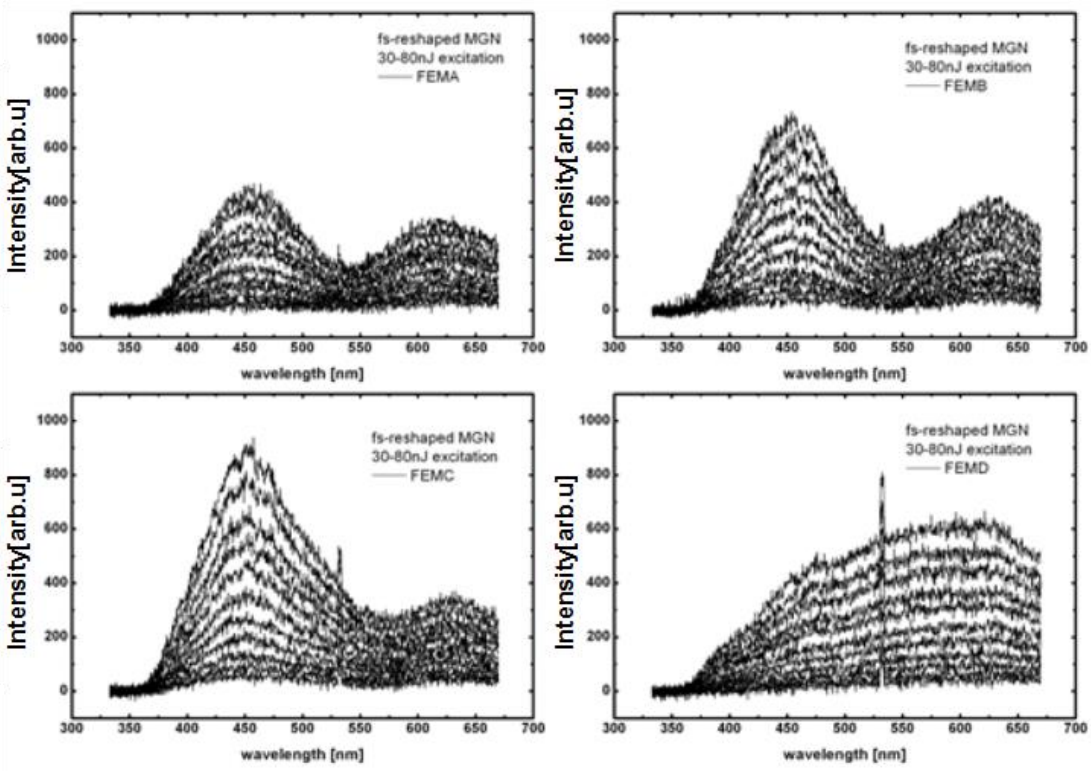

Figure 5-31 Spectrally resolved signal obtained from fs-MGN. Evolution of signal as a function of fundamental pulse energy is shown

Pulse energies between 30 nJ and 80 nJ were used. It can be observed that along the SHG peak, two additional bands appear. First at ~450 nm and the second at ~650 nm. It can be also seen in the figure that spectral distribution of these bands are dependent on the type of the reshaping

Also, ps-reshaped nanoparticles have been observed under illumination of the fundamental beam and the results can be seen in Figure 5-32. In these type of reshaped nanoparticles only the ~650 nm band could be seen. Also, the increase of number of pulses per spot fired during the reshaping had a significant effect on the size of this band (increasing with it).

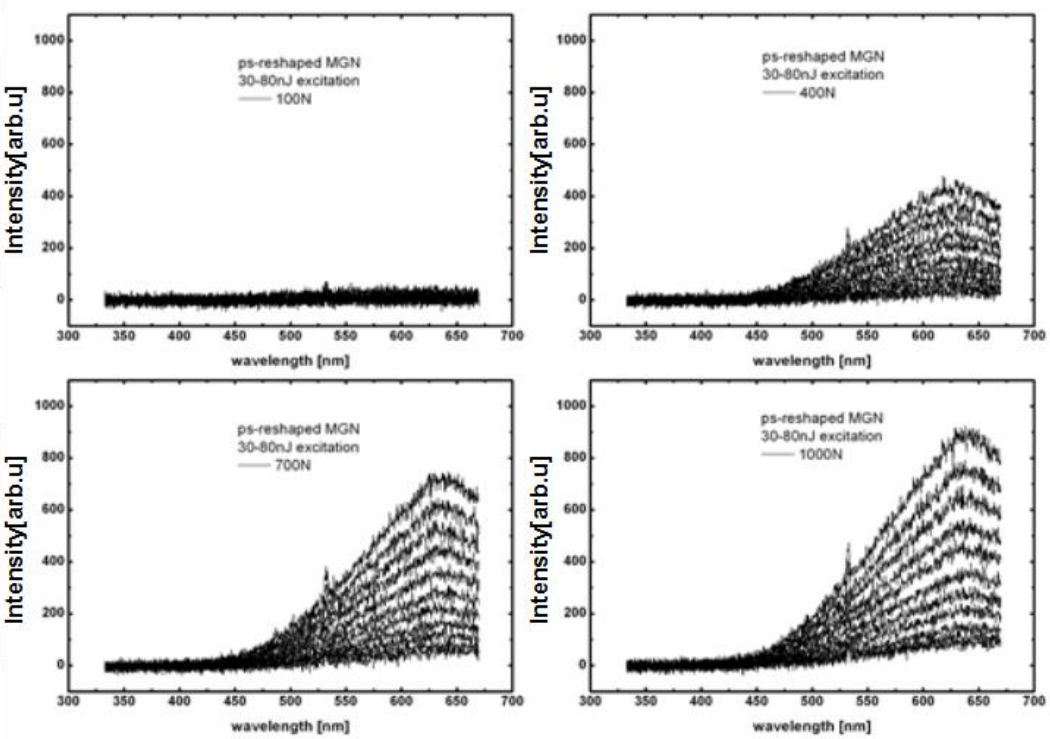

Figure 5-32 Spectrally resolved signal obtained from ps-MGN. Evolution of signal as a function of fundamental pulse energy is shown

A comparison between all of the samples used for experimentation in this chapter can be seen in Figure 5-33. Normalized intensity spectra can be seen in the figure, which were produced by illuminating samples with 50 nJ of pulse energy.

A MAIL process was proposed as an explanation of higher order processes that were present when illuminating MGNs with 1064 nm beam. It can be noticed in Figure 5-33 that for smaller elongation rations in FEMA-D, two peaks of MAIL were present: ~450 nm and ~650 nm. The blue peak in FEMA-C was growing in intensity much more than the orange peak. However in FEMD (where double irradiation was performed leading to higher elongation of nanoparticles), blue peak vanished leaving only the orange peak as the dominant. Because of the short wavelength side slope of this peak vanishing slowly it can be concluded that the blue band is still present in this sample but has very little intensity. Ps-reshaped samples showed however only the orange band which peaked sharply leading to a conclusion that no involvement from the blue band peak was present for these type of samples. For MS sample, the 450 nm band peak was the most pronounced.

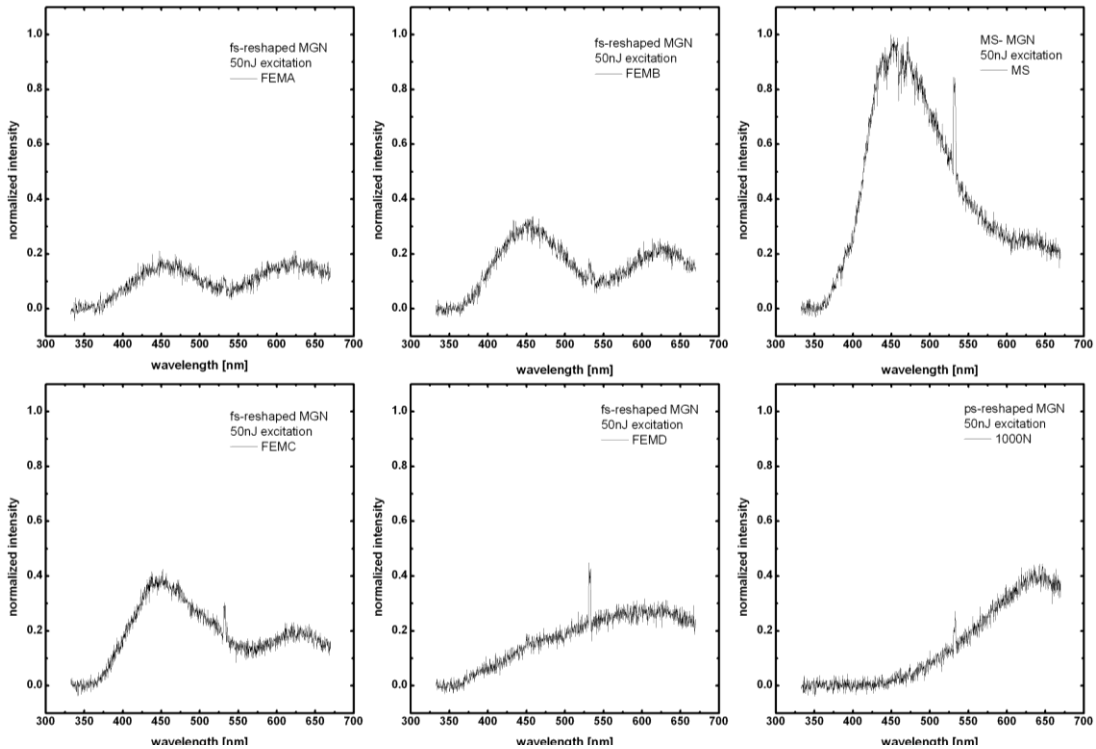

Figure 5-33 Comparison between spectrally resolved signal obtained from fs-, ps- and MS-MGN. 50 nJ pulse enrgy was used for all measurements

The MAIL peak at around 625 nm was believed to be attributed to the formation of small ion species (Ag_2^+, Ag_2^{2+}, Ag_3^+ and Ag_3^{2+}) in the vicinity of the reshaped nanoparticle and their involvement in radiative transition [138]. From observation of types of samples having this most intense band, it was established that laser reshaping was the main cause for these species to appear. It is a well-known fact that this process happens and it was described in more detail in previous chapter. Because of the fact that ps- reshaped samples show a more intense 650 nm band, the longer laser pulse may have effect on promoting a higher rate of formation of this species. Luminescence experiments presented earlier proved these statements. Also, enhancement of fluorescence of various molecules in the vicinity of metallic nanoparticles has been reported in research journals [192]–[194].

A multi-pulse irradiation of nanoparticles caused a Coulomb explosion of a nanoparticle which effectively left a ‘halo’ of silver ions a few nanometres around the nanoparticle (this was described in previous chapters). Small silver species responsible for the orange peak must have been formed by clustering and partial reduction of Ag ions produced during the reshaping process. Growth of the 625 nm band along with the increase of number of pulses per spot used, that can be observed both in fs- as well as in ps-

reshaped samples, showed this effect as increase of pulses fired increased the ‘halo’ effect.

MS- MGN, while having the highest elongation ratio of NPs, did not exhibit an orange band, because the mechanism of formation of nano-ellipsoids did not involve laser irradiation therefore formation of Ag species. The MAIL band that peaked at ~450 nm could be attributed to the presence of small Ag ions of lower concentration in the volume of the sample, formed during the ion-exchange process [195], [196]. It was observed that the laser reshaped samples showed diminished blue band (FEMA-D) or did not show it at all (ps-reshaped MGNs). This effect could be explained by the fact that by applying an increased number of pulses per spot during irradiation, destruction of small Ag ions occurred in the volume of the sample by heat accumulation, hence blue band vanished. For FEMA-C samples, firing small number of pulses per spot initiated the reshaping process and enhanced the luminescence in the blue band by local field enhancement (which was greater for ellipsoids than for spheres), while not accumulating enough heat for the small Ag ions dissolution. Within a picosecond regime of reshaping even a few pulses per spot (e.g. 100) accumulated heat to levels high enough for dissolution of aforementioned ions.

Also, the 450 nm band could be attributed to THG at 355 nm, which was reabsorbed by small species formed during making process of samples.

Explanation of the MAIL effect involvement on the intensity slopes measured in samples and showed in previous figures, can be explained by the origin of MAIL. This effect involved absorption of the excitation photon and reemission in a radiative transition. SHG however involved a virtual state energy transition instead of a real state energy transition. SHG, by contrast to MAIL was not a process involving absorption of photons. Instead, an intense laser field induces a second-order polarisation wave resulting in coherent light wave in exactly twice the incident frequency. It was shown that this difference in nonlinear responses was caused by the ratio of scattering to absorption cross-sections from nanoparticles as proposed by Deng et al. [181]. In order to prove that this effect took place in our samples, Discrete Dipole Approximation (DDA) simulations have been performed for elongation ratios present in measured samples.

First, all elongation ratios had to be related to the DDA calculations. For this reason simulations of extinction spectra were performed and p-polarised SPR peaks were spectrally matched with aspect ratios of nanoparticles (Figure 5-34 and Figure 5-35).

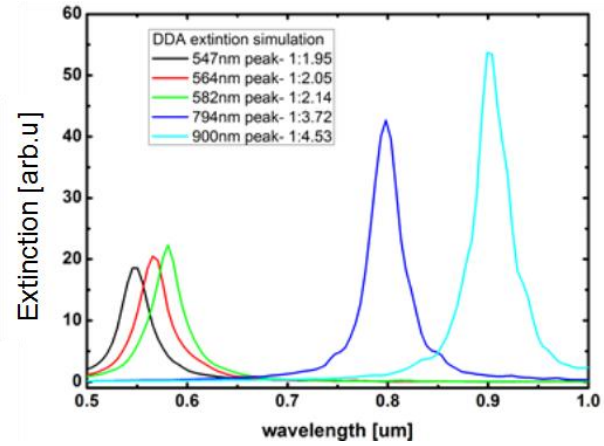

Figure 5-34 p-pol DDA simulations of extinction cross section for silver nano ellipsoids embedded in soda-lime glass

DDA parameters were chosen to match exactly the centre peaks of the real p-polarised extinction spectra that were measured.

Ps- MGNs elongation ratios were calculated from fitting p-pol extinction peaks to the elongation ratio as a function of extinction peak position, also, to match the measured value.

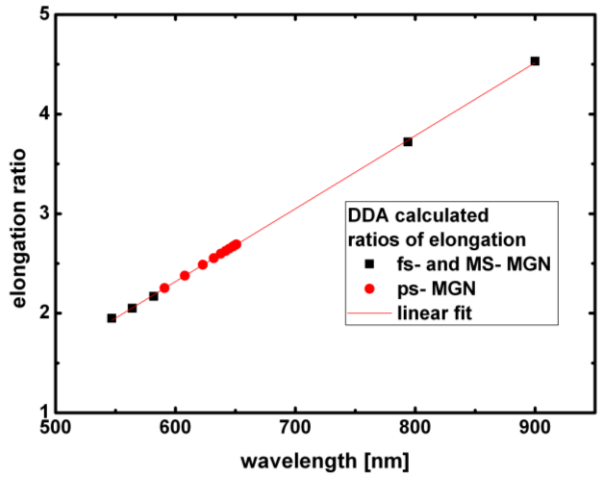

Figure 5-35 linear fit to elongation ratio calculated with DDA as a function of p-pol extinction position

DDA simulation was set for a spherical nanoparticle of silver in a soda-lime environment. Then, the ratio between axes was changed to achieve the desired p-polarised peaks. The number of dipoles used in simulations was ~300k. Because of the

hardware capability constraints resulting in lengthy simulation times, a number of elongation ratios were excluded (100-900 number pulses per spot in ps- reshaping). Simulated sample parameters can be seen in Table 2

	p-polarised extinction peak position [nm]	**Elongation ratio calculated with DDA**
FEMA	547	1.95
FEMB	564	2.05
FEMC	582	2.17
FEMD	794	3.72
1000N (ps-MGN)	651	2.70
MS-MGN	900	4.53

Table 2 Measured p-pol extinction peak positions along with simulated elongation ratios

It was concluded that three main wavelengths were the main contributors to effects seen in samples. These were:

1) 1064 nm- fundamental beam wavelength. This was the prime wavelength with which nanoparticles interacted, and according to the hypothesis presented, when scattered were leading to SHG and when absorbed to MAIL.

2) 532 nm – SH of the fundamental beam. This wavelength similarly to 1064 nm could have not only be created but also re-absorbed by various Ag species and emitted in form of MAIL

3) 355 nm – TH of the fundamental beam. It was possible for these type of samples to create the TH and reabsorb it creating the 450 nm TAIL peak (Three-photon-Absorption-Induced Luminescence).

For these three wavelengths the simulation was performed and parameters measured: absorption, scattering, extinction and abs/scat ratio. In DDA, the wavelength choice corresponded to the ability of the measured structure to either absorb this wavelength, scatter or extinct it, therefore it would have simulated the effect of illumination with this particular wavelengths or their reabsorption.

DDA simulation for 1064 nm can be seen in Figure 5-36.

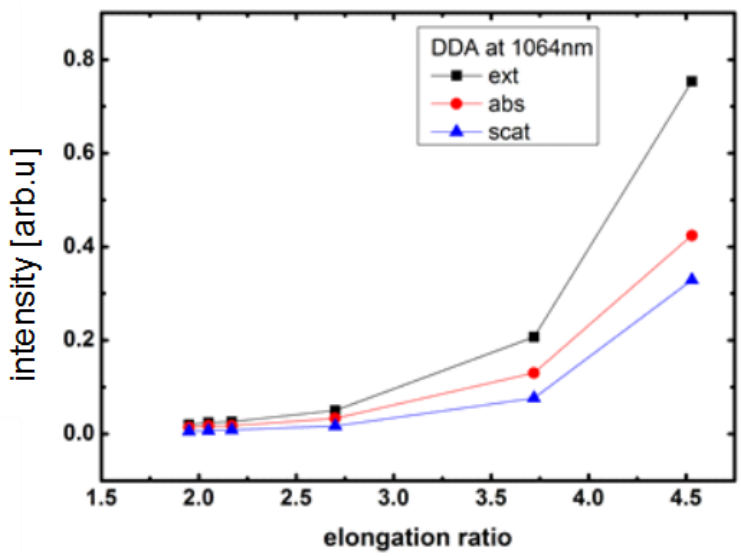

Figure 5-36 DDA simulation of extinction, absorption and scattering cross sections as a function of nanoparticle elongation ratio – for 1064 nm.

It was observed (as expected) that the extinction increased along with the elongation ratio of nanoparticles. Absorption was more intense than scattering and both were increasing in the same manner as their extinction.

DDA simulation for 532 nm was performed and is seen in Figure 5-37. All parameters behaved in the opposite way to the previous wavelength- decrease along with the elongation ratio can be observed. This effect was also expected as it was known that when the elongation ratio increased it spectrally moved the p-polarised extinction band to longer wavelengths, therefore decreasing the plasmon coupling with the incident light.

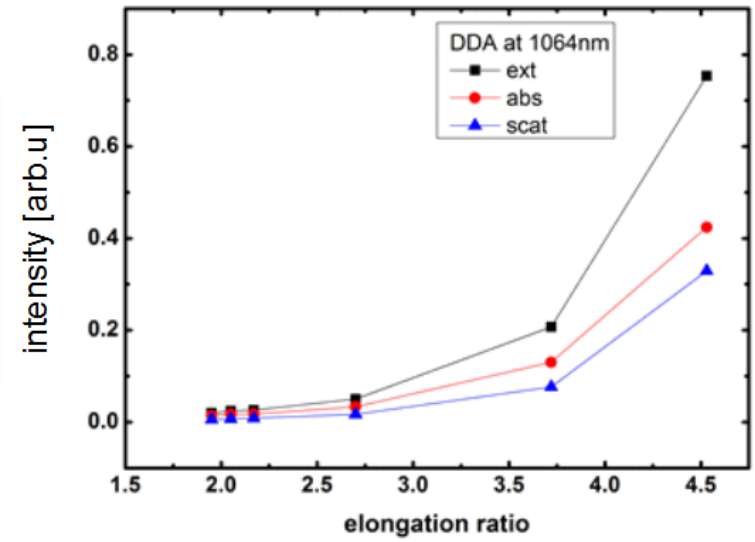

Figure 5-37 DDA simulation of extinction, absorption and scattering cross sections as a function of nanoparticle elongation ratio – for 532 nm.

DDA simulation for 355 nm showed similar results (Figure 5-38) to 532 nm with a slightly lower intensity slopes.

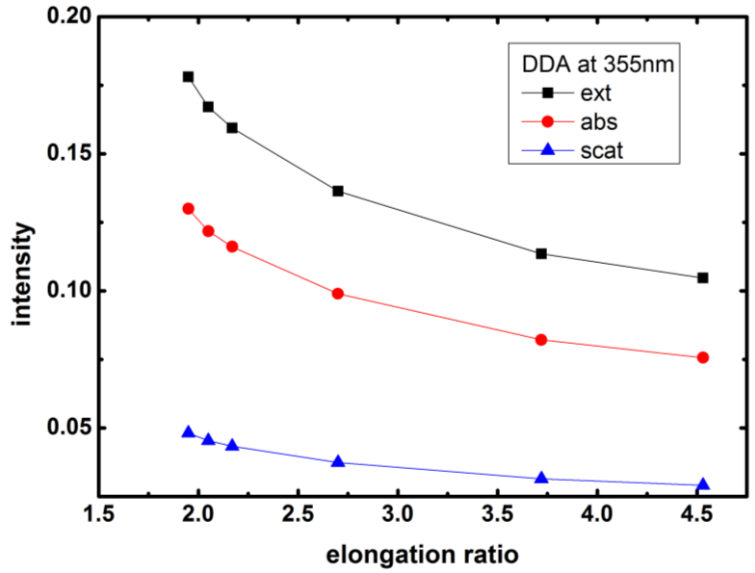

Figure 5-38 DDA simulation of extinction, absorption and scattering cross sections as a function of nanoparticle elongation ratio – for 355 nm.

The reason for that was the effect of the overall intensity of all parameters – low in comparison to the previous wavelength. A decreasing trend was present, which related to the theory mentioned earlier.

Extinction spectra for all three wavelengths can be seen in Figure 5-39.

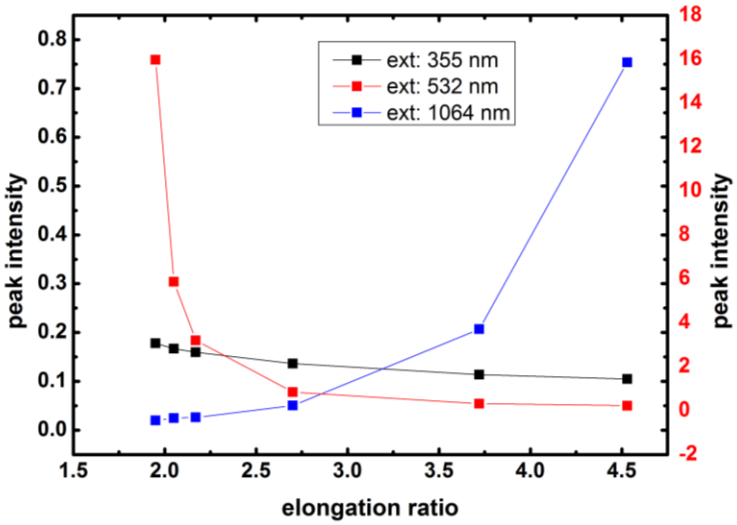

Figure 5-39 DDA simulation of extinction cross sections as a function of nanoparticle elongation ratio – for 1064, 532, and 355 nm.

A significant increase in 1064 nm extinction and decrease of 532 nm extinction can be observed. This effect was caused by the shift of the p-polarised SPR band toward longer wavelengths, hence increasing the plasmon coupling. A small decrease of extinction could be seen for 355 nm as this wavelength was placed spectrally in a bigger distance away from the main SPR band of nanoparticles.

The experimental part of this chapter showed SHG for 1064 nm illumination. The abs/scatt ratio was said to be responsible for either high SHG signal (when abs<scatt) or MAIL signal (when abs>scat). MAIL signal itself was also hypothesised to be created by energy transitions from created photons ~ 532 and 355 nm (SHG and THG) to nearby ion species. The abs-to-scatt ratio is presented in Figure 5-40.

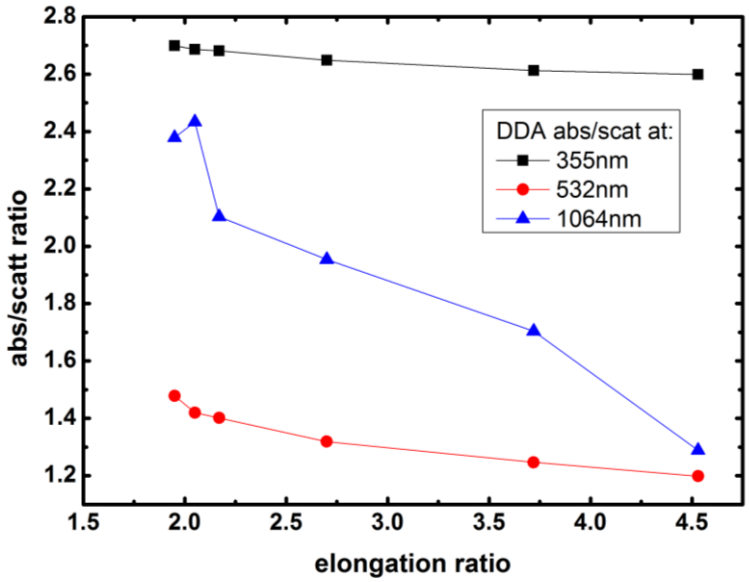

Figure 5-40 DDA simulations of abs/scatt ratio as a function of elongation ratio of nanoparticles – at 1064, 532, and 355 nm.

Three main observations can be made from these results, obtained by the DDA simulation:

1) For all wavelengths, abs/scatt ratio is higher than unity.
2) Decrease in the abs/scatt ratio exists for all wavelengths, with a difference in the rate of decrease
3) Smallest ratios for the most elongated nanoparticles were obtained for 532 nm and 1064 nm

Important conclusions can be made from these observations. Knowing that all ratios are higher than unity suggests that in every elongation ratio part of the signal obtained will be shown as MAIL. Although, for the most elongated nanoparticles MAIL should have the smallest influence on the obtained signal and the SHG should have the highest. This was observed in this chapter, where MS-MGN intensity slope was ~2 and the least elongated sample (FEMA) was ~2.5. Also, the smallest ratios were obtained for 532 nm wavelength which suggests that the SHG produced in the process of illumination with 1064 nm will be the least absorbed for the most elongated nanoparticles.

In case of the 355 nm results it can be established that the greatest effect observed for this wavelength is absorption of light by the nanoparticle. Elongation ratio did not make any significant difference. TAIL that can be created in samples containing nanoparticles can therefore be easily absorbed by Ag ions that are present in the vicinity of the nanoparticle and manifest itself in a luminescence band at ~ 450 nm.

Also, as described earlier, the type of elongation makes significant difference on obtained signal. The main reason for that is the dependence on the heat accumulation in the sample and the process used to obtain spherical nanoparticles.

A simplified Jabłoński diagram of established processes observed in elongated nanoparticles illuminated with 1064 nm wave can be seen in Figure 5-41.

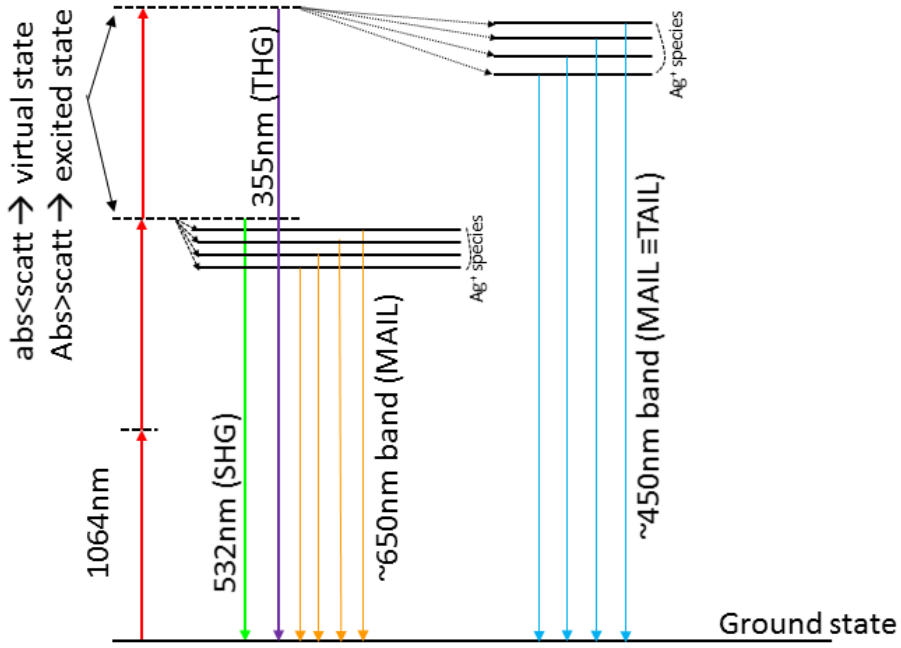

Figure 5-41 Jabłoński diagram concluding obtained results- both measured and simulated.

5.8 Conclusions

In this chapter, it was shown that both SHG and MAIL were present in MGNs containing elongated silver nanoparticles. SHG and MAIL effects were shown and their origin explained for three types of MGNs: ps-, fs- reshaped and mechanically stretched. Nonlinear optical effects were shown to not be originating from glass samples themselves, but rather from precisely engineered nano ellipsoids. Emitted signal dependence on the input beam polarisation was shown. Also, polarisation components of the emitted light were measured and described. It was shown that differences in structure and internal morphology existed between presented samples (manifested in a difference in the number of Ag ions present in the vicinity of nanoparticles) and were the cause of difference of MAIL signals and SHG intensities. Measurement of the

emitted signal as a function of the input pulse energy was performed and differences in the intensity slope was observed. Luminescence study was made and main excitation centres were found. It was also concluded that competition between SHG and MAIL arised from difference in absorption and scattering cross-sections of nanoparticles. DDA simulations were performed and it was determined that SHG was more noticeable for nanoparticles with higher aspect ratios. A Jabłoński diagram was proposed for visualisation of processes leading to observed SHG and MAIL.

Nano ellipsoids were proven to be good candidates for either SHG or MAIL converters. Second order nonlinear effect from these MGNs could be also utilized for applications like FROG (Frequency Resolved Optical Gating) where the traditionally used BBO could be replaced. Even though mechanically stretched nanoparticles proved to be the most efficient converters, the picosecond irradiation method showed to have more flexibility in shape and orientation modifications, therefore leading to a better ability to optimise these MGNs for SHG or MAIL.

It has to be noted however that MGNs' SHG and MAIL efficiency is still low compared to standard SH converters (BBO, LBO, etc.). Presented signals proved difficult to measure, even with the spectrometer and a cooled CCD camera (Chapter 3).

6 Laser induced reshaping of silver nanoparticles embedded in soda-lime glass with radially and azimuthally polarised light

6.1 Introduction

Chapter 6 will present a novel way of reshaping nanoparticles. Methods for laser reshaping presented in the previous chapter (Chapter 4) were based on a linear laser polarisation. The interaction between the ultra-short laser pulses with linear polarisation was characterised. It was shown how this type of MGN irradiation could produce silver nano ellipsoids (aligned along the laser direction of polarisation) in the volume of glass with highly efficient dichroic effect. Also, it has to be mentioned that linear laser polarisation could lead to formation of oblate spheroids, which was described in [131]. There, different shape changes were achieved with single pulse irradiation and with much higher laser intensity (over 2 TW/cm^2), where no dichroism was present but red-shift of the SPR caused by a halo of emitted photoelectrons around the nanoparticle. That process was based on the formation of dense electron plasma at the poles of a nanoparticle sphere and thermal expansion (and ablation) of the glass matrix. Very little has been described so far, both in this thesis and in any recent journal papers, about how the laser polarisation change in reshaping Ag nanoparticles embedded in soda-lime glass can lead to the formation of various different shapes of nanoparticles. Femtosecond laser irradiation on Ag nanoparticles in soda-lime glass revealed that by changing the incoming laser polarisation to circular, nanoparticle shape of nanodisks can be achieved [94]. There, the process of shape change was caused by the same mechanism as for the linearly polarised irradiation (that is directional ejection of electrons along the direction of the laser polarisation vector). The characteristic of circular polarisation was the reason for disc formation– spin angular momentum of the electromagnetic wave where the electric and magnetic fields rotated continuously

around the beam axis during propagation, therefore changing continuously the direction of electrons ejection in time, and covering the full angle.

Here, the interaction of radially and azimuthally polarised ps-pulsed laser beams with glass containing spherical Ag nanoparticles will be presented. Formation of peculiarly orientated Ag nano-ellipsoids will be shown along with a novel method for analysing their orientation within the irradiated lines using the known effect of Second Harmonic Generation (SHG) from elliptical nanoparticles [35]. It will be shown that the presented SHG cross-sectional scan method, conducted in the transmission geometry, allows for determination of the shape and position of nanoparticles within the modified areas.

6.2 Radially and azimuthally polarised beam irradiation

A range of experiments was performed in order to determine nanoparticle shape and position change under irradiation with a picosecond laser beam with its polarisation oriented radially or/and azimuthally. As described in chapter 3, an irradiation setup was used which included a ~10 ps pulsed laser, 532 nm wavelength and varying repetition rate (up to 200 kHz). Note that 532 nm irradiation is off-resonant which leads to higher reshaping ratios while using slightly higher laser intensities. This characteristic was shown in the previous chapter where MGNs were irradiated with this same wavelength with linear polarisation. The laser beam was expanded and a commercially available polarisation converter - an S-wave plate (made by Altechna) - was put in the optical path in order to achieve either radial or azimuthal polarisation (depending on the rotational alignment of the S-wave plate, relative to the linearly polarised incident beam). The beam was then focused on to a sample plane using a laser scanhead with a 100 mm F-theta lens attached. The system used allowed for a tight focusing of the laser beam down to ~ 22 μm measured at $1/e^2$.

The beam was polarised either radially or azimuthally. Figure 6-1 shows the distinction between these two polarisations.

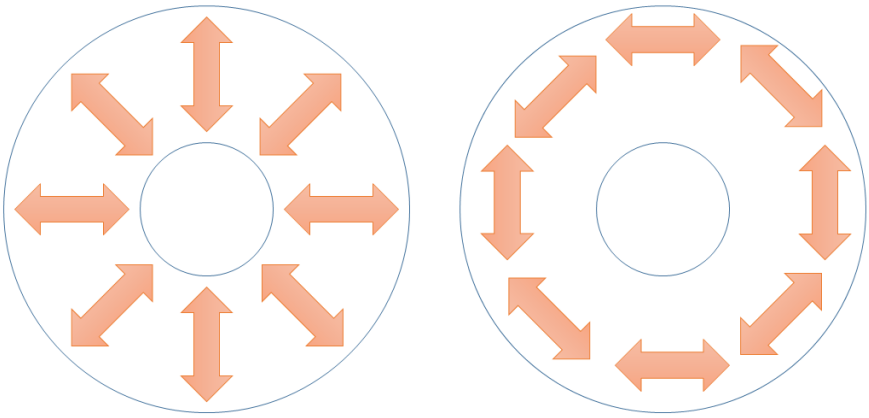

Figure 6-1 illustration of a) radially and b) azimuthally polarised laser beam.

It can be seen that the radially polarised beam has its polarisation direction set radially from the centre of the beam. Also, the azimuthally polarised beam has its polarisation direction set orthogonally to the radially polarised beam. An additional effect seen by passing a Gaussian intensity profile through the S-wave plate is the shape change of the beam to doughnut/ring-like. The S-wave plate was made by femtosecond direct writing in the volume of fused silica glass, creating subwavelength anisotropic modifications that resulted in shape and polarisation change [197]. For the purpose of this experiment the S-wave plate was commercially acquired.

The S-wave plate was extremely sensitive to misalignment. In order to determine the accurate position and alignment of the S-wave plate with regard to the optical path of the Gaussian beam and linear polarisation direction, a set-up was built. It consisted of a beam profiler (Spiricon) and a linear polariser and can be seen in Figure 6-2.

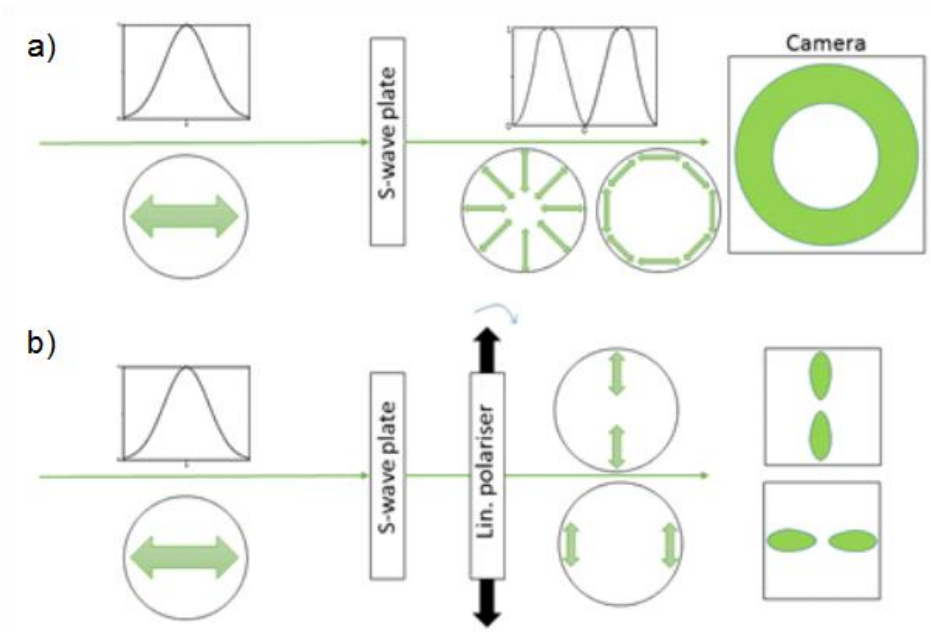

Figure 6-2 setup used for characterisation of the laser beam after shape modification with the s-wave plate

The laser beam was passed through the s-wave plate with a linear polarisation (horizontal in the illustration) and Gaussian intensity distribution. The resulting beam imaged on a beam profiler was a ring-like shape of intensity distribution, seen in Figure 6-2 a. By rotating the S-wave plate around its central axis, polarisations could be changed between radial and azimuthal, leaving the intensity distribution the same. In order to confirm that the right polarisation state was chosen, an additional linear polariser was added to the optical beam path for the alignment. It was used to separate the polarisation components and therefore visualise different parts of the ring intensity distribution on the beam profiling camera. Figure 6-2 b) shows this effect. If the polariser was placed with its polarisation direction set vertically, the vertical *bow-tie* on the camera represented vertical polarisation components of a radially polarised beam. The horizontal *bow-tie* showed the image seen when the azimuthally polarised beam was achieved (vertical components seen in this case at the left-right edges of the beam). The polariser could be rotated around its central axis in order to visualise other polarisation components on the camera of either radially or azimuthally polarised beam, for better alignment. Figure 6-3 shows images taken with the beam profiler where a) is the doughnut intensity distribution of a radially (in this case) polarised beam and (b – d) are images taken with addition of a linear polariser in the optical beam path which was positioned with its polarisation direction set vertically (b), and rotated clockwise until horizontal direction of polarisation was reached (c – d).

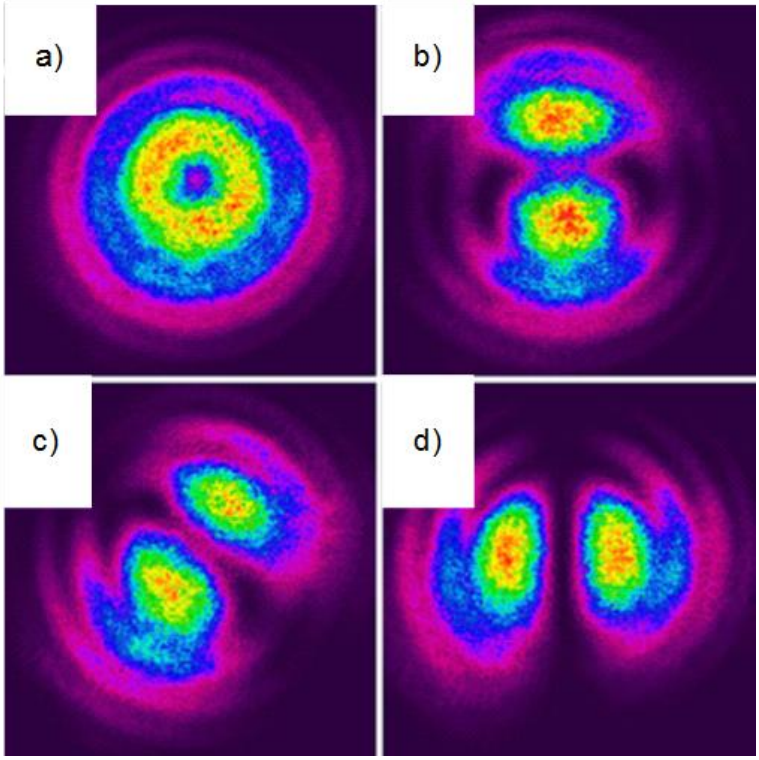

Figure 6-3 beam profiler images of a) radially polarised laser beam b)-d) with a polariser in the optical path rotated

For the azimuthally polarised laser beam the image (a) looked exactly the same as here. The difference was observed when the linear polariser was put in place i.e. b) would show a horizontal *bow-tie*, c) would be rotated by 90 degrees to the left and d) would have a vertical *bow-tie*. That effect was expected, knowing that azimuthally and radially polarised beams have orthogonally directed polarisation components.

The irradiation setup utilizing these polarisations was similar to the setup used for laser irradiations with a linear polarisation. The setup allowed modification of Ag nanoparticles in the sample plane in various directions and shapes.

6.3 Lines written with radially and azimuthally polarised laser beam

In order to observe the effect of irradiation of Ag spherical nanoparticles with either radially or azimuthally polarised laser beam an experiment was performed. Firstly, single lines were irradiated with varying laser pulse energy. Due to the effective beam diameter change and its intensity distribution (when comparing to linear polarisation

irradiation), the fluence for reshaping could have been different than the linear polarisation irradiation, therefore needed to be experimentally obtained.

Lines were irradiated with radially polarised laser beam as both polarisations had similar intensity distribution. The pulse energy for each line was varied in order to determine the optimal value. The laser repetition rate was set to 200 kHz and number of pulses per spot to ~2000 (higher value of number of pulses per spot could have been obtained due to the bigger size of the beam spot in comparison to linear laser polarisation irradiations). Figure 6-4 shows a microscope image of lines irradiated with the aforementioned technique. Pulse energies increment was set to 0.01 μJ. The line on the left hand side shows irradiations with 0.15 μJ (~40 mJ/cm^2) and on the right hand side with 0.28 μJ (74 mJ/cm^2). It can be seen that some structural changes appear for pulse energies between 0.24 and 0.28 μJ. Two additional lines were produced to see the changes in more details. Laser pulse energies of 0.29 (~ 76 mJ/cm^2) and 0.30 μJ (~78 mJ/cm^2) were used. Figure 6-5 presents lines irradiated with these two pulse energies. Structural changes can be easily seen in the central part of the irradiated lines. These changes are due to the effect presented in chapter 4 (*silvering*), where nanoparticles while being irradiated underwent an Oswald ripening process, forming bigger clusters and pushing them from the volume of nanoparticles to the surface of the glass. This effect was seen for the same range of pulse energies while irradiating MGNs with azimuthally polarised light.

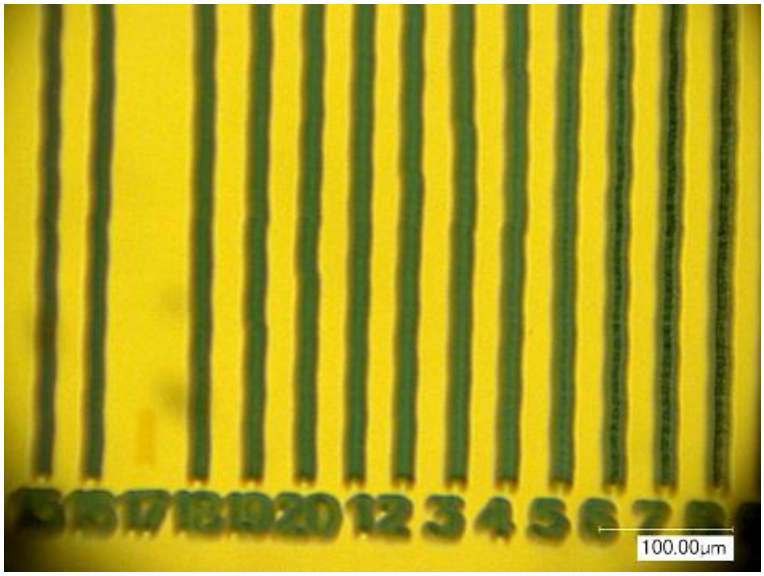

Figure 6-4 microscope image of lines irradiated vertically with radially polarised laser beam. Laser pulse energy has been varied between 0.15 µJ (line on the left hand side) and 0.28 µJ. Line with 0.17 µj was unsuccessfully irradiated.

It was concluded that for efficient reshaping of silver nanoparticles with polarisations presented, pulse energies must not be greater than 0.24 µJ.

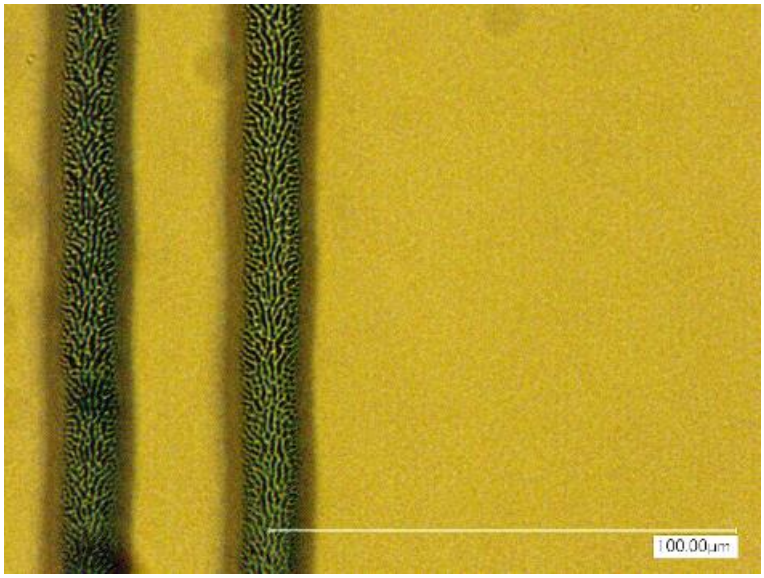

Figure 6-5 microscope image of lines irradiated with 0.29 (left) and 0.30 µj (right). Structural changes on the surface presented

For further experiments 0.24 µJ was used which corresponds to ~60 mJ/cm^2. Additionally, it can be seen in Figure 6-5 that the edge of each line has a darker shade and is of different colour than the central part of the line. Additional laser irradiations were made in order to explain this phenomenon.

Series of lines were irradiated on MGN with radially and azimuthally polarised laser beams. Figure 6-6 a) shows the directions of how the lines were irradiated: left-to-right and right-to-left. Both directions were performed for each of the polarisations (radial and azimuthal). Lines were then put under a digital microscope and the input light polarisation direction was changed and set to 0, 45, 90 or 135^0 (Figure 6-6 b). Similarly as in chapter 4 where linearly polarised irradiations were diagnosed, this kind of metrology gives a great input into how the nanoparticles are being reshaped within the irradiated areas (nanoparticles with green/blue colour indicate that their direction of elongation is parallel to the direction of polarisation of illuminating light).

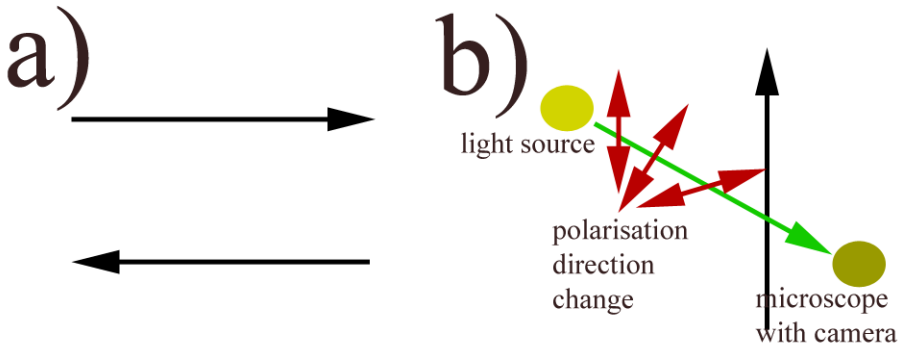

Figure 6-6 experiment explanation of a) directionality of irradiation b) design of irradiated lines metrology measurements

Azimuthally irradiated lines were analysed first and can be seen in Figure 6-7. As can be observed, lines were not uniformly coloured as was the case with linear polarisation irradiation. Here, certain areas existed that showed peculiar structuring of a single line. For illumination with vertical direction of polarisation (Figure 6-7 a and e) the middle of the line shows its colour to be green/blue, which indicated vertical alignment of linearly reshaped nano ellipsoids. On the other hand, illumination with light of orthogonal direction of polarisation (Figure 6-7 d and h) showed c0lour change in the edges of the lines, indicating horizontally aligned metallic nano ellipsoids in these areas.

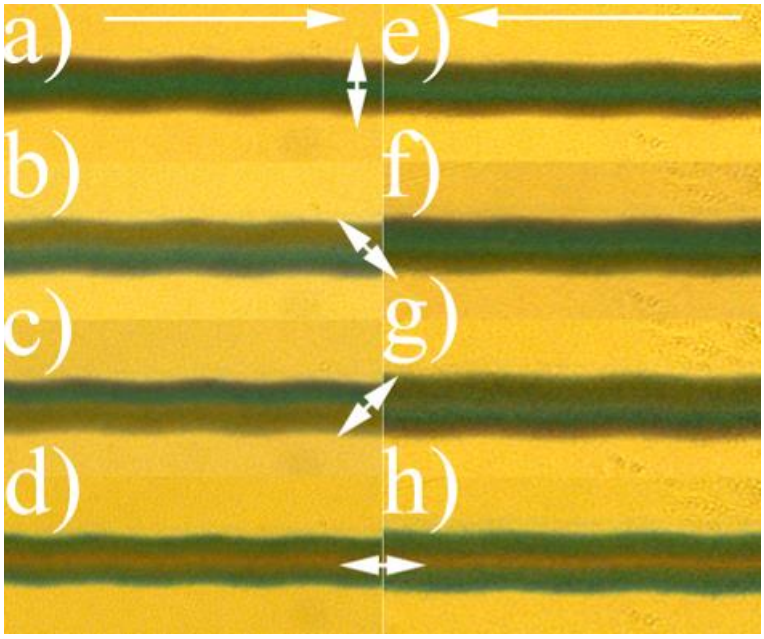

Figure 6-7 azimuthally polarised laser light irradiations. a)-d) left-to-right, e)-h) right-to-left. White double sided arrows indicate the direction of polarisation of light used for metrology

The same effect can be seen for both left-to-right and right-to-left irradiation. A completely different effect is visible for illumination with polarisation direction rotated +/- 45°. For left-to-right irradiation (Figure 6-7 b and c) bottom part of the line shows the green/blue colour for -45° (Figure 6-7 b) and upper part of the line shows this colour for +45° (Figure 6-7 c). This effect showed that nanoparticles at the edges of each irradiated line were aligned along +/- 45°. It can be also seen in these pictures that the thickness of the coloured regions differed slightly. The horizontal illumination green/blue area is slightly thinner and positioned more at the very edges of the line than the +/- 45°, which took some of the middle part of the line cross-section. Right-to-left irradiation (Figure 6-7 f and g) gave opposite effect where the upper part is coloured in green/blue at -45° and bottom part at +45°. This result indicated that the nanoparticles did not only positioned themselves under intense laser irradiations at +/- 45 ° but also their position was dependent on the direction of irradiation.

Secondly, radially polarised light irradiation was analysed. Figure 6-8 shows the results obtained under the microscope.

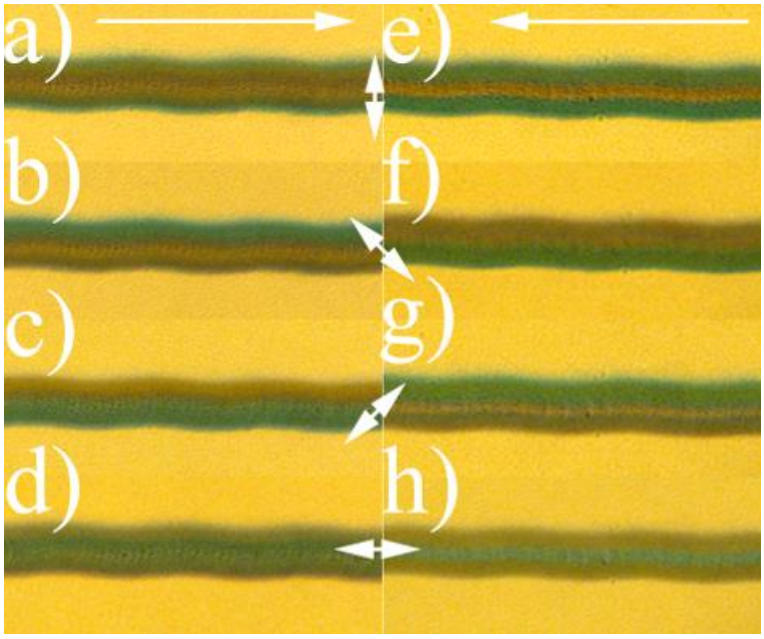

Figure 6-8 radially polarised laser light irradiations. a)-d) left-to-right, e)-h) right-to-left. White double sided arrows indicate the direction of polarisation of light used for metrology

It can be seen there that radial polarisation reshapes nanoparticles in complete opposite manner to azimuthal polarisation irradiation. It is also important to say that it was an expected effect as the radially polarised laser beam has its polarisation components oriented orthogonally to the azimuthal polarisation components, therefore effects of irradiations should have also be present in this manner.

Additionally, a line was irradiated with azimuthal polarisation of the laser beam while the sample was offset from the focal plane of the focusing f-theta lens. In this experiment thicker lines could have been irradiated which gave more detailed picture of how the colour of each line changed under polarised illumination. Also, it was expected that the laser beam polarisation and intensity distribution while slightly out of focus would have stayed the same as in the focus (M^2 <1.3), within certain degree of imperfection. Figure 6-9 a)-d) shows the irradiated lines. The measured thickness was ~ 100 µm and the pulse energy was increased to the level where MGN were not being damaged but high enough to observe significant reshaping. The blurriness of lines are the effect of pulse energies at lower levels of reshaping (~1 µJ). The figure confirms what has been observed earlier- middle of the line coloured in green/blue for vertical polarisation direction illumination, edges for horizontal polarisation direction of illumination and upper/lower part of a line for -/+ 45^o polarisation direction of illumination. In the same Figure 6-9, a single line is shown as an effect of irradiation of

MGN with linearly polarised laser beam. Parameters of irradiation are same as in chapter 4. It can be observed there how colours changed for this type of irradiation and compared it with azimuthally irradiated line.

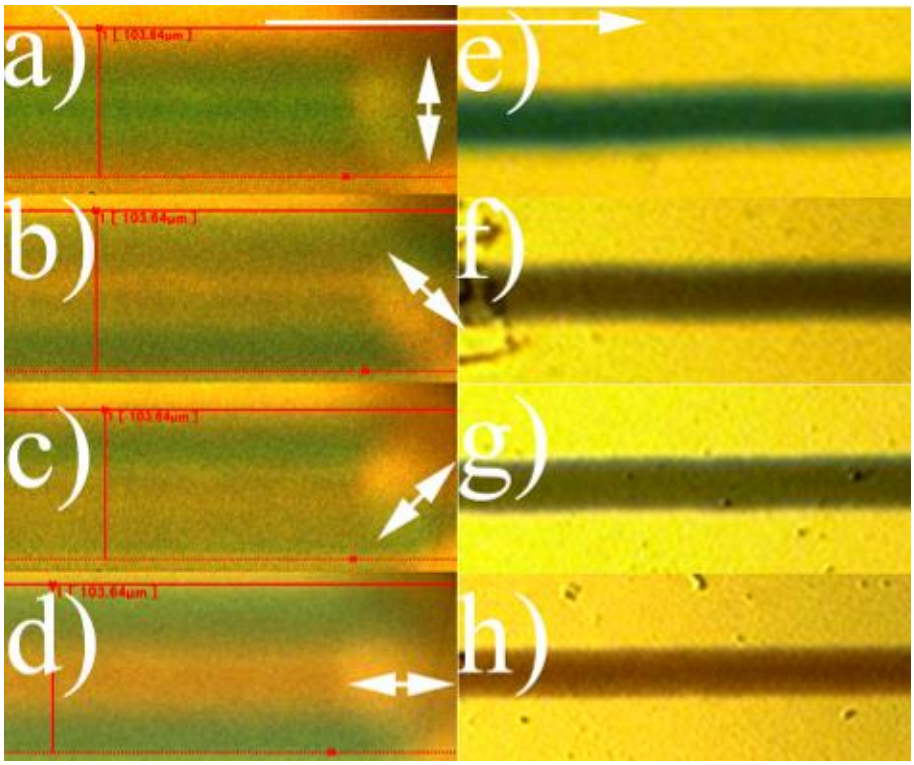

Figure 6-9 a)-d) thick lines irradiated with azimuthally polarised laser light, e)-h) liner irradiated with linearly polarised laser light. All irradiations were performed from left-to-right. Illumination with linearly polarised light with polarisation direction indicated with white arrows.

For instance, Figure 6-9 e) is fully coloured in green/blue as all the nanoparticles are positioned there along the direction of polarisation of the illuminating light (vertically). Brown/red colour for the s-polarisation and grey/green for in between. It showed that the lines irradiated with either radial or azimuthal polarisations had their components separated as in comparison to linear polarisation irradiation. Therefore this implied that certain parts of the polarisation components of either radial or azimuthal polarisation reshaped the area of MGN in a different way, but along certain direction.

Figure 6-10 shows a summary of how colours change along each line cross-section. Red lines indicate where the blue/green colour formation arose. Left hand side shows lines irradiated with azimuthal polarisation and right hand side with radial polarisation. Both images are made for left-to-right irradiation. Black arrows in the middle indicate the illumination polarisation direction. Below that, the proposed alignment of nanoparticles within each of these lines after irradiation is shown. The nanoparticles were drawn so

that they were aligned with their long axis parallel to the direction of polarisation of illumination.

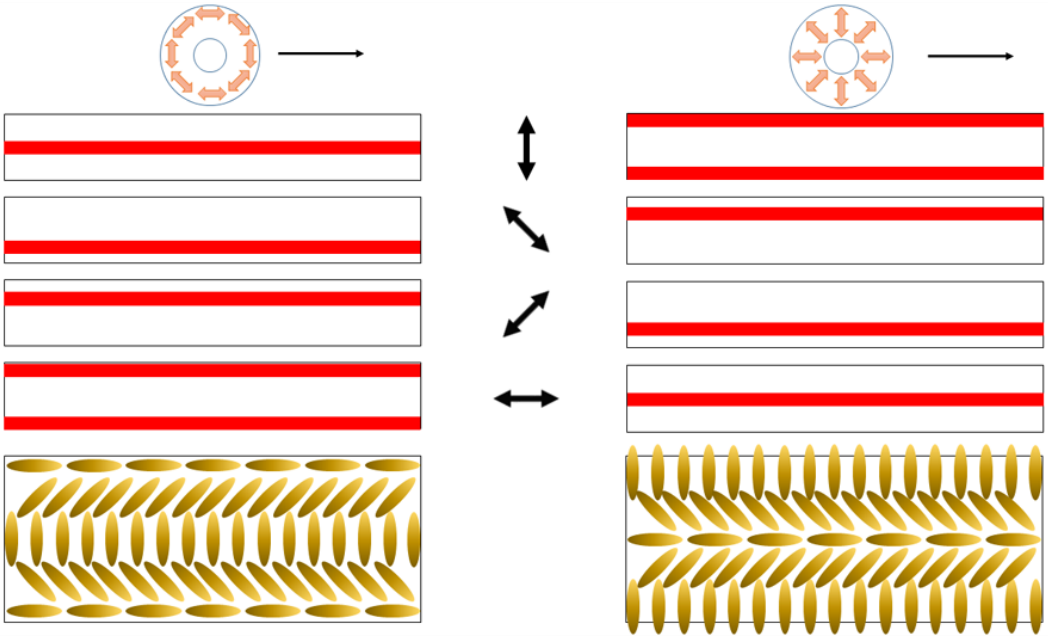

Figure 6-10 graphical representation of areas coloured in green/blue for azimuthal (left) and radial (right) and proposed nanoparticle alignment within the sample.

Single line irradiation (either with radial or azimuthal polarisation) exhibited nanoparticles oriented differently within the same line cross-section. It was assumed that the laser beam polarisation components reshaped the irradiated area along their direction separately. It was also important to note that while the top, the bottom and the middle of each line were reshaped in the direction of the polarisation components of the irradiating beam, The +/- 45^{o} areas of each line behaved differently. Example of azimuthally reshaped line, assuming the proposed theory that the nanoparticles are reshaped along the direction of polarisation components of each beam, shows that for the -45^{o} illumination, both upper-middle and bottom-middle parts of the line should change colour to blue/green. The experiment showed however, that only the bottom-middle part exhibited this effect. Similarly for the orthogonal illumination where the upper-middle part exhibited the effect (same with the radial irradiation). The observation showed that the tail of the irradiating beam had the biggest effect on the overall reshaping. Definite conclusions couldn't be made at this point as the character of reshaping needed to be determined more thoroughly.

6.4 Second Harmonic Generation cross-sectional scanning method

In the previous sub-chapter, single lines were irradiated with either azimuthal or radial polarisation of the laser beam. It was concluded from optical microscope image investigation that nanoparticles in each line did not take one certain shape after laser irradiation but rather created nano ellipsoids rotated along the cross-section of the irradiated line. In order to confirm these findings a special experiment was designed. According to chapter 3, silver nanoparticles embedded in the soda-lime glass possessed a unique property of Second Harmonic Generation (SHG) and Multi-absorption induced luminescence (MAIL). These two effects were polarisation dependent and exhibited their highest intensity while illuminating nanoparticles with the incident direction of polarisation aligned parallel to the long axis of nanoparticles (Figure 6-11). The experiment that was designed for characterisation of the cross-section of a single irradiated line was based on the principle of scanning irradiated areas with laser beam (across irradiated lines) and rotating its direction of polarisation in order to detect maxima of intensity.

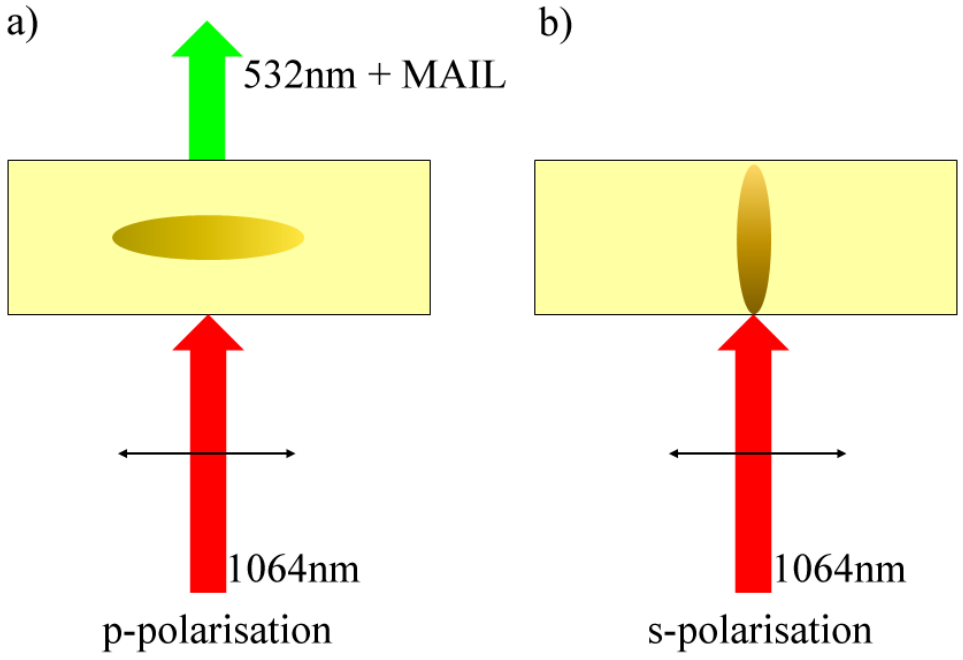

Figure 6-11 the idea behind the NPs alignment experiment. a) Presents a p-polarised 1064nm beam which is being converted to 532nm + mail b) presents s-polarisation which is not being converted

These maxima were then mapped spatially on the area in order to show the direction of nano-ellipsoids there. The exact setup was described in chapter 3. Figure 6-12 describes the idea behind the experiment.

Examples of spectra that would have been obtained are also shown for the situation where the horizontal direction of polarisation had the strongest intensity at a specific point in the sample.

In order to confirm this methodology by comparing it to other than radially and azimuthally polarised irradiations, linearly polarised lines were irradiated. Firstly, lines in two directions were irradiated (left-to-right and right-to-left) with laser polarised horizontally (parallel to the direction of irradiation). Secondly lines with laser polarised vertically were irradiated.

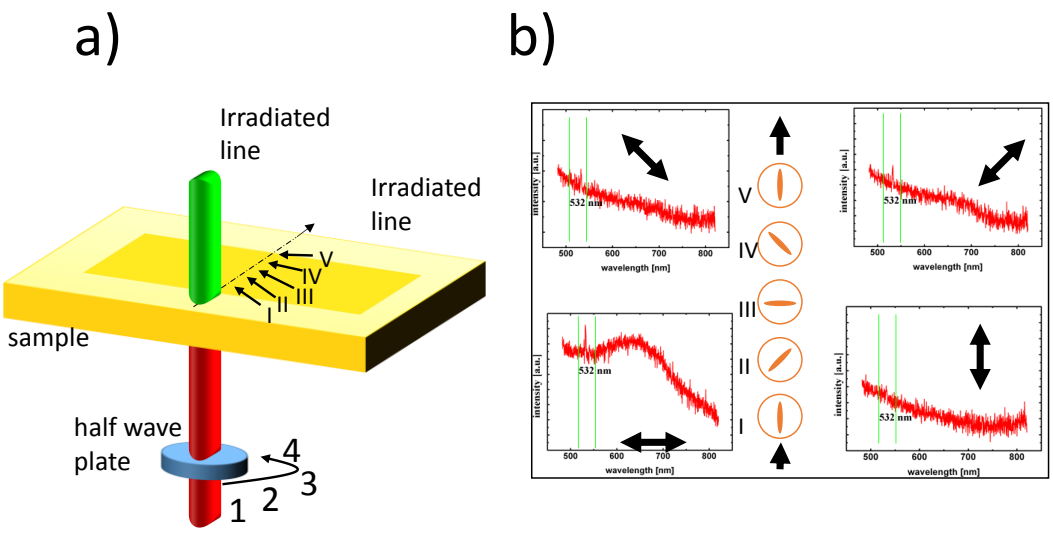

Figure 6-12 a) side view of the experiment. Fundamental beam illuminates from the bottom and shg+mail is being produced above b) top view. Circles in the centre show points where the data is being taken. Scan proceeds from bottom to top. Double arrows on the edges show the polarisation of the fundamental beam and example of intensity spectra taken.

Because in this mode of reshaping nanoparticles elongated along the direction of polarisation of laser beam, the expected result was that the highest intensity of the SHG and MAIL signal will be for fundamental light polarised along that direction. Minimum value of signal was expected for fundamental beam polarisation orthogonal to the direction of elongation of nanoparticles. All signals were expected to have their local maxima in the centre of the irradiated line cross-section and no change in the signal was expected to show up for two different directions of irradiation. Results of a cross-

sectional scan for irradiations made with horizontally polarised beam can be seen in Figure 6-13. Here, a vertical double arrow represents fundamental beam polarisation direction parallel to the polarisation of irradiating beam and horizontal double arrow polarisation direction perpendicular to it. In order to read this image properly, one has to imagine the x-axis of the image to be the irradiated line thickness. As expected, no change was measured between left-to-right and right-to-left directions of irradiation.

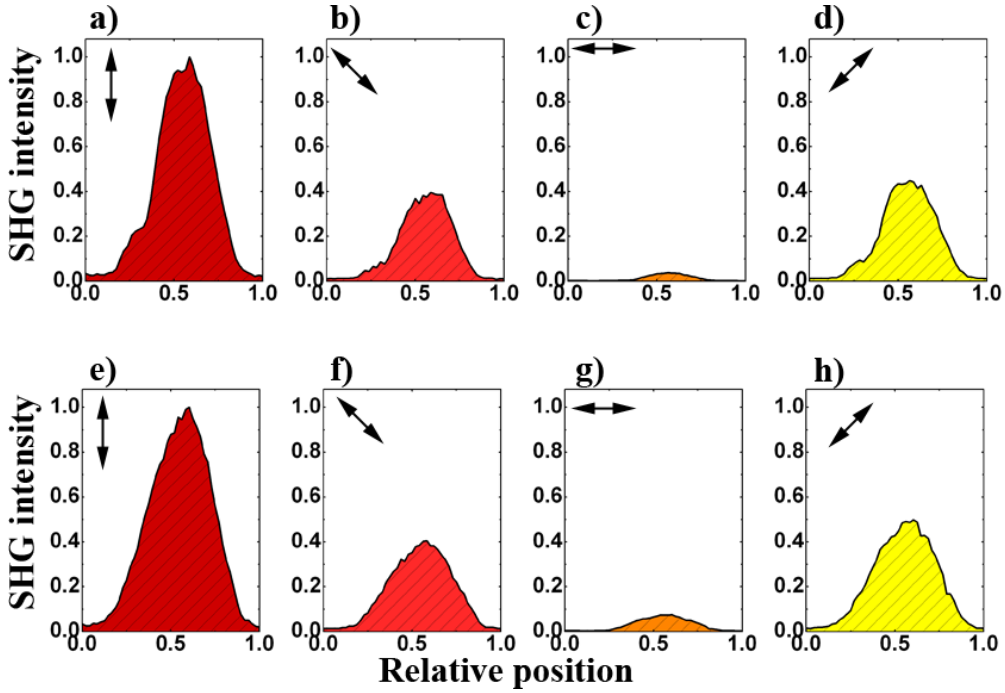

Figure 6-13 cross-sectional scan of an irradiated line with horizontal polarisation. (a)-(d) left-to-right irradiation, (e)-(h) right-to-left irradiation.

Vertically polarised irradiation beam was used for the second irradiation. Results of a cross-sectional scan can be seen in Figure 6-14.

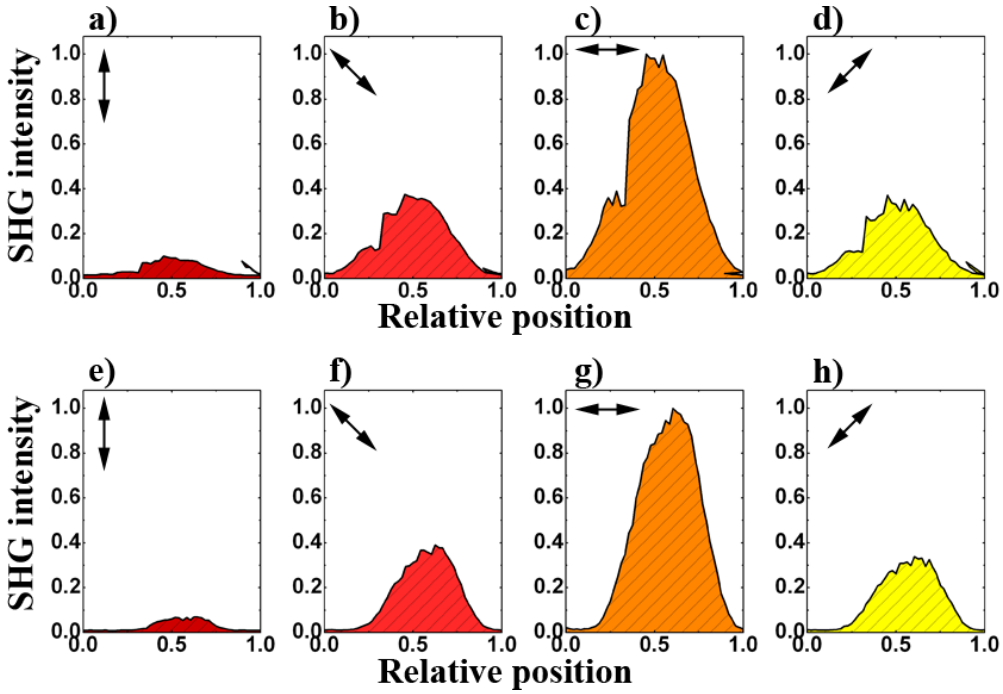

Figure 6-14 cross-sectional scan of an irradiated line with vertical polarisation (a)-(d) left-to-right irradiation, (e)-(h) right-to-left irradiation.

It can be seen that the horizontal double arrow, representing the polarisation direction of the fundamental beam, shows the highest intensity of SHG and MAIL and the vertical the lowest (similarly for other direction of irradiation). It agreed with expected results. These measurements could have been used to visualise how nanoparticles were aligned across each irradiated line. Figure 6-15 shows how nanoparticles were aligned while irradiating the sample with horizontal polarisation in two directions.

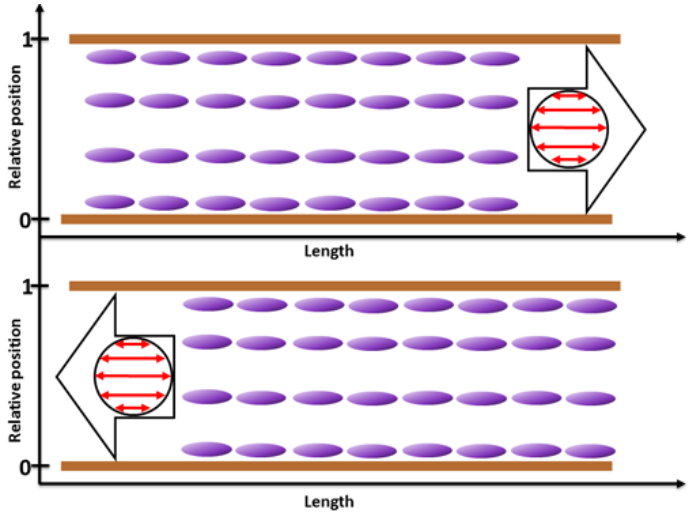

Figure 6-15 Schematic representation of nanoparticle orientation when irradiating with horizontal polarisation direction.

Figure 6-16 shows how a vertically polarized irradiation elongates nanoparticles.

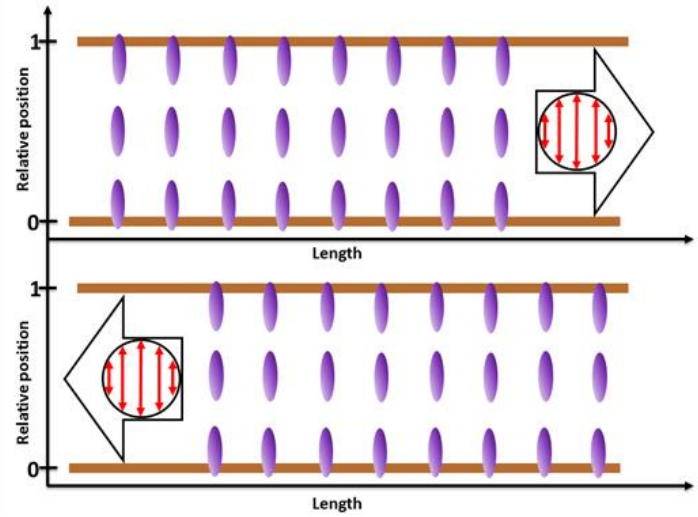

Figure 6-16 Schematic representation of nanoparticle orientation when irradiating with vertical polarisation direction.

Another set of lines was irradiated with either azimuthally or radially polarised laser beam. Similarly to the previous experiment, two directions of irradiation were used: left-to-right and right-to-left. Figure 6-17 presents left-to-right irradiation, where (a)-(d) represents cross-sectional results of azimuthally polarised irradiation and (e)-(h) radially polarised irradiation. It can be observed there that maxima of intensities of SHG and MAIL moved along the line cross-section depending on which fundamental polarisation direction was used for the experiment. In this figure, each measurement was normalised to its maximum value for simplicity in explanation of how these patterns position shifts across the line thickens (in a result, revealing directions of elongated nanoparticles).

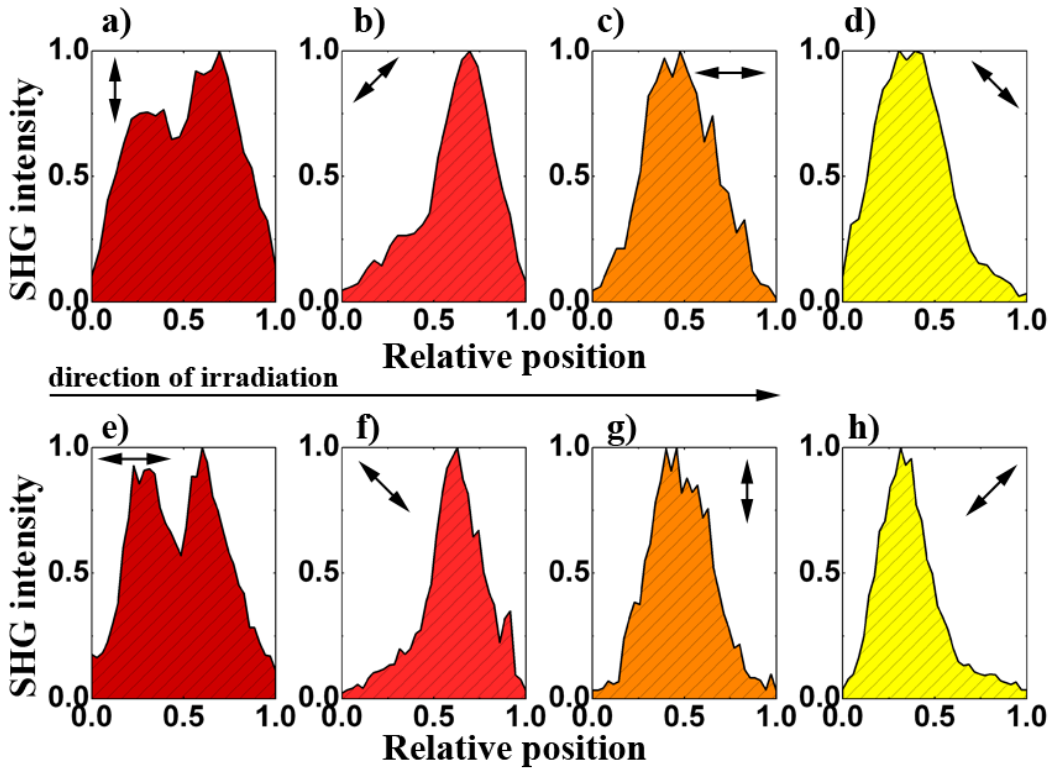

Figure 6-17 cross-sectional scan of an irradiated line with azimuthally (a)-(d) and radially (e)-(h) polarised laser. Left-to-right irradiation.

In Figure 6-17 (c), which shows the signal positioned in the very centre of the line cross section, a vertical polarisation dominates (horizontal double arrow). From there (b) is shifted to the right and (d) to the left (+45^{o} and -45^{o} degree polarisation respectively). In (a) two distinct peaks form at the edges of the line cross-section with horizontal polarisation (vertical double arrow) indicating two rows of nanoparticles that were elongated in the same direction - here, along the direction of irradiation. A double peak pattern was seen in (e) which indicated two rows of nanoparticles elongated perpendicularly to the direction of irradiation. In (f), (g), and (h) signal patterns were observed with polarisation pattern orthogonal to the azimuthal line irradiated in the very same direction (a-d). For comparison purposes, and also for clarity on how direction of irradiation influences the reshaping process, two additional lines were irradiated in opposite direction to previous (right-to-left). Figure 6-18 shows experimental results where (a-d) are azimuthal irradiations and (e-h) are radial. Similar patterns of shifts can be observed for both polarisations when compared to Figure 6-17.

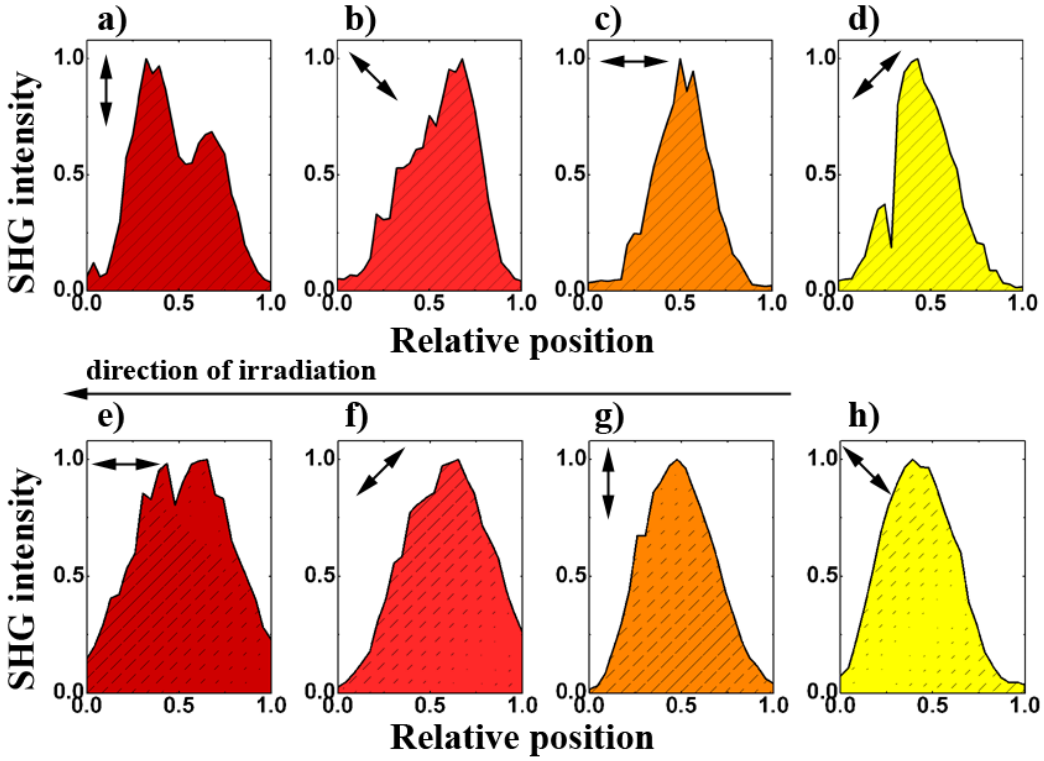

Figure 6-18 cross-sectional scan of an irradiated line with azimuthally (a)-(d) and radially (e)-(h) polarised laser. Right-to-left irradiation.

The difference between these two measurements lies in the direction of polarisation of left and right shifted signals (b, d and f, h), where polarisation directions are rotated by 90^{o} when compared to Figure 6-17. Also, radial irradiation shows smaller 'double peaks' than previous experiments, which can be attributed to a lower quality of irradiated line for this particular one.

These measurements, similar to the case of linear polarisation irradiation, can be transformed from spatial intensity mapping into nanoparticle elongation direction across the irradiated line. Figure 6-19 shows how nanoparticles are aligned for azimuthal irradiation in two directions (illustrated from data in Figure 6-17 and Figure 6-18: a-d), whereas Figure 6-20 shows nanoparticle alignment for radial irradiation (illustrated from data in Figure 6-17 and Figure 6-18: e-h).

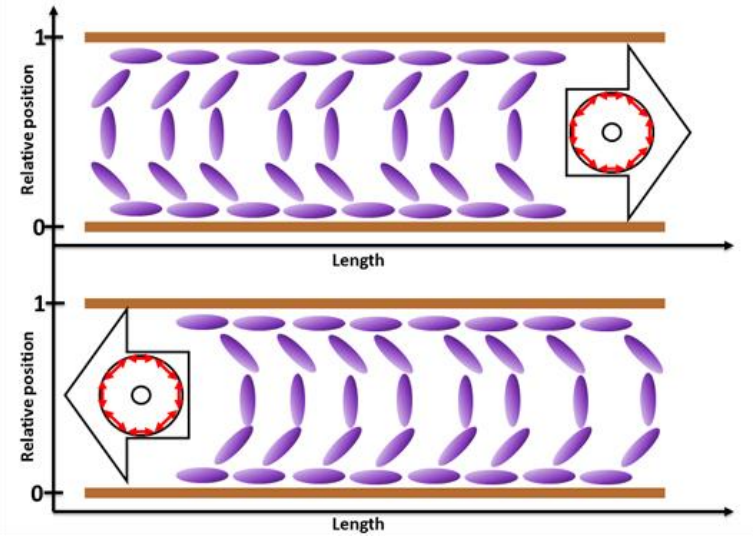

Figure 6-19 Schematic representation of nanoparticle orientation when irradiating with azimuthal polarisation in two direction of irradiation.

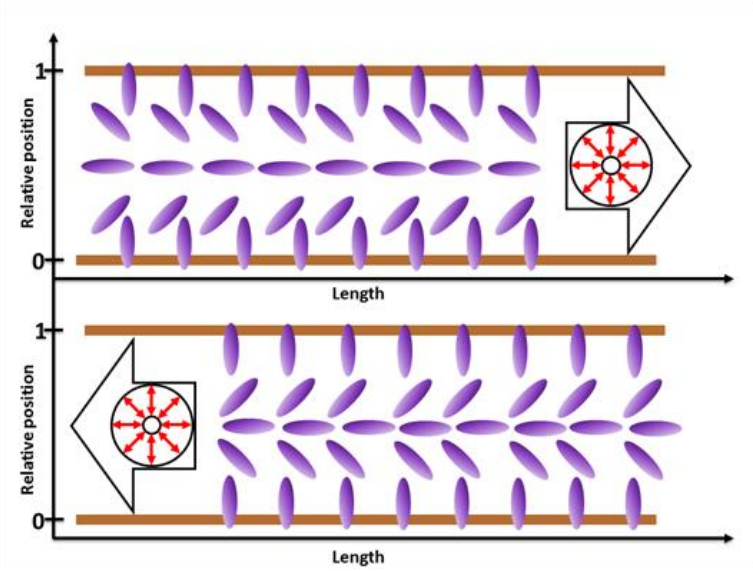

Figure 6-20 Schematic representation of nanoparticle orientation when irradiating with radial polarisation in two direction of irradiation.

It can be observed there that nanoparticles were being elongated and aligned with a certain pattern, which was unique and depended on both polarisation state of the laser beam as well as the direction of irradiation. From the above observation one may conclude that four different orientations of the nanoparticles are observed in each irradiated spot using the azimuthally/radially polarized beam. The cases of +/- 45^{o} were of particular interest here since these indicated that the final reshaping of the nanoparticles was dictated by the tails of laser pulses rather than their tips. This agreed with the reshaping mechanism presented earlier and added to the knowledge of reshaping with radial and azimuthal polarisation. It was also evident that linear

polarisation irradiation changed the direction of elongation of nanoparticles with the tail of the laser beam. This effect was previously unknown, and the presented method of observation proved to be an excellent tool for such investigation. Figure 6-21 summarises how nanoparticles are being reshaped with presented polarisations and which parts of the laser beam gives the most contribution to the final nano-ellipsoid orientation.

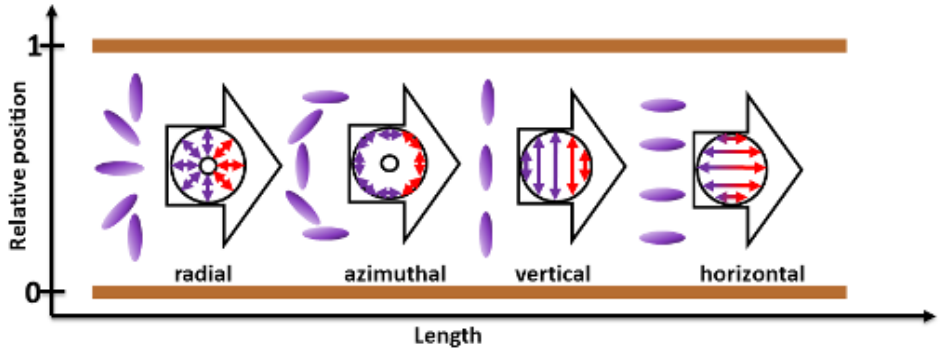

Figure 6-21 Schematic representation of nanoparticle reshaping with radial, azimuthal, linear-vertical, and linear-horizontal laser polarisations. In blue are tails of laser beams and in red their tips.

6.5 Line overlap and investigation - macroscopic optical effects.

In contrast to linear polarisation laser reshaping, where the whole of each irradiated line has nano-ellipsoids oriented along that polarisation, radial and azimuthal polarisation laser reshaping left the irradiated area with nanoparticles oriented in a pattern presented in the previous sub-section. This created a technical bottleneck in creation of larger irradiated areas, when lines during the raster scan had to be close to each other. It was possible that even smallest overlap of lines could modify the alignment of nano-ellipsoids and therefore interrupt further investigation of macroscopic optical properties. At the same time, lines needed to be in close proximity to each other.

6.5.1 Line overlap investigation

In order to investigate this effect and find the most desirable parameters for irradiation, lines were irradiated with azimuthal laser polarisation. Different rates of overlap were used (overlap of more than 50% of the beam waist were chosen) in order to see the overall effect. Figure 6-22 shows these irradiation seen under a microscope with

polarized illumination- black double arrows show the direction of illumination polarisation direction. Lines with hatch distance of 10, 9, 8, 7, and 6 µm were irradiated in the same direction (left-to-right). 8µm hatch distance was chosen to irradiate additional lines: 1) left-to-right and right-to-left, 2) three lines overlapped left-to-right. It can be clearly seen in all of the examples how the second line dominates the polarisation effect, therefore the direction of nanoparticles alignment.

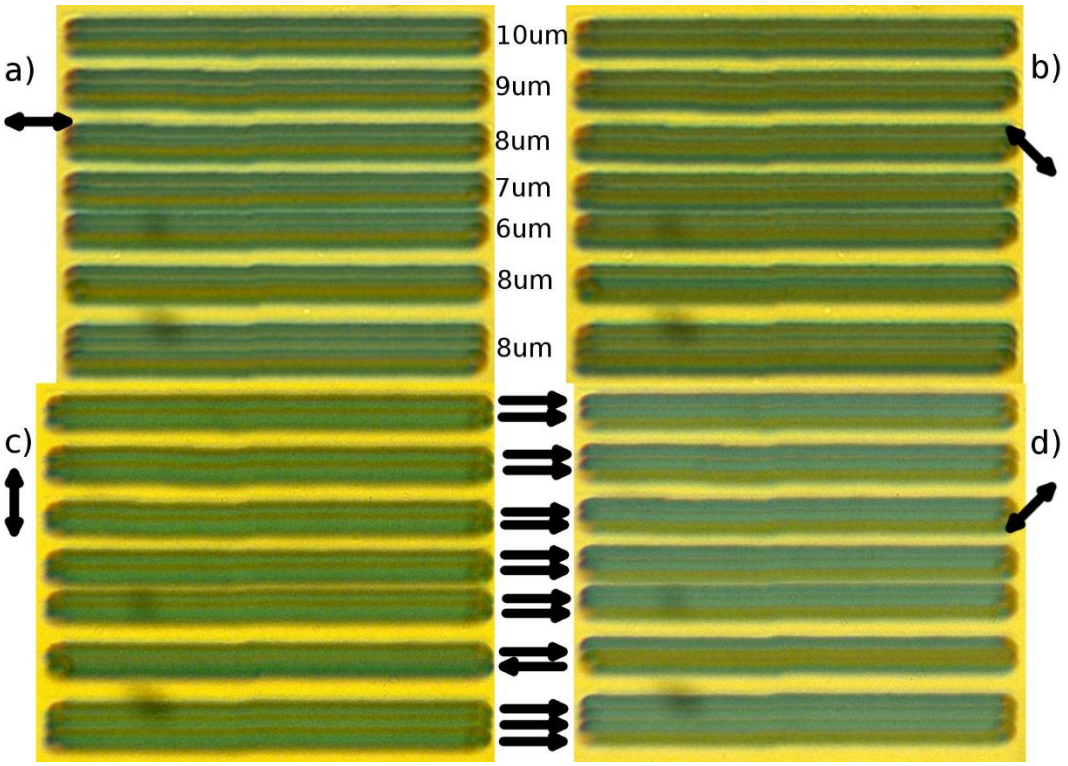

Figure 6-22 Microscope image of lines irradiated with azimuthal polarisation and various hatch distances. Black double arrows on the sides indicate the illumination polarisation direction. Black arrows in the middle indicate the direction of irradiation.

This effect manifested itself in the fact that the second line colours behaved in a manner of a single irradiated line - the line on the bottom (upper) has very little effect. Also, this behaviour of reshaping matched the result and observation that the tail of the beam influences orientation of nano-ellipsoids the most. This experiment showed that not only the tail but also the latest irradiated line engraves its reshaping on the sample. The 8µm lines irradiated in two directions showed this as an addition and a cancellation effect, especially seen in Figure 6-22 (b) an (d), where the second irradiation changed the orientation of nanoparticles in orthogonal direction resulting in the middle part of line (b) being parallel to the illumination polarisation. In (d) the blue colour part vanishes almost completely.

Three lines in the same direction visualised the amount of reshaped nanoparticles in the middle line, with conclusion that small hatch distances might not have been preferable as that could add or cancel out some of the optical effects. On the other hand, one could produce single thin lines of particular nanoparticle orientation (in 8µm two directions-b).

Another experiment was performed with larger hatch distance that was chosen to not overlap lines on each other but having a uniform coverage at the same time. A hatch distance of 18µm was used and the results can be seen in Figure 6-23 (azimuthal polarisation of the laser was used). Images were made under a light microscope with polarised illumination.

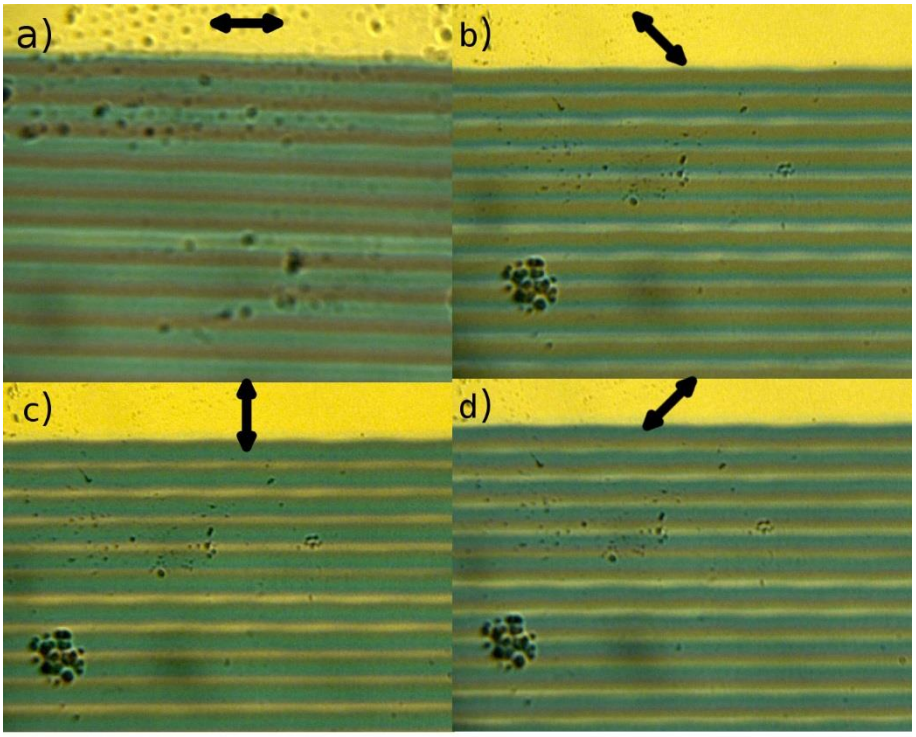

Figure 6-23 Microscope images of areas irradiated with azimuthal polarisation. No overlapp between lines was present. Left-to-right raster scan was used. Black arrows indicate the illumination polarisation direction

It can be seen there that lines changed their colours accordingly to what was described in the previous sub-chapter for azimuthal irradiation (left-to-right). Also, thin areas between lines can be seen with minimal reshaping in (c), whereas in (a) the image presented full coverage of the sample. It was a result of appropriate choice of the hatch distance where no or minimal overlap was present. In order to confirm this finding and analyse macroscopic optical properties of reshaping with both azimuthal and radial polarisations, 3 x 3 mm squares were raster scanned in the same manner as in Figure

6-23. Figure 6-24 below shows optical spectra made for squares irradiated with azimuthal polarisation with hatch distances of: 18, 14, 10, 6, and 2 µm.

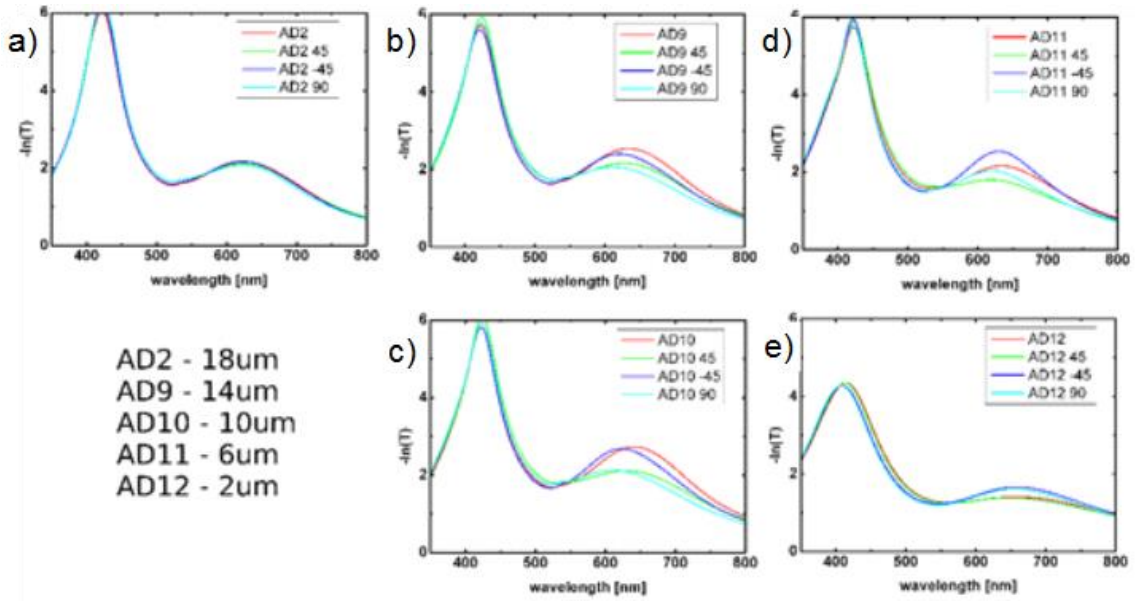

Figure 6-24 Extinction spectra for 3x3 mm squares irradiated with azimuthally polarised laser beam and various hatch distances. Linearly polarised light source was used.

Spectra were made with a linearly polarised light source in the spectrophotometer where 0^o is vertical polarisation direction (across each irradiated line) and 90^o is horizontal. In Figure 6-24 (a) it can be observed that for all four polarisations: {0, +45, -45, and 90}, red shifted peak appears at around 630nm and is of comparable intensity (very small extinction spread). When, however, the hatch distance for raster scan irradiation decreased the extinction spread increased. In (b) the 0^o peak height increased, followed by the -45^o and 45^0, 90^o. In (c) the -45^o peak height increased and became of similar intensity as 0^o, below is 45^o and 90^o. In (d) -45^o became dominant and 90^o increased, and in (e) overall intensity decreased of all polarisations.

Similar effect could have been observed for radial polarisation irradiation of 3x3 mm squares- Figure 6-25. When the hatch distance was chosen to be 18µm, peak intensities of red shifted bands were of similar intensity. Decrease in hatch distance resulted in first (b) higher intensity at 45^o and 90^o signals followed by increase of intensity of peak at 0^o (c), then decrease of signal at 90^o (d) and overall degradation of signal in (e).

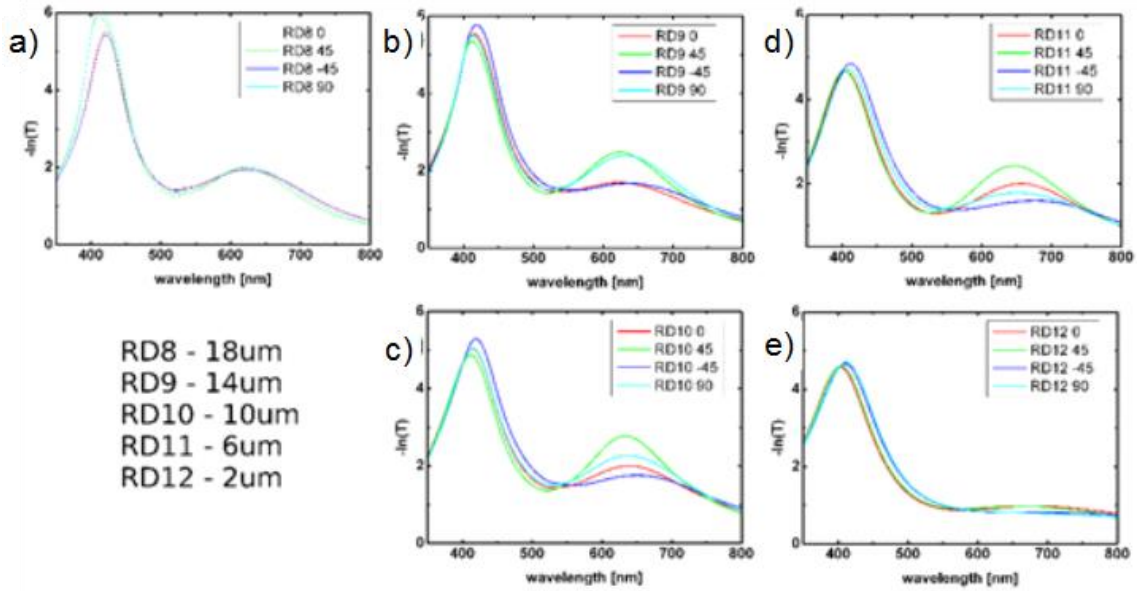

Figure 6-25 Extinction spectra for 3x3 mm squares irradiated with radially polarised laser beam and various hatch distances. Linearly polarised light source was used.

In both irradiations (azimuthal and radial) the spherical remnant of the SPR (positioned at ~430nm) decreased in intensity along with the decrease of the hatch distance. This observation agreed with the theory about dissolution of nanoparticles under high power laser irradiation, where highly overlapped lines can be assumed to reflect such an effect.

Changes in the red-shifted peak intensity for different illumination polarisations can be explained for both polarisations. When comparing these two irradiations and their spectra from Figure 6-24 and Figure 6-25 one can see that when decreasing the hatch distance between lines in the raster scan, completely opposite polarisation components behave in similar manner, i.e. for azimuthal irradiation two of the most intense peaks were for 0º and -45º components whereas for radial irradiation these were 90º and 45º. Similarly in azimuthal irradiation (d) 90º increased and in radial irradiation (d) 0º. Figure 6-26 visualises the behaviour of overlapped lines for an example of azimuthal irradiation. It shows which parts of each line became more dominant with the increase of hatch distance.

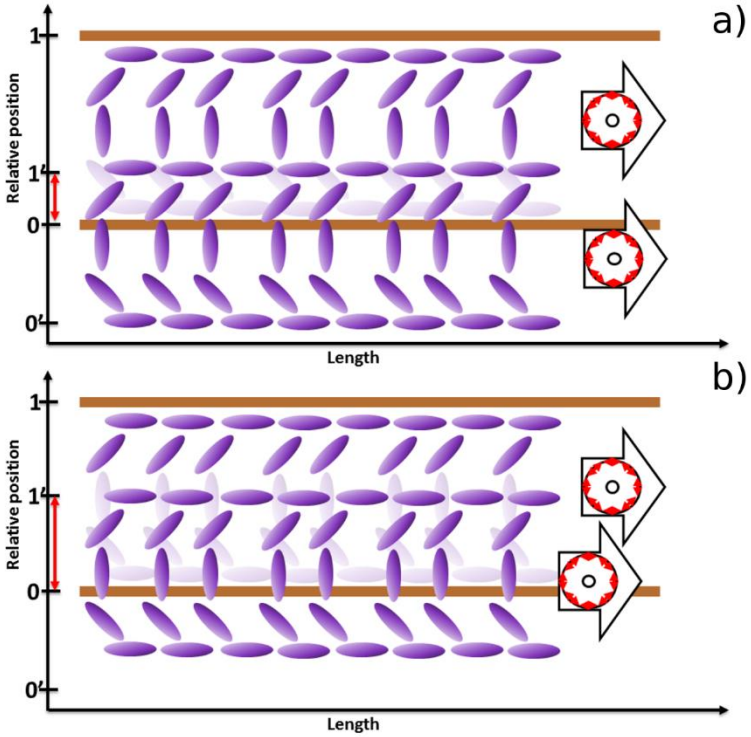

Figure 6-26 Schematic represntation of nano ellipsoids orientation for overlapped azimuthal polarisation irradiation. (a) small overlapp and (b) big overlapp are shown for left-to-right direction of irradiation.

In Figure 6-26 (a), where small overlap was present, a part of the irradiated line which was left un-overlapped (top), was placed on the top with nanoparticles orientation as follows (starting from top to bottom): {90^o, -45^o, 0^o}. If the overlap was bigger (shown in Figure 6-26 b), upper part of the beam consisted of nanoparticles orientation as follows: {90^o, -45^o}. It was shown in Figure 6-22 that every next line that was irradiated on top of a previous one dominated in terms of the orientation of nanoparticles. It was therefore obvious that the red-shifted peak intensity change represented exactly that effect. It has to be noted that in Figure 6-26, nanoparticle orientation of 90^o stayed unchanged for both overlaps (a and b) even though it was not a dominant polarisation component in the spectrophotometer results in Figure 6-24. This resulted from the fact that nanoparticles oriented in that direction were placed both on the top and the bottom of each line therefore even smallest line overlap would have decreased the amount of nanoparticles oriented in 90^o on the bottom of each line (unless the irradiation was designed to overlap from the top).

6.5.2 Results of misalignment of the S-wave plate

Additional findings needed to be added about the alignment of the S-wave plate. In order to achieve all of the optical parameters presented in previous sub-chapters the

polarisation needed to be of great quality (which was the case for the S-wave plate that was used).

It was found that the alignment of the S-wave plate was of paramount importance, especially when change from azimuthal to radial polarisations was performed. Below, an example of results of irradiation of a 3 x 3 mm square with misaligned s-wave plate is shown (Figure 6-27). Azimuthal polarisation state was chosen. It can be seen there that the red-shifted peak spread was much bigger when compared to Figure 6-24 for the same hatch distance (18 μm).

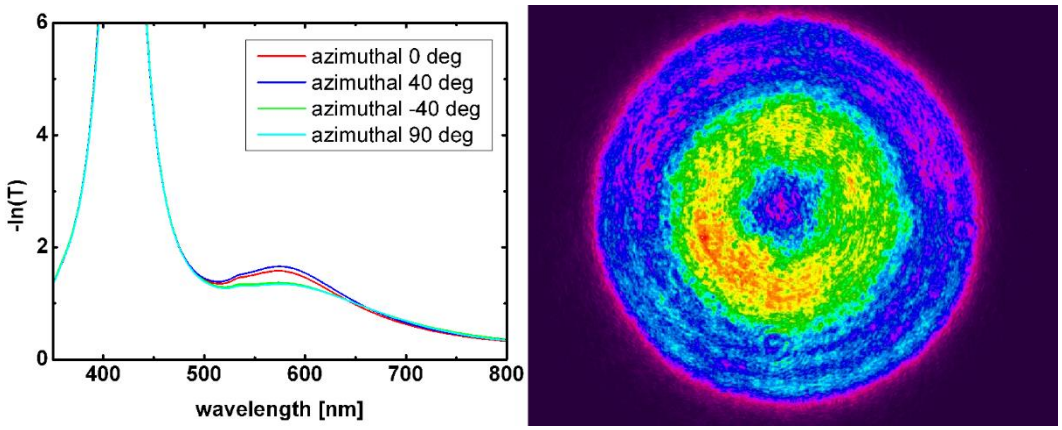

Figure 6-27 Extinction spectrum (a) and beam profile (b) of azimuthal irradiation with missaligned S-wave plate.

This result was achieved by a misaligned S-wave plate which produced a doughnut-shaped beam with irregular intensity distribution, seen in Figure 6-27 (b).

6.5.3 Macroscopic optical effects

For comparison purposes of macroscopic optical properties between radially and azimuthally polarised irradiations and linearly polarised irradiations another set of 3 x 3 mm squares was irradiated with these three different polarisation states. The extinction spectra of the irradiated areas as a function of wavelength were measured using the spectrophotometer with a linearly polarized light illumination. Spectra for four different incident polarisation directions of the illumination can be seen in Figure 6-28 for linear polarisation state of irradiation.

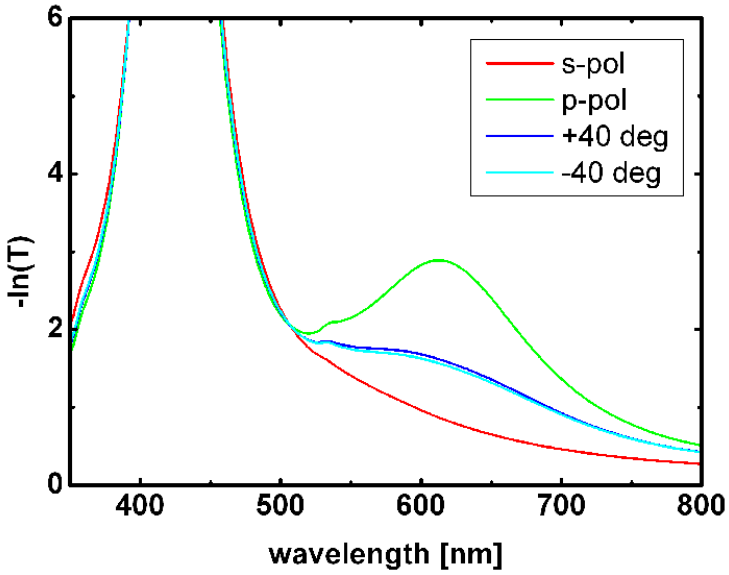

Figure 6-28 Extinction spectra measured for 3x3 mm squares irradiated with linearly polarised laser beam. Variable light polarisation was used

Figure 6-29 (a) and (b) present spectra of azimuthal and radial polarisation irradiation. Figure 6-29 (c)-(f) show microscope images of these irradiated areas. The linearly polarised microscope illumination in transmission was used to visualize the modified areas. The incident light polarisation direction was adjusted to be the same as in previous chapters, that is: 0^o, 90^o, and +/- 45^o. There was no clear dichroism present in the samples irradiated with the radial and azimuthal polarized laser beams, rather a permanent change to the SPR, with small variations in the intensity and peak position at the red-shifted band which could result from non-perfect s-wave plate alignment or overlap between lines in raster scan.

Moreover, the modification of the SPR band that can be seen from these images was rather similar for both radially and azimuthally polarized beam modified areas. The linearly polarised modified area, as explained in previous chapter, produced highly organized nano-ellipsoids (in the direction of laser polarisation).

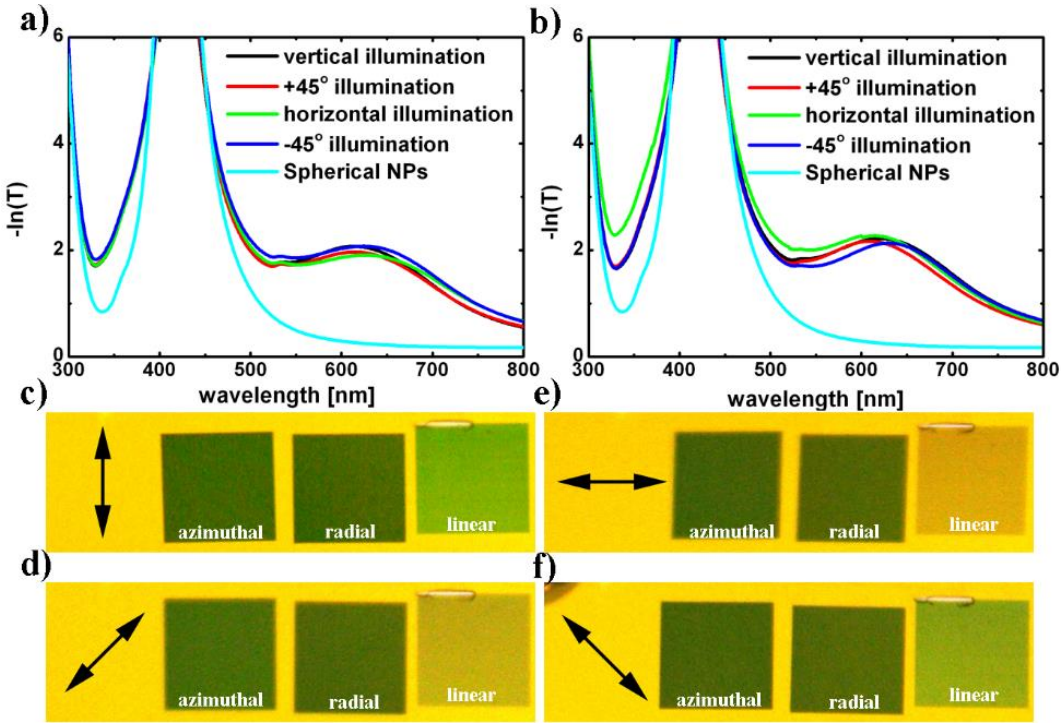

Figure 6-29 (a)-(b)Extinction spectra measured for 3x3 mm squares irradiated with azimuthal and radial polarisations. (c)-(f) Polarised microscope images of 3x3 mm squares irradiated with azimuthal, radial and linear laser polarisations.

The dichroic effect could be clearly observed as a change of colour from blue/green to brown/red between (c) and (e). Figure 6-29 (d) and (f) show an intermediate situation where both blue and red shifted SPRs are present. It should be noted that (f) has similar colour to (d), due to the fact that the direction of the nanoparticle elongation in the sample was not exactly vertical but slightly offset to the left.

6.6 Irradiation under different number of pulses per spot

It was shown in the previous chapter that irradiation under linear polarisation direction of the laser beam elongates nanoparticles along the direction of polarisation. Also, dependency of number of pulses shot on a sample was shown on the elongation rate of nanoparticles. It was concluded that the gap distance between the s- and p-polarised bands increased with the increase in number of pulses per spot.

Throughout this chapter, irradiations with 2000 pulses per spot were presented for both azimuthal and radial polarisations as that gave optimal results and was a higher value

that could have been achieved with linear polarisation, due to differences in the laser beam spot. An experiment was proposed in order to investigate the elongation ratios of nanoparticles for various number of pulses per spot. Squares of 3 x 3 mm were irradiated with azimuthal and radial polarisation using a raster scan method. The number of pulses per spot for each square were: {500, 750, 1000, 1250, 1500, 1750, and 2000}. Squares were then investigated under the spectrophotometer with linear direction of illumination polarisation as well as with an unpolarised illumination. Unpolarised illumination was found to be useful when the red-shifted peak intensity spread was small as it gave a peak position and intensity height averaged over that of single polarisation states. Figure 6-30 shows obtained spectra with unpolarised light. Only 500, 1000, 1500 and 2000 pulses per spot are shown for clarity. The band that peaked ~580nm clearly shifted towards longer wavelengths along with the increase of number of pulses shot. Also, degradation of the peak and the remnant SRP can be seen for the higher number of pulses. Small variation of peak height can be seen with azimuthal polarisation for 1000 pulses per spot, which was caused by non-perfect irradiation or unevenness of the nanoparticle layer in this part of the whole sample.

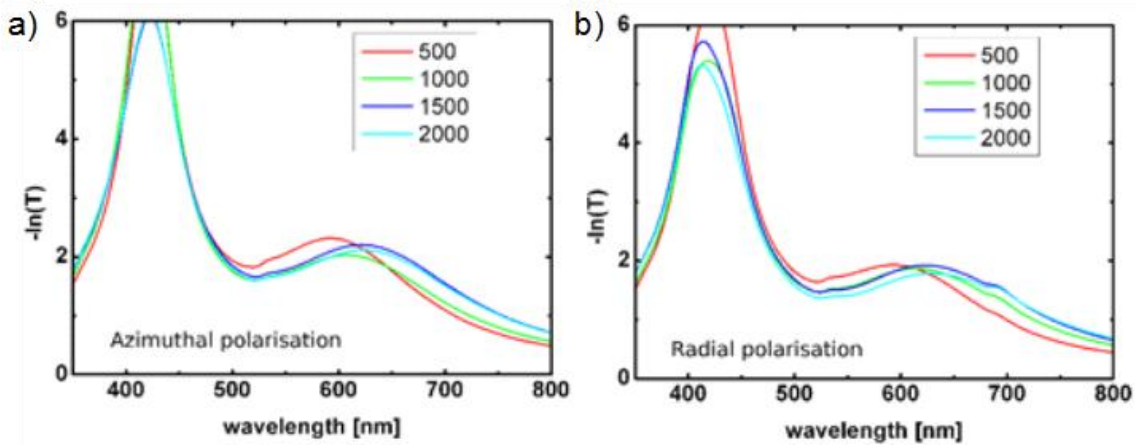

Figure 6-30 Extinction spectra for different number of pulses per spot used in irradiation with (a) azimuthal and (b) radial laser polarisations.

Separation gap distances were measured for all of the irradiated areas. Distances between red-shifted peak positions and the remnant SPR were calculated for each of the illumination polarisations. Figure 6-31 shows these gap distances as a function of number of pulses per spot.

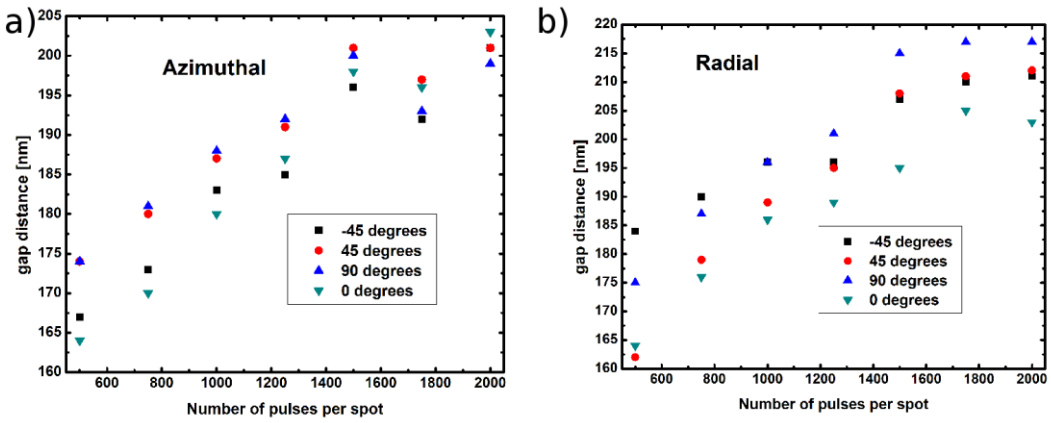

Figure 6-31 Separation gap distance as a function of number of pulses per spot for (a) azimuthal and (b) radial irradiations with increasing number of pulses per spot

The small spread in the gap distance can be seen for each irradiated area (~10 nm), which could have resulted from non-perfect S-wave plate alignment or overlap between lines in raster scan.

Results obtained from irradiation of areas with azimuthal and radial polarisation and with varying number of pulses per spot showed linear increase in the gap distance until ~1500 pulses fired. Then a saturation of the effect could have been seen, which was in agreement with linear irradiations presented in the previous chapter. It showed that the nanoparticles were being elongated in the very same manner and with the very same physics lying behind this process. The only difference lied in the fact that after irradiation, nanoparticles were oriented in all directions for both azimuthal and radial polarisation, leaving the irradiated area dichroic-less, which could be used in various engineering applications where this effect is not desired, but the ability to extinct the light of all polarisations.

6.7 Conclusions

In this chapter, radially and azimuthally polarised picosecond pulsed irradiation of Ag nanoparticles embedded in soda-lime glass has been presented. This resulted in elongation of previously spherical nanoparticles and formation of uniquely positioned nano-ellipsoids. Laser reshaping parameter change was presented as its effect on nanoparticles' modification: hatch distance, direction of irradiation and number of pulses per spot. The opposing character of reshaping between the radial and azimuthal

polarisations was presented. Macroscopically, linear optical properties for these two incident polarisations were in agreement. New linear and non-linear optical techniques were presented as a way of defining the shape and orientation of nanoparticles in reshaped MGNs. These were: polarised illuminated optical microscopy and Second-Harmonic-Generation cross-sectional scan.

The reshaping method presented in this chapter added an additional technique to shape manipulations of MGNs embedded in soda-lime glass. It expanded the knowledge base of already existing methods for versatile techniques of reshaping of nanoparticles with ultra-short laser pulses. It paved the way for nanoparticle shape modification in terms of future new experiments that could be performed with different laser polarizations in order to achieve more complicated nanoparticle modification [160], [198]–[202].

7 SHG and MAIL comparison for different types of MGNs

7.1 Introduction

Chapter 7 will describe how SHG and MAIL compares between all presented previously types of MGNs. Measurements describing output signal dependence on variable input beam polarisation will be shown, as well as the output signal dependence on output polariser direction. Emission spectra will be compared and results described according to the theory already presented (**Chapter 5)**. The absolute strength of emitted signal comparison will be performed and presented. It will add to the understanding of parameters responsible for the highest signal intensities achieved.

7.2 Illumination polarisation and output signal polarisation variation

For experiments aimed at describing the behaviour of SHG and MAIL signals and their dependence on the input polarisation, and for the output signal polarisation components description, the main emphasis will be put on comparison between ps-pulsed reshaped nanoparticles of linear elongation and other types:

1) MGNs irradiated under ~40^{o} angle of incidence
2) MGNs irradiated with radially/azimuthally oriented laser polarisation
3) MGNs irradiated with radially/azimuthally oriented laser polarisation, under ~40^{o} angle of incidence

Fs-reshaped and MS-MGNs have already been described in **Chapter 5,** and did not need additional experimental results. Also, comparison between samples produced with similar laser parameters was the most appropriate to draw reliable conclusions. Later in this chapter samples irradiated ps-irradiation will be presented:

1) *Silvering* MGNs,
2) High-fill factor MGNs,

3) MGNs reshaped from both sides of the glass sample

Their effect on created SHG and MAIL signal will be described.

Here, ps- MGNs with linear elongation of NPs (ps-MGN measured in this experiment was a ps-MGN irradiated with 1000 pulses per spot. Other parameters of irradiation presented in Chapter 4 stayed the same) was illuminated with 1064 nm fundamental laser beam while varying its direction of polarisation. The technique presented in **Chapter 5** (Figure 5-16 c) was used. The resulting signal intensity plot as a function of direction of polarisation can be seen in Figure 7-1.

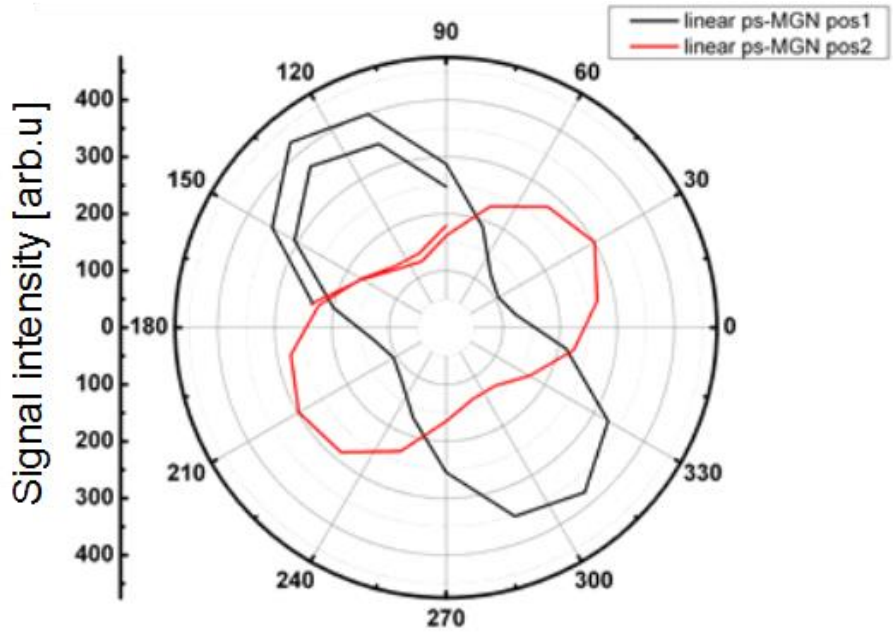

Figure 7-1 Polar plot of SHG intensity as a function of input laser polarisation direction. Samples were placed in two positions orthogonal to each other: 1 (black) and 2 (red). Ps-MGN was measured.

Two orthogonal positions of nanoparticles are presented on a polar diagram. Similarly to what was described in the **Chapter 5**, SHG and MAIL signal had the highest intensity when the input polarisation direction of the laser beam was parallel to the long axis of the nanoparticles (as presented in Table 3).

	Pos1	**Pos2**
NPs long axis direction	~120º, ~300º	~30º, ~210º
Direction when the highest SHG+MAIL intensity occurs	~120º, ~300º (same as above)	~30º, ~210º (same as above)

Table 3 Nano ellipsoids direction of long axis according to the polar plot and directions where the most intense signal was measured

Another set of samples used for this experiments involved ps-MGNs irradiated at 40º incidence angle (ps-MGN-angle at 1000 pulses per spot). The same measurement setup was used. Polar plot can be seen below (Figure 7-2). Similarly to the previous sample (ps-MGN), the highest intensity of the signal followed values from Table 3. Slightly lower intensities could be seen but comparable to ps-MGN were achieved. Lower intensities could have been a result of the effective length of nanoparticle projected on to the surface of the glass.

Assuming that NPs created in the volume of glass were on average ~30-40 nm in diameter, and that the elongation ratio for these laser parameters corresponded to ~2.70 (according to DDA calculations in **Chapter 5**, Table 2), one can calculate the projection of rotated nanoparticle on to the glass surface plane. Simplified calculations yield that the effective projected length of such ellipsoid would have an elongation ratio of ~2.07. One can compare this to previously presented FEMB sample which had elongation ratio of ~2.05, and slightly smaller emission strength in comparison to ps-MGN (**Chapter 5**).

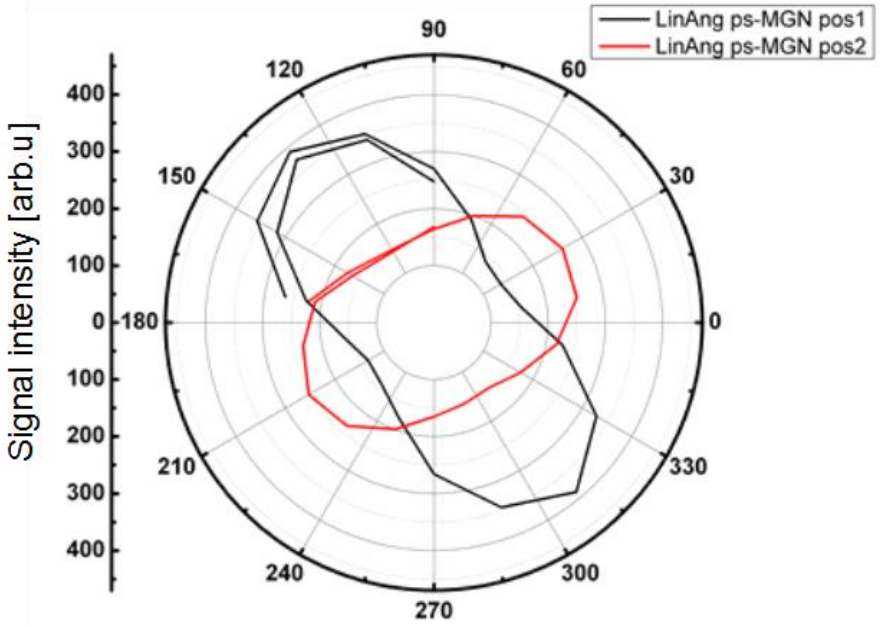

Figure 7-2 Polar plot of SHG intensity as a function of input laser polarisation direction. Samples were placed in two positions orthogonal to each other: 1 (black) and 2 (red). Ps-MGN irradiated at 40^{o} angle of incidence was measured.

Also, this result contradicted the empirically tested behaviour of MGNs in both **Chapter 5** Figure 5-14 and [35], where the incidence angle (~40^{o}) of the fundamental beam showed increase in the SHG signal. It could be then concluded that orientation of elongated silver NPs in soda-lime glass, in a presented experimental setup did not enhance the SHG signal, but actually decreased it slightly. The effect of enhancement was however measured for angled illumination where the NPs where placed perpendicularly to the surface of the glass. The volume effect however showed to increase the SHG signal intensity, where by rotating the sample, the thickness projection of the NP layer effectively increased.

Ps-reshaped MGNs with polarisations being either radial (ps-MGN-rad) or azimuthal (ps-MGN-azim) were also measured for their signal dependence on the incident polarisation direction. Samples presented in **Chapter 6**, Figure 6-29 were used. Measurements of ps-MGN-rad can be seen below:

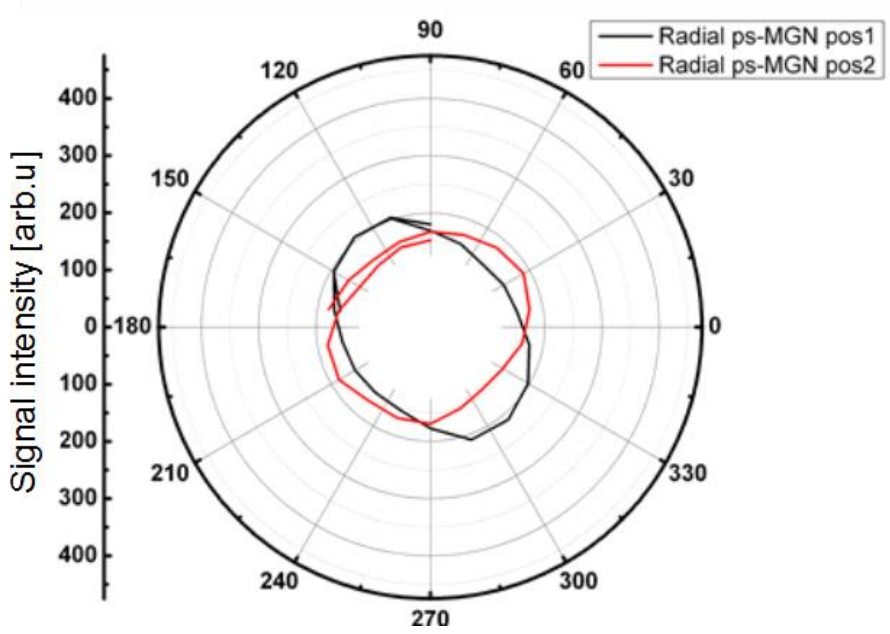

Figure 7-3 Polar plot of SHG intensity as a function of input laser polarisation direction. Samples were placed in two positions orthogonal to each other: 1 (black) and 2 (red). Ps-MGN-rad was measured.

A much smaller intensity of the emitted signal can be observed when compared to linearly irradiated MGNs. Also, this sample did not show a strong distinction between both: the position 1 or 2, and input laser polarisation direction. Small directionality can be observed however in the direction of polarisation previously named as p-pol. According to the Table 3, the highest intensity of the SHG and MAIL signal should have been seen when the long axis of nanoparticles were parallel to the input polarisation direction of the laser. It can be then concluded that ps-MGN-rad has certain directionality. It could be a result of higher elongation ratios in certain parts of each irradiated line (in the middle of each irradiated line, higher elongation ratios are expected if lines were not overlapped).

Ps-MGN-azim results can be seen in Figure 7-4.

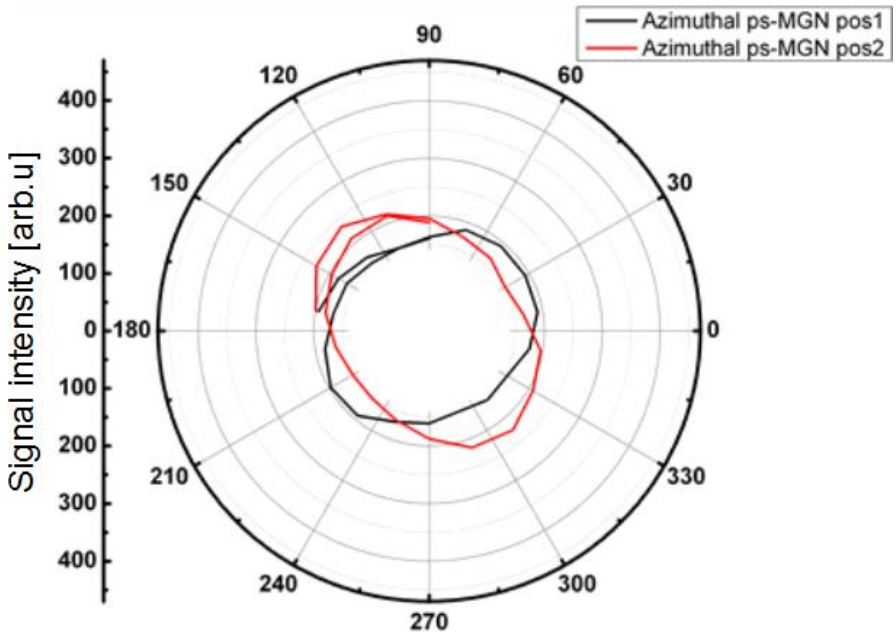

Figure 7-4 Polar plot of SHG intensity as a function of input laser polarisation direction. Samples were placed in two positions orthogonal to each other: 1 (black) and 2 (red). Ps-MGN-azim was measured.

Here, results are similar to the ps-MGN-rad, but with the directionality of the achieved signal being orthogonal to the radially irradiated sample. That corresponded to the character of reshaping that was presented in **Chapter 6**.

Samples irradiated under an angle of 40^{o} can be seen below (Figure 7-5 and Figure 7-6) for both radial and azimuthal polarisation irradiation. Similarly to the linear reshaping process, signals from samples irradiated under an angle were slightly smaller in the intensity, but the general response to the incident 1064 nm beam remained the same as the samples irradiated normal to the glass surface.

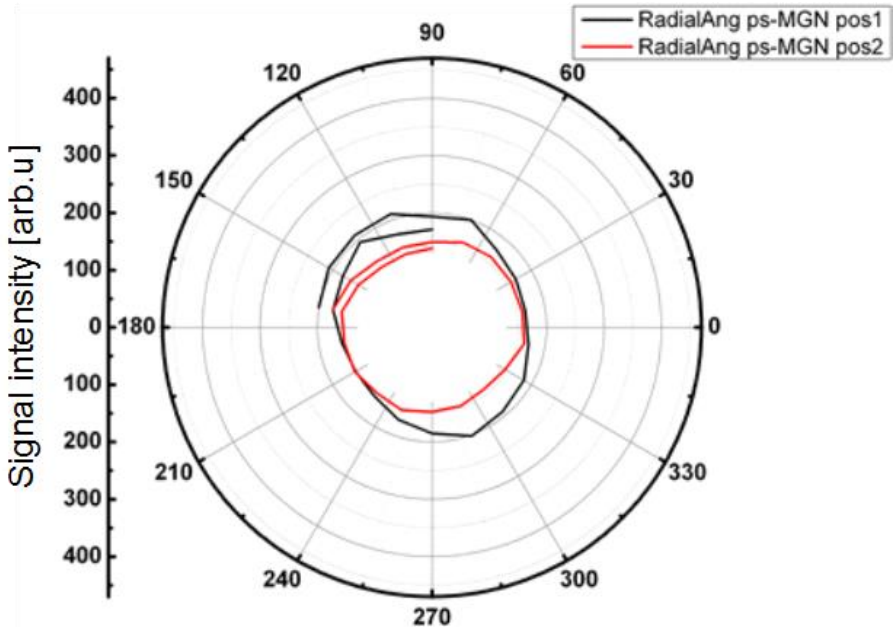

Figure 7-5 Polar plot of SHG intensity as a function of input laser polarisation direction. Samples were placed in two positions orthogonal to each other: 1 (black) and 2 (red). Ps-MGN-radANG was measured.

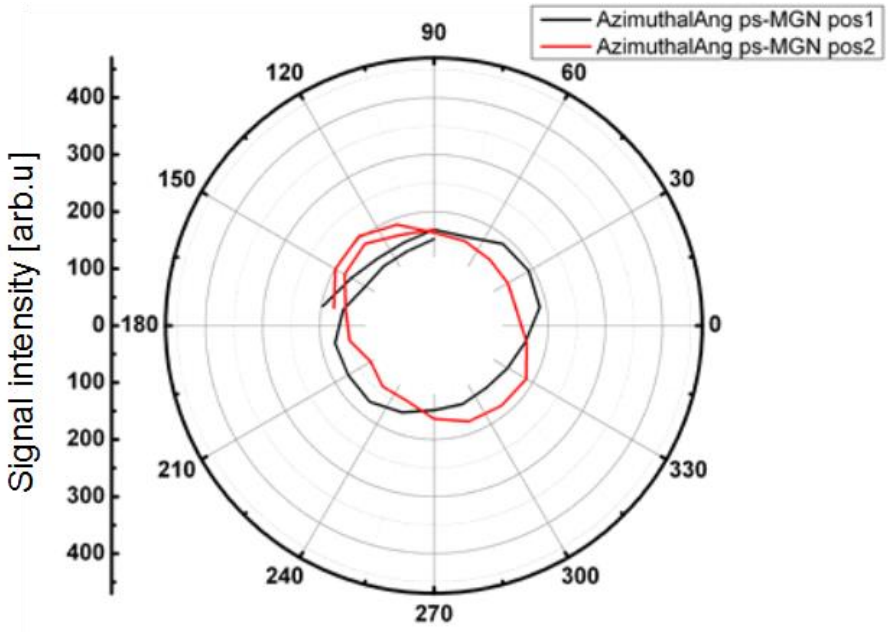

Figure 7-6 Polar plot of SHG intensity as a function of input laser polarisation direction. Samples were placed in two positions orthogonal to each other: 1 (black) and 2 (red). Ps-MGN-azimANG was measured.

In all of the presented figures, an intensity difference between position 1 and 2 exists. This effect could be present due to damage/degradation of the MGN under illumination of the fundamental beam.

Output signal polarisation components were also measured. The technique used in this experiment was presented in **Chapter 5** (Figure 5-16 d). The incident polarisation direction of the 1064 nm beam was kept constant (linear polarisation direction was aligned to the long axis of nanoparticles) while a polariser was placed at the spectrometer entrance. Rotational orientation of polariser was varied. Signal achieved for ps-MGN can be seen in Figure 7-7. A dipolar response in the signal was recorder similarly to previous samples presented in **Chapter 5.**

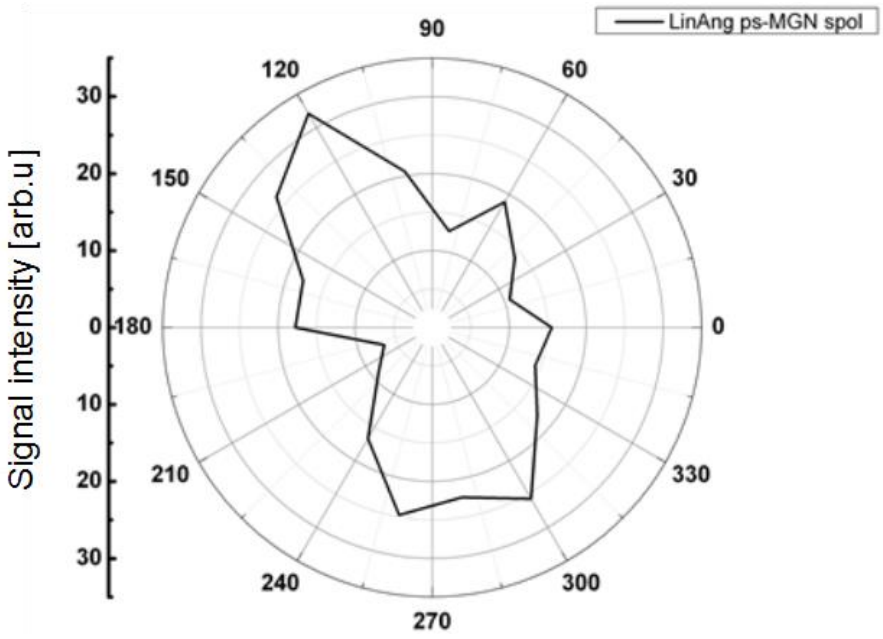

Figure 7-7 Polar plot of SHG intensity as a function of the output laser polarisation direction. P-polarisation of the fundamental beam was used. Ps-MGN was measured.

Similarly to the previous experiment, here, ps-MGN-azim (Figure 7-8) and ps-MGN-rad (Figure 7-9) were also measured and can be seen in Figure 7-8 and Figure 7-9:

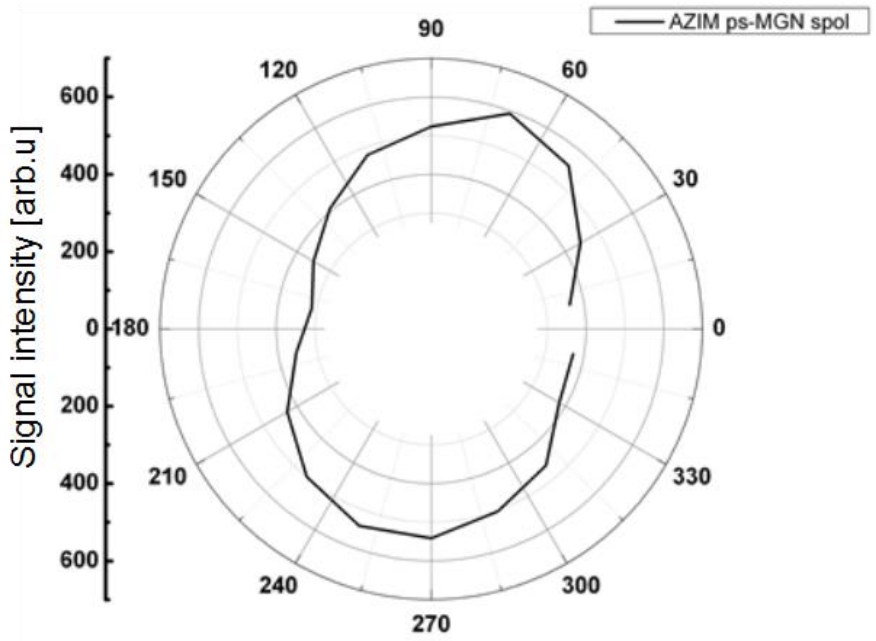

Figure 7-8 Polar plot of SHG intensity as a function of the output laser polarisation direction. P-polarisation of the fundamental beam was used. Ps-MGN-azim was measured.

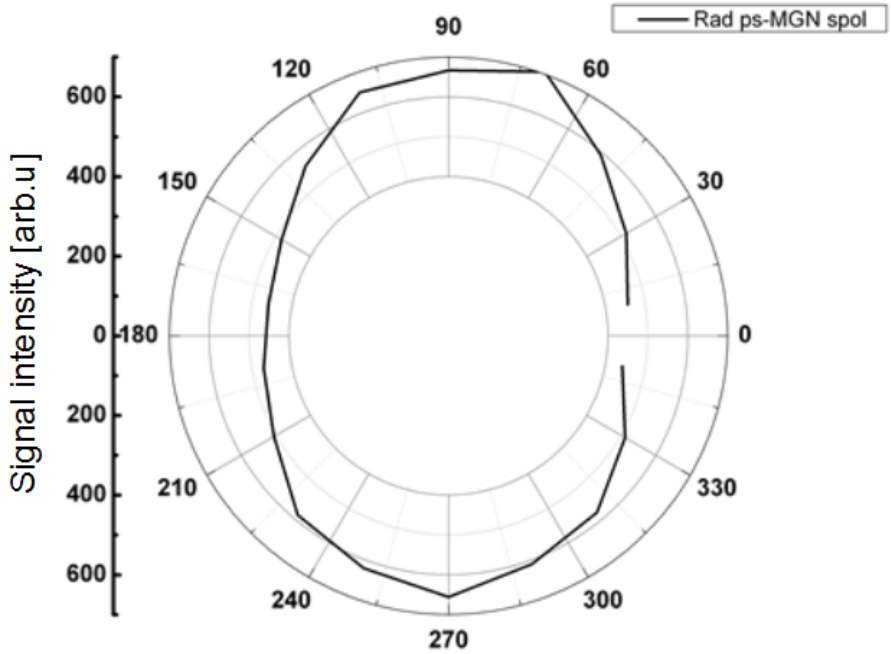

Figure 7-9 Polar plot of SHG intensity as a function of the output laser polarisation direction. P-polarisation of the fundamental beam was used. Ps-MGN-rad was measured.

Samples were illuminated with linear direction of polarisation (a p-polarisation in this case) which when passed directly through the measurement system with the absence of

MGN samples would have shown the highest signal for polariser orientation equals to 90^{o} and 270^{o}. The very same directions of highest intensity can be seen in all angular dependence plots: ps-MGN, ps-MGN-rad, ps-MGN-azim. This agrees with the expectation that the incoming beam created a dipolar field on the nanoparticle that matched the input field polarisation direction, which then re-radiated or re-scattered the newly formed electromagnetic wave in a dipolar fashion. Small rotational offsets can be seen in ps-MGN and ps-MGN-azim. This is an effect was caused by the precision to which the nanoparticles could have been aligned. Also, higher fluence values had to be used to ps-MGN-azim and ps-MGN-rad. Their signal in comparison to ps-MGN was much weaker and SHG less distinguishable. That led to higher absolute measurement points in presented figures due to MAIL involvement in the signal.

Samples ps-MGN-angle, ps-MGN-rad-angle, and ps-MGN-azim-angle were not part of these measurements. There was no fundamental reason for them to behave differently. Also, difficulty arose when attempts to measure the two latter samples were performed, due to their very weak absolute signal strength.

7.3 Emitted signal strength and spectrum comparison

A variety of MGNs has been produced by the laser-assisted reshaping process, using a ps-pulsed laser beam. Comparison between samples produced this way in terms of their SHG and MAIL signal strength was an important step towards a fully optimized sample. Some parameters of elongated nanoparticles had already been presented, especially comparing signals between linearly reshaped MGN with ps-pulsed laser, with a fs-pulsed laser and mechanically stretched. That was a part of **Chapter 5**. In this chapter, signal comparison will be shown between MGNs created with ps-pulsed reshaping. Types of MGNs presented in earlier chapters that were processed with a ps-pulsed laser and compared here are:

A	**ps-MGN (1000 pulses per spot, linear polarisation)**
B	**ps-MGN 'silvering'** (1000 pulses per spot, linear polarisation, higher overall fluence used)
C	**HighFill** (1000 pulses per spot, linear polarization, nanoparticles created in high filling factor substrates)
D	**ps-MGN-40 deg** (1000 pulses per spot, linear polarisation, 40^{o} angle of incidence)
E	**ps-MGN-rad** (radial polarisation irradiation, 1000 pulses per spot)
F	**ps-MGN-azim** (azimuthal polarisation irradiation, 1000 pulses per spot)
G	**ps-MGN-rad-40** (radial polarisation irradiation, 1000 pulses per spot, 40^{o} angle of incidence)
H	**ps-MGN-azim-40** (azimuthal polarisation irradiation, 1000 pulses per spot, 40^{o} angle of incidence)
I	**ps-MGN-double** (500+500 pulses per spot, double sided irradiation)

Table 4 List of samples used for SHG and MAIL signal intensity comparison

In order to record differences in behaviour between these samples two types of illumination polarisation were used: linear and circular. A λ/4 wave plate was used in the optical path in order to change original linear polarisation to circular. It was thought that circular polarisation could be especially insightful for radially and azimuthally polarised samples as their nanoparticles elongation direction is spread from 0^{o} to 180^{o}.

Each sample was illuminated with a 1064 nm laser beam at ~80 nJ (which corresponds to ~2.49 mJ/cm^{2}). Resulting and spectrally resolved data from linear illumination can be seen in Figure 7-10

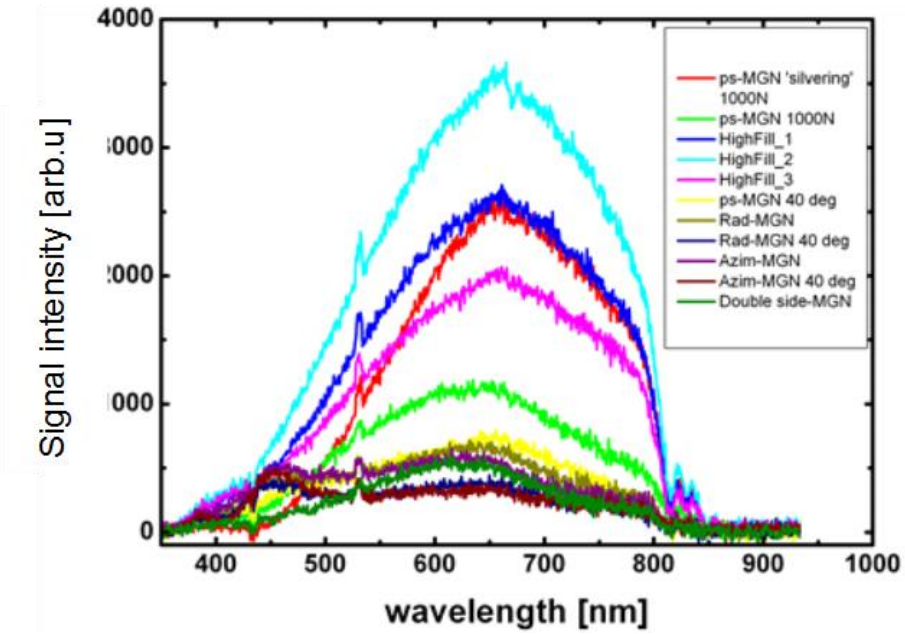

Figure 7-10 Spectrally resolved SHG and MAIL signals from samples listed in Table 2. Linear polarisation of fundamental beam was used.

Similarly as with ps-MGN, the most pronounced MAIL band was positioned spectrally at ~650 nm. Small intensity bands could be seen at ~450 nm for samples irradiated with radially and azimuthally polarized laser beam (along with their versions irradiated at 40^{o} angle).

The highest intensity of the SHG and MAIL signals were achieved for HighFill2 samples (in **Chapter 4** it was shown that HighFill samples were irradiated for three different pulse energies- 8, 10 and 13 μJ, which correspond to HighFill1, HighFill2, and HighFill3). It was observed that signal intensities (when looking at peak values of 650 nm MAIL band) for these type of samples were as follows:

	HighFill1	**HighFill2**	**Highfill3**
MAIL band intensity [arb.u.]	2500	3500	2000

Table 5 List of HighFill samples and their MAIL signal intensities

The increase and then the decrease of the signal could be explained by the dissolution of nanoparticles when irradiation with high fluence occurs. It was explained in the previous chapter, that increase in laser fluence while irradiating led to Coulomb

explosion of Ag ions from the NP and heat accumulation in the vicinity of NP. If the fluence was too high however, Ag ions could travel further distances which eventually led to lesser effect of them recoupling with ejected electrons on the poles of the nanoparticle. Heat accumulation around the NP could also lead to destruction of newly formed small ion species (**Chapter 5**). Irradiation results from **Chapter 4** in form of p-polarised extinction spectra, showed however no change in the p-pol band between HighFill2 and 3 (Figure 4-49). It was therefore believed that above laser fluences used for HighFill2 newly formed Ag ion species were destroyed by the heat.

Second type of MGNs with significantly higher intensity of both SHG and MAIL was ps-MGN 'silvering'. This sample was created by increasing the laser fluence. That led to Oswald ripening of silver particles and formation of a silver layer close to the percolation threshold on the surface of glass (**Chapter 4)**. It was shown in **Chapter 2** that the overall increase in the NP size, even for the spherical nanoparticle, can lead to higher extinction cross-sections. It was shown with SEM technique that bigger nanoparticle formation occurs in the ripening process, and it was believed to cause the higher intensity emission signal.

Radially and azimuthally polarised MGNs showed the smallest intensity of the emitted signal, due to spread of the elongation of nanoparticles in various directions.

MGNs were also illuminated with circularly polarised laser beam. Figure 7-11 presents spectrally resolved measurement data.

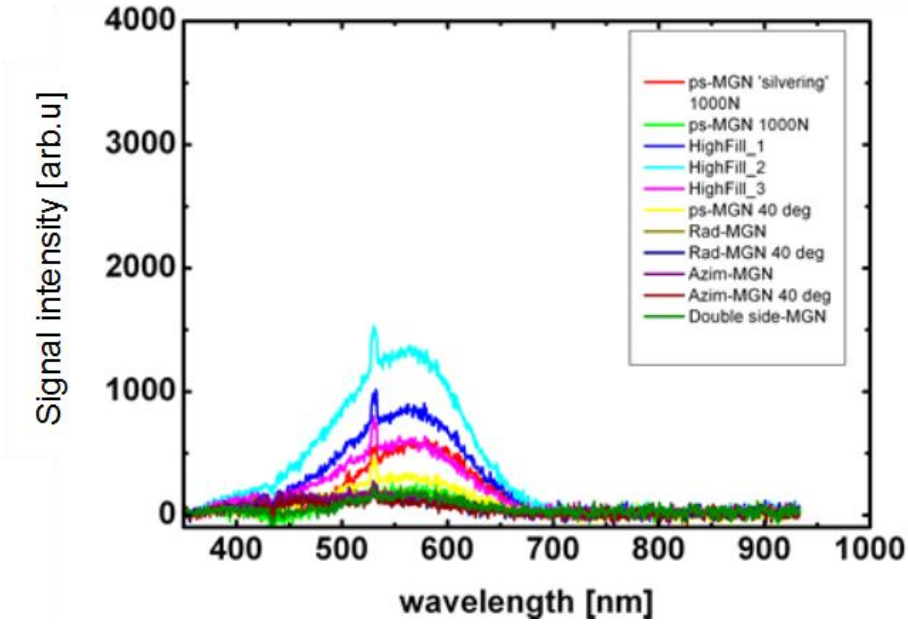

Figure 7-11 Spectrally resolved SHG and MAIL signals from samples listed in Table 2. Circular polarisation of fundamental beam was used.

Similarly to linear polarisation excitation, HighFill 1, 2, 3 and ps-MGN 'silvering' showed the highest signal intensities. SHG peak was also more pronounced than the MAIL band. Also, the MAIL signal peak at ~ 570 nm instead of ~650 nm. The observed shift in the MAIL signal could be explained by the presented hypothesis:

During the laser reshaping process of nanoparticles with a laser beam, a number of silver ions were ejected and recoupled at the poles of ellipsoidal nanoparticle. These aggregated during the same reshaping process and formed Ag species. 650 nm MAIL band is thought to be created by emission of absorbed photons in these species. However, when illuminating MGNs with circularly polarized laser beam, not only the Ag ions that are placed on poles of NPs are responsible for MAIL but also any other Ag species that were ejected into the glass matrix from Coulomb explosion. Also, the proportion of photon energy delivered to poles of the nanoparticle is lesser than to the sides of nanoparticles as the polarisation of the illumination beam rotates around its axis (due to its spin angular momentum). The interaction between the incident light and silver ions surrounding the nanoparticles at its side is the main contributor to the MAIL spectrum shown, whereas the lack of the 650 nm peak of MAIL can be explained by insufficient energies delivered to the certain Ag species located at poles of NP (it is believed that a range of these species are responsible for formation of the broad band that peaks at ~450 nm, therefore it was possible that species located lower on the energy level diagram may have been missed from interaction).

More experimental work needs to be performed to address the behaviour of MAIL signal on circularly polarised fundamental beam. The most important proposed experiment would be the luminescence observation of emission signals and its dependence on various excitation polarisation states. Greater understanding on morphology of MGNs around the whole nanoparticle after laser reshaping will also need to be addressed in the future.

7.3.1 Direct comparison between obtained signals

HighFill 2 MGN showed the highest SHG and MAIL intensity among all other MGNs that were previously treated with high power ps-pulsed laser beam. The direct comparison to the ps-MGN can be seen in Figure 7-12. Both linearly and circularly illuminated spectra can be observed.

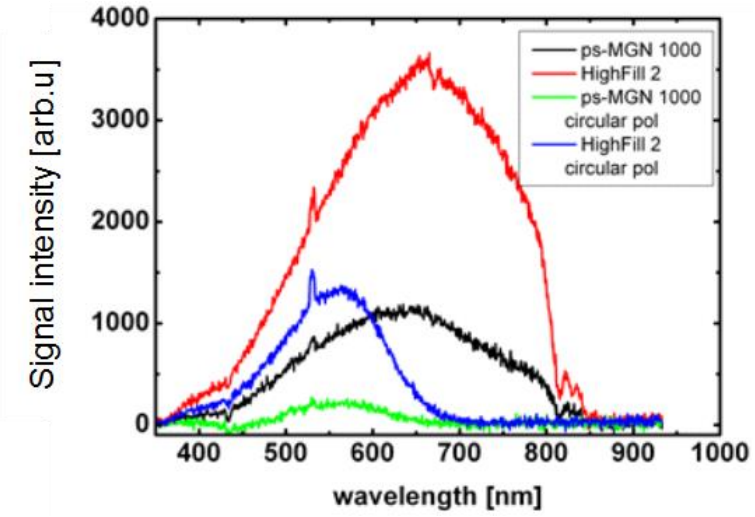

Figure 7-12 SHG and MAIL signal spectra. Comparison between ps-MGN and HighFill1 & 2 are shown for both linear and circular fundamental polarisation.

These results showed that the fill factor of the MGN played a significant role in the SHG and MAIL signal generation. In the **Chapter 4,** when the extinction spectra were created with the spectrophotometer, it was observed that the p-polarised extinction peak was much less pronounced for HighFill MGNs than for the ps-MGN samples. It was also shown that the HighFill samples had much broader SPR band and overall background extinction for 300-800 nm wavelength. Here however, HighFill MGNs show much greater signal intensity for both SHG and MAIL.

Another set of samples that were directly compared were the ‘silvering’ MGN as they also showed a significant SHG and MAIL intensity. Experimental results for ‘silvering’ MGNs can be seen below:

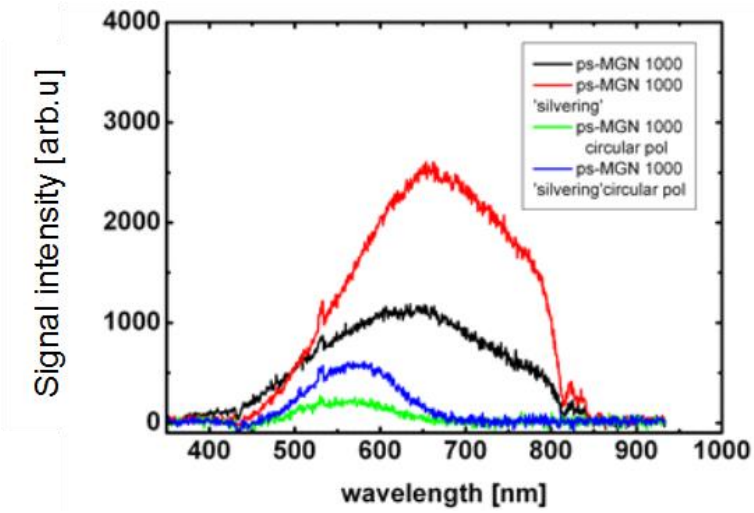

Figure 7-13 SHG and MAIL signal spectra. Comparison between ps-MGN and ‘silvering’ MGN are shown for both linear and circular fundamental polarisation.

As mentioned earlier, the higher signal intensity of the ‘silvering’ sample can be an effect of formation of much bigger nanoparticles, producing more intense extinction cross-sections. Circular polarisation results show the same emitted signal behaviour- the ‘silvering’ SHG and MAIL is of higher intensity than ps-MGN.

The comparison between ps-MGN and ps-MGN irradiated at 40^{o} incidence angle is shown in Figure 7-14.

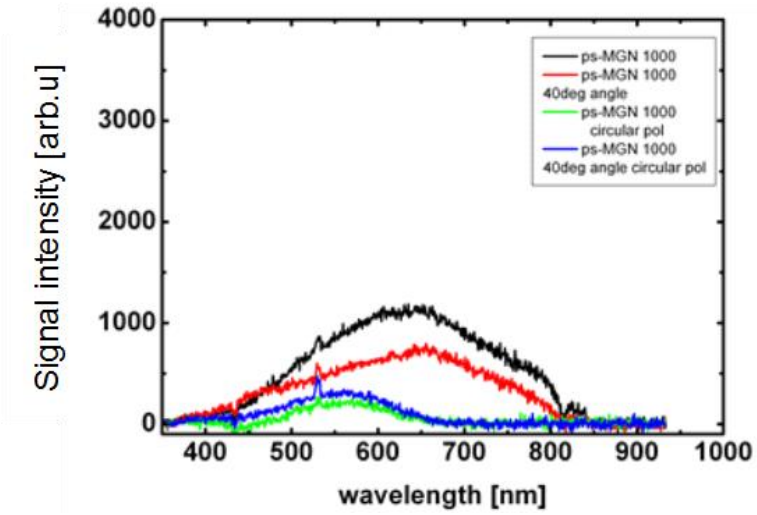

Figure 7-14 SHG and MAIL signal spectra. Comparison between ps-MGN and ps-MGN irradiated at 40^{o} are shown for both linear and circular fundamental polarisation.

It was already explained and is being confirmed here with results obtained, that MGNs irradiated at an angle show signals of weaker intensity. The main reason for that was the effect of the effective size and length of nanoparticle when illumination- that is a projected size of nanoparticle on to the glass surface. For circular polarisation illumination however, signals obtained for both samples are of similar intensity.

MGNs irradiated from both sides, which in **Chapter 4** showed much greater increase in the intensity of the p-polarised SPR peak, can be seen in Figure 7-15. Much smaller signal was obtained for them than for ps-MGN irradiated with 1000 pulses per spot. It was thought that irradiating nanoparticles with 500 pulses per spot twice (from top and bottom of the sample) increased the overall amount of nanoparticles that were elongated. However, elongation ratio might have stayed in the same range as if they were irradiated with 500 pulses per spot. Here a comparison between this sample and ps-MGN was shown which was irradiated with 1000 pulses per spot leading to higher elongation. It was believed that irradiating a MGN sample from both sides with 1000 pulses could however lead to dissolution of already reshaped from one side nanoparticles. It is also possible that 500 shots irradiation from both sides has already destroyed some Ag species along with NPs, leading to smaller SHG and MAIL signal intensity.

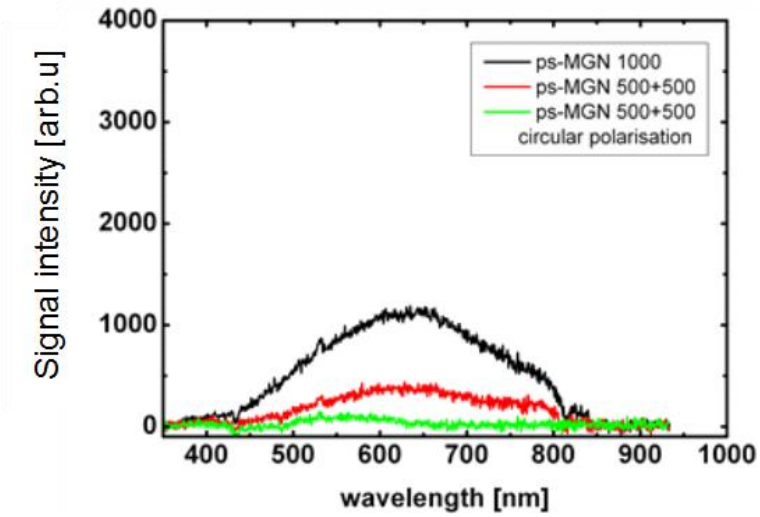

Figure 7-15 SHG and MAIL signal spectra. Comparison between ps-MGN and ps-MGN irradiated from both sides are shown for both linear and circular fundamental polarisation.

Ps-MGN-rad and ps-MGN-azim SHG and MAIL results can be seen below:

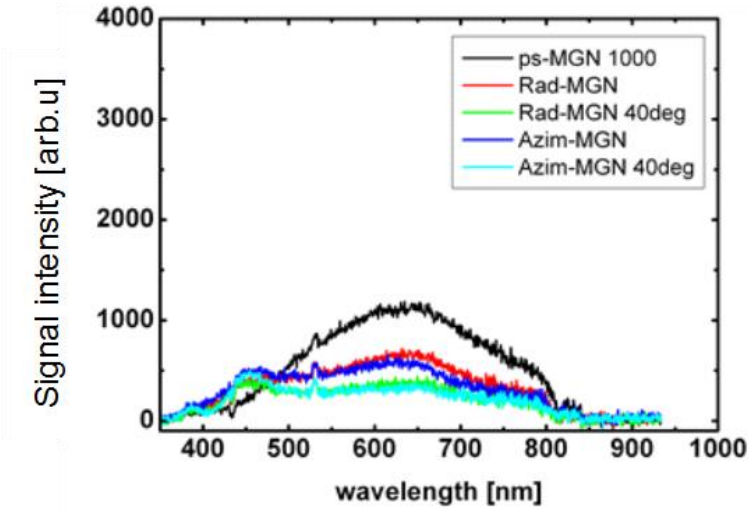

Figure 7-16 SHG and MAIL signal spectra. Comparison between ps-MGN and Rad-MGN, Rad-MGN 40 deg, Azim-MGN, Azim-MGN 40 deg are shown for linear fundamental polarisation.

Here, linear polarisation illumination results are only shown and compared. High similarity between Ps-MGN-rad and azim was observed. These types of MGNs were not much different in their elongated nanoparticle ratios and overall morphology, therefore it was expected that they would have similar signal strengths. Also, because of their projection of nano-ellipsoids to the glass surface the signal obtained from angled

samples was expected to be of smaller intensity (similarly to angled linear reshaped samples – ps-MGN-40).

Both radially and azimuthally irradiated samples were shown in **Chapter 4** to not behave in an optically dichroic way (in comparison to linearly reshaped samples). The reason for that was the orientational spread of elongated NPs around the centre axis. For the same reason it was expected that that circular polarisation illumination will give signal comparable or bigger to that of linearly reshaped nanoparticles. Experimental results can be seen in Figure 7-17

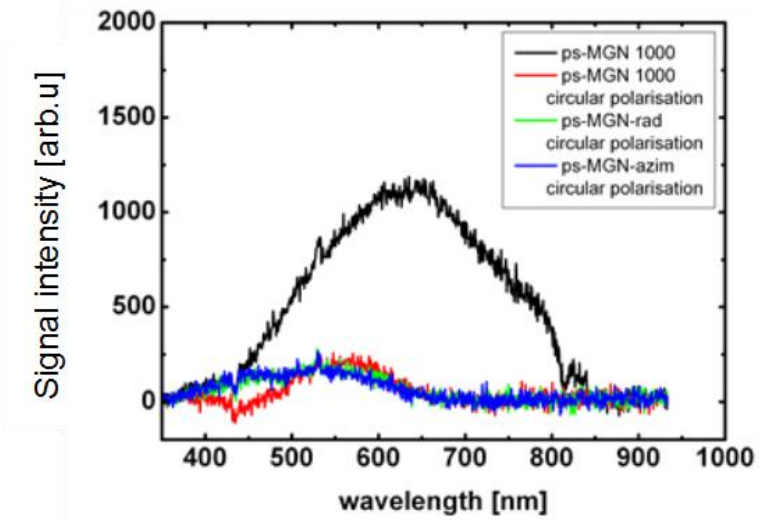

Figure 7-17 SHG and MAIL signal spectra. Comparison between ps-MGN, Rad-MGN, Azim-MGN, are shown for both linear and circular fundamental polarisation.

As seen in the figure, radially and azimuthally reshaped MGNs illuminated with circular polarisation show comparable SHG and MAIL signal to the linearly reshaped sample illuminated with the same polarisation state. Higher intensity signal for MGN-rad and MGN-azim could however be achieved in principle if the elongation ratio of radial and azimuthal MGNs were matched to that of ps-MGN.

It is important to mention that ps-MGN-rad and –azim can have a significant application if more engineering work is done to optimize their properties. These MGNs can be engineered to produce MAIL or SHG without the dependency on the incident laser polarisation, and also MGNs that will be matching or having higher signal intensity to that of linearly reshaped MGNs.

Various types of samples were shown and compared in this chapter. Presented experimental observations can lead to engineering an optimized solution for either a SHG or MAIL generator. For future reference, this chapter shows that the best

candidates for achieving the highest signals are MGNs with high filling factor as well as MGNs irradiated with laser parameters leading to Oswald ripening of silver nanoparticles in the volume and surface of the glass.

Also, it was confirmed that irradiation under an angle did not lead to increase in the SHG and MAIL signal. Work presented in **Chapter 5** as well as in the [35] paper showed how this effect depended on the effective thickness of the nanoparticle layer.

Interesting results were shown for radially and azimuthally reshaped MGNs. Their independence on input laser polarisation (small dependence in fact was shown but negligible when compared to linearly reshaped MGN) as well as signal strength comparable to linearly reshaped MGNs (under circular illumination), could lead to precise nano engineering of both SPR band position (in terms of their extinction spectrum) as well as their SHG and MAIL signal.

More experimental work needs to be performed in order to be described precisely the origin of the MAIL band shift to ~ 570 nm under circular polarisation illumination. Preferably, broader luminescence experiments could be made and presented in the future. Also, more experiments need to be devised in order to see how intensity slopes change for different samples in order to optimize the MGN to either an efficient SHG or MAIL producing device.

7.4 Conclusions

In this chapter, comparison has been performed between MGNs (presented in previous chapters) that were reshaped with a picosecond pulsed laser. Input polarisation variations and emitted polarisation components have been proved to be of similar characteristic to mechanically stretched samples. It was also shown that no increase in the SHG signal is present for nanoparticles irradiated under an angle. This leads to a better understanding of the SHG process (volume effect rather than surface).

Effect of exciting MGNs with a circularly polarised laser beam has been shown. It proved that the SHG and MAIL signals from radially and azimuthally reshaped nanoparticles can be as good as and, if optimised, better than linearly reshaped MGNs.

High Fill factor MGNs showed the highest intensity signals leading to conclusion that densely packed and elongated nanoparticles are the best candidates for future efficient SHG/MAIL converters. Also, *silvering* MGNs emitted more intense signals than

traditionally elongated nanoparticles. This showed to be a great way of optimization of emitted signal from nanoparticles when irradiating with a picosecond laser.

This work can be used as a foundation for the production of efficient SHG and MAIL converters. Various types of samples were shown and compared and conclusions were presented about the resulting signal emission.

8 Future work, applications, conclusions and summary

8.1 Introduction

This chapter will describe potential applications of presented findings. Two of the main applications will be presented, the first of which is based on MGN's ability to generate Second Harmonic, and the second of which is based on the main motivation of this thesis – THz field modulation. Experiments shown in this chapter were performed at STFC Daresbury Laboratory with the help of the laser group led by Steve Jamison.

Also, a summary of the findings of the presented thesis will be shown and conclusions formulated.

8.2 Frequency Resolved Optical Gating (FROG)

Frequency Resolved Optical Gating, or FROG, is a technique used to measure the properties of ultrashort pulses (pulse length and phase) [203], [204]. It is widely used for ultrashort pulse measurements, where there exist no shorter pulse to probe the one that is to be measured [205], [206]. In general, FROG is an upgrade of the autocorrelation technique, which is based on the pulse intensity measurement [207], [208]. There, laser pulses are separated into two optical beam paths, where one of them has a time delay stage. The two pulses are then focused together on to a nonlinear medium (i.e. SHG crystal) that produces an SH signal whenever pulses overlap on it. The intensity of the resulting signal is measured while the time delay is varied, and pulse length is calculated from it. Typical autocorrelation setup can be seen in Figure 8-1 below.

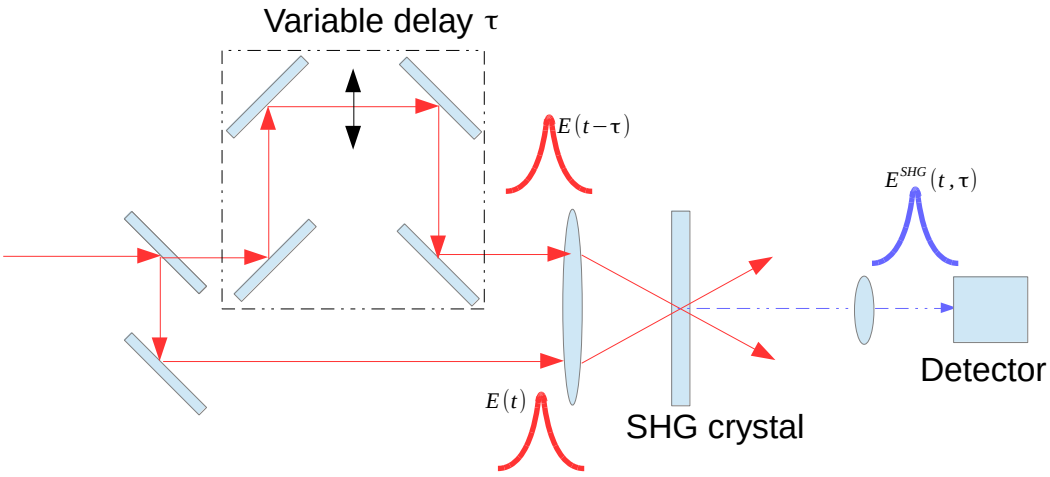

Figure 8-1 Autocorrelation measurement setup

Here, the produced SHG signal is described directly proportional to the product of two input fields with a time delay τ:

$$\boldsymbol{E}^{SHG}(t,\tau) \propto \boldsymbol{E}(t)\boldsymbol{E}(t-\tau) \qquad 8\text{-}1$$

The intensity of such field can be described as:

$$I^{SHG}(t,\tau) \propto I(t)I(t-\tau) \qquad 8\text{-}2$$

The intensity autocorrelation function can be then measured which can be described as:

$$I_{AC}(\tau) = \int_{-\infty}^{+\infty} |A^{SHG}(t,\tau)|^2 dt = \int_{-\infty}^{+\infty} I^{SHG}(t,\tau) dt \qquad 8\text{-}3$$

with the complex envelope A(t,τ) and intensity $I(t,\tau)=|A(t,\tau)|^2$. Because autocorrelation needs certain assumptions about the ultrashort pulse shape, the measured values may not be exact if a more complex pulse is present. A FROG technique is therefore needed in these situations. It is based on the autocorrelation technique, where a nonlinear medium is required. A time-frequency spectrogram is however measured instead of the intensity and a two-dimensional phase-retrieval algorithm used to obtain the field and phase information of an ultrashort pulse [209]. The FROG setup can be seen in Figure 8-2.

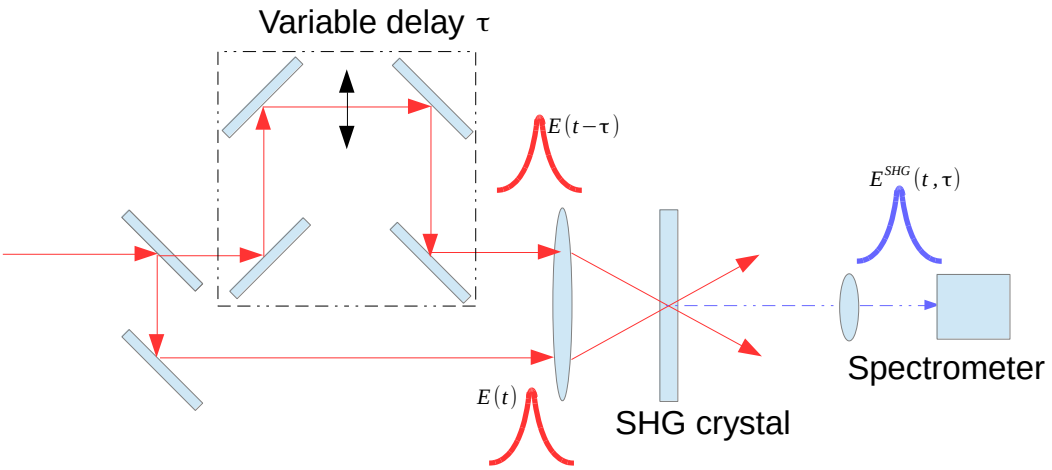

Figure 8-2 FROG based measurement setup. Here the SHG crystal would be replaced by a metallic nanoparticle composite.

Similarly to the autocorrelation, the resulting signal field is as in **8.1**. By spectrally resolving the obtained signal, a Fourier Transform with respect to time is obtained in the form of:

$$I_{FROG}^{SHG}(\omega,\tau) = \left|\int_{-\infty}^{+\infty} \boldsymbol{E}(t)\boldsymbol{E}(t-\tau)e^{(-i\omega t)}dt\right|^2 \qquad 8\text{-}4$$

An exact FROG measurement setup that was used in this thesis is presented in **Chapter 3.** There, the MS-MGN was put in place of the SHG crystal. The incidence angle was adjusted to ~40^o in order to increase the bulk contribution to the SHG signal (as described in previous chapters). Nanoparticles orientation was also adjusted in order to maximise the Surface Plasmon coupling with the incoming laser signal. The measured spectrogram along with a retrieved spectrogram can be seen in Figure 8-3. Also, the pulse profile can be seen there along with its phase information. It can be seen that the measured and retrieved pulse length was ~50 fs and its phase was flat along the pulse. This result agreed with the laser pulse length that was used. The spectrogram frequency data were centred at zero for calculations, whereas the actual measurement were taken at ~750 THz +/- 20 THz (~400 nm). The left hand side 'saw-like' phase signals are calculation artefacts that should not be assumed to be real.

Successful measurement was performed that utilised the SHG signal ability of the MS-MGN.

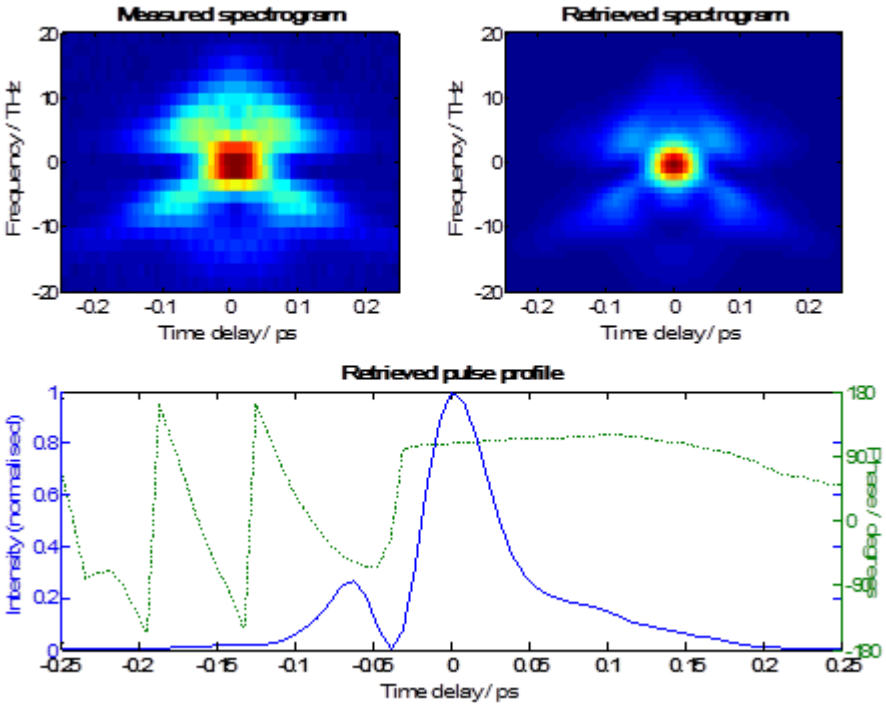

Figure 8-3 Measured and retrieved FROG spectrograms (top); Measured normalized pulse intensity in blue and phase of the pulse in green (bottom).

The ability of elongated nanoparticles to produce SHG and MAIL was shown in previous chapters. Here, the first real applications has shown that MGNs can be used in the future. It is important to mention that these results can be seen as a proof-of-principle experiment. MGNs are however versatile and their shape can be manipulated to achieve applicability in other regimes, i.e. FROG measurements for different laser wavelengths by adjusting the aspect ratio of nanoparticles to increase the plasmon coupling. Also, these types of composite can potentially be used with a different material than soda-lime glass as a host matrix and other material used for nanoparticles either. Electron-beam lithographic and lift-off methods can be utilised to produce metallic nanoparticles of various shapes and sizes on a fused silica substrate [210]. This can in theory be used in producing MGNs designed to measure ultrashort UV pulses (in the range of the lower transmittance band of the UVFS ~190 nm or even for shorter wavelengths where the surface coupling would be smaller but still measureable) utilizing the FROG technique in UV-laser sources and UV FEL facilities.

8.3 THz-based detection of ultra-short electron bunches in Free Electron Lasers and particle accelerators

The main goal for this thesis, since the very beginning, was to determine and deliver answers to the THz field interaction with nanoparticles embedded in glass. This was a very important part in the development of novel materials that could potentially swap the traditionally used Electro-Optic crystals like ZnTe or GaP in the EO detection of ultrashort electron bunches.

It was mentioned in Chapter 1 that EO methods are being used worldwide for non-destructive detection of electron beam bunch lengths. The measurement of this type is based on the first order EO property of the used crystal. This crystal then interacts with the THz field that is being produced by an electron bunch and a laser measurements setup is used for THz pulse (therefore electron bunch) length detection. The interaction of a THz pulse with an appropriate material induces an electric displacement **D** which can be described as:

$$\boldsymbol{D} = \epsilon_0 \boldsymbol{E_{THz}} + \boldsymbol{P} = \epsilon_0 (1 + \chi_e) \boldsymbol{E_{THz}} \qquad 8\text{-}5$$

Where **P** is the polarisation induced by the electric field of the THz pulse ($\mathbf{E}_{\mathrm{THz}}$). If the field is high enough, nonlinear terms can be taken into account that can be described using the Taylor expansion of the polarisation:

$$\boldsymbol{P} = \epsilon_0 \chi_e \boldsymbol{E_{THz}} = \epsilon_0 (\chi_e^{(1)} \boldsymbol{E_{THz}} + \chi_e^{(2)} \boldsymbol{E_{THz}^2} + \chi_e^{(3)} \boldsymbol{E_{THz}^3} + \cdots \qquad 8\text{-}6$$

The aforementioned crystals (ZnTe and GaP) are used for detection because of their ability to utilize their characteristic of second-order nonlinear susceptibility tensor component- χ_e^2 . The effect is described as the linear Pockels effect. This tensor susceptibility element is also always present in non-centrosymmetric materials and as a result of that in materials possessing the Second-Harmonic-Generation property.

Because of the electric field applied across the material, it becomes locally birefringent, leading to a change in the laser polarisation state, which can be later decoded to provide information about the electric field that was applied.

The main experiment that was used to provide information on nanoparticle interaction with a THz pulse was the system presented below:

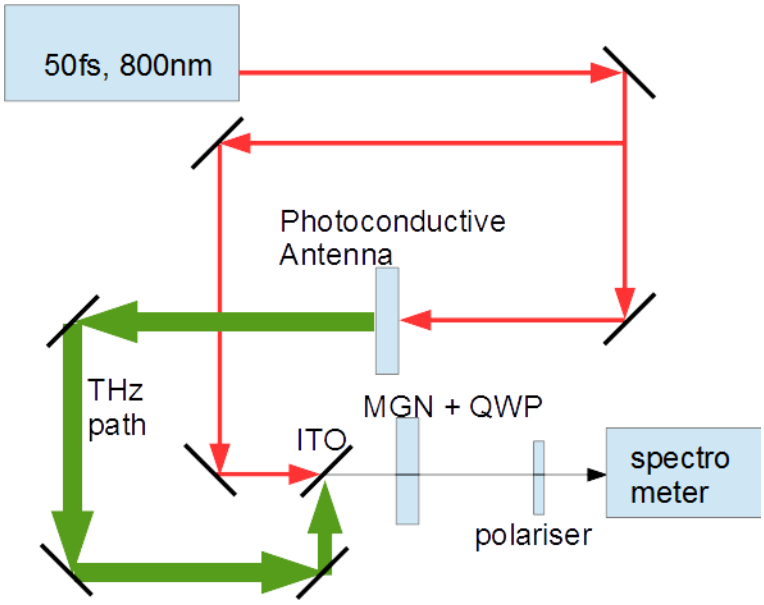

Figure 8-4 THz based measurement setup used for THz pulse interaction measurement with the nanoparticle.

In this experiment the laser pulse was split into two optical paths, where one of them was used to create a THz pulse with the use of a photoconductive antenna. ITO was later used to combine both laser pulse and the THz and the MS-MGN was used as a nonlinear EO medium along with a quarter-wave plate. It can be noted that usually for this type of measurements typical EO crystals are used in place of the MGN. The generated signal was then read out in the spectrometer.

Unfortunately, no measurable changes to the optical signal were measured. It was however not evident that the nanoparticles are an optical material that cannot be used for this purpose. Additional experiments are recommended for the future work in order to establish the optimal parameters of the nanoparticle position, orientation and shape that would interact with the THz pulse more intensely. Foundations for this type of experimentation were delivered with this thesis (with regards to nanoparticle reshaping) and should be used as a close guide to nanoparticles in glass morphology manipulation and optimisation. Additionally, a birefringence measurement would be recommended

for various types of MGNs along with simulations of their refractive indices dependence on wavelength. It is evident that the presented MGNs have an existing $\chi^{(2)}$ tensor element, which was shown and resulted in strong SHG and ability to measure FROG signals. Optimisation for THz frequencies needs to be added for successful EO measurements.

8.4 Conclusions and summary

This thesis has described a novel *meta-material* in a form of a composite of silver nanoparticles and soda-lime glass. Electro-Optical techniques used for length measurements of ultrashort electron bunches based on MGNs were proposed as a promising candidate for future experiments in places like CLIC CERN. Techniques for optimisation of nanoparticles morphology were presented and their linear and non-linear optical properties characterised. Although the preliminary test with EO setup was not successful, it is believed that more accurate optimisation of MGN for THz fields will be required and will show applicable results.

In the first experimental chapter, **Chapter 4**, laser assisted reshaping methodology of MGNs was presented in great detail. All of the main laser parameters were described and their effects on the process of irradiation shown. The laser fluence was shown to have an effect not only on reshaping but also on the size of the area affected by the laser. It was presented that the laser modification fluence must be greater than the threshold value for effective reshaping. Another parameter of number of pulses per spot fired on the sample was also shown to have a great effect on the irradiated sample. The technique of reshaping was also a parameter which needed to be established, which took into consideration the mechanical constrains of the irradiation setup and also the bi-directionality of laser reshaping shown in the literature. A polarised light microscope study was presented as an effective way of determining the nanoparticle orientation and shape. Surface Plasmon Resonances of presented MGNs were shown and its change dependence on the type of irradiation, directionality of laser path, and more. Dichroism was created in nanoparticles by elongating them upon linear ps-pulsed laser irradiation. It was also shown that the amount of elongation was proportional to the number of pulses per spot fired and to the laser repetition rate.

Also, a *silvering* effect was presented, which was caused by irradiation with higher laser fluence at multi pulse per spot regime. It was explained that a ripening effect was taking place that caused silver nanoparticle to coalesce and flow toward the surface of the glass

(eventually forming a percolated layer). Effect of *silvering* on SPR extinction band was explained. Additionally, a technique for modification of nanoparticle orientation along the axis normal to the surface was described. It was achieved by irradiation under an angle, and had a pronounced effect on the MGN SPR.

A method for optimisation of reshaping was proposed in a form of double-sided irradiation which increased the p-polarised band extinction. Moreover, a high filling factor MGN was irradiated with linear polarisation leading to elongation of nanoparticles and the SPR separation.

Chapter 5 showed comparison between different types of MGNs. These were: mechanically stretched (MS-MGN), reshaped by a femtosecond irradiation (FEMA-FEMB), and presented in **Chapter 4** MGNs reshaped by a picosecond irradiation. Second-Harmonic-Generation was shown to take place in all of these samples. It was also proved that the host matrix (soda-lime glass) did not caused the SHG in these samples, but the nanoparticles. Firstly, MS-MGN was characterised in term of its SHG parameters, as the sample that had the strongest signal due to the highest intensity of plasmon coupling with the fundamental laser beam (1064 nm @10 ps pulse width). Dependencies upon input laser polarisation change was presented. Also, polarisation components of the produced SHG were separated and spectrally resolved, and increase of the SHG signal as a function of the laser pulse energy was shown. Similar effects were presented for FEM MGNs and ps-MGNs.

Luminescence characterisation of presented MGNs was performed and results were used to explanation of the broad band signal that was observed in the background of the SHG. Multiphoton-Absorption-Induced-Luminescence (MAIL) was introduced as a result. Comparison between samples' spectrally resolved signals was performed and explanation for formation of optical MAIL bands presented.

Discrete-Dipole-Approximation (DDA) simulation method was used for modelling of the absorption, scattering and extinction SPR bands for nanoparticles embedded in soda-lime glass. Elongation ratios were estimated from DDA calculations and the ratio between absorption and scattering was shown and compared to the experimental results giving very good agreement. Lastly, a Jabłoński diagram was introduced in order to visualise the underlying cause for MAIL band formation.

Chapter 6 considered irradiation of MGNs with a laser polarisation transformed from linear to radial and/or azimuthal. There, lines of various thicknesses were irradiated and

analysed with a polarised light microscope technique introduced in **Chapter 4**. It was shown there that the single line's extinction changes within its cross section. A novel method was devised in order to determine changes in the modified single lines, which involved SHG and MAIL dependence on the elongated nanoparticle orientation (property introduced in **Chapter 5**). Evidence was provided that nanoparticles were elongating during the irradiation with either radial or azimuthal polarisation. Also, there were changing their orientation accordingly to the tail of the irradiating beam. SPR band dependence on hatching distance was shown to have a great impact and that it can be tailored to achieve desired effect.

Next, square 3x3 mm areas were irradiated and their macroscopic optical properties were discussed. It was shown that the SPR band did not change in a dichroic way (as seen with the linearly polarised irradiation) but rather stayed at a particular spectral position. Also, dependence of SPR separation on number of pulses per spot was presented for both polarisations.

Chapter 7 described a direct comparison between various types of reshaped MGNs that were introduced within this thesis. Firstly, SHG properties were characterised for: ps-MGNs, ps-MGNs irradiated under 40^{o} incidence angle, ps-MGN irradiated with either radial or azimuthal polarisation. Input polarisation dependence on SHG signal as well as the SHG polarisation components were shown. Secondly, SHG signal strength was compared for different types of reshaped MGNs:

1. ps-MGNs
2. ps-MGNs irradiated with laser parameters that led to the *silvering* effect
3. High filling factor sample, reshaped with a ps-laser
4. ps-MGN illuminated under 40^{o} incidence angle
5. ps-MGN-radial and ps-MGN-azimuthal
6. ps-MGN-radial and ps-MGN-azimuthal irradiated under 40^{o} incidence angle
7. ps-MGN-double sided irradiation

Measurements were performed for both linear and circular polarisation of the fundamental beam. It was shown how the MGN type, morphology and modification changes their response to SH generation. Samples with the highest amount of SHG were identified.

The beginning of this chapter (**Chapter 8**) showed some of the applications that can be used that utilize reshaped MGNs. It was shown that Frequency Resolved Optical Gating

(FROG) can be effectively used for measurements of ultrashort pulses when the nonlinear optical medium is replaced with an MGN sample.

Also, it was shown that MGNs can potentially be used in detection and bunch length measurements of relativistic electron bunches using Electro-Optical techniques. Although, direct measurements were performed and showed not successful result, it was concluded that optimisation of nanoparticles shape, orientation, size, needs to be performed in order for them to interact with the THz pulse effectively.

Work presented in this thesis could potentially be used in the future by the research community for optimization of the EO detection method. One of the main goals of this work was to provide the community with a toolbox that would be used in future research. Detailed theory of the light – nanoparticle interaction was presented with precise description of simulations used for this purpose as well as the temperatures models in the MGNs. Techniques for nanoparticle reshaping, linear optical characterisation, nonlinear optical characterisation, luminescence and SHG were presented, along with details on experimental setups used. Novel ways of characterisation of nanoparticle orientation was presented in a form of the SHG translation setup (Figure 3-14), UV-VIS spectrum analysis, as well as the simplified colour analysis. With such created toolbox, one should be able to not only reshape nanoparticles to desired shape and orientation, but also characterise them in detail in terms of their optical parameters (and potentially EO parameters).

8.5 Future work

Metal-glass nanocomposites were presented in this thesis along with both their linear and non-linear optical properties. Dichroism, Second Harmonic Generation and Multiphoton-Absorption-Induced Luminescence were the main ones. An effective toolset was shown that could be used in the future for further experimentation with reshaping of Ag-glass composites with a ps- pulsed laser. Properties presented here, along with specially devised characterisation techniques, could be used in the future for optimisation of MGNs to work efficiently with THz pulses for relativistic electron bunch measurements. That could involve direct THz-nanoparticle interaction experiments and variation of parameters of both the experimentation setup as well as the nanoparticle composite morphology and type. Strong emphasis should be put in the

future into theoretical investigation of this type of interaction of Surface Plasmons with the THz field. Refractive indices should be modelled in this frequency regime for different types and morphologies of MGNs, followed by their manufacturing and testing in a real EO setup.

Further investigations of the third-order non-linear parameters would be recommended with regards to potential application of MGNs in EO bunch length measurements utilising a TFISH technique (Terahertz Field-Induced Second Harmonic Generation)[211], [212]. This method is a third order phenomenon, where the TFISH intensity is proportional to $\chi^{(3)}$, $I_{fundamental}$, and I_{THz} as follows [213]:

$$I_{2\omega}^{TFISH} \propto (\chi^{(3)})^2 I_{fundamental}^2 I_{THz} \qquad 8\text{-}7$$

And can be implemented in the experimental system as follows:

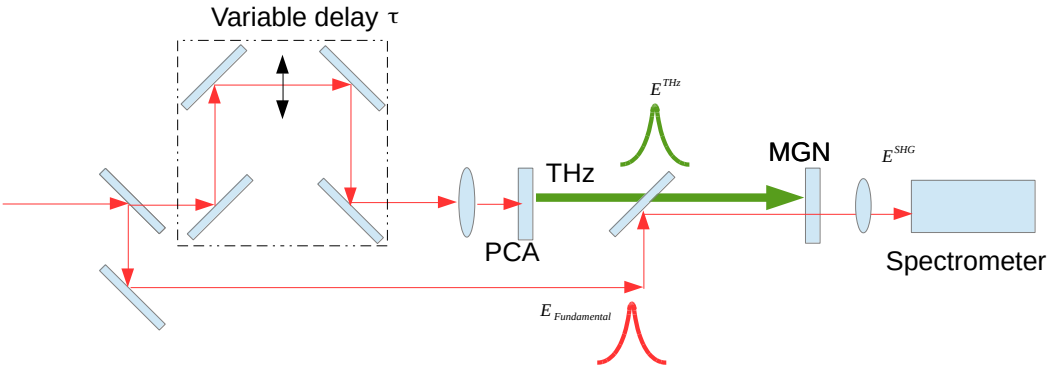

Figure 8-5 proposed TFISH technique measurement setup.

TFISH being primarily a third order effect could be potentially used for this type of experiment provided that the MGN would exhibit strong third order nonlinearity, which was documented in various other types of nanoparticles in the literature [174], [175] (but also it was shown that part of the MAIL signal was created by a third order process).

The last but a very important aspect of future improvements of MGNs that would need to be provided, are experimentations aimed at increasing the conversion efficiency for the SHG. It is believed that because photons that were created in the SHG process were 'wasted' to the background MAIL. It would be advised to quench this conversion and

absorption by the ion species in the glass, by devising a technique for the glass treatment that would result in MAIL being quenched and SHG increased.

Successful implementation of the aforementioned experiments and calculations, followed by an in-depth understanding of the nanoparticle composite interaction with a THz pulse can lead to a breakthrough in EO electron bunch measurements and be used with great success in future machines like CLIC-CERN and others.

9 References

[1] S. P. Jamison, G. Berden, A. M. Macleod, D. A. Jaroszynski, and B. Redlich, "Electro-optic techniques for temporal profile characterisation of relativistic Coulomb fields and coherent synchrotron radiation," *Nucl. Inst. Methods Phys. Res. A*, vol. 557, pp. 305–308, 2006.

[2] R. Pan, A. Andersson, W. Farabolini, A. N. Goldblatt, T. Lefevre, M. Martyanov, S. Mazzoni, L. Timeo, S. Rey, S. P. Jamison, S. D. L. Astec, W. Wa, U. Kingdom, W. A. Gillespie, D. Walsh, D. Dd, and U. Kingdom, "ELECTRO-OPTICAL BUNCH PROFILE MEASUREMENT AT CTF3," in *Proceedings of IPAC*, 2013, pp. 658–660.

[3] P. J. Phillips, W. A. Gillespie, S. P. Jamison, and A. M. Macleod, "ELECTRO-OPTIC DIAGNOSTICS ON THE DARESBURY ENERGY RECOVERY LINAC ELECTRO-OPTIC DIAGNOSTICS ON THE DARESBURY ENERGY RECOVERY LINAC," in *Tenth European Particle Accelerator Conference*, 2006, pp. 6–9.

[4] H. Tomizawa, K. Ogawa, M. Yabashi, H. Tanaka, T. Ishikawa, Y. Okayasu, S. Matsubara, T. Togashi, and J. Spring-, "THE FIRST DEMONSTRATION OF EOS 3D-BCD MONITOR TO MAXIMIZE 3D-OVERLAPPING FOR HHG-SEEDED FEL," in *Proceedings of IBIC*, 2013.

[5] A. L. Cavalieri, D. M. Fritz, S. H. Lee, P. H. Bucksbaum, D. A. Reis, J. Rudati, D. M. Mills, P. H. Fuoss, G. B. Stephenson, C. C. Kao, D. P. Siddons, D. P. Lowney, A. G. MacPhee, D. Weinstein, R. W. Falcone, R. Pahl, J. Als-Nielsen, C. Blome, S. Düsterer, R. Ischebeck, H. Schlarb, H. Schulte-Schrepping, T. Tschentscher, J. Schneider, O. Hignette, F. Sette, K. Sokolowski-Tinten, H. N. Chapman, R. W. Lee, T. N. Hansen, O. Synnergren, J. Larsson, S. Techert, J. Sheppard, J. S. Wark, M. Bergh, C. Caleman, G. Huldt, D. van der Spoel, N. Timneanu, J. Hajdu, R. A. Akre, E. Bong, P. Emma, P. Krejcik, J. Arthur, S. Brennan, K. J. Gaffney, A. M. Lindenberg, K. Luening, and J. B. Hastings, "Clocking Femtosecond X Rays," *Phys. Rev. Lett.*, vol. 94, no. 11, p. 114801, Mar. 2005.

[6] M. J. Fitch, A. C. Melissinos, P. L. Colestock, J.-P. Carneiro, H. T. Edwards, and W. H. Hartung, "Electro-optic Measurement of the Wake Fields of a Relativistic

Electron Beam," *Phys. Rev. Lett.*, vol. 87, no. 3, p. 34801, Jun. 2001.

[7] X. Yang, T. Tsang, T. Rao, J. B. Murphy, Y. Shen, and X. J. Wang, "Electron bunch length monitors using spatially encoded electro-optical technique in an orthogonal configuration," *Appl. Phys. Lett.*, vol. 95, no. 23, p. 231106, Dec. 2009.

[8] G. Berden, W. A. Gillespie, S. P. Jamison, E.-A. Knabbe, A. M. MacLeod, A. F. G. van der Meer, P. J. Phillips, H. Schlarb, B. Schmidt, P. Schmüser, and B. Steffen, "Benchmarking of Electro-Optic Monitors for Femtosecond Electron Bunches," *Phys. Rev. Lett.*, vol. 99, no. 16, p. 164801, Oct. 2007.

[9] X. Yan, A. M. Macleod, and W. A. Gillespie, "Subpicosecond Electro-optic Measurement of Relativistic Electron Pulses," *Phys. Rev. Lett.*, vol. 85, no. 16, pp. 3404–3407, 2000.

[10] S. Huang, Y. Ding, Z. Huang, and G. Marcus, "Generation of subterawatt-attosecond pulses in a soft x-ray free-electron laser," *Phys. Rev. Accel. Beams*, vol. 19, no. 8, p. 80702, Aug. 2016.

[11] CERN, "A Multi-TeV Linear Collider Based On CLIC Technology- CLIC Conceptual Design Report," 2012.

[12] A. D. Debus, M. Bussmann, U. Schramm, R. Sauerbrey, C. D. Murphy, Z. Major, R. Hörlein, L. Veisz, K. Schmid, J. Schreiber, K. Witte, S. P. Jamison, J. G. Gallacher, D. A. Jaroszynski, M. C. Kaluza, B. Hidding, S. Kiselev, R. Heathcote, P. S. Foster, D. Neely, E. J. Divall, C. J. Hooker, J. M. Smith, K. Ertel, A. J. Langley, P. Norreys, J. L. Collier, and S. Karsch, "Electron Bunch Length Measurements from Laser-Accelerated Electrons Using Single-Shot THz Time-Domain Interferometry," *Phys. Rev. Lett.*, vol. 104, no. 8, p. 84802, Feb. 2010.

[13] Z.-H. He, A. G. R. Thomas, B. Beaurepaire, J. A. Nees, B. Hou, V. Malka, K. Krushelnick, and J. Faure, "Electron diffraction using ultrafast electron bunches from a laser-wakefield accelerator at kHz repetition rate," *Appl. Phys. Lett.*, vol. 102, no. 6, p. 64104, Feb. 2013.

[14] L. M. Gorbunov, S. Y. Kalmykov, and P. Mora, "Laser wakefield acceleration by petawatt ultrashort laser pulses," *Phys. Plasmas*, vol. 12, no. 3, p. 33101, Mar. 2005.

[15] J. Grebenyuk, K. Floettmann, T. Mehrling, and J. Osterhoff, "LASER-

WAKEFIELD ACCELERATION WITH EXTERNAL BUNCH INJECTION AT REGAE ∗," in *Proceedings of RUPAC*, 2012, pp. 254–256.

[16] J. Zhu, R. W. Assmann, U. Dorda, and B. Marchetti, "Matching sub-fs electron bunches for laser-driven plasma acceleration at SINBAD," *Nucl. Instruments Methods Phys. Res. Sect. A Accel. Spectrometers, Detect. Assoc. Equip.*, vol. 829, pp. 229–232, Sep. 2016.

[17] F. Christie, J. Rönsch-Schulenburg, S. Schreiber, and M. Vogt, "Generation of Ultra-Short Electron Bunches and FEL Pulses and Characterization of Their Longitudinal Properties At FLASH2," *Proc. IPAC 2017, Copenhagen, Denmark*, vol. 2, no. 1, pp. 2600–2603, 2017.

[18] M. K. Weikum, G. Andonian, N. S. Sudar, M. G. Fedurin, M. N. Polyanskiy, C. Swinson, A. Ovodenko, F. O'Shea, M. Harrison, Z. M. Sheng, and R. W. Assmann, "Preliminary measurements for a sub-femtosecond electron bunch length diagnostic," *Nucl. Instruments Methods Phys. Res. Sect. A Accel. Spectrometers, Detect. Assoc. Equip.*, vol. 1, no. 1, pp. 1–5, 2018.

[19] B. Steffen, V. Arsov, G. Berden, W. A. Gillespie, S. P. Jamison, A. M. MacLeod, A. F. G. van der Meer, P. J. Phillips, H. Schlarb, B. Schmidt, and P. Schmüser, "Electro-optic time profile monitors for femtosecond electron bunches at the soft x-ray free-electron laser FLASH," *Phys. Rev. Spec. Top. - Accel. Beams*, vol. 12, no. 3, p. 32802, Mar. 2009.

[20] G. Berden, B. Redlich, A. F. G. Van Der Meer, S. P. Jamison, A. M. Macleod, and W. A. Gillespie, "REAL-TIME , SINGLE-SHOT TEMPORAL MEASUREMENTS OF SHORT ELECTRON BUNCHES , TERAHERTZ CSR AND FEL RADIATION," in *Proceedings of DIPAC*, 2005, pp. 69–71.

[21] G. Berden, B. Redlich, A. F. G. Van Der Meer, S. P. Jamison, A. M. Macleod, and W. A. Gillespie, "HIGH TEMPORAL RESOLUTION , SINGLE-SHOT ELECTRON BUNCH-LENGTH MEASUREMENTS," in *Proceedings of the 2004 FEL Conference*, 2004, pp. 343–346.

[22] G. Berden, A. F. G. Van Der Meer, S. P. Jamison, B. Steffen, B. Schmidt, P. Schmuser, A. M. Macleod, W. A. Gillespie, and P. J. Phillips, "ELECTRO-OPTIC TECHNIQUES FOR LONGITUDINAL ELECTRON BUNCH DIAGNOSTICS Electro-optic signal Time [ps]," in *Proceedings of FEL08*, 2008, pp. 413–416.

[23] S. P. Jamison, G. Berden, A. M. Macleod, B. Steffen, P. J. Phillips, and W. A. Gillespie, “FEMTOSECOND RESOLUTION BUNCH PROFILE MEASUREMENTS,” in *Proceedings of EPAC 2006*, 2006, pp. 915–919.

[24] M. J. Fitch, A. C. Melissinos, and P. L. Colestock, “ELECTRO-OPTIC DETECTION OF THE WAKEFIELD .,” in *Proceedings of the 1999 Particle Accelerator Conference*, 1999, pp. 2181–2183.

[25] I. Wilke, A. M. MacLeod, W. A. Gillespie, G. Berden, G. M. H. Knippels, and A. F. G. van der Meer, “Single-Shot Electron-Beam Bunch Length Measurements,” *Phys. Rev. Lett.*, vol. 88, no. 12, p. 124801, Mar. 2002.

[26] G. Berden, S. P. Jamison, A. M. MacLeod, W. A. Gillespie, B. Redlich, and A. F. G. van der Meer, “Electro-Optic Technique with Improved Time Resolution for Real-Time, Nondestructive, Single-Shot Measurements of Femtosecond Electron Bunch Profiles,” *Phys. Rev. Lett.*, vol. 93, no. 11, p. 114802, Sep. 2004.

[27] S. P. Jamison, G. Berden, P. J. Phillips, W. A. Gillespie, and A. M. MacLeod, “Upconversion of a relativistic Coulomb field terahertz pulse to the near infrared,” *Appl. Phys. Lett.*, vol. 96, no. 23, p. 231114, Jun. 2010.

[28] D. A. Walsh, E. W. Snedden, and S. P. Jamison, “The time resolved measurement of ultrashort THz-band electric fields without an ultrashort probe,” *Appl. Phys. Lett.*, vol. 106, no. 181109, pp. 1–4, 2015.

[29] S. Casalbuoni, H. Schlarb, B. Schmidt, P. Schmüser, B. Steffen, and A. Winter, “Numerical studies on the electro-optic detection of femtosecond electron bunches,” *Phys. Rev. Spec. Top. - Accel. Beams*, vol. 11, no. 7, p. 72802, Jul. 2008.

[30] Q. Wu, M. Litz, and X. -C. Zhang, “Broadband detection capability of ZnTe electro-optic field detectors,” *Appl. Phys. Lett.*, vol. 68, no. 21, pp. 2924–2926, May 1996.

[31] J. A. Valdmanis, G. Mourou, and C. W. Gabel, “Picosecond electro-optic sampling system,” *Appl. Phys. Lett.*, vol. 41, no. 3, pp. 211–212, Aug. 1982.

[32] Q. Wu and X. -C. Zhang, “Free-space electro-optic sampling of terahertz beams,” *Appl. Phys. Lett.*, vol. 67, no. 24, pp. 3523–3525, Dec. 1995.

[33] R. A. Kaindl, F. Eickemeyer, M. Woerner, and T. Elsaesser, “Broadband phase-matched difference frequency mixing of femtosecond pulses in GaSe:

Experiment and theory," *Appl. Phys. Lett.*, vol. 75, no. 8, pp. 1060–1062, 1999.

[34] S. P. Jamison, "Femtosecond resolution bunch profile diagnostics," in *FLS'12*, 2012, no. March.

[35] A. Podlipensky, J. Lange, G. Seifert, H. Graener, and I. Cravetchi, "Second-harmonic generation from ellipsoidal silver nanoparticles embedded in silica glass," *Opt. Lett.*, vol. 28, no. 9, p. 716, May 2003.

[36] M. Cirilli, "Hadron therapy: collaborating for the future," CERN Courier, 2011.

[37] J. Colin and J. Bourhis, "Hadrontherapy, a treatment for X-ray resistant cancers," Centre national de la recherche scientifique, 2010.

[38] O. Barbalat, "Applications of particle accelerators," CERN, 1994.

[39] APS, "Accelerators and Beams, 4th edition," *Am. Phys. Soc.*, 2013.

[40] A. J. Antolak, "Overview of accelerator applications for security and defense," *Rev. Accel. Sci. Technol.*, vol. 8, pp. 1–14, 2015.

[41] M. Silari, "Applications of particle accelerators in medicine," *Radiat. Prot. Dosimetry*, vol. 146, no. 4, pp. 440–450, 2011.

[42] "LA3NET page." [Online]. Available: https://www.liverpool.ac.uk/la3net/.

[43] "LA3NET Report Summary," *Community Research and Development Information Service*. [Online]. Available: http://cordis.europa.eu/result/rcn/182436_en.html.

[44] "MAPS group research." [Online]. Available: http://mapsatepm.org.uk/research-interests/.

[45] M. A. Tyrk, W. A. Gillespie, G. Seifert, and A. Abdolvand, "Picosecond pulsed laser induced optical dichroism in glass with embedded metallic nanoparticles," *Opt. Express*, vol. 21, no. 19, p. 21823, Sep. 2013.

[46] S. A. Zolotovskaya, M. A. Tyrk, A. Stalmashonak, W. A. Gillespie, and A. Abdolvand, "On second harmonic generation and multiphoton-absorption induced luminescence from laser-reshaped silver nanoparticles embedded in glass," *Nanotechnology*, vol. 27, pp. 435703–435711, 2016.

[47] M. A. Tyrk, S. A. Zolotovskaya, W. A. Gillespie, and A. Abdolvand, "Radially and azimuthally polarized laser induced shape transformation of embedded metallic nanoparticles in glass," *Opt. Express*, vol. 23, no. 18, p. 23394, Sep.

2015.

[48] D. R. H. Craig F. Bohren, *Absorption and Scattering of Light by Small Particles*. Wiley-VCH Verlag GmbH & Co. KGaA, 2004.

[49] S. A. Maier, *Plasmonic: Fundamentals and applications*. Springer, 2007.

[50] U. K. Vollmer, *Kreibig, Vollmer - Optical properties of metal clusters*. Springer, 1995.

[51] Johnson P. B. and Christy R. W., "Optical Constants of the Noble Metals," *Phys Rev B*, vol. 6, no. 12, pp. 4370–4379, 1972.

[52] L. S. Slaughter, W.-S. Chang, P. Swanglap, A. Tcherniak, B. P. Khanal, E. R. Zubarev, and S. Link, "Single-Particle Spectroscopy of Gold Nanorods beyond the Quasi-Static Limit: Varying the Width at Constant Aspect Ratio," *J. Phys. Chem. C*, vol. 114, no. 11, pp. 4934–4938, Mar. 2010.

[53] J. Sancho-Parramon, "Surface plasmon resonance broadening of metallic particles in the quasi-static approximation: a numerical study of size confinement and interparticle interaction effects," *Nanotechnology*, vol. 20, no. 23, p. 235706, Jun. 2009.

[54] O. Muskens, D. Christofilos, N. Del Fatti, and F. Vallée, "Optical response of a single noble metal nanoparticle," *J. Opt. A Pure Appl. Opt.*, vol. 8, no. 4, pp. S264–S272, Apr. 2006.

[55] K. S. Lee and M. A. El-Sayed, "Gold and silver nanoparticles in sensing and imaging: Sensitivity of plasmon response to size, shape, and metal composition," *J. Phys. Chem. B*, vol. 110, no. 39, pp. 19220–19225, 2006.

[56] J. Grand, P.-M. Adam, A.-S. Grimault, A. Vial, M. Lamy de la Chapelle, J.-L. Bijeon, S. Kostcheev, and P. Royer, "Optical Extinction Spectroscopy of Oblate, Prolate and Ellipsoid Shaped Gold Nanoparticles: Experiments and Theory," *Plasmonics*, vol. 1, no. 2–4, pp. 135–140, Nov. 2006.

[57] Jackson J D, "Classical Electrodynamics." Wiley, 1962.

[58] J. Homola, S. S. Yee, and G. Gauglitz, "Surface plasmon resonance sensors: review," *Sensors Actuators B Chem.*, vol. 54, no. 1–2, pp. 3–15, Jan. 1999.

[59] M. Rubin, "Optical properties of soda lime silica glasses," *Sol. Energy Mater.*, vol. 12, no. 4, pp. 275–288, Sep. 1985.

[60] M. Gustav, “Beiträge zur optik trüber medien, speziell kolloidaler metallösungen,” *Ann Phys*, vol. 330, pp. 377–445, 1908.

[61] G. Baffou, “Mie theory for metal nanoparticles,” *J. Phys. Chem. C*, vol. 119, pp. 28586–28596, 2015.

[62] K. L. Kelly, E. Coronado, L. L. Zhao, and G. C. Schatz, “The Optical Properties of Metal Nanoparticles: The Influence of Size, Shape, and Dielectric Environment,” *J. Phys. Chem. B*, vol. 107, no. 3, pp. 668–677, Jan. 2003.

[63] S. J. Oldenburg, G. D. Hale, J. B. Jackson, and N. J. Halas, “Light scattering from dipole and quadrupole nanoshell antennas,” *Appl. Phys. Lett.*, vol. 75, no. 8, pp. 1063–1065, 1999.

[64] F. Zhou, Z. Li, Y. Liu, and Y. Xia, “Quantitative Analysis of Dipole and Quadrupole Excitation in the Surface Plasmon Resonance of Metal Nanoparticles,” *J. Phys. Chem. C*, vol. 112, no. 51, pp. 20233–20240, Dec. 2008.

[65] H. DeVoe, “Optical Properties of Molecular Aggregates. I. Classical Model of Electronic Absorption and Refraction,” *J. Chem. Phys.*, vol. 41, no. 2, pp. 393–400, Jul. 1964.

[66] H. Devoe, “Optical Properties of Molecular Aggregates. II. Classical Theory of the Refraction, Absorption, and Optical Activity of Solutions and Crystals,” vol. 3199, 1965.

[67] E. M. Purcell and C. R. Pennypacker, “Scattering and absorption of light by nonspherical dielectrid grains,” *Astrophys. J.*, vol. 186, pp. 705–714, 1973.

[68] B. T. Draine and P. J. Flatau, “The discrete-doploe approximation and its application to interstellar graphite grains,” *J. Opt. Soc. Am. A*, vol. 11, no. 4, 1994.

[69] B. T. Draine and P. J. Flatau, “Discrete-dipole approximation for scattering calculations,” *J. Opt. Soc. Am. A*, vol. 11, no. 4, pp. 1491–1499, 1994.

[70] B. T. Draine and P. J. Flatau, “Discrete-dipole approximation for periodic targets : theory and tests,” *J. Opt. Soc. Am. A*, vol. 25, no. 11, pp. 2693–2703, 2008.

[71] M. A. Yurkin, A. G. Hoekstra, R. S. Brock, and J. Q. Lu, “Systematic comparison of the discrete dipole approximation and the finite difference time domain method for large dielectric scatterers,” *Opt. Express*, vol. 15, no. 26, pp.

17902–17911, 2007.

[72] V. L. Y. Loke, T. A. Nieminen, N. R. Heckenberg, and H. Rubinsztein-Dunlop, “T-matrix calculation via discrete-dipole approximation, point matching and exploiting symmetry,” *arXiv*, Dec. 2008.

[73] C. Hafner, *The Generalized Multipole Techniques for Electromagnetic and Light Scattering*. Artech House, 1990.

[74] T. Wriedt, J. Hellmers, E. Eremina, and R. Schuh, “Light scattering by single erythrocyte: Comparison of different methods,” *J. Quant. Spectrosc. Radiat. Transf.*, vol. 100, no. 1–3, pp. 444–456, Jul. 2006.

[75] M. A. Yurkin and A. G. Hoekstra, “The discrete dipole approximation: An overview and recent developments,” *J. Quant. Spectrosc. Radiat. Transf.*, vol. 106, no. 1–3, pp. 558–589, Jul. 2007.

[76] Y. J. Zhang, “Investigation of Gold and Silver Nanoparticles on Absorption Heating and Scattering Imaging,” *Plasmonics*, vol. 6, no. 2, pp. 393–397, Jun. 2011.

[77] J. P. Marton and J. R. Lemon, “Optical properties of aggregated metal systems: Real metals,” *J. Appl. Phys.*, vol. 44, no. 9, pp. 3953–3959, Sep. 1973.

[78] G. Xu, M. Tazawa, P. Jin, and S. Nakao, “Surface plasmon resonance of sputtered Ag films: substrate and mass thickness dependence,” *Appl. Phys. A*, vol. 80, no. 7, pp. 1535–1540, Apr. 2005.

[79] D. Riabinina, M. Chaker, and J. Margot, “Dependence of gold nanoparticle production on pulse duration by laser ablation in liquid media,” *Nanotechnology*, vol. 23, no. 13, p. 135603, Apr. 2012.

[80] E. Y. Lukianova-Hleb, A. N. Volkov, and D. O. Lapotko, “Laser Pulse Duration Is Critical For the Generation of Plasmonic Nanobubbles,” *Langmuir*, vol. 30, no. 25, pp. 7425–7434, Jul. 2014.

[81] A. H. Hamad, “Effects of Different Laser Pulse Regimes (Nanosecond, Picosecond and Femtosecond) on the Ablation of Materials for Production of Nanoparticles in Liquid Solution,” in *High Energy and Short Pulse Lasers*, InTech, 2016.

[82] F. Gonella, G. Mattei, P. Mazzoldi, E. Cattaruzza, G. W. Arnold, G. Battaglin, P.

Calvelli, R. Polloni, R. Bertoncello, and R. F. Haglund, “Interaction of high-power laser light with silver nanocluster composite glasses,” *Appl. Phys. Lett.*, vol. 69, no. 20, pp. 3101–3103, Nov. 1996.

[83] L. A. H. Fleming, G. Tang, S. A. Zolotovskaya, and A. Abdolvand, “Controlled modification of optical and structural properties of glass with embedded silver nanoparticles by nanosecond pulsed laser irradiation,” *Opt. Mater. Express*, vol. 4, no. 5, p. 969, May 2014.

[84] J. Doster, G. Baraldi, J. Gonzalo, J. Solis, J. Hernandez-Rueda, and J. Siegel, “Tailoring the surface plasmon resonance of embedded silver nanoparticles by combining nano- and femtosecond laser pulses,” *Appl. Phys. Lett.*, vol. 104, no. 15, p. 153106, Apr. 2014.

[85] D. Werner, S. Hashimoto, and T. Uwada, “Remarkable Photothermal Effect of Interband Excitation on Nanosecond Laser-Induced Reshaping and Size Reduction of Pseudospherical Gold Nanoparticles in Aqueous Solution,” *Langmuir*, vol. 26, no. 12, pp. 9956–9963, Jun. 2010.

[86] A. L. Stepanov, D. E. Hole, and P. D. Townsend, “Modification of size distribution of ion implanted silver nanoparticles in sodium silicate glass using laser and thermal annealing,” *Nucl. Instruments Methods Phys. Res. Sect. B Beam Interact. with Mater. Atoms*, vol. 149, no. 1–2, pp. 89–98, Jan. 1999.

[87] A. . Stepanov, D. . Holeb, A. . Bukharaev, P. . Townsend, and N. . Nurgazizov, “Reduction of the size of the implanted silver nanoparticles in float glass during excimer laser annealing,” *Appl. Surf. Sci.*, vol. 136, no. 4, pp. 298–305, Dec. 1998.

[88] V. K. Pustovalov, “Theoretical study of heating of spherical nanoparticle in media by short laser pulses,” *Chem. Phys.*, vol. 308, no. 1–2, pp. 103–108, Jan. 2005.

[89] F. Hubenthal, M. Alschinger, M. Bauer, D. Blazquez Sanchez, N. Borg, M. Brezeanu, R. Frese, C. Hendrich, B. Krohn, M. Aeschliman, and F. Trager, “Irradiation of supported gold and silver nanoparticles with continuous-wave, nanosecond, and femtosecond laser light: a comparative study,” in *Proceedings Volume 5838, Nanotechnology II*, 2005, p. 224.

[90] B. Hüttner and G. Rohr, “On the theory of ps and sub-ps laser pulse interaction

with metals I. Surface temperature," *Appl. Surf. Sci.*, vol. 103, no. 3, pp. 269–274, Nov. 1996.

[91] B. Hüttner and G. C. Rohr, "On the theory of ps and sub-ps laser pulse interaction with metals: II. Spatial temperature distribution," *Appl. Surf. Sci.*, vol. 126, no. 1–2, pp. 129–135, Apr. 1998.

[92] D. Werner, A. Furube, T. Okamoto, and S. Hashimoto, "Femtosecond Laser-Induced Size Reduction of Aqueous Gold Nanoparticles: In Situ and Pump−Probe Spectroscopy Investigations Revealing Coulomb Explosion," *J. Phys. Chem. C*, vol. 115, no. 17, pp. 8503–8512, May 2011.

[93] G. Baraldi, J. Gonzalo, J. Solis, and J. Siegel, "Reorganizing and shaping of embedded near-coalescence silver nanoparticles with off-resonance femtosecond laser pulses," *Nanotechnology*, vol. 24, no. 25, p. 255301, Jun. 2013.

[94] A. Stalmashonak, H. Graener, and G. Seifert, "Transformation of silver nanospheres embedded in glass to nanodisks using circularly polarized femtosecond pulses," *Appl. Phys. Lett.*, vol. 94, no. 19, p. 193111, May 2009.

[95] C. M. Aguirre, C. E. Moran, J. F. Young, and N. J. Halas, "Laser-Induced Reshaping of Metallodielectric Nanoshells under Femtosecond and Nanosecond Plasmon Resonant Illumination," *J. Phys. Chem. B*, vol. 108, no. 22, pp. 7040–7045, Jun. 2004.

[96] A. Arbouet, C. Voisin, D. Christofilos, P. Langot, N. Del Fatti, F. Vallée, J. Lermé, G. Celep, E. Cottancin, M. Gaudry, M. Pellarin, M. Broyer, M. Maillard, M. P. Pileni, and M. Treguer, "Electron-Phonon Scattering in Metal Clusters," *Phys. Rev. Lett.*, vol. 90, no. 17, p. 177401, Apr. 2003.

[97] S. Link and M. A. El-Sayed, "Shape and size dependence of radiative, non-radiative and photothermal properties of gold nanocrystals," *Int. Rev. Phys. Chem.*, vol. 19, no. 3, pp. 409–453, Jul. 2000.

[98] O. L. Muskens, N. Del Fatti, and F. Vallée, "Femtosecond Response of a Single Metal Nanoparticle," *Nano Lett.*, vol. 6, no. 3, pp. 552–556, Mar. 2006.

[99] J.-Y. Bigot, J.-Y. Merle, O. Cregut, and A. Daunois, "Electron Dynamics in Copper Metallic Nanoparticles Probed with Femtosecond Optical Pulses," *Phys. Rev. Lett.*, vol. 75, no. 25, pp. 4702–4705, Dec. 1995.

[100] C. Voisin, D. Christofilos, P. A. Loukakos, N. Del Fatti, F. Vallée, J. Lermé, M.

Gaudry, E. Cottancin, M. Pellarin, and M. Broyer, “Ultrafast electron-electron scattering and energy exchanges in noble-metal nanoparticles,” *Phys. Rev. B*, vol. 69, no. 19, p. 195416, May 2004.

[101] S. Hashimoto, D. Werner, and T. Uwada, “Studies on the interaction of pulsed lasers with plasmonic gold nanoparticles toward light manipulation, heat management, and nanofabrication,” *J. Photochem. Photobiol. C Photochem. Rev.*, vol. 13, no. 1, pp. 28–54, Mar. 2012.

[102] J. Bigot and V. Halte, “Electron dynamics in metallic nanoparticles,” *Chem. Phys.*, vol. 251, pp. 181–203, 2000.

[103] M. Aeschlimann, M. Bauer, and S. Pawlik, “Competing nonradiative channels for hot electron induced surface photochemistry,” *Chem. Phys.*, vol. 205, no. 1–2, pp. 127–141, Apr. 1996.

[104] J. Cao, Y. Gao, H. E. Elsayed-Ali, R. J. D. Miller, and D. A. Mantell, “Femtosecond photoemission study of ultrafast electron dynamics in single-crystal Au(111) films,” *Phys. Rev. B*, vol. 58, no. 16, pp. 10948–10952, Oct. 1998.

[105] E. Knoesel, A. Hotzel, and M. Wolf, “Ultrafast dynamics of hot electrons and holes in copper : Excitation , energy relaxation , and transport effects,” *Phys. Rev. B*, vol. 57, no. 20, pp. 12812–12824, 1998.

[106] W. S. Fann, R. Storz, H. W. K. Tom, and J. Bokor, “Electron thermalization in gold,” *Phys. Rev. B*, vol. 46, no. 20, pp. 13592–13595, Nov. 1992.

[107] C. Voisin, D. Christofilos, N. Del Fatti, F. Vallée, B. Prével, E. Cottancin, J. Lermé, M. Pellarin, and M. Broyer, “Size-Dependent Electron-Electron Interactions in Metal Nanoparticles,” *Phys. Rev. Lett.*, vol. 85, no. 10, pp. 2200–2203, Sep. 2000.

[108] J. R. M. Saavedra, A. Asenjo-Garcia, and F. J. García de Abajo, “Hot-Electron Dynamics and Thermalization in Small Metallic Nanoparticles,” *ACS Photonics*, vol. 3, no. 9, pp. 1637–1646, Sep. 2016.

[109] S. Link, C. Burda, Z. L. Wang, and M. A. El-Sayed, “Electron dynamics in gold and gold–silver alloy nanoparticles: The influence of a nonequilibrium electron distribution and the size dependence of the electron–phonon relaxation,” *J. Chem. Phys.*, vol. 111, no. 3, pp. 1255–1264, Jul. 1999.

[110] T. S. Ahmadi, S. L. Logunov, and M. A. El-Sayed, “Picosecond Dynamics of Colloidal Gold Nanoparticles,” *J. Phys. Chem.*, vol. 100, no. 20, pp. 8053–8056, Jan. 1996.

[111] G. V Hartland, “Electron-phonon coupling and heat dissipation in metal nanoparticles,” *Int. J. Nanotechnol.*, vol. 1, no. 3, p. 307, 2004.

[112] J. Hodak, I. Martini, and G. V Hartland, “Ultrafast study of electron–phonon coupling in colloidal gold particles,” *Chem. Phys. Lett.*, vol. 284, no. 1–2, pp. 135–141, Feb. 1998.

[113] T. W. Roberti, B. A. Smith, and J. Z. Zhang, “Ultrafast electron dynamics at the liquid–metal interface: Femtosecond studies using surface plasmons in aqueous silver colloid,” *J. Chem. Phys.*, vol. 102, no. 9, pp. 3860–3866, Mar. 1995.

[114] V. Juvé, M. Scardamaglia, P. Maioli, A. Crut, S. Merabia, L. Joly, N. Del Fatti, and F. Vallée, “Cooling dynamics and thermal interface resistance of glass-embedded metal nanoparticles,” *Phys. Rev. B*, vol. 80, no. 19, p. 195406, Nov. 2009.

[115] A. Plech, V. Kotaidis, S. Grésillon, C. Dahmen, and G. von Plessen, “Laser-induced heating and melting of gold nanoparticles studied by time-resolved x-ray scattering,” *Phys. Rev. B*, vol. 70, no. 19, p. 195423, Nov. 2004.

[116] N. SINGH, “TWO-TEMPERATURE MODEL OF NONEQUILIBRIUM ELECTRON RELAXATION: A REVIEW,” *Int. J. Mod. Phys. B*, vol. 24, no. 9, pp. 1141–1158, Apr. 2010.

[117] L. Jiang and H.-L. Tsai, “Improved Two-Temperature Model and Its Application in Ultrashort Laser Heating of Metal Films,” *J. Heat Transfer*, vol. 127, no. 10, p. 1167, 2005.

[118] S. I. Anisimov, B. L. Kapeliovich, and T. L. Perel’man, “Electron emission from metal surfaces exposed to ultrashort laser pulses,” *Sov. Phys.-JETP*, vol. 39, no. 2, pp. 375–377, 1974.

[119] P. C. Verburg, G. R. B. E. Römer, and A. J. Huis in ’t Veld, “Two-temperature model for pulsed-laser-induced subsurface modifications in Si,” *Appl. Phys. A*, vol. 114, no. 4, pp. 1135–1143, Mar. 2014.

[120] Z. Lin, L. V Zhigilei, and V. Celli, “Electron-phonon coupling and electron heat capacity of metals under conditions of strong electron-phonon nonequilibrium,”

Phys. Rev. B, vol. 77, no. 7, p. 75133, Feb. 2008.

[121] Z. Lin and L. V Zhigilei, "Electron Heat Capacity in Metals at High Electron Temperatures." [Online]. Available: http://www.faculty.virginia.edu/CompMat/electron-phonon-coupling/.

[122] J. Zhang, Y. Chen, M. Hu, and X. Chen, "An improved three-dimensional two-temperature model for multi-pulse femtosecond laser ablation of aluminum," *J. Appl. Phys.*, vol. 117, no. 6, p. 63104, Feb. 2015.

[123] A. A. Unal, A. Stalmashonak, G. Seifert, and H. Graener, "Ultrafast dynamics of silver nanoparticle shape transformation studied by femtosecond pulse-pair irradiation," *Phys. Rev. B*, vol. 79, no. 11, p. 115411, Mar. 2009.

[124] J.-Y. Bigot, V. Halté, J.-C. Merle, and A. Daunois, "Electron dynamics in metallic nanoparticles," *Chem. Phys.*, vol. 251, no. 1–3, pp. 181–203, Jan. 2000.

[125] S. Link and M. A. El-Sayed, "Size and Temperature Dependence of the Plasmon Absorption of Colloidal Gold Nanoparticles," *J. Phys. Chem. B*, vol. 103, no. 21, pp. 4212–4217, May 1999.

[126] S. Link, C. Burda, B. Nikoobakht, and M. a. El-Sayed, "Laser-Induced Shape Changes of Colloidal Gold Nanorods Using Femtosecond and Nanosecond Laser Pulses," *J. Phys. Chem. B*, vol. 104, no. 26, pp. 6152–6163, Jul. 2000.

[127] W. H. Qi and M. P. Wang, "Size and shape dependent melting temperature of metallic nanoparticles," *Mater. Chem. Phys.*, vol. 88, no. 2–3, pp. 280–284, Dec. 2004.

[128] A. Stalmashonak, A. A. Unal, H. Graener, and G. Seifert, "Effects of Temperature on Laser-Induced Shape Modification of Silver Nanoparticles Embedded in Glass," *J. Phys. Chem. C*, vol. 113, no. 28, pp. 12028–12032, Jul. 2009.

[129] A. A. Unal, A. Stalmashonak, H. Graener, and G. Seifert, "Time-resolved investigation of laser-induced shape transformation of silver nanoparticles," *Phys. Rev. B*, vol. 80, no. 11, p. 115415, Sep. 2009.

[130] A. Stalmashonak, A. A. Unal, H. Graener, and G. Seifert, "Effects of Temperature on Laser-Induced Shape Modification of Silver Nanoparticles Embedded in Glass," *J. Phys. Chem. C*, vol. 113, no. 28, pp. 12028–12032, Jul. 2009.

[131] A. Stalmashonak, A. Podlipensky, G. Seifert, and H. Graener, “Intensity-driven, laser induced transformation of Ag nanospheres to anisotropic shapes,” *Appl. Phys. B*, vol. 94, no. 3, pp. 459–465, Mar. 2009.

[132] A. V. Podlipensky, “Laser assisted modification of optical and structural properties of composite glass with silver nanoparticles,” der Martin-Luther Universität Halle-Wittenberg, 2005.

[133] W. Pfeiffer, C. Kennerknecht, and M. Merschdorf, “Electron dynamics in supported metal nanoparticles: relaxation and charge transfer studied by time-resolved photoemission,” *Appl. Phys. A*, vol. 78, no. 7, pp. 1011–1028, Apr. 2004.

[134] S. Zou and G. C. Schatz, “Silver nanoparticle array structures that produce giant enhancements in electromagnetic fields,” *Chem. Phys. Lett.*, vol. 403, no. 1–3, pp. 62–67, Feb. 2005.

[135] E. Hao and G. C. Schatz, “Electromagnetic fields around silver nanoparticles and dimers,” *J. Chem. Phys.*, vol. 120, no. 1, pp. 357–366, Jan. 2004.

[136] D. C. Marinica, A. K. Kazansky, P. Nordlander, J. Aizpurua, and A. G. Borisov, “Quantum Plasmonics: Nonlinear Effects in the Field Enhancement of a Plasmonic Nanoparticle Dimer,” *Nano Lett.*, vol. 12, no. 3, pp. 1333–1339, Mar. 2012.

[137] K. Tanabe, “Field Enhancement around Metal Nanoparticles and Nanoshells: A Systematic Investigation,” *J. Phys. Chem. C*, vol. 112, no. 40, pp. 15721–15728, Oct. 2008.

[138] A. . Podlipensky, V. Grebenev, G. Seifert, and H. Graener, “Ionization and photomodification of Ag nanoparticles in soda-lime glass by 150 fs laser irradiation: a luminescence study,” *J. Lumin.*, vol. 109, no. 3–4, pp. 135–142, 2004.

[139] G. Schulze, “Versuche über die Diffusion von Silber in Glas,” *Ann. Phys.*, vol. 345, no. 2, pp. 335–367, 1913.

[140] P. Mazzoldi, S. Carturan, A. Quaranta, and C. Sada, “Ion exchange process: History, evolution and applications,” *Riv. Nuovo Cim.*, vol. 36, no. 9, pp. 397–460, 2013.

[141] J. E. Shelby, *Introduction to Glass Science and Technology*. Cambridge: Royal Society of Chemistry, 2005.

[142] H. Mehrer, a W. Imre, and E. Tanguep-Nijokep, “Diffusion and ionic conduction in oxide glasses,” *J. Phys. Conf. Ser.*, vol. 106, p. 12001, Mar. 2008.

[143] A. V. Redkov, V. V. Zhurikhina, and A. A. Lipovskii, “Formation and self-arrangement of silver nanoparticles in glass via annealing in hydrogen: The model,” *J. Non. Cryst. Solids*, vol. 376, pp. 152–157, Sep. 2013.

[144] Y. Kaganovskii, A. Lipovskii, M. Rosenbluh, and V. Zhurikhina, “Formation of nanoclusters through silver reduction in glasses: The model,” *J. Non. Cryst. Solids*, vol. 353, no. 22–23, pp. 2263–2271, 2007.

[145] M. Suszynska, L. Krajczyk, R. Capelletti, A. Baraldi, and K. J. Berg, “Microstructure and silver nanoparticles in ion-exchanged and deformed soda-lime silicate glasses,” *J. Non. Cryst. Solids*, vol. 315, no. 1–2, pp. 114–123, Jan. 2003.

[146] A. Podlipensky, A. Abdolvand, G. Seifert, H. Graener, O. Deparis, and P. G. Kazansky, “Dissolution of Silver Nanoparticles in Glass through an Intense dc Electric Field,” *J. Phys. Chem. B*, vol. 108, no. 46, pp. 17699–17702, Nov. 2004.

[147] O. Deparis, P. G. Kazansky, A. Podlipensky, A. Abdolvand, G. Seifert, and H. Graener, “Poling-assisted bleaching of soda-lime float glasses containing silver nanoparticles with a decreasing filling factor across the depth,” *J. Appl. Phys.*, vol. 100, no. 4, p. 44318, Aug. 2006.

[148] “Keyence microscope specifications.” [Online]. Available: http://www.keyence.co.uk/products/microscope/digital-microscope/vhx-1000/index.jsp.

[149] M. D. K.-D. Schicke, H. Hofmeister, “Nucleation and growth of silver nanoparticles upon thermal proccessing of ion exchanged soda lime float glass,” *Proc. Prog. Adv. Mater. Sci. through Electron Microsc.*, 2002.

[150] W. Cai, H. Hofmeister, and M. Dubiel, “P HYSICAL J OURNAL D Importance of lattice contraction in surface plasmon resonance shift for free and embedded silver particles Importance of lattice contraction in surface plasmon resonance shift for free and embedded silver particles,” vol. 253, pp. 245–253, 2001.

[151] A. Berger, K. J. Berg, and H. Hofmeister, “Aggregates of small silver particles in surface layers of glasses - electron microscopy and optical microspectroscopy,” *Zeitschrift für Phys. D Atoms, Mol. Clust.*, vol. 20, no. 1, pp. 313–315, 1991.

[152] K. J. Berg, A. Berger, and H. Hofmeister, “Small silver particles in glass surface layers produced by sodium-silver ion exchange ? their concentration and size depth profile,” *Z. Phys. D*, vol. 20, no. 1–4, pp. 309–311, Mar. 1991.

[153] H. Graener, A. Podlipensky, G. Seifert, M. Leitner, and B. Sepiol, “Shape Analysis of Laser Deformed Metallic Nanoparticles,” *CLEO Conf. poster Sess. I*, pp. 2–3, 2007.

[154] S. Wackerow and A. Abdolvand, “Optical analyses of the formation of a silver nanoparticle-containing layer in glass.,” *Opt. Express*, vol. 20, no. 21, pp. 23227–34, 2012.

[155] Coherent, “Talisker Manual.” [Online]. Available: https://www.coherent.com/lasers/laser/talisker-1000-and-he.

[156] Nutfield, “XLR8 Two Axis Scan Head Hardware Manual.” [Online]. Available: https://nutfieldtech.com/xlr8-7-packaged-2-axis-scan-head-2/.

[157] R. Trebino, P. Bowlan, P. Gabolde, X. Gu, S. Akturk, and M. Kimmel, “Simple devices for measuring complex ultrashort pulses,” *Laser Photonics Rev.*, vol. 3, no. 3, pp. 314–342, Apr. 2009.

[158] J. Extermann, L. Bonacina, F. Courvoisier, D. Kiselev, Y. Mugnier, R. Le Dantec, C. Galez, and J.-P. Wolf, “Nano-FROG: Frequency resolved optical gating by a nanometric object,” *Opt. Express*, vol. 16, no. 14, p. 10405, Jul. 2008.

[159] A. Stalmashonak, “Laser-induced shape transformation of silver nanoparticles embedded in glass,” der Martin-Luther-Universität Halle-Wittenberg, 2009.

[160] A. Stalmashonak, A. Abdolvand, and G. Seifert, “Metal-glass nanocomposite for optical storage of information,” *Appl. Phys. Lett.*, vol. 99, no. 20, p. 201904, Nov. 2011.

[161] “ImageJ.” [Online]. Available: https://imagej.nih.gov/ij/.

[162] G. Seifert, M. Kaempfe, K.-J. Berg, and H. Graener, “Production of ‘dichroitic’ diffraction gratings in glasses containing silver nanoparticles via particle deformation with ultrashort laser pulses,” *Appl. Phys. B Lasers Opt.*, vol. 73, no. 4, pp. 355–359, Sep. 2001.

[163] A. Podlipensky, A. Abdolvand, G. Seifert, and H. Graener, “Femtosecond laser assisted production of dichroitic 3D structures in composite glass containing Ag

nanoparticles," *Appl. Phys. A*, vol. 80, no. 8, pp. 1647–1652, May 2005.

[164] P. G. Kazansky, W. Yang, E. Bricchi, J. Bovatsek, A. Arai, Y. Shimotsuma, K. Miura, and K. Hirao, "'Quill' writing with ultrashort light pulses in transparent materials," *Appl. Phys. Lett.*, vol. 90, no. 15, p. 151120, Apr. 2007.

[165] O. . Efimov, L. . Glebov, S. Grantham, and M. Richardson, "Photoionization of silicate glasses exposed to IR femtosecond pulses," *J. Non. Cryst. Solids*, vol. 253, no. 1–3, pp. 58–67, Aug. 1999.

[166] A. Stalmashonak, G. Seifert, and A. Abdolvand, *Ultra-Short Pulsed Laser Engineered Metal-Glass Nanocomposites*, SpringerBr. Heidelberg: Springer International Publishing, 2013.

[167] L. A. H. Fleming, G. Tang, S. A. Zolotovskaya, and A. Abdolvand, "Controlled modification of optical and structural properties of glass with embedded silver nanoparticles by nanosecond pulsed laser irradiation," *Opt. Mater. Express*, vol. 4, no. 5, p. 969, May 2014.

[168] A. Stalmashonak, A. Podlipensky, A. Abdolvand, A. A. Unal, U. Skrzypczak, G. Seifert, and H. Graener, "Influence of nanoparticles concentration on laser-induced dichroism in composite glasses," *unpublished*.

[169] "CODIXX AG." [Online]. Available: www.codixx.de.

[170] P. Pantazis, J. Maloney, D. Wu, and S. E. Fraser, "Second harmonic generating (SHG) nanoprobes for in vivo imaging," *Proc. Natl. Acad. Sci.*, vol. 107, no. 33, pp. 14535–14540, Aug. 2010.

[171] H. Linnenbank and S. Linden, "Second harmonic generation spectroscopy on second harmonic resonant plasmonic metamaterials," *Optica*, vol. 2, no. 8, p. 698, Aug. 2015.

[172] P. C. Ray, "Size and Shape Dependent Second Order Nonlinear Optical Properties of Nanomaterials and Their Application in Biological and Chemical Sensing," *Chem. Rev.*, vol. 110, no. 9, pp. 5332–5365, Sep. 2010.

[173] W. P. Dempsey, S. E. Fraser, and P. Pantazis, "SHG nanoprobes: Advancing harmonic imaging in biology," *BioEssays*, vol. 34, no. 5, pp. 351–360, May 2012.

[174] M. Lippitz, M. A. van Dijk, and M. Orrit, "Third-Harmonic Generation from Single Gold Nanoparticles," *Nano Lett.*, vol. 5, no. 4, pp. 799–802, Apr. 2005.

[175] B. Lamprecht, J. R. Krenn, A. Leitner, and F. R. Aussenegg, “Resonant and Off-Resonant Light-Driven Plasmons in Metal Nanoparticles Studied by Femtosecond-Resolution Third-Harmonic Generation,” *Phys. Rev. Lett.*, vol. 83, no. 21, pp. 4421–4424, Nov. 1999.

[176] Y. Zeng, W. Hoyer, J. Liu, S. W. Koch, and J. V. Moloney, “Classical theory for second-harmonic generation from metallic nanoparticles,” *Phys. Rev. B*, vol. 79, no. 23, p. 235109, Jun. 2009.

[177] B. K. Canfield, S. Kujala, K. Jefimovs, J. Turunen, and M. Kauranen, “Linear and nonlinear optical responses influenced by broken symmetry in an array of gold nanoparticles,” *Opt. Express*, vol. 12, no. 22, p. 5418, 2004.

[178] J. Butet, J. Duboisset, G. Bachelier, I. Russier-Antoine, E. Benichou, C. Jonin, and P.-F. Brevet, “Optical Second Harmonic Generation of Single Metallic Nanoparticles Embedded in a Homogeneous Medium,” *Nano Lett.*, vol. 10, no. 5, pp. 1717–1721, May 2010.

[179] J. Nappa, G. Revillod, I. Russier-Antoine, E. Benichou, C. Jonin, and P. F. Brevet, “Electric dipole origin of the second harmonic generation of small metallic particles,” *Phys. Rev. B*, vol. 71, no. 16, p. 165407, Apr. 2005.

[180] H. Wang, E. C. Y. Yan, E. Borguet, and K. B. Eisenthal, “Second harmonic generation from the surface of centrosymmetric particles in bulk solution,” *Chem. Phys. Lett.*, vol. 259, no. 1–2, pp. 15–20, Aug. 1996.

[181] H.-D. Deng, G.-C. Li, Q.-F. Dai, M. Ouyang, S. Lan, V. a Trofimov, and T. M. Lysak, “Size dependent competition between second harmonic generation and two-photon luminescence observed in gold nanoparticles,” *Nanotechnology*, vol. 24, no. 7, p. 75201, Feb. 2013.

[182] M. B. Dowling, L. Li, J. Park, G. Kumi, A. Nan, H. Ghandehari, J. T. Fourkas, and P. DeShong, “Multiphoton-Absorption-Induced-Luminescence (MAIL) Imaging of Tumor-Targeted Gold Nanoparticles,” *Bioconjug. Chem.*, vol. 21, no. 11, pp. 1968–1977, Nov. 2010.

[183] D. C. Dai, S. J. Xu, S. L. Shi, M. H. Xie, and C. M. Che, “Efficient multiphoton-absorption-induced luminescence in single-crystalline ZnO at room temperature,” *Opt. Lett.*, vol. 30, no. 24, p. 3377, Dec. 2005.

[184] M. Eichelbaum, B. E. Schmidt, H. Ibrahim, and K. Rademann, “Three-photon-

induced luminescence of gold nanoparticles embedded in and located on the surface of glassy nanolayers," *Nanotechnology*, vol. 18, no. 35, p. 355702, Sep. 2007.

[185] R. a Farrer, F. L. Butterfield, V. W. Chen, and J. T. Fourkas, "Highly Efficient Multiphoton-Absorption-Induced Luminescence from Gold Nanoparticles," *Nano Lett.*, vol. 5, no. 6, pp. 1139–1142, Jun. 2005.

[186] Boyd, Yu, and Shen, "Photoinduced luminescence from the noble metals and its enhancement on roughened surfaces.," *Phys. Rev. B. Condens. Matter*, vol. 33, no. 12, pp. 7923–7936, Jun. 1986.

[187] X. Wang, S. Fardad, S. Das, A. Salandrino, and R. Hui, "Direct observation of bulk second-harmonic generation inside a glass slide with tightly focused optical fields," *Phys. Rev. B*, vol. 93, no. 16, p. 161109, Apr. 2016.

[188] R. W. Boyd, *Nonlinear Optics*. Elsevier Science, 2003.

[189] R. A. Farrer, F. L. Butterfield, V. W. Chen, and J. T. Fourkas, "Highly Efficient Multiphoton-Absorption-Induced Luminescence from Gold Nanoparticles," *Nano Lett.*, vol. 5, no. 6, pp. 1139–1142, Jun. 2005.

[190] M. B. Dowling, L. Li, J. Park, G. Kumi, A. Nan, H. Ghandehari, J. T. Fourkas, and P. DeShong, "Multiphoton-Absorption-Induced-Luminescence (MAIL) Imaging of Tumor-Targeted Gold Nanoparticles," *Bioconjug. Chem.*, vol. 21, no. 11, pp. 1968–1977, Nov. 2010.

[191] A. Mooradian, "Photoluminescence of Metals," *Phys. Rev. Lett.*, vol. 22, no. 5, pp. 185–187, Feb. 1969.

[192] I. Gryczynski, J. Malicka, Y. Shen, Z. Gryczynski, and J. R. Lakowicz, "Multiphoton Excitation of Fluorescence near Metallic Particles: Enhanced and Localized Excitation," *J. Phys. Chem. B*, vol. 106, no. 9, pp. 2191–2195, Mar. 2002.

[193] W. Wenseleers, F. Stellacci, T. Meyer-Friedrichsen, T. Mangel, C. A. Bauer, S. J. K. Pond, S. R. Marder, and J. W. Perry, "Five Orders-of-Magnitude Enhancement of Two-Photon Absorption for Dyes on Silver Nanoparticle Fractal Clusters," *J. Phys. Chem. B*, vol. 106, no. 27, pp. 6853–6863, Jul. 2002.

[194] P. Anger, P. Bharadwaj, and L. Novotny, "Enhancement and Quenching of Single-Molecule Fluorescence," *Phys. Rev. Lett.*, vol. 96, no. 11, p. 113002, Mar.

2006.

[195] E. Borsella, G. Battaglin, M. A. Garcìa, F. Gonella, P. Mazzoldi, R. Polloni, and A. Quaranta, “Structural incorporation of silver in soda-lime glass by the ion-exchange process : a photoluminescence spectroscopy study,” *Appl. Phys. A*, vol. 132, no. 71, pp. 125–132, 2000.

[196] S. Paje, “Optical spectroscopy of silver ion-exchanged As-doped glass,” *J. Non. Cryst. Solids*, vol. 318, no. 3, pp. 239–247, Apr. 2003.

[197] M. Beresna, M. Gecevicius, P. G. Kazansky, and T. Gertus, “Radially polarized optical vortex converter created by femtosecond laser nanostructuring of glass,” *Appl. Phys. Lett.*, vol. 98, no. 20, p. 201101, May 2011.

[198] S. . Oldenburg, R. . Averitt, S. . Westcott, and N. . Halas, “Nanoengineering of optical resonances,” *Chem. Phys. Lett.*, vol. 288, no. 2–4, pp. 243–247, May 1998.

[199] Y. Jin, O. J. Allegre, W. Perrie, K. Abrams, J. Ouyang, E. Fearon, S. P. Edwardson, and G. Dearden, “Dynamic modulation of spatially structured polarization fields for real-time control of ultrafast laser-material interactions,” *Opt. Express*, vol. 21, no. 21, p. 25333, Oct. 2013.

[200] J. Ouyang, W. Perrie, O. J. Allegre, T. Heil, Y. Jin, E. Fearon, D. Eckford, S. P. Edwardson, and G. Dearden, “Tailored optical vector fields for ultrashort-pulse laser induced complex surface plasmon structuring,” *Opt. Express*, vol. 23, no. 10, p. 12562, May 2015.

[201] S. Tripathi and K. C. Toussaint, “Versatile generation of optical vector fields and vector beams using a non-interferometric approach,” *Opt. Express*, vol. 20, no. 10, p. 10788, May 2012.

[202] Z.-Y. Rong, Y.-J. Han, S.-Z. Wang, and C.-S. Guo, “Generation of arbitrary vector beams with cascaded liquid crystal spatial light modulators,” *Opt. Express*, vol. 22, no. 2, p. 1636, Jan. 2014.

[203] D. J. Kane and R. Trebino, “Characterization of arbitrary femtosecond pulses using frequency-resolved optical gating,” *IEEE J. Quantum Electron.*, vol. 29, no. 2, pp. 571–579, 1993.

[204] R. Trebino, K. W. DeLong, D. N. Fittinghoff, J. N. Sweetser, M. A. Krumbügel, B. A. Richman, and D. J. Kane, “Measuring ultrashort laser pulses in the time-frequency domain using frequency-resolved optical gating,” *Rev. Sci. Instrum.*,

vol. 68, no. 9, pp. 3277–3295, Sep. 1997.

[205] A. Kosuge, T. Sekikawa, X. Zhou, T. Kanai, S. Adachi, and S. Watanabe, “Frequency-Resolved Optical Gating of Isolated Attosecond Pulses in the Extreme Ultraviolet,” *Phys. Rev. Lett.*, vol. 97, no. 26, p. 263901, Dec. 2006.

[206] Y. Mairesse and F. Quéré, “Frequency-resolved optical gating for complete reconstruction of attosecond bursts,” *Phys. Rev. A*, vol. 71, no. 1, p. 11401, Jan. 2005.

[207] J. K. Ranka, A. L. Gaeta, A. Baltuska, M. S. Pshenichnikov, and D. a Wiersma, “Autocorrelation measurement of 6-fs pulses based on the two-photon-induced photocurrent in a GaAsP photodiode,” *Opt. Lett.*, vol. 22, no. 17, p. 1344, Sep. 1997.

[208] K. Sala, G. Kenney-Wallace, and G. Hall, “CW autocorrelation measurements of picosecond laser pulses,” *IEEE J. Quantum Electron.*, vol. 16, no. 9, pp. 990–996, Sep. 1980.

[209] R. Trebino, *Frequency-Resolved Optical Gating: The Measurement of Ultrashort Laser Pulses*. Boston, MA: Springer US, 2000.

[210] R. Czaplicki, M. Zdanowicz, K. Koskinen, J. Laukkanen, M. Kuittinen, and M. Kauranen, “Dipole limit in second-harmonic generation from arrays of gold nanoparticles,” *Opt. Express*, vol. 19, no. 27, p. 26866, Dec. 2011.

[211] M. Cornet, J. Degert, E. Abraham, and E. Freysz, “Terahertz-field-induced second harmonic generation through Pockels effect in zinc telluride crystal,” *Opt. Lett.*, vol. 39, no. 20, p. 5921, Oct. 2014.

[212] D. J. Cook, J. X. Chen, E. a. Morlino, and R. M. Hochstrasser, “Terahertz-field-induced second-harmonic generation measurements of liquid dynamics,” *Chem. Phys. Lett.*, vol. 309, no. 3–4, pp. 221–228, Aug. 1999.

[213] J. Dai, X. Xie, and X.-C. Zhang, “Detection of Broadband Terahertz Waves with a Laser-Induced Plasma in Gases,” *Phys. Rev. Lett.*, vol. 97, no. 10, p. 103903, Sep. 2006.

Appendix A

Sphere in a uniform electric field

It was discussed in Chapter 2 that the *quasi static approximation* can lead to simpler treatment of the metallic nanoparticle in an electric field. That is as a small sphere (radius *a*) with a dielectric constant ε placed in a uniform electric field, which at large distances from this sphere can be treated as E_o along the z axis.

The calculation of the electric potential as per Jackson [57], yields the general solution of the Laplace equation is in the form:

$$\Phi(r,\theta) = \sum_{l=0}^{\infty} \left[A_l r^l + B_l r^{-(l+1)}\right] P_l(cos\theta) \qquad \textbf{(1)}$$

This equation can be separated into the inside and the outside of the sphere. In order to determine the potential within the spherical region, one must assume that there is no charge at the origin. Also, for the inner region since the potential at $r = 0$ is finite, then the $r^{-(l+1)}$ term must vanish and leave $B_l = 0$ for all *l*. Then the inside and the outside potential of the sphere can be described as:

$$\Phi_{in} = \sum_{l=0}^{\infty} A_l r^l P_l(cos\theta) \qquad \textbf{(2)}$$

$$\Phi_{out} = \sum_{l=0}^{\infty} \left[B_l r^l + C_l r^{-(l+1)}\right] P_l(cos\theta) \qquad (3)$$

Applying boundary conditions at the radius of the sphere equal to a:

$$Tangential\ E: \qquad -\frac{1}{a}\frac{\partial \Phi_{in}}{\partial \theta}\bigg|_{r=a} = -\frac{1}{a}\frac{\partial \Phi_{out}}{\partial \theta}\bigg|_{r=a} \qquad \textbf{(4)}$$

$$Normal\ D: \qquad -\epsilon \frac{\partial \Phi_{in}}{\partial r}\bigg|_{r=a} = -\epsilon_m \frac{\partial \Phi_{out}}{\partial r}\bigg|_{r=a} \qquad \textbf{(5)}$$

Applying the first boundary condition (4) one can get:

$$\sum_{l=0}^{\infty} A_l r^l P_l(cos\theta) = \sum_{l=0}^{\infty} \left[B_l r^l + C_l r^{-(l+1)}\right] P_l(cos\theta) \qquad \textbf{(6)}$$

Knowing that at large distances from the sphere (r>>a) the potential is given by $\Phi_{out}(r,\theta) \cong -E_0 z = -E_0 r cos\theta$, the B_l can be set to zero apart from $B_1(=-E_0)$.

$$\sum_{l=0}^{\infty} A_l r^l P_l(cos\theta) = -E_0 a cos\theta + \sum_{l=0}^{\infty} \frac{C_l}{a^{l+1}} P_l(cos\theta) \qquad \textbf{(7)}$$

Form this, first coefficients can be calculated:

$$A_1 = -E_0 + \frac{C_1}{a^3}, \qquad l = 1 \qquad \textbf{(8)}$$

$$A_l = \frac{C_l}{a^{2l+1}}, \qquad l \neq 1 \qquad (9)$$

The second boundary condition can be now written as:

$$\epsilon \sum_{l=0}^{\infty} A_l l a^{l-1} P_l(cos\theta) = -\epsilon_m E_0 a cos\theta - \epsilon_m \sum_{l=0}^{\infty} \frac{(l+1)C_l}{a^{l+2}} P_l(cos\theta) \qquad \textbf{(10)}$$

This leads to:

$$\frac{\epsilon}{\epsilon_m} A_1 = -E_0 - 2\frac{C_1}{a^3}, \qquad l = 1 \qquad \textbf{(11)}$$

$$\frac{\boldsymbol{\epsilon}}{\boldsymbol{\epsilon_m}} l A_1 = -(l+1)\frac{C_1}{a^{2l+1}}, \qquad l \neq 1 \qquad (12)$$

Solving these equations for l=1 leads to:

$$A_1 = -\left(\frac{3\epsilon_m}{\epsilon + 2\epsilon_m}\right) E_0 \qquad \textbf{(13)}$$

$$C_1 = \left(\frac{\epsilon - \boldsymbol{\epsilon_m}}{\boldsymbol{\epsilon + 2\epsilon_m}}\right) a^3 \boldsymbol{E_0} \qquad (14)$$

For $l \neq 1$, the solution is $A_l = C_l = 0$.

The potential is therefore:

$$\Phi_{in} = -\left(\frac{3\epsilon_m}{\epsilon + 2\epsilon_m}\right) E_0 r cos\theta \quad \textbf{(15)}$$

$$\Phi_{out} = -E_0\, r\, cos\theta + \frac{\epsilon - \epsilon_m}{\epsilon + 2\epsilon_m} E_0 a^3 \frac{cos\theta}{r^2} \quad (16)$$

Appendix B

Matlab calculations of the Mie Resonances using [61]

The main code:

```
clear all
close all
%% importing data from Johnston and Christy
a=importdata('Ag_trzecie'); %
Ag=a.data;
Ag(:,1)=Ag(:,1)*1000;
%% turning data to a useable format
for ii=1:length(Ag)
   wave(ii,1)=Ag(ii,1);
   nAg(ii,1)=Ag(ii,2)+i*Ag(ii,3);
end
%% using MieScattering2 for the SPR calculation
% in this example the nanoparticle radius is set to 20nm
% and the glass refractive index to 1.52
   for j=1:length(Ag)
    [Qext,Qsca,Qabs]=MieScattering2(wave(j),20,1.52,nAg(j,1));
    ext(j,1)=Qext;
    ext(j,2)=Qsca;
    ext(j,3)=Qabs;
   end
% figure plotting
figure;plot(wave(:,1),ext(:,1));hold on;
plot(wave(:,1),ext(:,2),'r');
plot(wave(:,1),ext(:,3),'b'); hold off
xlim([400 600])
ylim([0 40000]);
legend('Qext','Qscatt','Qabs');
xlabel('wavelength [nm]');
ylabel('Q [arb.u.]')
text(650,25000,'40nm diameter')
```

Function used in the main code for calculations (as per [61])

```
function [Qext,Qsca,Qabs]=MieScattering2(lambda0,r0,n_m,n_Au)

%% SCATTERING BY A SPHERICAL NANOPARTICLE USING MIE THEORY
%% inputs
```

```
%n_m        optical index of the medium
%lambda0    wavelength in nm
%r0         radius of the particle in nm
%N=5        maximum n-pole
   %% parameters
   m=n_Au/n_m;
   k=2*pi*n_m/lambda0;
   x=k*r0;
   z=m*x;
   N=round(2+x+4*x^(1/3));
   %% computation
   j=(1:N);
   sqr=sqrt(pi*x/2);
   sqrm=sqrt(pi*z/2);
   phi=sqr.*besselj(j+0.5,x);
   xi=sqr.*(besselj(j+0.5,x)+i*bessely(j+0.5,x));
   phim=sqrm.*besselj(j+0.5,z);
   phi1=[sin(x), phi(1:N-1)];
   phi1m=[sin(z), phim(1:N-1)];
   y=sqr*bessely(j+0.5,x);
   y1=[-cos(x), y(1:N-1)];
   phip=(phi1-j/x.*phi);
   phimp=(phi1m-j/z.*phim);
   xip=(phi1+i*y1)-j/x.*(phi+i*y);
   aj=(m*phim.*phip-phi.*phimp)./(m*phim.*xip-xi.*phimp);
   bj=(phim.*phip-m*phi.*phimp)./(phim.*xip-m*xi.*phimp);
   Qsca=sum( (2*j+1).*(abs(aj).*abs(aj)+abs(bj).*abs(bj)) );
   Qext=sum( (2*j+1).*real(aj+bj) );
   Qext=Qext*2*pi/(k*k);
   Qsca=Qsca*2*pi/(k*k);
   Qabs=Qext-Qsca;
```

Data used for silver refractive index, taken from [51]

```
Silver trzecie, johnson n christy
1 2 3 4 5 = columns for wave, Re(n), Im(n), eps1, eps2
wave(um) Re(n) Im(n) eps1 eps2
1.937 0.24 14.08 -198.19 6.7584
1.61 0.15 11.85 -140.40 3.555
1.393   0.13    10.1    -101.99 2.626
1.216   0.09    8.828   -77.93  1.58904
1.088   0.04    7.795   -60.76  0.6236
0.984   0.04    6.992   -48.89  0.55936
0.892   0.04    6.312   -39.84  0.50496
0.8211  0.04    5.727   -32.80  0.45816
0.756   0.03    5.242   -27.48  0.31452
0.7045  0.04    4.838   -23.40  0.38704
0.6595  0.05    4.483   -20.09  0.4483
0.6168  0.06    4.152   -17.24  0.49824
0.5821  0.05    3.858   -14.88  0.3858
0.5486  0.06    3.586   -12.86  0.43032
0.5209  0.05    3.324   -11.05  0.3324
0.4959  0.05    3.093   -9.56   0.3093
0.4714  0.05    2.869   -8.23   0.2869
0.4509  0.04    2.657   -7.06   0.21256
0.4305  0.04    2.462   -6.06   0.19696
0.4133  0.05    2.275   -5.17   0.2275
0.3974  0.05    2.07    -4.28   0.207
0.3815  0.05    1.864   -3.47   0.1864
0.3679  0.07    1.657   -2.74   0.23198
0.3542  0.1     1.419   -2.00   0.2838
0.3425  0.14    1.142   -1.28   0.31976
```

0.3315	0.17	0.829	-0.66	0.28186
0.3204	0.81	0.392	0.50	0.63504
0.3107	1.13	0.616	0.90	1.39216
0.3009	1.34	0.964	0.87	2.58352
0.2924	1.39	1.161	0.58	3.22758
0.2844	1.41	1.264	0.39	3.56448
0.2761	1.41	1.331	0.22	3.75342
0.2689	1.38	1.372	0.02	3.78672
0.2616	1.35	1.387	-0.10	3.7449
0.2551	1.33	1.393	-0.17	3.70538
0.249	1.31	1.389	-0.21	3.63918
0.2426	1.3	1.378	-0.21	3.5828
0.2371	1.28	1.367	-0.23	3.49952
0.2313	1.28	1.357	-0.20	3.47392
0.2262	1.26	1.344	-0.22	3.38688
0.2214	1.25	1.342	-0.24	3.355
0.2164	1.22	1.336	-0.30	3.25984
0.2119	1.2	1.325	-0.32	3.18
0.2073	1.18	1.312	-0.33	3.09632
0.2033	1.15	1.296	-0.36	2.9808
0.1993	1.14	1.277	-0.33	2.91156
0.1953	1.12	1.255	-0.32	2.8112
0.1916	1.1	1.232	-0.31	2.7104
0.1879	1.07	1.212	-0.32	2.59368

Appendix C

Full text journal papers published by the author.

Picosecond pulsed laser induced optical dichroism in glass with embedded metallic nanoparticles

Mateusz A. Tyrk,[1] W. Allan Gillespie,[1] Gerhard Seifert,[2] and Amin Abdolvand[1,*]

[1]*School of Engineering, Physics and Mathematics, University of Dundee, Dundee DD1 4HN, UK*
[2]*Institut für Physik, Martin-Luther Universität Halle-Wittenberg, Halle D-06120, Germany*
[*]*a.abdolvand@dundee.ac.uk*

Abstract: Picosecond (~10 ps) pulsed laser irradiation at 532 nm led to the efficient and scalable fabrication of dichroic areas in glass with spherical silver nanoparticles of ~30 – 40 nm in diameter embedded in a surface layer of thickness ~20 μm. The observed dichroism is due to the uniform and permanent shape transformation of the nanoparticles - from spherical to spheroidal shapes - throughout the irradiated areas and along the laser polarization direction, paving the way for affordable manufacture of polarization-selective diffractive optical elements. The shape modification threshold and the dichroism as a result of Surface Plasmon Resonance band separation were identified. The process was then studied as a function of the laser polarization, repetition rate and the number of pulses fired per spot.

OCIS codes: (140.3390) Laser materials processing; (160.4236) Nanomaterials; (160.4670) Optical materials; (160.2750) Glass and other amorphous materials.

References and links

1. U. Kreibig and M. Vollmer, *Optical Properties of Metal Clusters* (Springer, 1995).
2. K. L. Kelly, E. Coronado, L. L. Zhao, and G. C. Schatz, "The optical properties of metal nanoparticles: The influence of size, shape, and dielectric environment," J. Phys. Chem. B **107**(3), 668–677 (2003).
3. R. Jin, Y. C. Cao, E. Hao, G. S. Métraux, G. C. Schatz, and C. A. Mirkin, "Controlling anisotropic nanoparticle growth through plasmon excitation," Nature **425**(6957), 487–490 (2003).
4. M. S. Gudiksen, L. J. Lauhon, J. Wang, D. C. Smith, and C. M. Lieber, "Growth of nanowire superlattice structures for nanoscale photonics and electronics," Nature **415**(6872), 617–620 (2002).
5. P. Chakaraborty, "Metal nanoclusters in glasses as nonlinear photonic materials," J. Mater. Sci. **33**(9), 2235–2249 (1998).
6. A. Abdolvand, A. Podlipensky, S. Matthias, F. Syrowatka, U. Goslele, G. Seifert, and H. Graener, "Metallodielectric two-dimensional photonic structures made by electric field microstructuring of nanocomposite glass," Adv. Mater. **17**(24), 2983–2987 (2005).
7. A. Stalmashonak, A. Abdolvand, and G. Seifert, "Metal-glass nanocomposites for optical storage of information," Appl. Phys. Lett. **99**(20), 201904 (2011).
8. L. A. H. Fleming, S. Wackerow, A. C. Hourd, W. A. Gillespie, G. Seifert, and A. Abdolvand, "Diffractive optical element embedded in silver-doped nanocomposite glass," Opt. Express **20**(20), 22579–22584 (2012).
9. A. Podlipensky, A. Abdolvand, G. Seifert, and H. Graener, "Femtosecond laser assisted production of dichroitic 3D structures in composite glass containing Ag nanoparticles," Appl. Phys., A Mater. Sci. Process. **80**(8), 1647–1652 (2005).
10. M. Kaempfe, G. Seifert, K.-J. Berg, H. Hofmeister, and H. Graener, "Polarization dependence of the permanent deformation of silver nanoparticles in glass by ultrashort laser pulses," Eur. Phys. J. D **16**(1), 237–240 (2001).
11. G. Seifert, M. Kaempfe, K.-J. Berg, and H. Graener, "Femtosecond pump-probe investigation of ultrafast silver nanoparticle deformation in a glass matrix," Appl. Phys. B **71**(6), 795–800 (2000).
12. S. Wackerow, G. Seifert, and A. Abdolvand, "Homogenous silver-doped nanocomposite glass," Opt. Mater. Express **1**(7), 1224–1231 (2011).
13. K.-J. Berg, A. Berger, and H. Hofmeister, "Small silver particle in glass-surface layers produced by sodium-silver ion-exchange-their concentration and size depth profile," Z. Phys. D **20**(1-4), 309–311 (1991).
14. V. G. Farafonov and N. V. Voshchinnikov, "Optical properties of spheroidal particles," Astrophys. Space Sci. **204**(1), 19–86 (1993).
15. A. Stalmashonak, A. A. Unal, H. Graener, and G. Seifert, "Effects of temperature on laser-induced shape modification of silver nanoparticles embedded in glass," J. Phys. Chem. C **113**(28), 12028–12032 (2009).

#193285 - $15.00 USD Received 2 Jul 2013; revised 7 Aug 2013; accepted 14 Aug 2013; published 9 Sep 2013

16. A. Stalmashonak, A. Podlipensky, G. Seifert, and H. Graener, "Intensity-driven, laser induced transformation of Ag nanospheres to anisotropic shapes," Appl. Phys. B **94**(3), 459–465 (2009).
17. A. Stalmashonak, G. Seifert, and A. Abdolvand, *Ultra-Short Pulsed Laser Engineered Metal-Glass Nanocomposites* (Springer, 2013).

1. Introduction

Dielectrics containing metal nanoparticles are of interest due to their unique linear and nonlinear optical properties. These properties are dominated by the strong surface plasmon resonances (SPRs) of the metal nanoparticles. The spectral position and shape of the SPRs can be designed within a wide spectral range throughout the visible and near-infrared spectra by choice of the metal and the dielectric matrix [1], plus manipulation of nanoparticle size [2], shape [3], and spatial distribution [4]. Therefore, these nanocomposites comprise a promising class of materials for many applications in optoelectronics [5–8].

The material under consideration here is glass with embedded spherical silver nanoparticles. Recently it was discovered that femtosecond (fs) pulsed laser irradiation at near the SPR of this class of metal-glass nanocomposites leads to the production of dichroic areas [7, 9, 10]. The nanoscopic origin of this effect was identified as laser-induced permanent deformation of the particles from spherical to spheroidal shapes and along the polarization direction of the laser beam. It was identified that trapping of the directionally emitted electrons during the reshaping process takes approximately 10 to 100 ps [11].

Our aim here is to investigate this finding and study the changes in the optical properties of glass containing spherical silver nanoparticles induced by repetitive irradiation with picosecond (~10 ps) laser pulses at 532 nm. The nanoparticle shape modification threshold was identified to be close to that of reported for fs irradiation. The effect was studied as a function of laser polarization, number of applied pulses and laser fluence. A spectral gap of ~240 nm for the SPR band separation was achieved for the laser repetition rate of 200 kHz and after 1000 pulses per spot were fired into the nanocomposite. These effects are of particular interest for technical applications given that ps pulsed laser sources are industrially friendly and that methods of producing pulses in this regime are robust and more affordable as compared with fs laser pulses.

2. Experimental methods

Glass with embedded nanoparticles has traditional been fabricated using ion-exchange techniques [12]. Here, the silver-doped nanocomposite glass samples were prepared from a 1 mm thick soda-lime float glass (comprising in wt.-%: 72.5 SiO_2, 14.4 Na_2O, 6.1 CaO, 0.7 K_2O, 4.0 MgO, 1.5 Al_2O_3, 0.1 Fe_2O_3, 0.1 MnO, 0.4 SO_3) by Ag^+-Na^+ ion exchange and subsequent annealing in a H_2 reduction atmosphere [13]. This resulted in the formation of spherical silver nanoparticles of 30-40 nm mean diameter in a thin surface layer of ~20-25 µm on both sides of the glass substrate. The extinction spectrum of the original sample and an image of the sample are shown in Figs. 1(a) and 1(b).

The original sample shows a strong and broad SPR band at around 430 nm corresponding to the embedded spherical silver nanoparticles of ~30 to 40 nm in diameter with high volume fill factor. The nanoparticle-containing layers were formed some 30 nm beneath the surface of the glass. Single-sided samples were used in our experiments, made by removing the nanoparticle containing layer from one side of the samples by etching in 12% HF acid.

In order to visualize the depth profile of the silver particle-containing layer, one of the samples was cut and a thin slice was prepared – Fig. 1(c). For this, we embedded the sample in an epoxy resin (Specifix-20, Struers Limited) to prevent chipping of the glass and to make it physically manageable for grinding, polishing etc. The resin cures at room temperature. The ~30 µm thick section was polished on both sides.

The sample was irradiated using a linearly polarized 10 ps laser beam at 532 nm (Coherent Talisker Ultra System). Figure 2 shows the experimental setup used for the

#193285 - $15.00 USD Received 2 Jul 2013; revised 7 Aug 2013; accepted 14 Aug 2013; published 9 Sep 2013

irradiation. The laser beam had a Gaussian intensity profile ($M^2 < 1.3$) and was focused on to the target surface using a flat field scanning lens system with a focal length of 100 mm - a specialized lens system in which the focal plane of the deflected laser beam is a flat surface. The flat field scanning lens systems are commonly used in laser processing applications to offset the off-axis deflection of the beam through the focusing lens system.

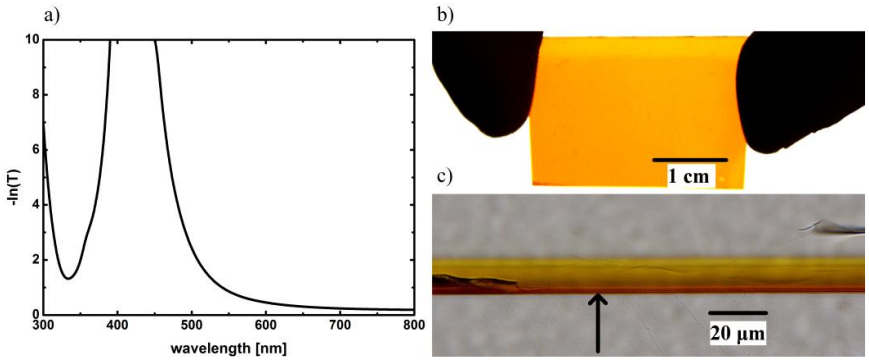

Fig. 1. a) Extinction spectrum measured for a soda-lime glass sample containing spherical silver nanoparticles of ~30 – 40 nm in diameter. The Surface Plasmon Resonance band has its maximum at ~430 nm. b) Image of the original sample – Top view. c) Cross section of the sample showing the layer of silver nanoparticles embedded in the glass. The black arrow indicates the sample surface. The characterizations of the sample were performed using a JASCO V-670 UV/VIS/NIR Spectrophotometer and KEYENCE Digital Microscope VHX-1000.

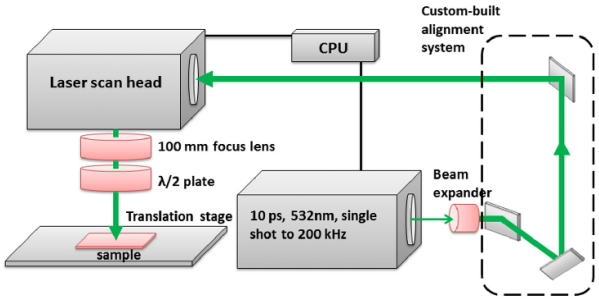

Fig. 2. Experimental setup used for laser irradiation. The maximum average power of the laser at 532 nm is ~8 W. The linearly polarized laser beam was focused on the sample with a 100 mm focal length lens, which resulted in a ~12 µm diameter beam in air. A fully automatized system allowed us to scan different patterns on the sample.

The beam spot diameter on the target was measured to be ~12 µm. The beam was raster scanned over the surface of the target irradiating 5 mm × 5 mm squares at different velocities using a computer-controlled scanner system. The modification threshold of the material was measured to be ~20 mJ/cm^2. Measurements were performed for single pulse per spot irradiation and care was taken to only modify the nanoparticle layer such that the thin glass surface layer stayed unaffected. It is worth pointing out that the modified spot diameter on the sample shows a high dependence on laser fluence, so that it increases for higher laser fluence values. In order to achieve uniform and homogenous dichroic areas a laser fluence of ~88 mJ/cm^2 was required. After the irradiation, samples were annealed at 200 °C for 1 hour, to remove color centers and other defects in glass that could influence the quality of the optical measurements.

#193285 - $15.00 USD Received 2 Jul 2013; revised 7 Aug 2013; accepted 14 Aug 2013; published 9 Sep 2013

3. Results and discussion

A number of experiments were performed in order to prove the ability for uniform reshaping of spherical nanoparticles upon ps pulsed laser irradiation: changing the irradiation density by varying the applied number of pulses per spot, changing the laser repetition rate and fluence. In each case dichroism was observed, as a result of elongation of the originally spherical silver nanoclusters along the polarization direction of the laser beam.

As can be seen from Fig. 3(a), linearly polarized laser irradiation (1000 pulses per spot at the laser fluence of 88 mJ/cm^2) resulted in the separation of the SPR band for light polarized parallel and perpendicular to the polarization of the laser beam. The SPR band separation is due to the nanoparticle shape modification. Spheroids exhibit separation of their SPR band - one for each of their geometrical axes [14]. Knowing the separation distance between the peaks of the long (p- polarization) and short (s- polarization) axes is of paramount importance when estimating the nanoparticle aspect ratio. The latter can be tuned by changing the laser fluence values. This is shown in Fig. 3(b) where the change in the laser fluence values, from just above the modification threshold (22 mJ/cm^2) to approximately 88 mJ/cm^2, is shown.

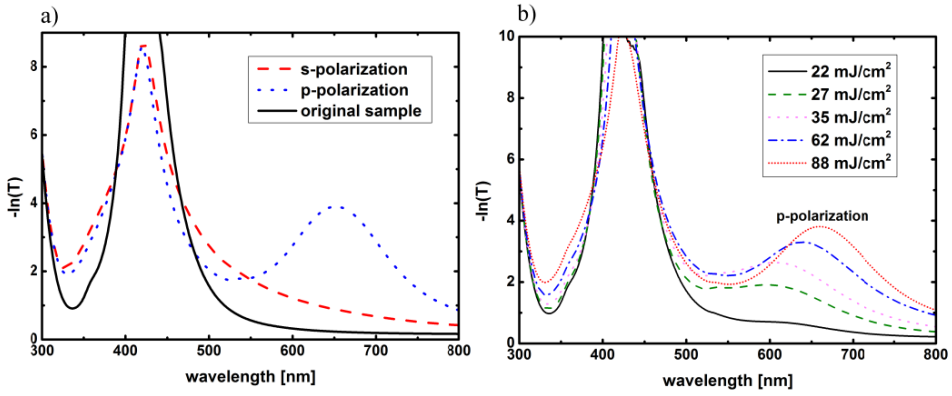

Fig. 3. Extinction spectra as a function wavelength for: a) Sample irradiated with 1000 pulses per spot, laser fluence of 88 mJ/cm^2 and repetition rate of 200 kHz. S- polarization / P-polarizations are the polarization of light in the spectrophotometer, that is perpendicular / parallel to the polarization of the laser beam, respectively. Separation of the SPR band is a result of shape transformation of silver nanoparticles from spherical to spheroidal along the polarization the laser beam. For the p- polarization spectrum there is still the remnant of the spectrum from spherical nanoparticles, this is due to the fact that the employed modification wavelength of 532 nm is far from the SPR peak of 430 nm and that not all nanoparticles were being elongated in the focal volume. This issue could be overcome by using a sample with thinner nanoparticle-containing layer. b) Sample irradiated with different laser fluence values starting just above the modification threshold value (which is 18 mJ/cm^2) and ending on a value that gives the most uniform dichroism (88 mJ/cm^2). Irradiation was performed with the laser repetition rate of 200 kHz and 1000 pulses per spot were fired into the target. The employed laser intensities are (from lowest to highest): 2.21 GW/cm^2, 2.65 GW/cm^2, 3.54 GW/cm^2, 6.19 GW/cm^2 and 8.84 GW/cm^2.

As can be seen, the SPR band (especially pronounced for the p- polarized light) experiences a shift towards the longer wavelengths and at the same time exhibits higher extinctions as the fluence increases. Peaks of the red shifted bands are at (from lowest fluence to the highest): 590 nm, 596 nm, 607 nm, 639 nm, and 660 nm. Furthermore, as the laser fluence increases more nanoparticles are being uniformly reshaped. This exhibits itself as an increase in the peak of the absorption band.

We have also observed that the SPR band separation and hence dichroism occurs for different regimes of irradiation. Figure 4(a) shows the change in the SPR gap between the red shifted p- polarized and s- polarized bands when changing the applied number of pulses per

#193285 - $15.00 USD Received 2 Jul 2013; revised 7 Aug 2013; accepted 14 Aug 2013; published 9 Sep 2013

spot value. Figure 4(b) demonstrates that changing the laser repetition rate affects the spectrum in a similar manner.

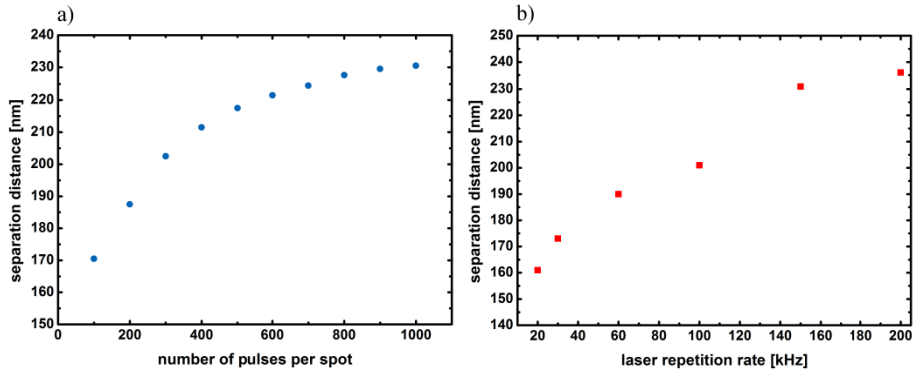

Fig. 4. (a) Surface Plasmon Resonance band separation distance as a function of number of pulses per spot. Irradiation was performed for 88 mJ/cm^2 (8.84 GW/cm^2) and a 200 kHz laser repetition rate. (b) Surface Plasmon Resonance band separation distance as a function of laser repetition rate. Irradiation performed with 88 mJ/cm^2 (8.84 GW/cm^2) and 1000 pulses per spot. Both graphs represent the degree of elongation that the nanoparticle experiences. They also show a similar relation, that the SPR gap separation rises to its maximum value of ~240 nm.

These observations are in agreement with the temperature model presented for fs pulsed laser modification in [15]. According to the model each pulse during irradiation accumulates the effect of elongation by heating up the nanoparticle (Two Temperature Model) and then spreading its heat to the glass matrix by heat diffusion (Three Temperature Model). The overall effect of reshaping increases for each pulse because the system relaxes to a slightly higher temperature than it had before. Approaching high temperatures results in dissolution of the nanoparticles in the glass matrix due to the increase mobility of the emitted silver ions and their diffusion into the glass matrix during the irradiation [16, 17]. Therefore high repetition rates or firing large number of pulses per spot can lead to undesirable effects.

Here, the maximum achieved SPR gap is about 240 nm. At this value the temperature in the close vicinity of the nanoparticles is approaching its maximum value for silver ions coupling with the electrons on the poles of the nanoparticles. Higher temperatures would lead to diffusion of silver ions further away from the original silver lattice and electrons, leading to the dissolution of the nanoparticles into the glass matrix. The results of the large area picosecond irradiation of glass with embedded spherical silver nanoparticles at 532 nm at 200 kHz are presented in Fig. 5. The laser fluence is 88 mJ/cm^2 and the number of pulses fired per spot was varied. As can be seen, the irradiated areas and the observed dichroism are homogeneous (island-free). These results are very similar to the ones observed in fs pulsed laser irradiation of glass with embedded silver nanoparticles. However, for 150 fs pulsed laser irradiation at 400 nm the dissolution was reported to occur for the laser operating at just below 100 kHz repetition rate and the modification threshold was reported to be ~0.2 TW/cm^2 (~30 mJ/cm^2) [16]. These values are fairly close to our measured values for the 532 nm ps pulsed laser modification threshold of ~20 mJ/cm^2. It is worth stressing the fact that here the irradiation wavelength is far from the SPR peak absorption. For the ps pulsed laser irradiation at 532 nm most of the experiments have been performed using a laser intensity of ~9 GW/cm^2 (~88 mJ/cm^2). The fact that pulses of ~10 ps duration can produce dichroism as efficiently as fs pulses confirms our previous conclusions [15–17] about the characteristic time scale of the processes of particle deformation and that the emitted electrons during the process are penetrating and settling down in the matrix within 10-20 ps.

#193285 - $15.00 USD Received 2 Jul 2013; revised 7 Aug 2013; accepted 14 Aug 2013; published 9 Sep 2013

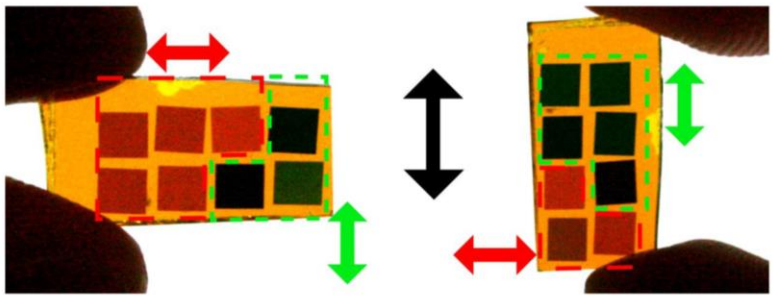

Fig. 5. Top view images of the 5 × 5 mm squares irradiated at laser fluence of 88 mJ/cm^2 at 200 kHz. Number of pulses per spot in the irradiation areas on the left hand side are (from left to right): 500, 300, 100, 200 (top row) and 400, 200, 100, 100 (bottom row). The right hand side image shows the same as the one on the left but flipped 90° clockwise. The black arrow represents the polarization of the light penetrating the samples from the back of the image (perpendicular to the paper). The red arrow represents the polarization direction of the laser beam for irradiation of the areas grouped within the red dash-lines. The green arrow represents the polarization direction of the laser beam for irradiation of the areas grouped within the green dash-lines. The dichroic effect is easily observable, with higher extinction for the nanoparticles elongated along the polarization direction of the penetrating light.

4. Conclusion

Picosecond pulsed laser irradiation of glass containing spherical silver nanoparticles led to the homogenous deformation of the nanoparticles without destruction of the sample. This effect, which is nanoscopically caused by permanent deformation of the initially spherical particles to non-spherical shapes along the polarization direction of the laser beam was studied as a function of laser polarization, repetition rate and number of the applied pulses using a 10 ps, Nd:YVO_4 laser at 532 nm. A spectral gap of ~240 nm for the SPR band was achieved for a repetition rate of 200 kHz after 1000 pulses per spot were fired into the sample.

Previously, and in order to achieve an optimum dichroism *via* fs pulsed laser irradiation of the nanocomposites in ambient temperature [16, 17], a laser repetition rate of 10 kHz was suggested. This hindered the operation where high processing speeds are required. The experimentally applied values here can be tailored depending on the requirements. This should lead to an industrially affordable fabrication of new optical elements such as wavelength- and polarization-selective diffraction gratings based on glasses containing metallic nanoparticles.

Acknowledgments

This work was conducted under the aegis of the Engineering and Physical Sciences Research Council (EPSRC) of the United Kingdom (EP/I004173/1), and has been supported by the CLIC Project under CERN collaboration agreement KE1865/TE. We are very grateful to CODIXX AG of Barleben/Germany for providing the samples for this study. MAT is a Marie Curie Fellow within the LA3NET Network (Grant Agreement Number 289191). AA is currently an EPSRC Career Acceleration Fellow at the University of Dundee.

#193285 - $15.00 USD Received 2 Jul 2013; revised 7 Aug 2013; accepted 14 Aug 2013; published 9 Sep 2013

Radially and azimuthally polarized laser induced shape transformation of embedded metallic nanoparticles in glass

Mateusz A. Tyrk, Svetlana A. Zolotovskaya, W. Allan Gillespie, and Amin Abdolvand*

Materials & Photonic Systems Group, School of Engineering, Physics and Mathematics, University of Dundee, Dundee DD1 4HN, Scotland, UK

*a.abdolvand@dundee.ac.uk

Abstract: Radially and azimuthally polarized picosecond (~10 ps) pulsed laser irradiation at 532 nm wavelength led to the permanent reshaping of spherical silver nanoparticles (~30 – 40 nm in diameter) embedded in a thin layer of soda-lime glass. The observed peculiar shape modifications consist of a number of different orientations of nano-ellipsoids in the cross-section of each written line by laser. A Second Harmonic Generation cross-sectional scan method from silver nanoparticles in transmission geometry was adopted for characterization of the samples after laser modification. The presented approach may lead to sophisticated marking of information in metal-glass nanocomposites.

OCIS codes: (140.3390) Laser materials processing; (160.4236) Nanomaterials; (160.4670) Optical materials; (160.2750) Glass and other amorphous materials.

References and links

1. U. Kreibig and M. Vollmer, *Optical Properties of Metal Clusters* (Springer Series in Materials Science, Springer, 1995).
2. K. L. Kelly, E. Coronado, L. L. Zhao, and G. C. Schatz, "The optical properties of metal nanoparticles: The influence of size, shape, and dielectric environment," J. Phys. Chem. B **107**(3), 668–677 (2003).
3. M. A. Tyrk, W. A. Gillespie, G. Seifert, and A. Abdolvand, "Picosecond pulsed laser induced shape transformation of metallic nanoparticles embedded in a glass matrix," Opt. Express **21**(19), 21823–21828 (2013).
4. A. Stalmashonak, G. Graener, and G. Seifert, "Transformation of silver nanospheres embedded in glass to nanodisks using circularly polarized femtosecond pulses," Appl. Phys. Lett. **94**(19), 193111 (2009).
5. A. Stalmashonak, G. Seifert, and A. Abdolvand, *Ultra-short Pulsed Laser Engineered Metal-Glass Nanocomposite* (SpringerBrief in Physics, Springer, 2013).
6. M. Kaempfe, T. Rainer, K.-J. Berg, G. Seifert, and H. Graener, "Ultrashort laser pulse induced deformation of silver nanoparticles in glass," Appl. Phys. Lett. **74**(9), 1200 (1999).
7. J. Doster, G. Baraldi, J. Gonzalo, J. Solis, J. Hernandez-Rueda, and J. Siegel, "Tailoring the surface plasmon resonance of embedded silver nanoparticles by combining nano- and femtosecond laser pulses," Appl. Phys. Lett. **104**(15), 153106 (2014).
8. G. Baraldi, J. Gonzalo, J. Solis, and J. Siegel, "Reorganizing and shaping of embedded near-coalescence silver nanoparticles with off-resonance femtosecond laser pulses," Nanotechnology **24**(25), 255301 (2013).
9. D. Werner, S. Hashimoto, and T. Uwada, "Remarkable photothermal effect of interband excitation on nanosecond laser-induced reshaping and size reduction of pseudospherical gold nanoparticles in aqueous solution," Langmuir **26**(12), 9956–9963 (2010).
10. D. Werner, A. Furube, T. Okamoto, and S. Hashimoto, "Femtosecond laser-induced size reduction of aqueous gold nanoparticles: in situ and pump-proble spectroscopy investigations revealing coulomb explosion," J. Phys. Chem. C **115**(17), 8503–8512 (2011).
11. M. Gordel, J. Olesiak-Banska, K. Matczyszyn, C. Nogues, M. Buckle, and M. Samoc, "Post-synthesis reshaping of gold nanorods using a femtosecond laser," Phys. Chem. Chem. Phys. **16**(1), 71–78 (2014).
12. C. M. Aguirre, C. E. Moran, J. F. Young, and N. J. Halas, "Laser-induced reshaping of metallodielectric nanoshels under femtosecond and nanosecond plasmon resonant illumination," J. Phys. Chem. B **108**(22), 7040–7045 (2004).
13. M. Beleites, C. Matyssek, H.-H. Blaschek, and G. Seifert, "Near-field optical microscopy of femtosecond-laser-reshaped silver nanoparticles in dielectric matrix," Nanoscale Res. Lett. **7**(1), 315 (2012).
14. A. Podlipensky, J. Lange, G. Seifert, H. Graener, and I. Cravetchi, "Second-harmonic generation from ellipsoidal silver nanoparticles embedded in silica glass," Opt. Lett. **28**(9), 716–718 (2003).

#244262 Received 2 Jul 2015; revised 12 Aug 2015; accepted 18 Aug 2015; published 27 Aug 2015

15. K.-J. Berg, A. Berger, and H. Hofmeister, "Small silver particle in glass-surface layers produced by sodium-silver ion-exchange-their concentration and size depth profile," Z. Phys. D **20**(1-4), 309–311 (1991).
16. V. G. Farafonov and N. V. Voshchinnikov, "Optical properties of spheroidal particles," Astrophys. Space Sci. **204**(1), 19–86 (1993).
17. S. J. Oldenburg, R. D. Averitt, S. L. Westcott, and N. J. Halas, "Nanoengineering of optical resonances," Chem. Phys. Lett. **288**(2-4), 243–247 (1998).
18. A. Stalmashonak, A. Abdolvand, and G. Seifert, "Metal-glass nanocomposites for optical storage of information," Appl. Phys. Lett. **99**(20), 201904 (2011).
19. A. Stalmashonak, G. Seifert, A. A. Unal, U. Skrzypczak, A. Podlipensky, A. Abdolvand, and H. Graener, "Toward the production of micropolarizers by irradiation of composite glasses with silver nanoparticles," Appl. Opt. **48**(25), F37–F44 (2009).
20. Y. Jin, O. J. Allegre, W. Perrie, K. Abrams, J. Ouyang, E. Fearon, S. P. Edwardson, and G. Dearden, "Dynamic modulation of spatially structured polarization fields for real-time control of ultrafast laser-material interactions," Opt. Express **21**(21), 25333–25343 (2013).
21. J. Ouyang, W. Perrie, O. J. Allegre, T. Heil, Y. Jin, E. Fearon, D. Eckford, S. P. Edwardson, and G. Dearden, "Tailored optical vector fields for ultrashort-pulse laser induced complex surface plasmon structuring," Opt. Express **23**(10), 12562–12572 (2015).
22. S. Tripathi and K. C. Toussaint, Jr., "Versatile generation of optical vector fields and vector beams using a non-interferometric approach," Opt. Express **20**(10), 10788–10795 (2012).
23. Z.-Y. Rong, Y.-J. Han, S.-Z. Wang, and C.-S. Guo, "Generation of arbitrary vector beams with cascaded liquid crystal spatial light modulators," Opt. Express **22**(2), 1636–1644 (2014).

1. Introduction

Metallic nanoparticles embedded in dielectric matrices are a novel type of nanocomposite that exhibit unique linear and nonlinear optical properties that are dominated by the Surface Plasmon Resonance (SPR) of the nanoparticles. The spectral position and shape of the SPR band can be tuned in order to achieve the desired characteristics by choice of the metal and the dielectric matrix, or indeed by manipulation of the nanoparticle size, shape and spatial distribution [1, 2]. In order to adjust the SPR for spherical silver (Ag) nanoparticles embedded in dielectric matrix, femtosecond (fs-), picosecond (ps-) as well as nanosecond (ns-) pulsed laser irradiation of these materials have been investigated [3–8]. The polarization state of the laser is of paramount importance for the reshaping process. Nanospheroids with their long axis along the polarization of the laser beam are produced upon irradiation with linearly polarized light [3], while a circularly polarized irradiation led to the formation of nanodisks [4]. Reshaping of different metallic nanoparticles and nanoshels in other embedding media has been reported [9–13]

Here we present the interaction of radially and azimuthally polarized ps-pulsed laser beams with glass containing spherical Ag nanoparticles. We demonstrate formation of peculiarly orientated Ag nano-ellipsoids and analyze their orientation within the irradiated lines using the known effect of Second Harmonic Generation (SHG) from elliptical nanoparticles [14]. Here, the presented SHG cross-sectional scan method, conducted in the transmission geometry, allowed for determination of the shape and position of nanoparticles within the modified areas.

2. Experimental methods

Spherical Ag nanoparticles embedded in soda-lime glass were utilized in the experiments. The Ag^+-Na^+ ion exchange fabrication method was used with the glass comprising in wt.-%: 72.5 SiO_2, 14.4 Na_2O, 6.1 CaO, 0.7 K_2O, 4.0 MgO, 1.5 Al_2O_3, 0.1 Fe_2O_3, 0.1 MnO, 0.4 SO_3 and subsequent annealing at 400 °C in a H_2 reduction atmosphere [15]. This produced a ~20 µm layer of uniformly distributed spherical Ag nanoparticles on both sides of the 1 mm glass substrate. The embedded nanoparticle diameters range between 30 and 40 nm. Single layered samples were used in our experiments produced by etching away one layer with 12% concentrated hydrofluoric (HF) acid. The extinction spectra of such Metal-Glass-Nanocomposites (MGNs) exhibit characteristic SPR band centered at ~430 nm wavelength.

Irradiation of MGNs with linearly polarized ps or fs laser pulses at a wavelength matching or close to the SPR band of the nanoparticles leads to the uniform reshaping of the particles

#244262 Received 2 Jul 2015; revised 12 Aug 2015; accepted 18 Aug 2015; published 27 Aug 2015

along the polarization direction of the beam [3, 5]. The dichroic effect that is present after irradiation of the sample in a multi-pulsed regime (e.g. Fig. 1) results in separation of the original SPR band into two: the first one shifted to longer wavelengths (representing the optical spectrum from the long axis of nanoparticles which is aligned to the laser polarization), and the second one to shorter wavelengths (representing the optical spectrum from the short axis of nanoparticles) [5, 16]. The separation distance between these two bands depends on a number of factors such as the number of pulses fired per spot, intensity and wavelength of the laser beam [3].

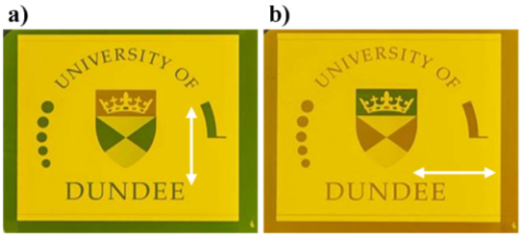

Fig. 1. Logotype (16 mm × 20 mm) produced by ps pulsed laser assisted reshaping of a piece of MGN at 532 nm. The sample is shown for vertically (a) and horizontally (b) polarized illumination (indicated by the white arrows).

In this contribution, *radially* and *azimuthally* polarized laser beams have been used for reshaping. Figure 2 shows the experimental setup used and the laser beam polarization states. The laser source was a Coherent Talisker Ultra System at 532 nm wavelength, 200 kHz repetition rate and ~10 ps pulse width. A commercially available polarization convertor (s-wave plate, Altechna) was used to produce radially and azimuthally polarized light where the polarization state was changed depending on the s-wave plate orientation relative to the linearly polarized incident beam. The beam was then focused with a 100 mm F-theta lens and controlled by an automated scanning system. The beam had a doughnut-like intensity profile and the diameter at the focus was measured to be ~22 μm at $1/e^2$ level. The setup allowed modification of Ag nanoparticles in the sample plane in various directions and shapes. A set of single lines and squares have been written with 2000 pulses per spot at a laser fluence of ~60 mJ/cm^2.

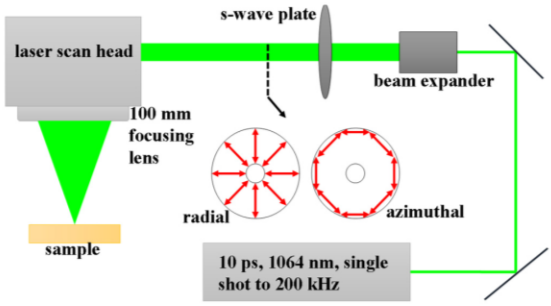

Fig. 2. Experimental setup used for irradiation of 3 mm × 3 mm squares and single lines in MGNs. A linearly polarised beam was expanded and then passed through the s-wave plate that changed the polarization state of the laser to either radial or azimuthal (depending on the rotation angle of the s-wave plate).

These were determined to be the optimal parameters for the reshaping process resulting in the highest value of the SPR separation gap with no nanoparticle dissolution. After the laser irradiation, the samples were characterized in a JASCO V-670 UV/VIS/NIR spectrophotometer and a KEYENCE VHX-1000 digital microscope system.

#244262 Received 2 Jul 2015; revised 12 Aug 2015; accepted 18 Aug 2015; published 27 Aug 2015

It has been shown [14] that the elongated Ag nanoparticles embedded in a dielectric matrix demonstrate SHG when excited by ultra-short laser pulses. The highest SH signal is observed for the linearly polarized excitation beam with the polarization vector aligned parallel to the long axis of the nanoparticles. This concept was used for further characterization of the reshaped nanoparticles. The SHG measurements were conducted in an inverted microscope setup in the transmission geometry as depicted in Fig. 3.

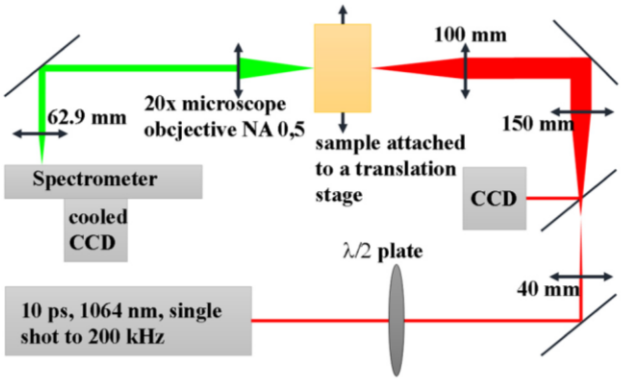

Fig. 3. Setup used for the characterisation of the MGN with reshaped Ag nanoparticles.

Here, a linearly polarized 1064 nm laser beam with pulse duration of ~10 ps at a repetition rate of 200 kHz was used as an excitation source. The incident polarization direction was adjusted using a half-wave plate (λ/2 plate). The beam was passed through a two-lens telescopic system (4 ×) and then focused onto the sample at normal incidence with a 100 mm focusing lens. The beam diameter on the MGN surface was measured to be ~20 µm. For these experiments a laser fluence of ~3 mJ/cm^2 was used. A CCD was used to aid the sample alignment. A high precision translation stage was used to scan the irradiated MGN samples across the excitation laser beam. *Four* different incident polarization directions of the excitation beam were utilized in the experiment - parallel, perpendicular and ± 45° to the direction of the irradiated line. The SHG signal was collected with a 20 × microscope objective (Nikon, NA = 0.5) and then focused with a 63 mm focal length lens into a spectrograph (ORIEL MS257, 1200 grooves/mm grating) equipped with a TE-cooled CCD camera (Andor Newton).

3. Results and discussion

Squares of 3 mm × 3 mm were written line by line in the MGN sample for radially and azimuthally polarized incident irradiation. The extinction spectra of the irradiated areas as a function of wavelength were measured using the spectrophotometer with a linearly polarized light illumination. The spectra for *four* different incident polarization directions of the illumination can be seen in Figs. 4(a) and 4(b) along with the spectrum of the sample before irradiation. Figures 4(c)-4(f) show microscope images of the irradiated areas. The linearly polarized microscope illumination in transmission was used to visualize the modified areas. The incident light polarization direction was adjusted to be at 0°, 90° and ± 45° to the irradiated lines.

As can be seen, there is no clear dichroism present in the samples irradiated with the radial and azimuthal polarized laser beams, rather a permanent change to the SPR, with small variations in the intensity and peak position at the 'red-shifted' band. Moreover the modification of the SPR band that can be seen from the images is rather similar for both radially and azimuthally polarized beam modified areas. In addition, and for comparison purposes, Figs. 4(c)-4(f) also show an area irradiated with linearly polarized light which produced highly organized nano-ellipsoids (in the direction of laser polarisation). The

#244262 Received 2 Jul 2015; revised 12 Aug 2015; accepted 18 Aug 2015; published 27 Aug 2015

dichroic effect can be clearly observed as a change of color from blue/green to brown/red between Figs. 4(c) and 4(e). Figures 4(d) and 4(f) show an intermediate situation where both blue and red shifted SPRs are present. It should be noted that Fig. 4(f) has similar color to Fig. 4(d), due to the fact that the direction of the nanoparticle elongation in the sample was not exactly vertical but slightly offset to the left.

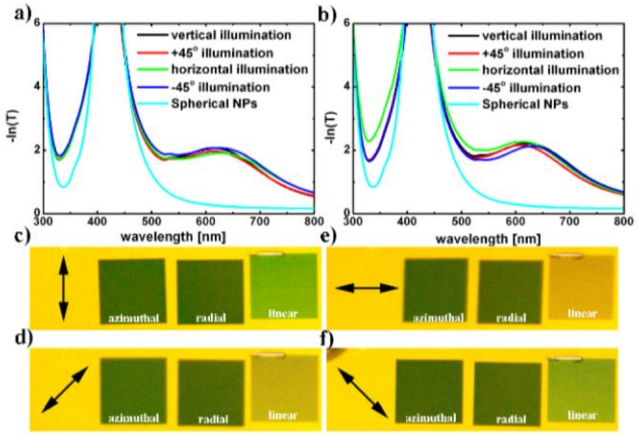

Fig. 4. Extinction spectra as a function of wavelength for samples irradiated with 2000 pulses per spot, laser fluence of ~60 mJ/cm^2, repetition rate of 200 kHz. Samples irradiated with (a) radial and (b) azimuthal polarizations. Spectra measured for different incident polarization directions of the illumination. The turquoise line shows extinction spectrum of the non-modified area of the sample that has spherical Ag nanoparticles. The microscope images of the 3 × 3 mm irradiated areas (c)-(f) of the sample in transmission with the linearly polarized illumination. Black arrows indicate the incident light polarization direction.

For further analyses, single lines were written in the MGN sample by scanning the laser beam, at first, from *left* to *right* with the same laser parameters as for the squares in order to define the laser-induced modifications at a smaller scale. The digital microscope images of the lines are shown in Fig. 5 with the microscope settings as in Fig. 4(c)-4(f). The lines possess somewhat noticeable "waviness" due to some instabilities in the beam scanning system. This, however, did not affect our further analyses. Figure 5(a) shows the lines irradiated with azimuthally polarized beam for *four* different incident polarizations of the illumination; Fig. 5(b) shows the radially polarized beam irradiated line. Two separate areas can be distinguished in each line - the blue/green colored part associated with the 'red-shifted' SPR band and the brown/red part that represents the 'blue-shifted' SPR. The left hand side insets in Fig. 5 indicate the position of the blue part on each line cross-section. The non-uniform coloration of the lines and its dependence on the polarization of illumination led us to believe that the blue/green part of each line is caused by the formation of ellipsoidal nanoparticles during irradiation with different angular positions along the cross-section of each line. This effect was obviously averaged for the large area squares presented earlier - Fig. 4(c)-4(f). It is also evident that these two lines irradiated with both azimuthally and radially polarized laser beams differ from each other antagonistically which can be a result of the very character of these polarizations - their polarization components are orthogonal to each other, e.g. the long axis of the Ag nano-ellipsoids is positioned vertically in the center of the azimuthally polarized beam irradiated line and horizontally on the edges- Fig. 5(a), whereas in the radially polarized beam irradiated line- Fig. 5(b), the vertically positioned Ag nano-ellipsoids are at the edges of the line and horizontally orientated ellipsoids are in the central part of the line- similar to the other illumination polarizations. In order to confirm these findings, a precise experimental setup, discussed in experimental methods and shown in Fig. 2, was constructed.

#244262 Received 2 Jul 2015; revised 12 Aug 2015; accepted 18 Aug 2015; published 27 Aug 2015

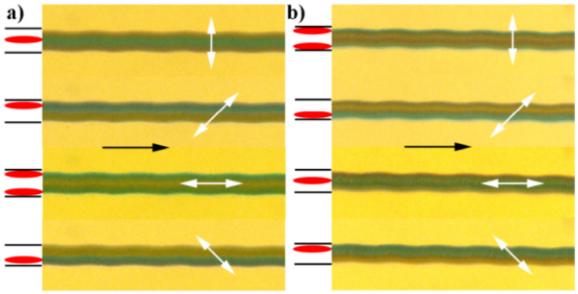

Fig. 5. Digital microscope images of the laser-modified single lines taken in transmission with different polarization directions of the illumination (white arrows). The lines were irradiated with (a) azimuthally and (b) radially polarized laser beams. The black arrows show the direction of irradiation. The blue/green areas of the lines (indicated by the red marker on the left hand side insets) show the long wavelength shifted part of the SPR - Ag nanoparticles are orientated parallel to the polarization direction of the illumination.

Intensities of the SH signal were measured as a function of the incident laser light polarization directions across the cross-sections of the azimuthally and radially polarized light modified lines. The intensity of the SHG is the highest for the polarization vector of the excitation beam aligned along the long axis of the nanoparticles. As previously mentioned the ellipsoidal shape modification and different orientations of the nano-ellipsoids within the laser modified lines are assumed. Results of the measurements are presented in Fig. 6. The normalized intensities of the SHG signals are shown in Figs. 6(a) and 6(b) as a function of the relative position within the line cross-section. The black arrows show the polarization of the incident laser beam. These results allowed us to determine the shape and orientation of the Ag nanoparticles in the laser modified areas for both azimuthal and radial polarizations. Figure 6(a) shows the results for azimuthally polarized laser modification. Here, the position of the highest intensity region is in agreement with the assumption made before: scanning across the line from the top to bottom- Figs. 6(c)-6(d), for horizontal polarization of the 1064-nm excitation beam the highest intensity of SH signal was registered at the edges (borders) of the line (top and bottom) corresponding to two peaks. Scanning from the top edge of the line down, based on the SH signal intensity changes the nano-ellipsoids orientated at 45° were found, followed by the 90°-orientated ellipsoids, for the excitation light being vertically polarized. The SH signal changes accordingly further down the cross-sectional scan for nanoparticles orientated at −45°. It is worth noting the orientation of the nanoparticles reshaped in this single scan. It is known from irradiation using linearly polarized light either at 400 nm or 532 nm that the originally spherical nanoparticles are reshaped to elliptical ones with their long axis along the polarization of the irradiated beam [3, 5]. From the above observations, one may conclude that in each irradiated spot using the azimuthally polarized beam *four* different orientations of the nanoparticles are observed. The cases of ± 45° are of particular interest here since these indicate that the final reshaping of the nanoparticles was dictated by the tails of laser pulses rather than their tips.

The SHG cross-sectional scans of the lines modified using radially polarized beam are presented in Fig. 6(b). Similarly scanning across the line from top to bottom- Figs. 6(c)-6(d), for the vertical polarization of the excitation beam at 1064 nm the largest SH signal was observed at the edges (borders) of the line (top and bottom) corresponding to two peaks. Further down the nano-ellipsoids orientated at −45° followed by the horizontally and + 45° orientated ellipsoids were identified. The peculiar orientations of the nanoparticles observed within each irradiated spot follow the same argument as for the azimuthal polarization. This supports the reshaping mechanism and the argument centered around the role of the tail of the laser pulses for nanoparticles orientated at ± 45°. It is worth nothing that for irradiation from

#244262 Received 2 Jul 2015; revised 12 Aug 2015; accepted 18 Aug 2015; published 27 Aug 2015

right-to-*left* the orientation of the nanoparticles situated at ± 45° are reversed as compared with irradiation from l*eft*-to-*right* considered above.

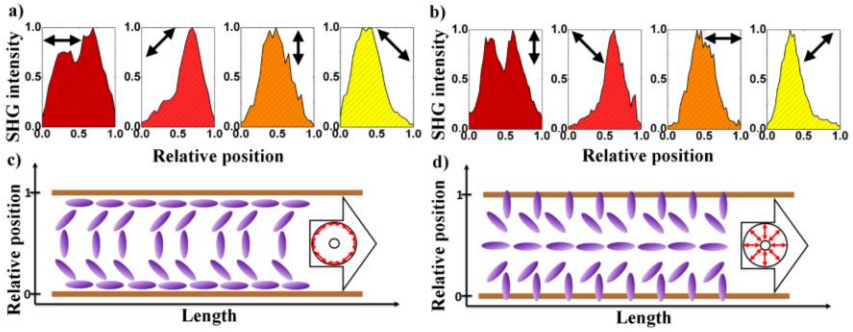

Fig. 6. Normalized SHG intensities as a function of the normalized line thickness for (a) azimuthally polarized irradiation and (b) radially polarized irradiation. Cross-sectional scans for different excitation beam (1064 nm) polarization directions - indicated by black arrows. Simplified depiction of the Ag ellipsoids orientations (c) and (d) within the line cross section according to (a) and (b) for both irradiation polarization directions - shown with red arrows.

4. Conclusions

Radially and azimuthally polarized picosecond pulsed irradiation of Ag nanoparticles embedded in soda-lime glass resulted in elongation of previously spherical nanoparticles and formation of uniquely positioned nano-ellipsoids. For this work, a picosecond pulsed laser (10 ps) at 532 nm was employed delivering 2000 pulses per spot at 200 kHz. The directionality of the nano-ellipsoids within the irradiated area was set by the laser polarization components - radial or azimuthal. A permanent SPR band shift has been observed in a multi-pulse irradiation regime. Characterization of the created nano-structures was performed with the use of SHG from the reshaped nanoparticles. This effect gave a precise description of the structures obtained at the micro- and nano-scale, showing that the nanoparticles were elongated in different directions within each of the irradiated line cross sections. The opposing character of reshaping between the radial and azimuthal polarizations was presented. Macroscopically, linear optical properties for these two incident polarizations were in agreement.

The reshaping method presented adds an additional technique to shape manipulations of MGNs embedded in soda-lime glass. It expands the knowledge base of already existing methods for versatile techniques of reshaping of nanoparticles with ultra-short laser pulses. It paves the way for nanoparticle shape modification in terms of future new experiments that could be performed with different laser polarizations in order to achieve more complicated nanoparticle modification [17–23]. This method can lead to nano-engineering of novel optical materials for applications in security and data storage with highly improved marking capacity due to fine nanoparticle position control. The functionality and applicability of these types of material in photonics could be vast, and the method of fabrication using ps pulsed laser sources proves to be robust and cost effective.

Acknowledgments

This work was conducted under the aegis of the Engineering and Physical Sciences Research Council (EPSRC) of the United Kingdom (EP/I004173/1). We are very grateful to CODIXX AG of Barleben/Germany for providing the samples for this study. MAT is a Marie Curie Early Career Fellow within the LA^{3}NET Network (Grant Agreement Number 289191). All data created during this research are openly available from the University of Dundee Institutional Repository at http://dx.doi.org/10.15132/10000104.

#244262 Received 2 Jul 2015; revised 12 Aug 2015; accepted 18 Aug 2015; published 27 Aug 2015

OPEN ACCESS
IOP Publishing
Nanotechnology

Nanotechnology **27** (2016) 435703 (8pp)
doi:10.1088/0957-4484/27/43/435703

On second harmonic generation and multiphoton-absorption induced luminescence from laser-reshaped silver nanoparticles embedded in glass

S A Zolotovskaya[1,4], M A Tyrk[2,4], A Stalmashonak[3], W A Gillespie[2] and A Abdolvand[2]

[1] Materials Science Institute, Engineering Department, Lancaster University, Lancaster LA1 4YW, UK
[2] Materials & Photonic Systems Group, School of Science & Engineering, University of Dundee, Dundee DD1 4HN, UK
[3] CODIXX AG, Steifeldstr. 3, D-39179 Barleben, Germany

E-mail: a.abdolvand@dundee.ac.uk

Received 15 July 2016, revised 17 August 2016
Accepted for publication 31 August 2016
Published 23 September 2016

Abstract

Spherical silver nanoparticles (NPs) of 30 nm diameter embedded in soda-lime glass were uniformly reshaped (elongated) after irradiation by a linearly polarised 250 fs pulsed laser operating within the NPs' surface plasmon resonance band. We observed second harmonic generation (SHG) and multiphoton-absorption-induced luminescence (MAIL) in the embedded *laser-reshaped* NPs upon picosecond (10 ps) pulsed laser excitation at 1064 nm. A complementary study of SHG and MAIL was conducted in soda-lime glass containing embedded, *mechanically-reshaped* silver NPs of a similar elongation ratio (aspect ratio) to the *laser-reshaped* NPs. This supports the notion that the observed difference in SHG and MAIL in the studied nanocomposite systems is due to the shape modification mechanism. The discrete dipole approximation method was used to assess the absorption and scattering cross-sections of the reshaped NPs with different elongation ratios.

Keywords: surface plasmon resonance, metal-glass nanocomposites, metallic nanoparticles, nonlinear properties

(Some figures may appear in colour only in the online journal)

1. Introduction

Metallic nanoparticles (NPs) have gained a great deal of attention in recent years due to their unique linear and nonlinear optical properties. These properties result from localised surface plasmon resonances (SPRs) originated from collective charge density oscillations of free electrons in metal particles. Alkali-rich glass of soda-lime variety has been proposed as one of host matrices for the formation of embedded silver (Ag) NPs [1], thus forming a Metal-Glass Nanocomposite (MGN). It was shown that optical and structural properties of the MGNs are easily manipulated upon irradiation with nano-, pico- and femtosecond pulse laser sources [2–8]. Ultra-short-pulse laser irradiation is a well-established *spatially selective* method for Ag NP shape modification, which depends strongly on the polarisation state of the incident laser beam. For instance, linearly polarised irradiation at low intensity ($\leqslant 0.5\,\mathrm{TW\,cm^{-2}}$) leads to the formation of Ag nano-ellipsoids with their long axis aligned

[4] Authors contributed equally to this work.

along the laser polarisation direction [3, 5, 6]; circular polarisation leads to the formation of nano-discs; radial (or azimuthal) polarisation results in a set of ellipsoids orientated in the directions reflecting the local polarisation state of the incident beam [9]. Laser-assisted shape modification of NPs leads to the observation of *local* optical dichroism achieved via spatially selective modification of the SPR position depending on the laser parameters. On the other hand, simultaneous heating and tensile deformation of MGNs results in *global* shape modification of Ag NPs, producing uniformly orientated ellipsoids in the volume of the glass matrix. These mechanically stretched MGNs are routinely used as high-contrast polarisers [10], and have also demonstrated second harmonic generation (SHG) when subjected to femtosecond pulse laser excitation at 800 nm [11].

In this paper, for the first time to our knowledge, we demonstrate SHG from *locally* reshaped (*laser-reshaped*) Ag NPs embedded in soda-lime glass. The spectrally resolved nonlinear optical response in these MGNs revealed the presence of multiphoton-absorption-induced luminescence (MAIL) along with the SH signal. Complementary studies of SHG were carried out in a mechanically stretched MGN containing ellipsoidal Ag NPs with a similar aspect ratio. The dependence of SHG and MAIL on the aspect ratio of Ag nano-ellipsoids in the laser-reshaped MGNs is reported and compared to the results of modelling obtained using a discrete dipole approximation (DDA) approach [12].

2. Experimental techniques

Two glass substrates ($40 \times 40\,mm^2$) containing spherical Ag NPs (*MGN-I* and *MGN-II*) were used for SHG measurements (figure 1). In both cases, the formation of Ag clusters in the glass matrix was achieved via a thermally assisted Ag^+/Na^+ ion-exchange process—described in detail elsewhere [13–15]. A 1 mm soda-lime silica float glass (glass composition in wt.-%: 72.5 SiO_2, 14.4 Na_2O, 6.1 CaO, 0.7 K_2O, 4.0 MgO, 1.5 Al_2O_3, 0.1 Fe_2O_3, 0.1 MnO, 0.4 SO_3) was immersed in a mixed melt of $AgNO_3$ and KNO_3 at 400 °C (for a duration of 30 min at 400 °C in a mixed melt of 2 weight-% $AgNO_3$ and 98 weight-% KNO_3) and was subsequently annealed at about 500 °C in a H_2 reduction atmosphere for approximately 12 h [15]. This resulted in the formation of *spherical* Ag particles of $30 - 40$ nm in diameter in ~20 μm surface layers on both sides of the glass sample. Single-sided samples were produced by removal of the nanoparticle-containing layer from one side of the samples by etching the samples in a solution of 12% hydrofluoric acid. An extinction spectrum of the samples containing spherical Ag NPs (shown in figure 1(a)—black line) exhibits a strong SPR band at ~430 nm, which is consistent with the NP size.

2.1. Introducing MGN-I

The laser-assisted reshaping of one of the MGNs (henceforth called *MGN-I*) was conducted using a 250 fs Yb:KGW laser system (PHAROS laser, Light Conversion Ltd) equipped with a collinear optical parametric amplifier (ORPHEUS OPA, Light Conversion Ltd) operating at 500 kHz. The laser beam was focused into a spot of 30 μm full width at $1/e^2$ intensity level. Figure 1(c) shows *four* areas of $5 \times 5\,mm^2$ of *MNG-I* sample that were irradiated with different laser parameters in order to achieve different Ag ellipsoid aspect ratios (the $R = a/b$ ratio of the long a to short b axis). After the first irradiation step (Irradiation 1, table 1) for FEM A–D, the laser was tuned to an off-resonance position (Irradiation 2, table 1) for one of the irradiated areas, namely FEM D. This subsequent irradiation at 750 nm (long-wavelength side of the already modified SPR) allowed for further elongation of the NPs and led to the aspect ratio of $R \sim 4.1$ in FEM D, hence pronounced optical dichroism in comparison to what is expected after only a single-wavelength irradiation [5]. The employed laser parameters are summarised in the table 1.

The polarised extinction spectra of *MGN-I* sample were measured using a spectrophotometer (JASCO V-670 UV/VIS/NIR) and are shown in figure 1(a). After laser irradiation the original SPR band of the spherical Ag NPs, peaked at about 430 nm, splits into *two* polarisation dependent bands (FEM A, B, C, and D) with the long axis of the NPs being orientated along the laser polarisation (p-polarisation). The p-polarised SPR bands for all four irradiated areas are shown in figure 1(a). It can be seen that consecutive irradiations at longer wavelengths lead to a larger spectral gap between the polarised SPR bands (larger red-shift of the p-polarisation) thus confirming increase in the aspect ratio of the reshaped NPs with the maximum laser-assisted elongation achieved for FEM D sample. The observed residual absorption at 430 nm in all laser-reshaped samples are due to the presence of some unmodified spherical Ag NPs within the NP containing layer and further away from the *MGN-I* sample surface. Furthermore, in FEM D sample the residual peak at ~580 nm is also due to the 'non-modified' NPs after the second irradiation (subsequent irradiation). Therefore, FEM D contains reshaped NPs with aspect ratios of both 2.6 and 4.1.

2.2. Introducing MGN-II

The mechanical reshaping of Ag NPs was carried out by subjecting a 1 mm thick MGN sample with a nanoparticle-containing layer of about 20 μm to tensile deformation with simultaneous heating below the transition temperature of the glass [21]. This results in uniformly orientated Ag ellipsoids without visible stress-induced birefringence in the glass matrix, figure 1(d). After mechanical deformation the total thickness of the *MGN-II* sample and nanoparticle-containing layer were reduced to ~200 μm and 4 μm, respectively. The polarised extinction spectra of the mechanically stretched *MGN-II* are shown in figure 1(b), showing splitting of the SPR band. The increased bandwidth of the p-polarised SPR band is due to uniform deformation of Ag NPs. The aspect ratio of the mechanically stretched Ag NPs was estimated to be ~4.9.

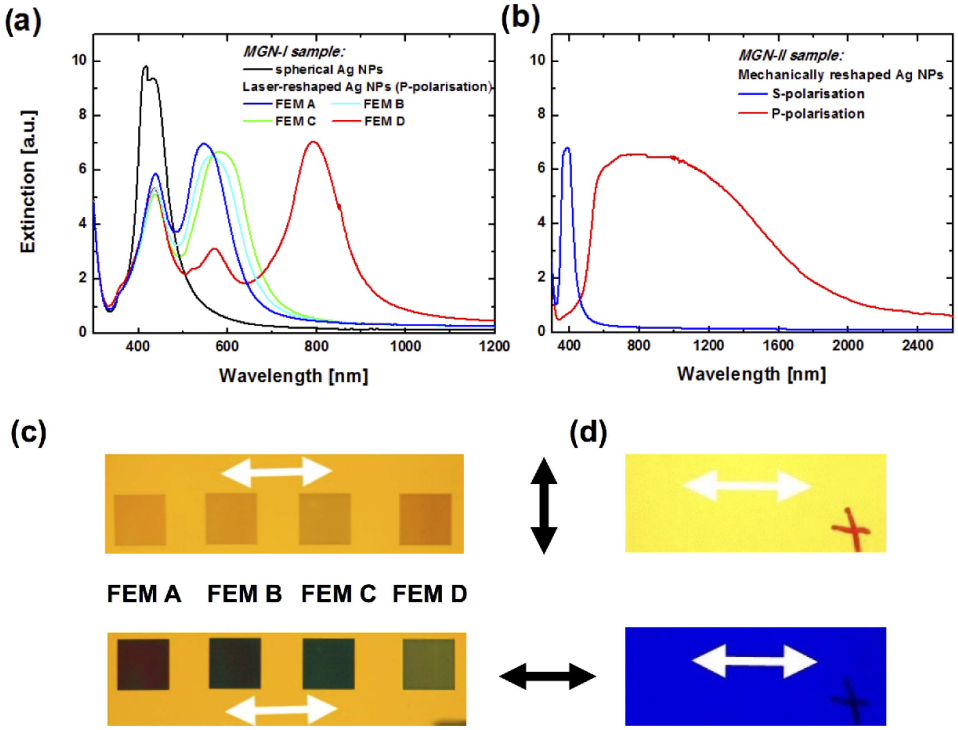

Figure 1. Note that p-polarisation is for the light polarised parallel to the long axis while s-polarisation is parallel to the short axis of the Ag prolate spheroids. (a) Polarised extinction spectra of the original MGN containing spherical Ag NPs (black line) and laser-reshaped Ag NPs (*MGN-I*). Here only p-polarisation spectra of *MGN-I* are shown. (b) Polarised extinction spectra of the sample containing mechanically reshaped Ag NPs (*MGN-II*). Here both s- and p-polarisation spectra of *MGN-II* are shown for clarity. Images of the laser (c) and mechanically (d) reshaped MGNs are taken in polarised light. Black arrows indicate the polarisation direction of the incident light; white arrows show the orientation of the long axis of the Ag nano-ellipsoids.

Table 1. Laser-assisted reshaping of MGNs: femtosecond pulse laser irradiation parameters (λ_L—laser wavelength; P_p—peak pulse intensity; N_p—number of pulses per spot; λ_{SPR}—*longitudinal* SPR peak position; R—aspect ratio). The work on estimating aspect ratios is explained in the text.

	Irradiation 1			Irradiation 2				
Sample	λ_{L1} (nm)	P_{p1} (TW cm $^{-2}$)	N_{p1}	λ_{L2} (nm)	P_{p2} (TW cm $^{-2}$)	N_{p2}	λ_{SPR} (nm)	R
FEM A	515	0.362	200				547	2.3
FEM B	515	0.362	300				567	2.5
FEM C	515	0.317	500				585	2.6
FEM D	515	0.317	500	750	0.288	500	792	4.1

2.3. Estimating aspect ratios

The aspect ratios of the laser-reshaped Ag NPs, summarised in table 1, and also Ag NPs in *MGN-II* were estimated using Gans's extension of Mie theory for non-spherical particles [16]. The extinction coefficient γ of randomly orientated particles in the dipole approximation is given by [16, 17]:

$$\gamma = \frac{2\pi N V \epsilon_m^{3/2}}{3\lambda} \sum_j \frac{(1/P_j^2)\epsilon_2}{\left(\epsilon_1 + \frac{1-P_j}{P_j}\epsilon_m\right)^2 + \epsilon_2^2}, \quad (1)$$

where N is the number of particles per unit volume, V is the particle volume, ϵ_m is the dielectric constant of the host medium, λ is the wavelength of the interacting light, and ϵ_1 and ϵ_2 are the real and imaginary part of the dielectric constant of the metal inclusions. For the *three* axes a, b, and c of the ellipsoid with dimensions $a > b$ and $b = c$, the depolarisation factors P_j are defined as:

$$P_a = \frac{1-r^2}{r^2}\left[\frac{1}{2r}\ln\left(\frac{1+r}{1-r}\right) - 1\right], \quad (2)$$

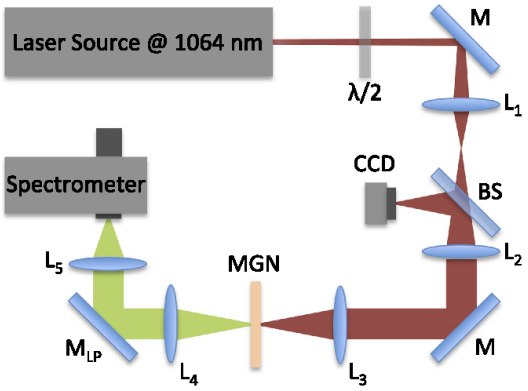

Figure 2. Schematic of the optical setup for SHG/MAIL measurements: $\lambda/2$–half-wave plate at 1064 nm; M–mirror; L_1 and L_2–a 1.3× laser beam expander; CCD–a CCD camera used for sample positioning, L_3–a 100 mm focal length lens; MGN–a metal-glass nanocomposite sample; L_4–a 75 mm focal length lens; M_{LP}–a longpass dichroic mirror with a cut-off wavelength at 900 nm; L_5–a 63 mm focal length lens.

$$P_b = P_c = \frac{1 - P_a}{2}, \tag{3}$$

where $r = \sqrt{1 - (b/a)^2}$.

This approach, was adopted in [18, 19] to simulate extinction spectra of gold nano-rods, demonstrated the *linear* relationship between the longitudinal SPR peak position and the aspect ratio of the nano-rods. Therefore it can be used to estimate the NPs elongation ratios for certain SPR band positions by considering that the resonance condition for the longitudinal mode is nearly fulfilled at [17]:

$$\epsilon_1 = -\frac{(1 - P_a)\epsilon_m}{P_a}. \tag{4}$$

For our estimates, the Ag dielectric constant was adopted from [20] and the host medium dielectric constant was 2.33 for the soda lime glass with the refractive index of 1.53. The real part of the dielectric constant for Ag was found to be almost linear in the spectral range from 500 to 900 nm: $\epsilon_1(\lambda) = 28.52 - 0.075\lambda_{SPR}$. Similarly $(1 - P_a)/P_a$ plotted as a function of the aspect ratio R from 2 to 6 and linearised in accordance with: $(1 - P_a)/P_a = -4.64 + 4.35R$. The longitudinal SPR band positions were determined from the extinction spectra, figures 1(a), (b) and summarised in table 1.

2.4. SHG set-up

Figure 2 illustrates the experimental arrangement. A linearly polarised 10 ps pulse laser at 1064 nm with a repetition rate of 200 kHz (Talisker Ultra, Coherent) was used as an excitation source for the SHG measurements. The measurements were performed in transmission geometry with the 1064 nm fundamental beam focused at normal incidence on the MGN sample surfaces. A half-wave plate ($\lambda/2$) at 1064 nm was employed to control the polarisation plane of the incident beam relative to the axes of the Ag nano-ellipsoids. A lens (L_3) with a focal length of 100 mm was used to focus the beam into ~64 μm diameter spot at $1/e^2$ intensity level. The SH signal was collected with a 75 mm focal length lens (L_4) and the fundamental beam was filtered out with a long-pass dichroic mirror (M_{LP}, 900 nm cut-off wavelength). The SH signal was then focused with a 63 mm focal length lens (L_5) on to the spectrometer (MS257, Oriel Instruments) equipped with a TE-cooled CCD at −70 °C (Newton 920, Andor). The MGNs were illuminated by the fundamental harmonic with fluences of up to 2 mJ cm^{-2} to avoid photo-induced dissolution discussed elsewhere [22]. The accumulated signal (total *four* accumulations, each 1 s integration time) was analysed.

3. Results and discussion

In order to establish possible contributions to SH signal from the host matrix impurities, residual Ag ions and unmodified spherical Ag NPs, *three* sample groups of (*i*) undoped soda-lime glass, (*ii*) soda-lime glass doped with Ag ions, and (*iii*) soda-lime glass embedded with spherical Ag NPs (original MGN substrate before laser and/or mechanical modification) were investigated under identical experimental conditions. Neither SH nor MAIL signals were observed in any of the samples.

First, the dependence of SH intensity on the polarisation plane orientation of the laser operating at its fundamental harmonic of 1064 nm was investigated in the *MGN-II* sample containing mechanically reshaped Ag NPs. Since its SPR band position coincided well with the excitation wavelength, the highest incident field coupling and local field enhancement was expected. The polarisation plane of the laser beam was rotated relative to the long axis of elongated NPs by a $\lambda/2$-wave plate. The SH signal reached maximum for the fundamental harmonic polarised parallel to the long axis of the Ag NPs, i.e. for the fundamental harmonic polarisation angle equal to 0° (p-pol fundamental harmonic), as shown in figure 3(a).

The SH signal polarisation components, denoted as p-pol SH and s-pol SH in figure 3(b), were selected by placing a rotating polariser at the entrance slit of the spectrometer while keeping the polarisation plane of the fundamental beam parallel to the long axis of Ag NPs (p-pol fundamental harmonic). Two SH signal maxima were observed for p-pol SH where the SH polarisation plane is parallel to the long axis of the Ag nano-ellipsoids, at ±90° in figure 3(b). Therefore, the character of the SH signal obtained from *MGN II* is purely dipolar.

The spectrally resolved nonlinear optical response obtained in the laser reshaped (*MGN I*: FEM A, B, C & D) and mechanically reshaped (*MGN-II*) samples of MGN are shown in figure 4. The SH signal peaked at 532 nm accompanied by strong photo-induced luminescence can be seen in the spectra. The observed photoluminescence is attributed to the excitation via multiphoton absorption. Indeed, MAIL has been observed in a number of noble metal-based structures upon irradiation with ultra-short pulsed lasers [23–28]. For bulk metals the light emission follows the excitation of

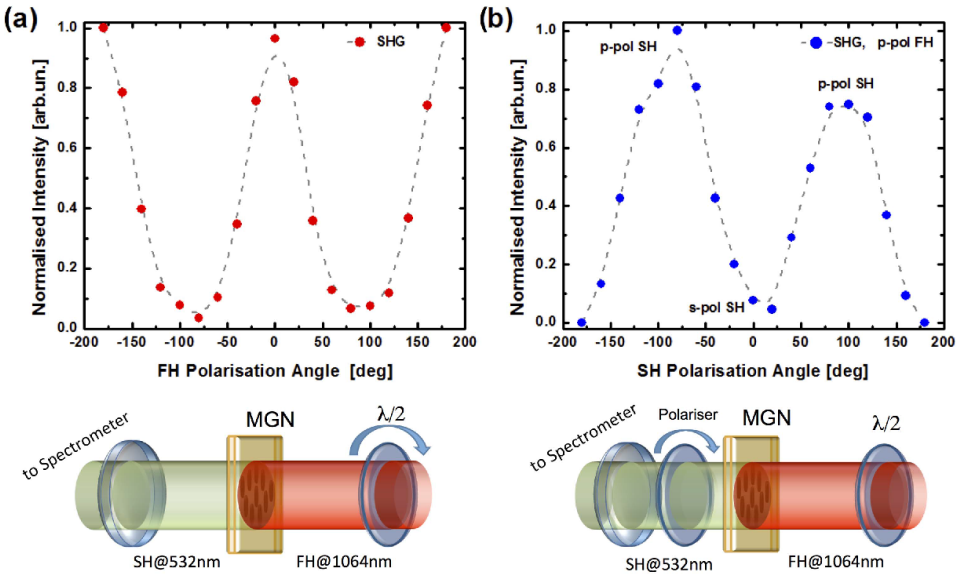

Figure 3. Measured SH intensity of mechanically reshaped MGN (*MGN-II*). (a) Polarisation dependence of SH signal intensity on orientation of the fundamental harmonic (*noted FH in the image for brevity*) beam polarisation plane (0 deg. corresponds to the incident excitation beam polarisation direction parallel to the long axis of Ag NPs). (b) SH signal polarisation components with the fundamental harmonic beam polarised parallel to the long axis of Ag NPs, p-pol fundamental harmonic (p-pol SH and s-pol SH are the SH signals polarised parallel to the long and short axes of Ag NPs respectively). Corresponding schematics of the experimental conditions are also shown for clarity.

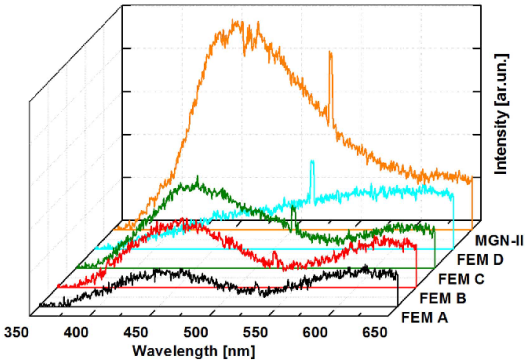

Figure 4. Spectrally resolved nonlinear optical responses of the laser reshaped (*MGN I*: FEM A, B, C and D) and mechanically reshaped (*MGN-II*) samples of MGN for the excitation pulse energy of 50 nJ. The spectra were processed using Savitzky–Golay smoothing filter (5 point quadratic polynomial order) for clarity in the presented data.

electron transition from 5*d*- to 6*ps*-bands [29]. It is known that in low dimensional systems the light emission is considerably enhanced by the local fields associated with the surface plasmons. Furthermore, the dielectric environment can play a significant role in the efficiency of MAIL, quenching or enhancing the signal due to different energy transfer processes.

Two maxima peaked at around 450 and 625 nm can be identified in MAIL spectra of the laser-reshaped FEM A, B and C samples, figure 4. The intensity of the blue band at ~450 nm increases with increase in Ag nano-ellipsoid aspect ratio from 2.3 to 2.6 for these samples. It is also the most intense band observed in mechanically reshaped MGN (*MGN-II*, figure 4) with the highest aspect ratio of 4.9. One may assume that the coupling into SPR improves with increasing aspect ratio of the NPs. Note that this band is suppressed in FEM D sample. This observation may be attributed to the fact that FEM D contains reshaped NPs with aspect ratios of both 2.6 and 4.1 due to the subsequent irradiation, hence quenching the signal at ~450 nm. Some background contribution into the blue band component of MAIL at 450 nm may also be attributed to Ag^+ ions inhomogenously distributed within the volume of the glass during the fabrication step and as a result of the Ag^+–Na^+ ion exchange process [30], and to Ag^+–Ag^+ interaction pairs due to the high concentration of the Ag^+ ions in the glass [31, 32].

One also observes that the MAIL spectrum of the laser-reshaped sample FEM D with an aspect ratio of 4.1 is dominated by 625 nm band, figure 4. The 625 nm MAIL band can be attributed to the small charged clusters such as Ag_2^+, Ag_2^{2+}, Ag_3^+ and Ag_3^{2+} formed during laser-assisted reshaping. This band was also observed in the single-photon luminescence studies on laser-induced ionisation and photo-modification of Ag NPs in soda lime glass [30]. The laser-assisted reshaping, described in detail elsewhere [5], results in formation of the cationic shell in the vicinity of the Ag NPs. The density of this cationic shell is higher around the Ag nano-

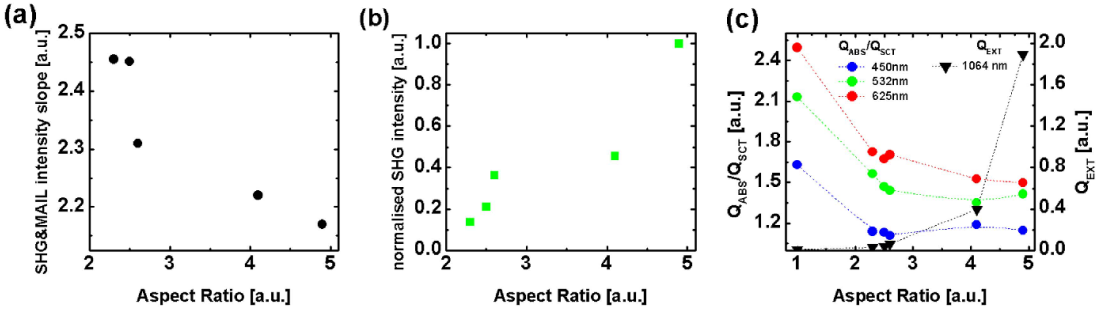

Figure 5. (a) SHG and MAIL integrated intensity slopes obtained for the pulse energies from 10 to 80 nJ in the MGN with corresponding aspect ratios. (b) Integrated SH signal achieved at pump pulse energy of 50 nJ in MGNs with different elongation ratios. (c) Absorption (Q_{ABS}), scattering (Q_{SCT}) at the wavelengths of 450, 532 and 625 nm and extinction (Q_{EXT}) at 1064 nm efficiency factors calculated using DDA.

ellipsoids with large aspect ratios. This explains the 625 nm band intensity increase observed with increase in the aspect ratio of laser-reshaped MGNs and the fact that the band is not pronounced in the MAIL spectrum of the mechanically stretched *MGN-II*.

Indeed MAIL-in contrast to SHG-involves absorption of an excitation photon followed by its re-emission in a radiative transition. As shown in [24], the difference in observed nonlinear responses from Ag nano-ellipsoids with different aspect ratios can be associated with the relative strength of scattering and absorption in NPs. It has also been shown [24] that for elongated metal NPs, there is a competition between SHG and MAIL. Figure 5(a) shows the SHG and MAIL intensity slopes achieved in our MGN samples for the excitation pulse energies between 10 and 80 nJ. For the MGN sample containing least modified NPs (*MGN I*: FEM A with aspect ratio of 2.3) the intensity slope is ~2.45, whereas for FEM D, with the estimated aspect ratio of 4.1, it falls to ~2.2, and finally to ~2.17 for the mechanically stretched (*MGN-II*) sample with aspect ratio of 4.9. Since SHG and two-photon-induced luminescence scale quadratically with intensity of the incident light, observed slope deviations may suggest that three-photon-induced processes are also present in the MAIL signal around 360 nm. Therefore, in MGNs containing Ag NPs with large aspect ratios, SHG is likely to be the dominant process (figure 5(b)).

Figure 5(c) shows the absorption (Q_{ABS}), scattering (Q_{SCT}) and extinction (Q_{EXT}) efficiency factors of Ag NPs with different elongation ratios estimated using the DDA method [12, 33, 34]. The Ag dielectric constant was adopted from [20]. The host medium refractive index of 1.53 was assumed to be constant in the wavelength range under consideration. The effective radius (a_{eff}) used for the NPs in the simulations was taken to be 15 nm. The number of dipoles, equal to a target size of 60 × 60 × 60, was kept constant and only the aspect ratio was varied in accordance with the values summarised in table 1. The incident radiation in the model was assumed to be linearly polarised along the long axis of the target reflecting the experimental conditions used. The DDA simulation results confirm that the extinction for Ag NPs at 450, 532 and 625 nm is dominated by absorption for all aspect ratios under consideration. The decrease in absorption to scattering ratio (Q_{ABS}/Q_{SCT}) observed for large aspect ratios (i.e. the laser-reshaped *MGN I*: FEM D and mechanically-reshaped *MGN-II* with 4.1 and 4.9 aspect ratios, respectively) also correlate with experimentally observed increase in SHG intensity (figure 5(b)).

The simulation results confirm that MAIL phenomenon is dominant in the Ag nano-ellipsoids with small aspect ratios (i.e. the laser-reshaped *MGN-I*: FEM A, B and C with estimated aspect ratios of 2.3, 2.5 and 2.6 respectively). It is worth noting that the spectrally resolved optical response in the laser-reshaped MGNs, registered in transmission geometry and shown in figure 4, can be substantially modified due to the self-absorption in reshaped and unmodified spherical Ag NPs within the NPs containing layer, as simulation results suggest for the Ag NPs with aspect ratio of 1, in figure 5(c).

4. Conclusions

It has been shown that both SHG and MAIL are present for ellipsoidal Ag NPs embedded in soda-lime glass. SHG and MAIL spectra were explained for *two* different types of nanoparticle reshaping mechanisms: laser reshaped (*local modification*) and mechanically stretched (*global modification*). It was argued that ion species in the vicinity of the laser reshaped NPs and small Ag ions in the volume of the NP containing layer are responsible for the observed MAIL signal in the visible range. It was concluded that competition between SHG and MAIL arises from the difference in scattering and absorption cross-sections of the NPs. It was shown that SHG is prominent for NPs with higher aspect ratios.

Both mechanical stretching and laser-assisted reshaping of the Ag NPs provide a simple and yet effective tool for spectral manipulation of the SPRs. By subsequent irradiation of MGNs with precisely chosen wavelengths, elongation effects greater than the values presented here can be achieved, leading to higher scattering cross sections and effectively

better frequency doubling abilities. Laser reshaping (unlike mechanical stretching) provides spectral selectivity, and more importantly the much needed *spatial selectivity,* for fast and local nanoprocessing of MGNs, paving the way for the fabrication of micro-patterned optical elements [35] in photonics, security and data storage [36].

Acknowledgments

This research was conducted under the aegis of the Engineering and Physical Sciences Research Council (EPSRC) of the United Kingdom (EP/I004173/1). MAT was a Marie Curie Early Career Fellow within the LA^{3}NET Network (Grant Agreement Number 289191) at the University of Dundee when part of this work was conducted. All data created during this research are openly available from the University of Dundee Institutional Repository.

References

[1] Kreibig U and Vollmer M 1995 *Optical Properties of Metal Clusters* (*Springer Series in Materials Science*) (Berlin: Springer)
[2] Fleming L A H, Tang G, Zolotovskaya S A and Abdolvand A 2014 Controlled modification of optical and structural properties of glass with embedded silver nanoparticles by nanosecond pulsed laser irradiation *Opt. Mater. Express* **4** (5) 969
[3] Tyrk M A, Gillespie W A, Seifert G and Abdolvand A 2013 Picosecond pulsed laser induced shape transformation of metallic nanoparticles embedded in a glass matrix *Opt. Express* **21** 21823–8
[4] Stalmashonak A, Graener G and Seifert G 2009 Transformation of silver nanospheres embedded in glass to nanodisks using circularly polarized femtosecond pulses *Appl. Phys. Lett.* **94** 193111
[5] Stalmashonak A, Seifert G and Abdolvand A 2013 *Ultra-short Pulsed Laser Engineered Metal-Glass Nanocomposite* (*SpringerBrief in Physics*) (Berlin: Springer)
[6] Kaempfe M, Rainer T, Berg K-J, Seifert G and Graener H 1999 Ultrashort laser pulse induced deformation of silver nanoparticles in glass *Appl. Phys. Lett.* **74** 1200
[7] Doster J, Baraldi G, Gonzalo J, Solis J, Hernandez-Rueda J and Siegel J 2014 Tailoring the surface plasmon resonance of embedded silver nanoparticles by combining nano- and femtosecond laser pulses *Appl. Phys. Lett.* **104** 153106
[8] Baraldi G, Gonzalo J, Solis J and Siegel J 2013 Reorganizing and shaping of embedded near-coalescence silver nanoparticles with off-resonance femtosecond laser pulses *Nanotechnology* **24** 255301
[9] Tyrk M A, Zolotovskaya S A, Gillespie W A and Abdolvand A 2015 Radially and azimuthally polarized laser induced shape transformation of embedded metallic nanoparticles in glass *Opt. Express* **23** 23394–400
[10] https://codixx.de/en/home.html
[11] Podlipensky A, Lange J, Seifert G, Graener H and Cravetchi I 2003 Second-harmonic generation from ellipsoidal silver nanoparticles embedded in silica glass *Opt. Lett.* **28** 716–8
[12] Draine B T 1988 The discrete-dipole approximation and its application to interstellar graphite grains *Astrophys. J.* **333** 848–72
[13] Quaranta A, Cattaruzza E and Gonella F 2008 Modelling the ion exchange process in glass: phenomenological approaches and perspectives *Mater. Sci. Eng.* B **149** 133–9
[14] Opilski A, Rogozinski R, Gut K, Blahut M and Opilski Z 2000 Present state and perspective involving application of ion exchange in glass *Opto-Electron. Rev.* **8** 117–27
[15] Berg K-J, Berger A and Hofmeister H 1991 Small silver particle in glass-surface layers produced by sodium-silver ion-exchange-their concentration and size depth profile *Z. Phys.* D **20** 309–11
[16] Gans R 1915 Über die form ultramikroskopischer silberteilchen *Ann. Phys.* **47** 270–84
[17] Papavassiliou G C 1979 Properties of small inorganic and organic metal particles *Prog. Solid State Chem.* **12** 185–271
[18] Link S, Mohamed M B and El-Sayed M A 1999 Simulation of the optical absorption spectra of gold nanorods as a function of their aspect ratio and the effect of the medium dielectric constant *J. Phys. Chem.* B **103** 3073–7
[19] Link S and El-Sayed M A 1999 Simulation of the optical absorption spectra of gold nanorods as a function of their aspect ratio and the effect of the medium dielectric constant *J. Phys. Chem.* B **103** 3073–7
Link S and El-Sayed M A 2005 *J. Phys. Chem.* B **109** 10531–2 erratum
[20] Johnson P B and Christy R W 1972 Optical constants of the noble metals *Phys. Rev.* B **6** 4370–9
[21] Hofmeister H, Drost W-G and Berger A 1999 Orientated prolate silver nanoparticles in glass-characteristics of novel dichroic polarizers *Nanostr. Mat.* **12** 207–10
[22] Stalmashonak A, Unal A A, Graener H and Seifert G 2009 Effects of temperature on laser-induced shape modification of silver nanoparticles embedded in glass *J. Phys. Chem.* C **113** 12028–32
[23] Eichelbaum M, Schmidt B E, Ibrahim H and Rademann K 2007 Three-photon-induced luminescence of gold nanoparticles embedded in and located on the surface of glassy nanolayers *Nanotechnology* **18** 355702
[24] Deng H-D, Li G-C, Dai Q-F, Ouyang M, Lan S, Trofimov V A and Lysak T M 2013 Size dependent competition between second harmonic generation and two-photon luminescence observed in gold nanoparticles *Nanotechnology* **24** 075201
[25] Boyd G T, Yu Z H and Shen Y R 1986 Photoinduced luminescence from the noble metals and its enhancement on roughened surfaces *Phys. Rev.* B **33** 7923–36
[26] Farrer R A, Butterfield F L, Chen V W and Fourkas J T 2005 Highly efficient multiphoton-absorption-induced luminescence from gold nanoparticles *Nano Lett.* **5** 1139–42
[27] Dowling M B, Li L, Park J, Kumi G, Nan A, Ghandehari H, Fourkas J T and DeShong P 2010 Multiphoton-absorption-induced-luminescence (MAIL) Imaging of tumor-targeted gold nanoparticles *Bioconjugate Chem.* **21** 1968–77
[28] Dai D C, Xu S J, Shi S I and Xie M H 2005 Efficient multiphoton-absorption-induced luminescence in single-crystalline ZnO at room temperature *Opt. Lett.* **30** 3377–9
[29] Mooradian A 1969 Photoluminescence of metals *Phys. Rev. Lett.* **22** 185
[30] Podlipensky A V, Grebenev V, Seifert G and Graener H 2004 Ionization and photomodification of Ag nanoparticles in soda-lime glass by 150 fs laser irradiation: a luminescence study *J. Lumin.* **109** 135–42
[31] Cattaruzza E, Mardegan M, Trave E, Battaglin G, Calvelli P, Enrichi F and Gonella F 2011 Modifications in silver-doped silicate glasses induced by ns laser beams *Appl. Surf. Sci.* **257** 5434–8
[32] Borsella E, Battaglin G, García M A, Gonella F, Mazzoldi P, Polloni R and Quaranta A 2000 Structural incorporation of silver in soda-lime glass by the ion-exchange process: a

photoluminescence spectroscopy study *Appl. Phys.* A **71** 125–32
[33] Draine B T and Goodman J 1993 Beyond clausius-mossotti: wave propagation on a polarizable point lattice and the discrete dipole approximation *Astrophys. J.* **405** 685–97
[34] Draine B T and Flatau P J 1994 Discrete dipole approximation for scattering calculations *J. Opt. Soc. Am.* A **11** 1491–9
[35] Seifert G, Unal A A, Skrzypczak U, Podlipensky A, Abdolvand A and Graener H 2009 Toward the production of micropolarizers by irradiation of composite glasses with silver nanoparticles *Appl. Opt.* **48** F38–44
[36] Stalmashonak Andrei, Abdolvand Amin and Seifert Gerhard 2011 Metal-glass nanocomposite for optical storage of information *Appl. Phys. Lett.* **99** (20) 201904